

INVESTIGATING STRUCTURE AND DYNAMICS  
OF ZEOLITES AND ZEOTYPES  
WITH DENSITY FUNCTIONAL THEORY CALCULATIONS

**Habilitationsschrift**

(in englischer Sprache)

zur Erlangung der *venia legendi*

im Lehr- und Forschungsgebiet

*Computational Mineralogy and Crystallography*

Dem Fachbereich Geowissenschaften  
der Universität Bremen

vorgelegt von

**Dr. Michael Fischer**

Bremen

im

Oktober 2022

## SUMMARY

Zeolites and zeolite-like materials (zeotypes) are crystalline, inorganic frameworks built up from corner-sharing tetrahedra. There are a number of zeolite minerals that are of considerable relevance in a geoscientific context and as natural resources. Economically, however, synthetic zeolites are of an even greater importance, with large-scale applications in catalysis, separation, and ion exchange. For example, a large fraction of currently used transport fuels is produced via the catalytic cracking of hydrocarbons, which uses zeolite catalysts. Zeolites can also be found in many households, as they are utilised as water-softening agents in laundry detergents. Beyond these established uses, there are ongoing efforts to develop other applications, and the synthesis and characterisation of new zeolites and zeotypes is a thriving field of research.

Complementing experiments, computational chemistry methods at different levels of theory are widely employed to study structures and various properties of zeolites and related materials. This thesis compiles results from electronic structure calculations performed in the framework of density functional theory (DFT), addressing three distinct, but interrelated research areas. The first part focusses on a thorough validation of DFT approaches against experimental data for zeolites and zeotypes from different groups (all-silica zeolites, aluminophosphates [AlPOs] and silicoaluminophosphates [SAPOs], aluminosilicate zeolites). Exchange-correlation functionals using the generalised gradient approximation (GGA) in conjunction with different dispersion correction schemes were used in the calculations, which also considered different target quantities. With regard to crystal structures, the results unambiguously showed that the inclusion of a dispersion correction greatly improved the DFT-computed unit cell parameters, whereas bond lengths and angles were less affected. Dispersion interactions were found to be even more important when trying to reproduce the relative stability of all-silica zeolites with respect to  $\alpha$ -quartz. While it was evident that the use of a dispersion correction was pivotal, a wide-ranging investigation comparing different formalisms revealed remarkable differences among some of the approaches. On the basis of this study, recommendations for robust dispersion-corrected GGA functionals that reproduce both structures and relative energies of all-silica zeolites with acceptable accuracy were made. Moreover, it was observed that a reasonable prediction of pressure-dependent properties of zeolite frameworks (bulk moduli, pressure-induced phase transitions) poses a particular challenge, even for DFT approaches that perform well for other quantities.

Motivated by the significance of the "fluoride route" of zeolite synthesis, especially for the preparation of new framework types and of large, defect-free zeolite crystals, the second part brings together results from a series of computational investigations addressing the local environment of fluoride anions in neutral-framework zeolites and zeotypes, as well as their dynamic behaviour. While DFT structure optimisations were employed to predict the lowest-energy locations of fluoride anions, their dynamics were investigated with DFT-based *ab initio* molecular dynamics (AIMD) simulations. Studies of zeolites and zeotypes having the AST framework type, which contains cube-like double four-membered rings (*d4r* units), revealed pronounced variations in the equilibrium position of the fluoride anions: Depending on which elements occupy the corners of the *d4r* cage, fluoride is either located at a centre-of-cage position or displaced towards one of the corners, forming localised T-F bonds (T = tetrahedrally coordinated atom). These differences in the local environment also affect the extent of the dynamic motion



of fluoride. The fluoride dynamics were at the core of investigations addressing all-silica zeolites with trigonal-bipyramidal  $[\text{Si}^{[5by]}\text{O}_{4/2}\text{F}]^-$  units, where experimental studies have provided evidence for a dynamic disorder of fluoride anions in some, but not all systems. The AIMD simulations reproduced the experimentally observed occurrence/absence of dynamic disorder in the zeolites under study. Besides, the analysis of the AIMD results helped to elucidate the microscopic origins of the dynamic behaviour. Although the spatial arrangement of the Si atoms in the vicinity of the fluoride anion was identified as the main determining factor, attractive longer-range interactions with the organic structure-directing agents were found to suppress dynamic jumps in specific cases. A final case study addressed ITQ-13 silicogermanates, which have a rather peculiar structure that contains fluoride anions in *d4r* cages and in  $[\text{T}^{[5by]}\text{O}_{4/2}\text{F}]^-$  units (T = Si, Ge). As only incomplete information on the local environments can be inferred from commonly used experimental techniques, the computations were pivotal to identify the energetically preferred germanium distributions and their evolution as a function of Ge content.

The third part consists of a group of thematically more loosely connected studies, all of which are related in one way or another to the interaction of AIPO and SAPO zeotypes with adsorbed  $\text{H}_2\text{O}$  molecules. Due to the potential application of these materials in adsorption-based thermal energy storage, initial investigations aimed to elucidate the impact of framework type, of variations in the local structure, and of defects on the affinity towards water, employing DFT optimisations of hydrated structures. While only a modest impact of framework type or local heterogenities was observed for near-saturation conditions (AIPOs and SAPOs), the local environment of the framework protons in SAPOs affected the interaction energy at low water loadings more significantly. These comparative investigations were complemented by case studies of three individual systems: First,  $\text{AlPO}_4\text{-H3}$  was studied as an example for a small-pore aluminophosphate in which the water adsorption sites have been determined experimentally. In addition to predicting the stability of partially hydrated phases, all of which were found to be less stable than fully hydrated  $\text{AlPO}_4\text{-H3}$ , vibrational spectra were computed to develop correlations between the local environment of the water molecules and their spectroscopic signature. Furthermore, the dynamic behaviour of adsorbed water molecules was studied with AIMD simulations. The second case study addressed ECR-40, an unusual SAPO that violates Löwenstein's rule due to the presence of Al–O–Al linkages. Combining DFT optimisations and AIMD simulations, it was found that protons associated with these linkages are less acidic than those associated with Si–O–Al links. As a consequence, the Al–O–Al linkages are less likely to be deprotonated upon hydration. A coordination of water molecules to the Al atoms at opposite ends of these links occurred during AIMD simulations of fully hydrated ECR-40, pointing to irreversible structural changes that are probably the cause for the (experimentally observed) instability of hydrated ECR-40 towards recalcination. The third case study, an AIMD investigation of AIPO-11, aimed primarily at an understanding of the local structure of the calcined form. The simulations revealed remarkable differences between the time-averaged and instantaneous structures at room temperature, which were found to be due to a precession-like motion of oxygen atoms belonging to certain Al–O–P linkages. These deviations could explain some chemically implausible features in the published crystal structure of calcined AIPO-11. Further calculations on partially hydrated AIPO-11 structures in which the  $\text{H}_2\text{O}$  molecules were located in the vicinity of different Al atoms were used to predict the preferred water adsorption sites. The formation of octahedrally coordinated Al sites upon hydration was found to suppress the precession-like motion of framework oxygen atoms.

Altogether, the investigations compiled in this thesis have contributed to the advancement of computational zeolite science in different areas: Whereas the thorough validation of DFT methods against experimental data presented in the first part will facilitate the choice of suitable approaches in future studies, the main achievement of the studies compiled in the second and third part lies in their contribution to the atomic-level understanding of complex zeolite-like materials, both in terms of local structure and dynamic behaviour. The results fill a certain gap in the literature, as fluoride-containing zeolites/zeotypes and hydrated AlPOs/SAPOs had been relatively rarely explored with DFT methods, let alone AIMD simulations, prior to these studies. Although such fundamental insights are not directly transferable to any particular application, it can be anticipated that they will ultimately have an impact on more practically oriented research areas, *e.g.*, in the development of targeted synthesis routes or of zeotypes with improved hydration stability.

## ACKNOWLEDGMENTS

First of all, I am deeply grateful to Reinhard X. Fischer, former head of the Crystallography group, for welcoming me into his group as an "outsider" from the field of computational modelling, for his continued support over the past eight years, and for providing crucial advice and ideas at several points during this thesis project. Since our very first discussions about a postdoc project proposal (held in March 2013 at the "Roxie" restaurant in Hamburg's university quarter), Reinhard granted me a maximum amount of independence, allowing me to develop my research ideas freely and without constraints. I would like to thank Reinhard, his successor Ella M. Schmidt, and all other past and present members of the group (in alphabetical order), Johannes Birkenstock, Jakob Brauer, Manfred Burianek, Rosa M. Danisi, Gabi Ebert, Kristin Hoffmann, Paul B. Klar, Stephan Lenz, Hanna Lühns, Thomas Messner, Lobna Saeed, Hartmut Schneider, Iris Spieß, Christoph Vogt, Li Wang, and Michael Wendschuh for creating a friendly and collegial working atmosphere and for many enjoyable conversations (some science-related, some not).

Within the Faculty of Geosciences, I am especially indebted to Andreas Lüttge, Rolf S. Arvidson, and other present and former members of the Mineralogy group for generous access to their computing cluster "Asgard", on which a significant part of the calculations were run, for providing technical support, and for their advice in various matters. I am also grateful to numerous other people in the Faculty of Geosciences (too many to name individually) for their accessibility and helpfulness at countless occasions over the years.

Within the University of Bremen, I would like to acknowledge my collaboration partners from the Faculty of Chemistry, Thorsten M. Gesing, M. Mangir Murshed, Lars Robben, and their co-workers for allowing me to contribute to various interesting research projects that broadened my horizon. I greatly benefitted from my membership in the MAPEX Center for Materials and Processes, and I am grateful to the former and current MAPEX speakers, Lucio Colombi Ciacchi and Kurosch Rezwan, as well as the scientific coordinator Hanna Lühns (already mentioned above, but in a different role) for getting me involved in MAPEX, and for their continued support.

As outlined in 2.4, funding was provided by Central Research Development Funds of the University of Bremen and by the German Research Foundation. In addition to acknowledging these agencies as a whole, I would like to thank Corinna Volkmann (CRDF) and Susanne Faulhaber (DFG) for their help and advice.

The body of calculations that form the basis of this thesis would not have been feasible without extensive use of the resources provided by the North-German Supercomputing Alliance (Norddeutscher Verbund für Hoch- und Höchstleistungsrechnen – HLRN). I am grateful to Lars Neger, Thorsten Cordes (both Bremen), and Simone Knief (Kiel) for administrative support, and to Christian Tuma (Berlin) and various other members of the HLRN support staff for help with technical issues.

It goes without saying that the contributions of my co-authors, described in more detail in **Chapter 2**, have been pivotal for the success of various research projects compiled in this thesis. I would therefore like to thank – in order of appearance – Felix O. Evers (Bremen), Filip Formalik (formerly Wrocław, now Chicago), Adam Olejniczak (Wrocław), Ross J. Angel (Pavia), Won June Kim (formerly Nancy, now Changwon), Michael Badawi (Saint-Avold), Sébastien Lebègue (Nancy), Linus Freymann (Bremen), Carlos Bornes, Luís Mafra, and João Rocha (all Aveiro) for their respective contributions. This list of names includes people from various career stages, from aspiring students to scientists with decades of experience. I enjoyed working with all of them, and I can state with confidence I learnt more from them than *vice versa*. Although they were not directly involved in the research compiled in this thesis, a special mention in this context goes to Chieh-Min Hsieh and Joseph Sileola Akinbodunse, who were daring enough to undertake Master thesis projects under my supervision, allowing me to gain experience in the thesis supervisor role.

Since many of the articles compiled in this thesis are single-author papers, I heavily relied on colleagues and friends for proof-reading the draft manuscripts prior to a journal submission. In addition to the most prolific protagonist, Frank Hoffmann (Hamburg), who provided feedback on numerous manuscripts, I am also indebted to – again, in order of appearance – Johannes Birkenstock, Ross J. Angel, Filip Formalik, Diego Gatta (Milan), Gloria Tabacchi (Como), German Sastre (Valencia), Reinhard X. Fischer, Richard Darton (Keele), Jörn Droste (Münster), Linus Freymann, Rob Bell (London), and Ella M. Schmidt for their comments on individual articles. After the submissions, the (usually constructive) criticism by (mostly anonymous) reviewers was pivotal to improve the manuscripts, in some cases resulting in far-reaching changes. Although I sometimes lost sleep over reviewers' comments, I have to thank them in hindsight for their efforts.

Frank Hoffmann, Reinhard X. Fischer, and (for parts of the work) Filip Formalik also volunteered to proof-read this thesis, pointing out errors and inconsistencies and making suggestions for its improvement. Once again: Thank you!

*In the public version of the thesis, the last paragraph of the Acknowledgments has been redacted for data protection reasons.*

# CONTENTS

<i>Summary</i> . . . . .	i
<i>Acknowledgments</i> . . . . .	iv
<b>1. Introduction</b> . . . . .	<b>1</b>
1.1 Zeolites and zeotypes . . . . .	1
1.1.1 Definition and overview of zeolites and zeotypes . . . . .	1
1.1.2 Topological description of zeolites . . . . .	2
1.1.3 Beyond tetrahedral coordination in zeolites and zeotypes . . . . .	4
1.2 Applications of zeolites . . . . .	7
1.2.1 Ion exchange . . . . .	7
1.2.2 Catalysis . . . . .	8
1.2.3 Adsorption-based separations . . . . .	9
1.2.4 Zeolites in thermal energy storage . . . . .	10
1.2.5 Applications of natural zeolites . . . . .	12
1.3 Computational studies of zeolite structures and properties . . . . .	12
1.3.1 Computational studies of zeolites I: Force field methods . . . . .	13
1.3.2 Computational studies of zeolites II: Density functional theory . . . . .	17
<b>2. Overview and Co-Author Contribution Information</b> . . . . .	<b>26</b>
2.1 Chapter 3: Benchmarking DFT Calculations against Zeolite Structure Data (and Other Quantities) . . . . .	26
2.2 Chapter 4: Structure and Dynamics of Fluoride-Containing Zeolites and Zeotypes . . . . .	28
2.3 Chapter 5: Interaction of (Silico)Aluminophosphates with Adsorbed Water Molecules . . . . .	29
2.4 Funding information . . . . .	30
<b>3. Benchmarking DFT Calculations against Zeolite Structure Data (and Other Quantities)</b> . . . . .	<b>31</b>
3.1 Broader context and previous work . . . . .	31
3.1.1 Pitfalls in zeolite crystal structure determination . . . . .	31
3.1.2 Benchmarking DFT calculations for periodic solids . . . . .	32
3.1.3 Previous benchmarking works on zeolites: Structures and relative energies . . . . .	33
3.2 Key questions addressed in this chapter . . . . .	34
3.3 <b>Article A1: Structure and Bonding of Water Molecules in Zeolite Hosts: Benchmarking Plane-Wave DFT against Crystal Structure Data</b> . . . . .	35
3.3.1 Outline . . . . .	35
3.3.2 Summary of results . . . . .	36
3.4 <b>Article A2: Benchmarking DFT-GGA Calculations for the Structure Optimisation of Neutral-Framework Zeotypes</b> . . . . .	37
3.4.1 Outline . . . . .	37
3.4.2 Summary of results . . . . .	38

3.5	<b>Article A3:</b> <i>Accurate Structures and Energetics of Neutral-Framework Zeotypes from Dispersion-Corrected DFT Calculations</i> . . . . .	40
3.5.1	Outline . . . . .	40
3.5.2	Summary of results . . . . .	40
3.6	<b>Article A4:</b> <i>Benchmarking the Performance of Approximate van der Waals Methods for the Structural and Energetic Properties of SiO<sub>2</sub> and AlPO<sub>4</sub> Frameworks</i> . . . . .	42
3.6.1	Outline . . . . .	42
3.6.2	Summary of results . . . . .	43
3.7	<b>Article A5:</b> <i>Template Effects on the Pressure-Dependent Behavior of Chabazite-Type Fluoroaluminophosphates: A Computational Approach</i> . . . . .	44
3.7.1	Outline . . . . .	44
3.7.2	Summary of results . . . . .	45
3.8	Conclusions . . . . .	46
3.9	Outlook . . . . .	47
4.	<b>Structure and Dynamics of Fluoride-Containing Zeolites and Zeotypes</b> . . . . .	49
4.1	Broader context and previous work . . . . .	49
4.1.1	The "fluoride route" of zeolite synthesis . . . . .	49
4.1.2	Experimental characterisation of fluoride environments . . . . .	50
4.1.3	Previous computational investigations of fluoride-containing zeolites . . . . .	52
4.2	Key questions addressed in this chapter . . . . .	55
4.3	<b>Article B1:</b> <i>Local Environment and Dynamic Behavior of Fluoride Anions in Silicogermanate Zeolites: A Computational Study of the AST Framework</i> . . . . .	56
4.3.1	Outline . . . . .	56
4.3.2	Summary of results . . . . .	56
4.4	<b>Article B2:</b> <i>Local Distortions in a Prototypical Zeolite Framework Containing Double Four-Ring Cages: The Role of Framework Composition and Organic Guests</i> . . . . .	58
4.4.1	Outline . . . . .	58
4.4.2	Summary of results . . . . .	58
4.5	<b>Article B3:</b> <i>Influence of Organic Structure-Directing Agents on Fluoride Dynamics in As-Synthesized Silicalite-1</i> . . . . .	60
4.5.1	Outline . . . . .	60
4.5.2	Summary of results . . . . .	61
4.6	<b>Article B4:</b> <i>Fluoride Anions in All-Silica Zeolites: Studying Preferred Fluoride Sites and Dynamic Disorder with Density Functional Theory Calculations</i> . . . . .	62
4.6.1	Outline . . . . .	62
4.6.2	Summary of results . . . . .	62
4.7	<b>Article B5:</b> <i>Elucidating the Germanium Distribution in ITQ-13 Zeolites by Density Functional Theory</i> . . . . .	64
4.7.1	Outline . . . . .	64
4.7.2	Summary of results . . . . .	65
4.8	Conclusions . . . . .	66
4.9	Outlook . . . . .	67

5.	<i>Interaction of (Silico)Aluminophosphates with Adsorbed Water Molecules</i>	71
5.1	Broader context and previous work	71
5.1.1	Interaction of water with AIPOs and AIPO-based zeotypes	71
5.1.2	AIPOs and related zeotypes in adsorption-based heat transformations	71
5.1.3	Experimental investigations of host-guest interactions in hydrated AIPOs and SAPOs	73
5.1.4	Computational studies	81
5.2	Key questions addressed in this chapter	85
5.3	<b>Article C1:</b> <i>Water Adsorption in SAPO-34: Elucidating the Role of Local Heterogeneities and Defects using Dispersion-Corrected DFT Calculations</i>	86
5.3.1	Outline	86
5.3.2	Summary of results	87
5.4	<b>Article C2:</b> <i>Interaction of Water with (Silico)Aluminophosphate Zeotypes: A Comparative Investigation Using Dispersion-Corrected DFT</i>	88
5.4.1	Outline	88
5.4.2	Summary of results	88
5.5	<b>Article C3:</b> <i>First-Principles Study of AIPO<sub>4</sub>-H3, a Hydrated Aluminophosphate Zeotype Containing Two Different Types of Adsorbed Water Molecules</i>	90
5.5.1	Outline	90
5.5.2	Summary of results	90
5.6	<b>Article C4:</b> <i>Proton Acidity and Proton Mobility in ECR-40, a Silicoaluminophosphate that Violates Löwenstein's Rule</i>	92
5.6.1	Outline	92
5.6.2	Summary of results	92
5.7	<b>Article C5:</b> <i>Revisiting the Structure of Calcined and Hydrated AIPO-11 with DFT-Based Molecular Dynamics Simulations</i>	93
5.7.1	Outline	93
5.7.2	Summary of results	94
5.8	Conclusions	95
5.9	Outlook	97
6.	<i>Final Remarks</i>	100
	<i>Bibliography</i>	103
	<i>Appendix: Original Articles and Copyright Information</i>	133

# CHAPTER 1

## INTRODUCTION

### 1.1 Zeolites and zeotypes

#### 1.1.1 Definition and overview of zeolites and zeotypes

As stated in the *Atlas of Zeolite Framework Types* (6<sup>th</sup> edition), "zeolites and zeolite-like materials do not comprise an easily definable family of crystalline solids" (Baerlocher et al., 2007). The definition below was proposed by Coombs et al. (1997), representing the *Subcommittee on Zeolites of the International Mineralogical Association* (IMA):

*A zeolite mineral is a crystalline substance with a structure characterised by a framework of linked tetrahedra, each consisting of four O atoms surrounding a cation. This framework contains open cavities in the form of channels and cages. These are usually occupied by H<sub>2</sub>O molecules and extra-framework cations that are commonly exchangeable. The channels are large enough to allow the passage of guest species. In the hydrated phases, dehydration occurs at temperatures mostly below about 400 °C and is largely reversible. The framework may be interrupted by (OH,F) groups; these occupy a tetrahedron apex that is not shared with adjacent tetrahedra.*

Although this definition is explicitly restricted to zeolite minerals, synthetic zeolite-like compounds also fulfill the main crystal-chemical criteria.

The term **zeolite**, derived from the Greek words *zein* (to boil) and *lithos* (stone), was coined by the Swedish scientist Axel Fredrik Cronstedt (1756), who observed, upon heating, the evaporation of water from a mineral specimen (probably largely composed of the zeolite stellerite; Colella and Gualtieri (2007)). In the following centuries, numerous other zeolites were discovered, and the compilations by Baur and Fischer (2000 to 2017) list more than 120 minerals with zeolite-like **frameworks** (it has to be noted, however, that their list includes various minerals that do not conform to the narrower IMA definition given above). Typically, zeolites are either formed in cavities or veins through precipitation from circulating waters (amygdaloidal zeolites) or as alteration products of volcanic rocks under diagenetic or very low-grade metamorphic conditions (sedimentary zeolites). In 1948, Richard M. Barrer reported the first successful zeolite syntheses, using a hydrothermal synthesis route to mimic geological conditions (Barrer, 1948a,b). While one of these zeolites was a direct analogue of the mineral mordenite, the other of these earliest synthetic zeolites had a structure that is not found in any naturally occurring mineral. The field of zeolite synthesis started to burgeon in the 1950s, when the first applications in separation and catalysis commenced (Masters and Maschmeyer, 2011). At the time of writing, 248 unique zeolite frameworks (plus several intergrowth families) have been recognised by the Structure Commission of the International Zeolite Association (IZA; Baerlocher and McCusker (2022)). Only about 60 of these framework types occur in minerals (Baur and Fischer, 2000 to 2017).

The large majority of zeolite minerals and the most common synthetic zeolites have aluminosilicate composition, with silicon and aluminium occupying the tetrahedral sites (**T sites**). The negative charge of the framework is balanced through positively charged **extra-framework species** (metal cations or



organic cations, as in the example of NaA shown in **Figure 1.1**) or through **framework protons** bonded to oxygen atoms. The range of **Si/Al ratios** extends from 1 to infinity (these all-silica zeolites have a pure-SiO<sub>2</sub> composition and, hence, a neutral framework). Si/Al ratios below 1 would violate Löwenstein’s rule, which states that corner-sharing AlO<sub>4</sub> tetrahedra are unstable (Loewenstein, 1954), and it remains a matter of debate if and under what circumstances such violations might occur (Fletcher et al., 2017; Heard et al., 2019). Since the late 1970s, various materials with zeolite-like structures, but other compositions have been synthesised. This includes neutral-framework materials like silicogermanates, aluminophosphates (AlPOs), and gallophosphates (GaPOs) as well as charged-framework materials like silicoaluminophosphates (SAPOs), metal aluminophosphates (MeAPOs), and borosilicates. While some authors employ the term zeolite to encompass all these compositions, others use **zeotype** to designate non-aluminosilicate materials having a zeolite-like structure. It is worth noting that there are even a few zeotype minerals, such as the beryllophosphates pahasapaite and weinebeneite (Armbruster and Gunter, 2001).

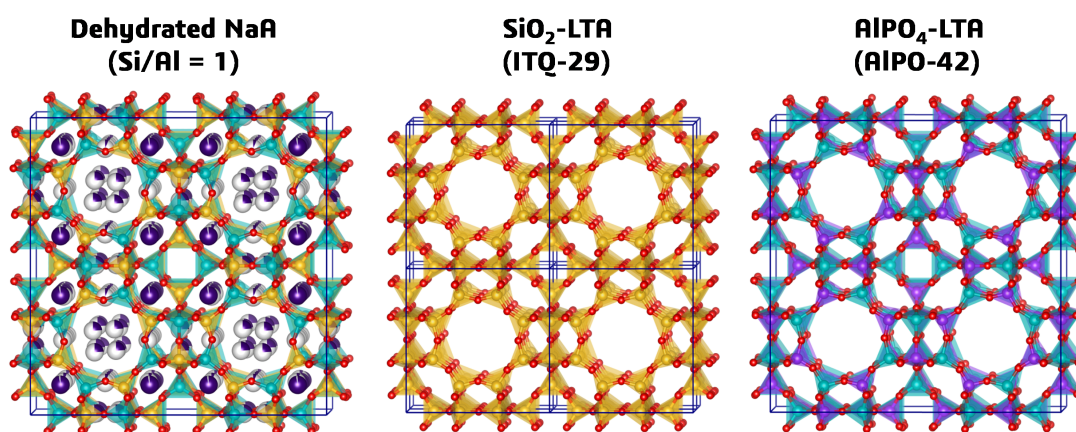


**Figure 1.1:** Crystal structure of representative LTA-type zeolites and zeotypes. **Left:** Dehydrated zeolite NaA (Pluth and Smith, 1980). **Middle:** All-silica zeolite ITQ-29 (Corma et al., 2004). **Right:** Aluminophosphate AIPO-42 (DFT-optimised structure from Fischer (2017)). Colour scheme: yellow = Si, turquoise = Al, purple = P, red = O, dark purple = Na. Fractionally occupied Na sites are partially coloured to reflect their occupancy. Unless otherwise noted, structure figures were prepared using VESTA (Momma and Izumi, 2011).

### 1.1.2 Topological description of zeolites

From the point of view of **topology**, zeolite frameworks can be described as three-periodic **nets** of four-connected **vertices**, with the T sites constituting the vertices (Smith, 2000). The edges connecting the vertices are formed by the T–O–T linkages. The International Zeolite Association assigns a three-letter **Framework Type Code (FTC)** to each topology that has been observed in natural or synthetic zeolites or zeolite-like materials, and the structural information is collected in the *IZA Database of Zeolite Structures* (Baerlocher and McCusker, 2022). **Figure 1.1** shows three zeolites/zeotypes having the same framework type (LTA = Linde Type A), but different composition. In a given structure, every non-equivalent T site can be characterised using the **coordination sequence**, which lists the number of  $N$ -th nearest neighbouring T sites up to  $N = 10$ , and the **vertex symbol**, which comprises the sizes of the smallest rings associated with all 6 tetrahedral angles, where a **ring** is defined as a closed cycle of linked TO<sub>4</sub> tetrahedra that is not the sum of two smaller cycles (Blatov et al., 2007). Every framework

type can be identified unambiguously through its specific combination of coordination sequences and vertex symbols (Baerlocher et al., 2007). In addition to this "numerical" description of a framework type, several ways to decompose zeolite frameworks into smaller building units have been suggested. Somewhat trivially, the **primary building units** are the  $\text{TO}_4$  tetrahedra. The following larger building units have been proposed:

- **Secondary building units (SBUs)** are entities consisting of up to 16 T atoms. By definition, SBUs are constructed in a way that the whole framework can be built up by assembling a single type of SBU. The definition is not unique, and many frameworks can be assembled using different SBUs (Baerlocher and McCusker, 2022). For example, the LTA framework can be built up from six different types of SBUs, including the SBUs 4, 6, and 8 that correspond to four-, six-, and eight-membered rings (4MRs/6MRs/8MRs), as shown in **Figure 1.2**. Conversely, several complex zeolite frameworks cannot be decomposed into a single type of SBU.
- **Composite building units (CBUs)** correspond to more intuitively defined building units that are typically present in several zeolite frameworks. Prototypical examples for CBUs are double four-membered rings (labelled *d4r* in the *IZA Database of Zeolite Structures*), sodalite (*sod*) cages, and "alpha" (*lta*) cages. The LTA framework can be constructed by assembling these three types of CBUs, as shown in **Figure 1.2**. The most comprehensive list of CBUs, termed **polyhedral units** in that work, was compiled by Smith (2000). As the author pointed out himself, a key disadvantage of polyhedral units/CBUs is the lack of mathematical rigour in their derivation.

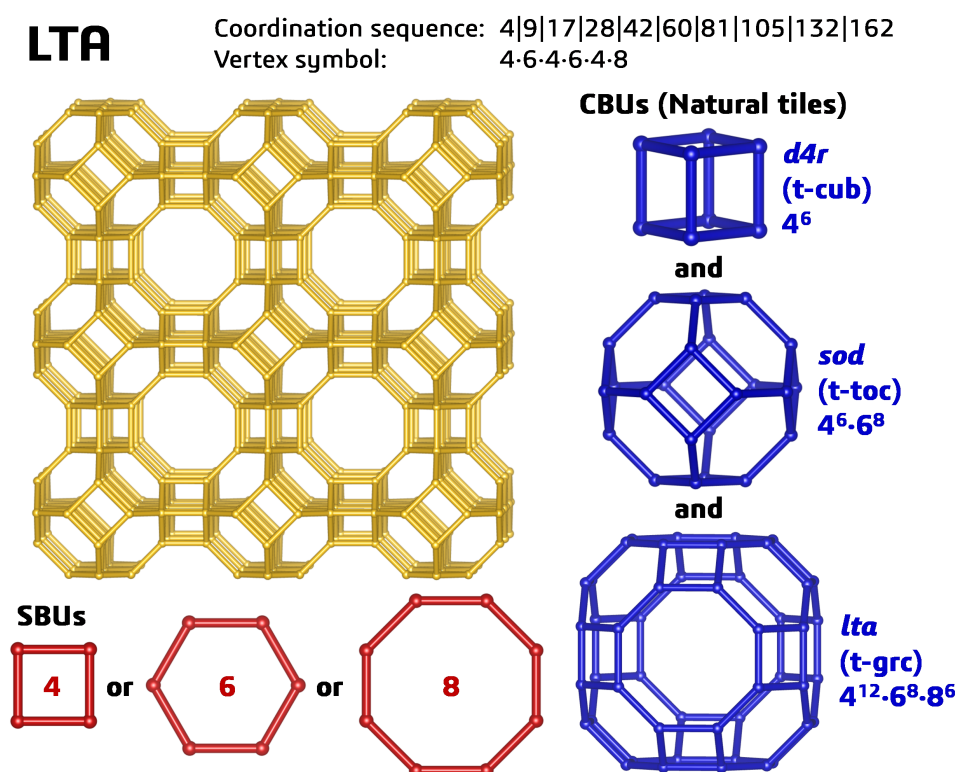


**Figure 1.2:** Skeletal representation of the LTA framework, coordination sequence, vertex symbol, and decomposition into different types of building units (SBUs, CBUs, natural tiles). CBU and natural tiling are equivalent in this case. The face symbol of every CBU/tile is also given. Data were taken from the *IZA Database of Zeolite Structures* (Baerlocher and McCusker, 2022).

- The problem of arbitrariness is removed through the concept of **natural tilings**, which provides an unambiguous, mathematically defined way to decompose any net into constituent tiles (Blatov et al., 2007). Natural tilings for all zeolite frameworks known at the time were described by Anurova et al. (2010), and tilings of all recognised frameworks are included in the *IZA Database of Zeolite Structures*. For the relatively simple LTA framework, the natural tiling approach gives equivalent results to the CBU approach, as is visible in **Figure 1.2**. However, this rigorous concept provides much more exhaustive means for the systematic analysis and comparison of frameworks, e.g., in terms of pore topology and connectivity (Blatova et al., 2019).

### 1.1.3 Beyond tetrahedral coordination in zeolites and zeotypes

As discussed in the previous sections, zeolites/zeotypes are tetrahedral frameworks; in other words, the coordination number (CN) of the T atoms is usually 4. There are, however, scenarios where additional ions or molecules may coordinate to some T sites, increasing the CN to 5 or 6. Examples for such additional bonding partners are hydroxyl groups, fluoride anions, water molecules, and certain functional groups of organic structure-directing agents (OSDAs). In many cases, they are bonded to a single T site and do not form new linkages to any other site. Such deviations from tetrahedral coordination merely constitute local perturbations in a tetrahedrally connected framework. In other instances, however, the coordinated species may "bridge" between adjacent T sites. Such bridging modes of the additional bonding partners occur primarily in fluoride-containing aluminosilicates and gallosphosphates (Caullet et al., 2005; Loiseau and Férey, 2007).

As zeolites and zeotypes having T atoms with CNs larger than 4 play a role in some chapters of this work, cases of particular relevance are presented below, limiting the description to key structural features and representative examples. The notation recommended by the *Subcommittee on the Nomenclature of Inorganic Structure Types of the International Union of Crystallography* (Lima-de Faria et al., 1990) is used to designate different coordination environments. It employs superscripted symbols  $[4t]$ ,  $[5by]$ , and  $[6o]$  to represent tetrahedral, trigonal-bipyramidal, and octahedral coordination, respectively.

- If all-silica/high-silica zeolites are synthesised in hydroxide media, the charge of the cationic OSDAs is typically balanced through negatively charged defects in the  $\text{SiO}_2$  framework (Koller et al., 1995; Shantz et al., 2000; Brunklaus et al., 2016). For at least one system, MFI-type Silicalite-1, crystallographic evidence for a direct coordination of hydroxyl anions to some Si atoms has been presented, which leads to the formation of  $[\text{Si}^{[5by]}\text{O}_{4/2}\text{OH}]^-$  entities (Schmidt et al., 2007).
- Framework-bound hydroxyl groups have also been found in some as-synthesised AIPOs, where the OH groups typically bridge between two  $\text{Al}^{[5by]}$  atoms. Examples include AIPO-21 (AWO topology; Bennett et al. (1985)), AIPO-40 (AFR topology; Ramaswamy et al. (1999)), and AEN-type IST-1 (Jordá et al., 2003).
- In all-silica/high-silica zeolites synthesised in the presence of fluoride anions, these anions balance the charge of the OSDA molecules (Cambor and Villaescusa, 1999; Caullet et al., 2005). They are typically incorporated in small cages of the as-synthesised zeolites' crystal structures. If  $d4r$  cages are present in the structure, the fluoride anions are located at the centre of these cages, for example in AST-type octadecasil (Caullet et al., 1991). In the absence of such building units, the fluoride anions tend to form a bond to one Si atom, forming trigonal-bipyramidal  $[\text{Si}^{[5by]}\text{O}_{4/2}\text{F}]^-$  units (**Figure 1.3**). This bonding situation was first observed in the crystal structure of as-synthesised nonasil (NON topology) by van de Goor et al. (1995). Subsequently,  $[\text{Si}^{[5by]}\text{O}_{4/2}\text{F}]^-$  units were

found in several other all-silica zeolites synthesised in the presence of fluoride, including MFI-type Silicalite-1 (Aubert et al., 2002). The fluoride anions are dynamically disordered over two symmetry-equivalent sites within the same cage in Silicalite-1, whereas only static disorder occurs in nonasil. Solid-state nuclear magnetic resonance (NMR) spectroscopy investigations can provide complementary information with regard to their local environment and dynamic behaviour (Koller et al., 1997, 1999).

- As the presence of germanium tends to stabilise the formation of  $d4r$  units, many germanates and silicogermanates contain these building units (Sastre et al., 2005a). There has been some disagreement regarding the precise location of fluoride anions incorporated in Ge-containing  $d4r$  cages: While experimental crystal structure refinements indicate a centre-of-cage location, for example for an AST-type germanate (Wang et al., 2003), evidence from NMR studies and atomistic calculations at different levels of theory points to a displacement from the cage centre, possibly going as far as a formation of F–Ge bonds (Villaescusa et al., 2002; Wang et al., 2003; Sastre et al., 2005b; Pulido et al., 2006b).

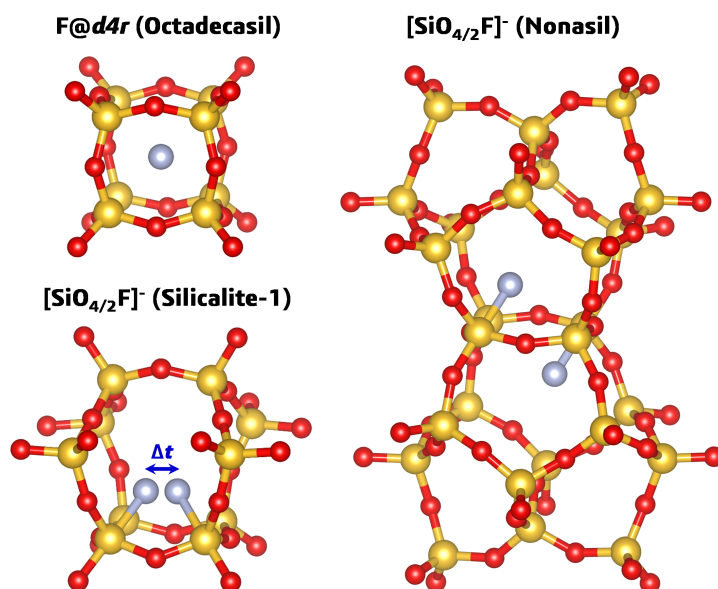


**Figure 1.3:** Typical environments of fluoride anions (light blue) in all-silica zeolites. **Top left:** Incorporation at the centre of a  $d4r$  unit in octadecasil (Caullet et al., 1991). **Bottom left:** Dynamic disorder over two positions in the same cage in Silicalite-1 (Aubert et al., 2002). **Right:** Static disorder over two positions in different cages in nonasil (van de Goor et al., 1995). In Silicalite-1 and nonasil, the F positions are 50% occupied.

- A variety of binding modes of fluoride anions have been observed in fluoride-containing AlPOs and GaPOs: First of all, the anions may be incorporated in  $d4r$  units, where they are either found at the cage centre (*e.g.*, in AST-type AlPO-16; Schott-Darie et al. (1994); and in GaPO<sub>4</sub>-LTA; Simmen et al. (1993)) or slightly displaced towards one of the faces (*e.g.*, in rhombohedrally distorted AlPO<sub>4</sub>-LTA; Schreyeck et al. (1998); and in the gallophosphate cloverite; Estermann et al. (1991)). Second, they may be bound to a single T atom as terminal (non-bridging) species, as is the case for some of the fluoride anions in GaPO<sub>4</sub>-ZON (Meden et al., 1997). Finally, fluoride anions can bridge between adjacent T atoms. Often, two anions are bonded to the same two T atoms, resulting in pairs of edge-sharing  $[\text{Al}^{[60]}/\text{Ga}^{[60]}\text{O}_{4/2}\text{F}_{2/2}]^-$  octahedra (Figure 1.4). Such octahedral

connectivities within otherwise tetrahedral frameworks are found, for example, in CHA- and GIS-type fluoroaluminophosphates (Harding and Kariuki, 1994; Paillaud et al., 1996).

- In hydrated aluminophosphates, water molecules may bond to framework Al atoms, leading to an expansion of the coordination environment to trigonal-bipyramidal or octahedral. Some  $\text{AlPO}_4 \cdot n \text{H}_2\text{O}$  minerals like variscite and metavariscite also contain such  $[\text{Al}^{[6o]}\text{O}_{4/2}(\text{H}_2\text{O})_2]$  octahedra (Kniep and Mootz, 1973; Kniep et al., 1977). In synthetic aluminophosphates, the first evidence for the presence of some octahedrally coordinated Al atoms was obtained in  $^{27}\text{Al}$ -NMR experiments on as-synthesised and hydrated AIPO samples by Blackwell and Patton (1984). The following year, the crystal structure of APC-type  $\text{AlPO}_4\text{-H3}$  was determined (Pluth and Smith, 1985, 1986): Here, two of the three non-equivalent  $\text{H}_2\text{O}$  molecules are coordinated to one of the two Al sites (**Figure 1.4**, the third water molecule occupies the channels of the structure). Subsequent crystallographic and NMR investigations on various other hydrated AIPOs showed that  $\text{Al}^{[5by]}$  and  $\text{Al}^{[6o]}$  atoms occur frequently, but that the fraction of non-tetrahedral Al sites can vary considerably among different structures.

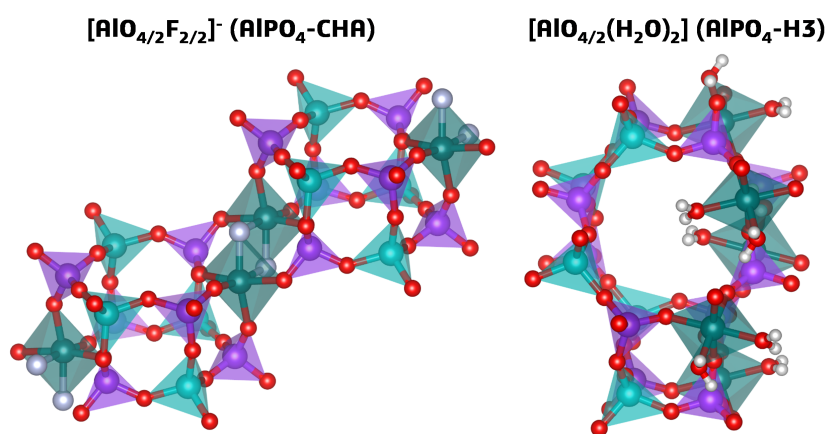


**Figure 1.4:** **Left:** Part of the crystal structure of CHA-type fluoroaluminophosphate including edge-sharing  $[\text{Al}^{[6o]}\text{O}_{4/2}\text{F}_{2/2}]^-$  octahedra (Harding and Kariuki, 1994). **Right:** Channel segment of the structure of  $\text{AlPO}_4\text{-H3}$  showing  $[\text{Al}^{[6o]}\text{O}_{4/2}(\text{H}_2\text{O})_2]$  octahedra (Pluth and Smith, 1986). Octahedrally coordinated atoms are shown in a darker shade of green.

- Whereas the OSDA molecules typically interact with the framework through non-directional van der Waals interactions and, potentially, hydrogen bonds to framework oxygen atoms, a direct coordination to framework Al atoms occurs in some AIPOs and AIPO derivatives. The term "framework-bound OSDA-containing molecular sieves" was coined in relatively recent work of Lee et al. (2015, 2016) on the MEI-type SAPO ECR-40, where alkanolammonium (or alkanolamine) OSDAs are bonded to some Al atoms via hydroxyl oxygen atoms. The phenomenon itself, however, had been observed before in some other AIPO zeotypes, including monoclinic  $\text{AlPO}_4\text{-SOD}$ , where dimethylformamide molecules are bonded to framework Al atoms via their oxygen atom (Vidal et al., 1998), and in IST-1, where methylamine molecules are coordinated via their nitrogen atom (Jordá et al., 2003). The recently reported STA-28 contains framework-bound 1,10-phenantroline OSDAs whose two nitrogen atoms are coordinated to the same Al atom (Watts et al., 2020). In all mentioned examples, those framework Al atoms that interact with the OSDAs are octahedrally coordinated.



## 1.2 Applications of zeolites

The most important applications of zeolites and related materials are connected to the presence of accessible cavities in the structures: Due to the ability of guest species to diffuse in and out of the pores, the extra-framework content occupying the cavities can be modified through a change of external conditions. Firstly, the charge-balancing species in zeolites having a negatively charged framework can be exchanged against other cations (**ion exchange**). Secondly, the reactivity of molecules adsorbed in the pores will be affected by the confinement, and the zeolite can act as solid acid catalyst for transformations of adsorbed molecules (**catalysis**). Thirdly, the affinity of a zeolite towards different guest molecules will vary, leading to the possibility to use zeolites in separations of gaseous or liquid mixtures (**adsorption-based separation**). The following subsections will provide a brief description of the use of synthetic zeolites as ion exchangers, catalysts, and adsorbents, as all of these applications are of tremendous industrial relevance (Wright, 2007). Other (potential) applications that are of lesser (or no) economic importance at present include adsorption-based thermal energy storage, membrane-based separations using zeolite membranes or zeolite-containing composites (Rangnekar et al., 2015), gas sensing (Mintova et al., 2015), and uses as low- $\kappa$  dielectrics (Hunt et al., 2010) and as host materials in drug delivery (Mintova et al., 2015). Of these, only thermal energy storage will be described in some detail in a dedicated subsection, as this application provides a key motivation for some studies included in this thesis. Finally, a short overview of applications of natural zeolites is given.

### 1.2.1 Ion exchange

If the internal cavities in structures of aluminosilicate zeolites or charged-framework zeotypes are accessible, the charge-balancing extra-framework cations are (usually) exchangeable. In other words, if a zeolite containing  $Q^{m+}$  cations is brought in contact with a solution containing  $P^{n+}$  cations, a replacement of  $Q^{m+}$  by  $P^{n+}$  cations can occur in the zeolite structure. In addition to external conditions (temperature, concentration), the exchange behaviour (degree of preference for  $Q^{m+}$  or  $P^{n+}$ ) also depends on zeolite composition and structure. For example, zeolite A preferentially incorporates  $\text{Na}^+$  over other alkali cations, and most alkaline earth cations over  $\text{Na}^+$  (Wright, 2007). Historically, the ability to exchange cations was first reported for chabazite by Eichhorn in 1858. It was soon recognised that ion exchange properties could be used in **water softening** (*i.e.*, removal of  $\text{Ca}^{2+}$  and  $\text{Mg}^{2+}$  cations from water, **Figure 1.5**), and the first commercial applications appeared in the early 20th century (Masters and Maschmeyer, 2011).

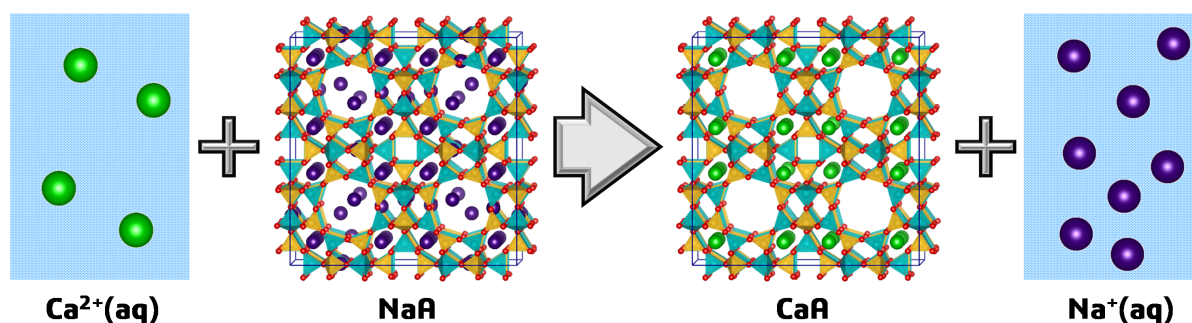


**Figure 1.5:** Schematic visualisation of ion exchange using zeolite NaA: Upon contact with a  $\text{Ca}^{2+}$ -containing aqueous solution,  $\text{Na}^+$  cations in the crystal structure are replaced by  $\text{Ca}^{2+}$  ions, resulting in a reduced calcium content in the aqueous phase ("water softening").

The large-scale use of zeolites as **detergent additives** (builders) responsible for the removal of  $\text{Ca}^{2+}$  cations during the washing process began in the 1970s, when the negative environmental impact of phosphate builders became apparent (Townsend and Coker, 2001). Today, it is the largest application of synthetic zeolites in terms of volume, and about 1,270 kilotons were estimated to be consumed in detergent applications in 2008 (Kulprathipanja, 2010). Because a larger amount of framework Al atoms means that more cations are needed to balance the charge, the ion exchange capacity can be maximised through use of zeolites with a low Si/Al ratio. Common laundry detergents that are on the market today contain sodium-exchanged zeolites with a Si/Al ratio of 1, either LTA-type zeolite NaA or GIS-type "maximum aluminium P" (Townsend and Coker, 2001).

Besides the use in detergents, there are also some environmental applications that exploit the ion exchange capabilities of zeolites. Specifically, they can be used to remove ammonia, ammonium ions, and heavy metal cations from wastewaters, and for the removal of certain radionuclides ( $^{137}\text{Cs}^+$ ,  $^{90}\text{Sr}^{2+}$ ) from radioactively contaminated waters (Townsend and Coker, 2001). Finally, it should be noted that the possibility to exchange the extra-framework cations is also important with regard to other uses of zeolites, as it provides a convenient means to "tune" their properties, *e.g.*, allowing to incorporate cations having a high affinity towards a given species for separation applications, or to introduce catalytically active sites.

### 1.2.2 Catalysis

Many zeolites and zeotypes possess an intrinsic acidity, leading to the possibility to use them as **solid-state acid catalysts**. In protonated zeolites, the framework protons pointing into the pores act as Brønsted acid sites (Wright, 2007; Li and Pidko, 2019). The reactivity of these Brønsted acid sites depends strongly on the local environment (pore shape and size, arrangement of T atoms) and on the composition (Si/Al ratio in zeolites, Si/(Al+P+Si) ratio in SAPOs, etc.). As a consequence, variation of zeolite topology and/or composition can enable an optimisation of the catalytic properties for a given reaction. Furthermore, extra-framework aluminium species as well as cations incorporated in the framework (*e.g.*,  $\text{Ti}^{4+}$ ,  $\text{Sn}^{4+}$ ) or on extra-framework sites (*e.g.*, rare earth cations) can act as Lewis acid sites. Besides exploiting the intrinsic acidity of zeolites, it is also possible to dope zeolites with catalytically active metals (*e.g.*, incorporating noble metals for hydrogenation reactions), leading to bifunctional catalysts (Vermeiren and Gilson, 2009).

In addition to their acidity, the well-defined geometry of the zeolite pores and their apertures is another advantage of zeolite catalysts, as it can promote shape-selective effects, such as reactant or product diffusion selectivity or transition state selectivity (Wright, 2007). These effects can drastically influence the product distribution and, in favourable cases, result in highly selective reactions. Other properties rendering zeolites attractive for catalytic applications are their stability under harsh conditions (with typical reaction temperatures between 400 and 800 °C), their non-corrosive and non-toxic nature, and the relatively straightforward formulation into extrudates or spheres, which facilitates the handling in various reactor setups (Vermeiren and Gilson, 2009).

The industrial use of zeolite catalysts began in the late 1950s and early 1960s, when researchers at Union Carbide and Mobil developed **hydrocracking** and **fluid catalytic cracking (FCC)** processes using FAU-type zeolite catalysts (Rabo and Schoonover, 2001; Masters and Maschmeyer, 2011). Today, both these processes play a key role in oil refineries, where they are employed to convert heavy hydrocarbons from the crude oil distillation residue into lighter, more valuable species (FCC: mostly gasoline, hydrocracking: mostly diesel). Roughly 50% of all currently operating refineries are fitted with an FCC unit,

and developments in catalyst and reactor design have led to a continuous increase in the selectivity towards the most desirable hydrocarbon fractions, which is not only economically attractive, but also contributes to the efficient use of fossil feedstocks (Vogt and Weckhuysen, 2015). While FCC catalysts (mostly high-silica zeolite Y) account for about 95% of synthetic zeolites produced for catalytic applications, there are various smaller-scale uses in the petrochemical and chemical industry, with a 2009 review listing 25 different types of commercial processes employing zeolite-based catalysts (Vermeiren and Gilson, 2009). Although the production volume of zeolite catalysts is smaller than that of detergents, with an estimated consumption of about 300 kilotons in 2008, catalysis is the economically most important application, representing more than 50% of the market value (Rabo and Schoonover, 2001; Kulprathipanja, 2010). Along with their important role in the traditional, fossil-fuel based economy, zeolite catalysts are also under heavy investigation for the processing of renewable feedstocks, specifically, the conversion of biomass to biofuels or platform molecules (Perego and Bosetti, 2011; Ennaert et al., 2016). Given the constantly evolving demand, it can be expected that zeolites will continue to play a leading role in industrial catalysis, and much of the fundamental research that led to the discovery of many new zeolites and zeotypes in the past decades was driven by the search for improved zeolite catalysts.

### 1.2.3 Adsorption-based separations

By virtue of their porosity, zeolites can take up (adsorb) and release (desorb) guest molecules from the gas phase or liquid phase. If the affinity of a zeolite towards a species *A* is greater than that towards another species *B*, the adsorbent will preferentially adsorb *A* over *B*, leading to the possibility to separate an *A/B* mixture. In equilibrium adsorption processes, which form the basis for most adsorptive separations, the separation efficiency is related to the difference in interaction strength (Kulprathipanja, 2010). For example, species *A* might fit better into the zeolite pores than *B*, or interact more strongly with extra-framework cations, leading to a higher **heat of adsorption** and, hence, preferential adsorption. Rate-selective separations rely on differences in diffusivity, rather than equilibrium adsorption, among the adsorbed species. Finally, the well-defined pore size of zeolites will lead to the exclusion of species that do not fit into the pores. This **molecular sieving** effect can afford extremely high (theoretically infinite) selectivities, but it requires an appreciable difference in size among the constituents of the mixture (Kulprathipanja, 2010). Like in catalysis, the framework type, which determines size, shape, and connectivity of the pores, the chemical composition, and the presence and nature of extra-framework species all have a significant effect on the separation properties, providing various possibilities for adsorbent optimisation.

Molecular sieving by a zeolite was first reported by Weigel and Steinhoff (1924), who studied the adsorption of water and organic vapours on chabazite. Although Barrer (1942) filed a patent on the use of natural zeolites for hydrocarbon separation, the commercialisation of zeolite adsorbents became viable only after the discovery of synthetic zeolites A and X by Milton and Breck at Union Carbide in the 1950s (Breck et al., 1956). In industrial-scale adsorption processes, bulk **gas separations**, which involve a mixture of two or more major components, are distinguished from **purifications**, in which impurities are removed from a major phase (Sircar and Myers, 2003). In terms of process design, different means can be used to regenerate the adsorbent: In temperature swing adsorption (TSA), regeneration is achieved through an increase of the temperature, whereas a decrease of the pressure is used in pressure swing adsorption (PSA). Zeolites with low Si/Al ratios are used in various TSA-based purifications, for example in dehydration or desulfurisation processes using zeolites A or X (Sircar and Myers, 2003). PSA



processes are more typically employed in bulk separations, for example, in the production of  $N_2$  and  $O_2$  from air using Li-exchanged low-silica zeolite X (LiLSX, **Figure 1.6**; Yang (2003)) and in the removal of  $CO_2$  from  $CH_4$  ("upgrading" of natural gas or biogas; Tagliabue et al. (2009)). With ever-increasing atmospheric  $CO_2$  levels, the potential use of zeolites for the removal of  $CO_2$  from flue gases has received much attention in fundamental research (Samanta et al., 2012).

Because neither TSA nor PSA are suitable for liquid-phase separations, these use a desorbent to displace the adsorbed molecules from the zeolite (Kulprathipanja, 2010). Zeolites are widely used in the petrochemical industry to separate hydrocarbon mixtures, *e.g.*, in the separation of *p*-xylene from other xylene isomers (Kulprathipanja, 2010) and in the "deep" desulfurisation of transportation fuels (Hernández-Maldonado and Yang, 2004). Other potential applications arise in environmental remediation, where hydrophobic high-silica zeolites can be employed for the removal of organic molecules (phenols and other aromatics, nitrosamines, pharmaceuticals, etc.) from water (Roostaei and Tezel, 2004; Rossner et al., 2009; Koubaissy et al., 2011; De Ridder et al., 2012).

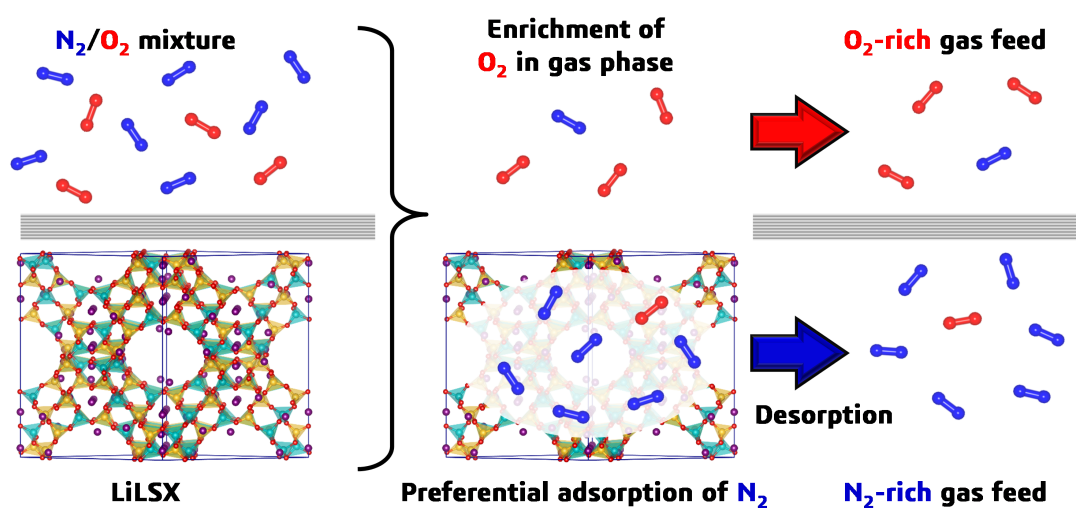


**Figure 1.6:** Schematic visualisation of an adsorption-based separation process,  $N_2/O_2$  separation using zeolite LiLSX. Because  $N_2$  is preferentially adsorbed,  $O_2$  is enriched in the gas phase. Desorption of the  $N_2$ -enriched phase is achieved by decreasing the pressure (PSA). The whole process is run in a cyclic fashion.

#### 1.2.4 Zeolites in thermal energy storage

Adsorption-based heat transformations employ adsorption-desorption cycles of a **working fluid** onto an adsorbent: When the pristine adsorbent is brought in contact with the working fluid, the exothermic nature of the adsorption process causes the system to heat up (= releasing heat from the storage reservoir, bottom part of **Figure 1.7**). The initial state of the adsorbent can be restored by using an external heat source to remove the adsorbed working fluid (= loading the heat storage reservoir, top part of **Figure 1.7**). The heat can now be stored without any additional thermal insulation as long as an exposition to the working fluid or other adsorbable gases is avoided, rendering this a (theoretically) loss-free means of heat storage (Henninger et al., 2012). Moreover, the storage vessel containing the adsorbent could be transferred between a waste heat source and another place where the heat can be used, *e.g.*, within a chemical plant. In addition to **heat storage**, adsorption-based heat pumps can be employed in **adsorption chillers**, for example for solar-powered refrigerators or air conditioners. The potential

of zeolite adsorbents in this area was recognised rather early, with first prototype applications being realised in the late 1970s, after the oil crisis of 1973 (Meunier, 2013).

Water is the most commonly used working fluid, as it is widely available, environmentally benign, and interacts rather strongly with many porous materials, but other working fluids like methanol and ammonia are also under consideration. Both the adsorbent's capacity and its affinity towards the working fluid determine the performance: On the one hand, a high affinity (high heat of adsorption) allows a high storage density. On the other hand, the removal of the working fluid will also require high temperatures, which may not be available. As a consequence, adsorbents of varying hydrophilicity could find use in different heat transformation applications using water as a working fluid, and various materials including silica-based materials, zeolites/zeotypes, metal-organic frameworks (MOFs), and composite materials are being investigated (Aristov, 2013; de Lange et al., 2015). Presently commercialised applications largely rely on porous silicas and zeolites (de Lange et al., 2015). For example, dishwashers fitted with a zeolite-containing compartment use the adsorption of water onto the zeolite, rather than additional electric heating, during the drying phase, thereby reducing the energy consumption of a washing cycle by about 20% (Hauer and Fischer, 2011). This technology, patented by BSH Hausgeräte about 15 years ago (Fauth et al., 2008), is used in many household dishwashers that are currently on the market, primarily in the upper price segment. Zeolite-based adsorption chillers are marketed, for example, for mobile and stationary cooling applications like transport boxes and self-cooling beer kegs (ZeoTech GmbH, 2022).

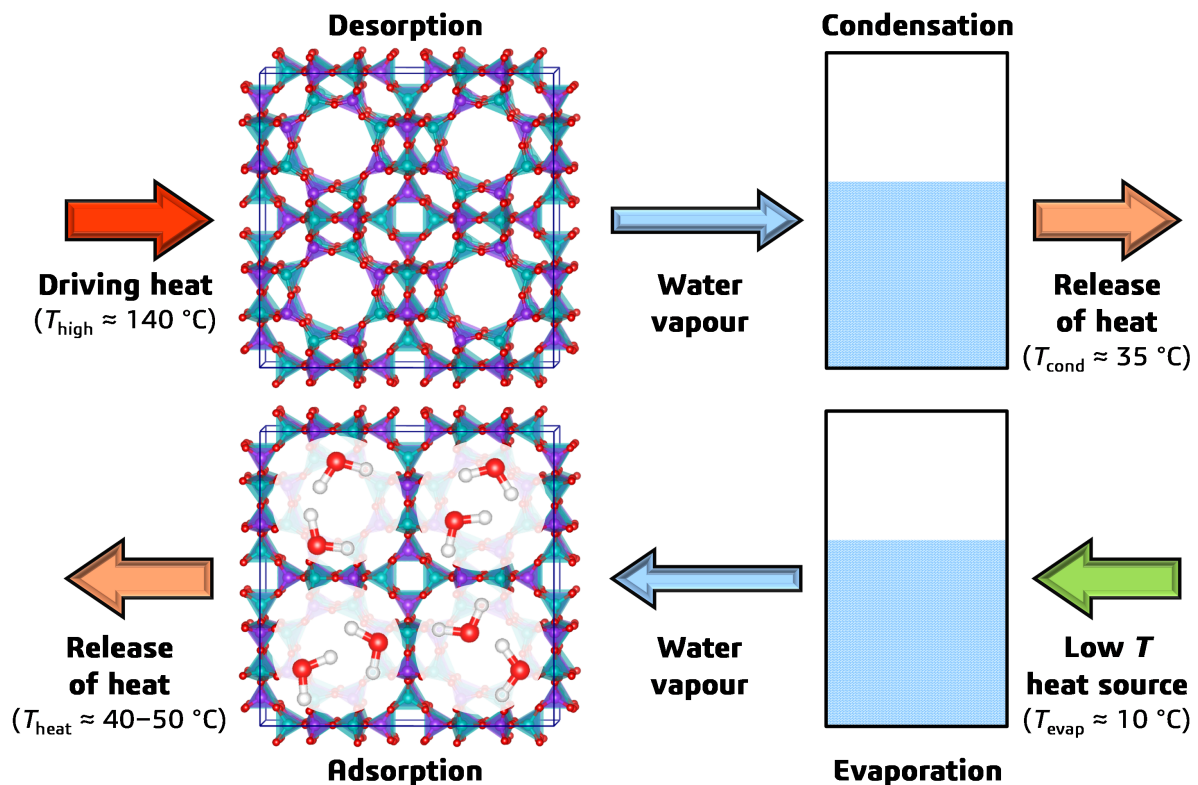


**Figure 1.7:** Principle of adsorption-based thermal energy storage using water as working fluid and AlPO-42 as adsorbent: Using a high-temperature heat source, the working fluid is desorbed (top). To discharge the storage reservoir, a low-temperature heat source is sufficient to evaporate the working fluid, which is then adsorbed onto the AlPO-42 material, releasing the stored heat (bottom). Figure designed after Henninger et al. (2012).

Zeolites with low Si/Al ratios like zeolite A and X are highly hydrophilic, requiring temperatures above 200 °C for their regeneration (Henninger et al., 2012; Aristov, 2013). They cannot be used in solar heating or cooling, where typical regeneration temperatures range from 90 to 140 °C. Due to their intermediate hydrophilicity, which results in S-shaped water adsorption isotherms (de Lange et al., 2015), zeolites with higher Si/Al ratios, AIPOs, SAPOs, and MeAPOs are more attractive for such applications. Promising results have been reported, among other materials, for zeolite Y (Henninger et al., 2010; Jänchen and Stach, 2014; Ristić et al., 2018), AEI-type AIPO-18 (Henninger et al., 2010), CHA-type AIPO-tric and SAPO-34 (Henninger et al., 2010; Ristić et al., 2012; Freni et al., 2015), and LTA-type AIPO-42 (Krajnc et al., 2017). For some of these materials, a stability over hundreds of adsorption-desorption cycles could be demonstrated. Apart from the intrinsic properties of the adsorbent, the possibility to produce adsorbent-containing shaped bodies or coatings also plays an important role. To mention just one example, an adsorbent heat exchanger coated with SAPO-34 was successfully prepared, and the performance enhancement was demonstrated on the lab scale (Freni et al., 2015).

### *1.2.5 Applications of natural zeolites*

Natural zeolites like clinoptilolite (HEU topology), mordenite (MOR), chabazite (CHA), and phillipsite (PHI) occur in mineable deposits in volcanoclastic sediments in various places around the world, including the Western US, Australia, Italy, and Cuba. While supply is, therefore, not an issue, their applicability in adsorption and catalysis is limited by rather low adsorption capacities and the inevitable presence of chemical and mineralogical impurities (foreign cations, secondary minerals). Even though the production of natural zeolites exceeded that of their synthetic counterparts by a ratio of about 5:3 in 2008 (natural zeolites: 3,000 kilotons, synthetic zeolites: 1,800 kilotons; Kulprathipanja (2010)), their economic importance is smaller. Historically, zeolite-bearing tuffs have been used as dimension stones in construction for more than 2,000 years, as they are lightweight materials that can easily be sawed into blocks (Mumpton, 1999). Today, natural zeolites are widely employed as supplementary cementitious materials ("pozzolans") in the production of cement (Tran et al., 2019b). Uses in ion exchange, which mostly rely on clinoptilolite, encompass the removal of ammonium, heavy metals ions, or radionuclides from wastewaters (Townsend and Coker, 2001). Furthermore, natural zeolites also play a role in agriculture, for example, as additives in animal nutrition, as soil amendments, and in the treatment of animal waste (Mumpton, 1999).

## *1.3 Computational studies of zeolite structures and properties*

Computational chemistry techniques play a major role in zeolite science, contributing, on the one hand, to their fundamental characterisation and, on the other hand, to the prediction and understanding of application-related properties (Van Speybroeck et al., 2015). This section covers the two most widely used methods, force field calculations and density functional theory (DFT). Each subsection starts with a concise description of the theoretical background before giving an overview of key fields of applications dealing with zeolites and zeotypes. Other computational modelling methods that are used in zeolite science in general, but not in studies contained in this thesis, are not included in this overview. For example, geometric simulation methods, which have been employed to study zeolite flexibility (Wells and Sartbaeva, 2015), are excluded. Combined quantum mechanics/molecular mechanics (QM/MM) methods, which treat a small part of the structure with a high-level method and the remainder at a more empirical level, and wave function theory (WFT) methods like Hartree-Fock or MP2 perturbation theory, which are rarely used for periodic zeolite models, are also omitted.

### 1.3.1 Computational studies of zeolites I: Force field methods

#### 1.3.1.1 Using force fields to model molecules and solids

In a **force field** (FF) description, the energetic contribution of individual interactions between the constituent atoms is calculated using simple analytical potentials. The total energy of a system is then computed as the sum over all contributions, and the forces on the atoms can also be calculated, allowing the optimisation of a given atomic arrangement. Organic molecules and other systems dominated by covalent bonds are typically described using a **molecular mechanics** (MM) approach (Allinger, 2010). In the MM framework, appropriate atom types are assigned to the constituent atoms or, if a united-atom model is used, to groups of atoms (for example, a  $-\text{CH}_3$  group may be treated as a single interaction site). The bonds between the interaction sites are predefined, and bond stretching, angle bending, and torsional terms (plus, possibly, other contributions) are described with harmonic potentials (for bond stretching and angle bending, **Figure 1.8**), cosine Fourier series (for torsions), or more complicated functional forms (*e.g.*, Morse potentials). The most important "non-bonded" interactions are electrostatic interactions, conveniently described by assigning point charges and applying Coulomb's law, and van der Waals (vdW) interactions, for which Lennard-Jones potentials or similar expressions are used to represent long-range attraction and short-range Pauli repulsion (**Figure 1.8**). Usually, non-bonded interactions are not considered between direct neighbours and atoms that are two and – in some FFs – three bonds apart.

The whole set of atom types, potentials, and parameters used in the description of a system is commonly referred to as "the force field". The derivation of the FF parameters can make use of a fitting to experimental data or to results from electronic structure calculations (or to a combination of both). Whereas system-specific FFs can provide a very accurate description for those species included in the parameterisation, "generic" FFs are more broadly applicable, but less accurate. In zeolite science, the DREIDING force field (Mayo et al., 1990) and the Consistent Valence Force Field (CVFF) (Dauber-Osguthorpe et al., 1988; Hill et al., 2000) are among the most widely used generic FFs. The TraPPE-zeo FF has been specifically designed to model the adsorption of small molecules in zeolites (Bai et al., 2013).

For dominantly ionic materials, force fields based on the Born model of ionic solids are more commonly used. These use a point-charge description of the atomic sites, most typically employing formal charges. Two-body terms are included to represent Pauli repulsion and vdW interactions, often using Buckingham-type potentials (Catlow, 1997). The atomic polarisability can be included via a **core-shell model**, where the sum of core and shell charges equals the formal charge. While the "core" represents the position of the nucleus, the "shell" can be somewhat displaced from this site to model a polarisation of the electron cloud. Core and shell are coupled by a harmonic spring to prevent unrealistically large displacements of the shell. In addition, these ionic potentials can be supplemented by further terms similar to those used in molecular mechanics FFs (Catlow, 1997). A core-shell FF that is widely used in studies of zeolites is based on Si and O potentials developed by Sanders et al. (1984). It was later expanded to include parameters for aluminosilicates (Jackson and Catlow, 1988; Schröder et al., 1992) and aluminophosphates (Gale and Henson, 1994).

Besides the two groups of FFs outlined above, more sophisticated approaches include the incorporation of polarisation effects into molecular mechanics FFs (Cieplak et al., 2009), reactive FFs (Senftle et al., 2016), and FFs trained on reference data via machine learning (Li et al., 2017). As these approaches play no role in this work, they are not further discussed here.

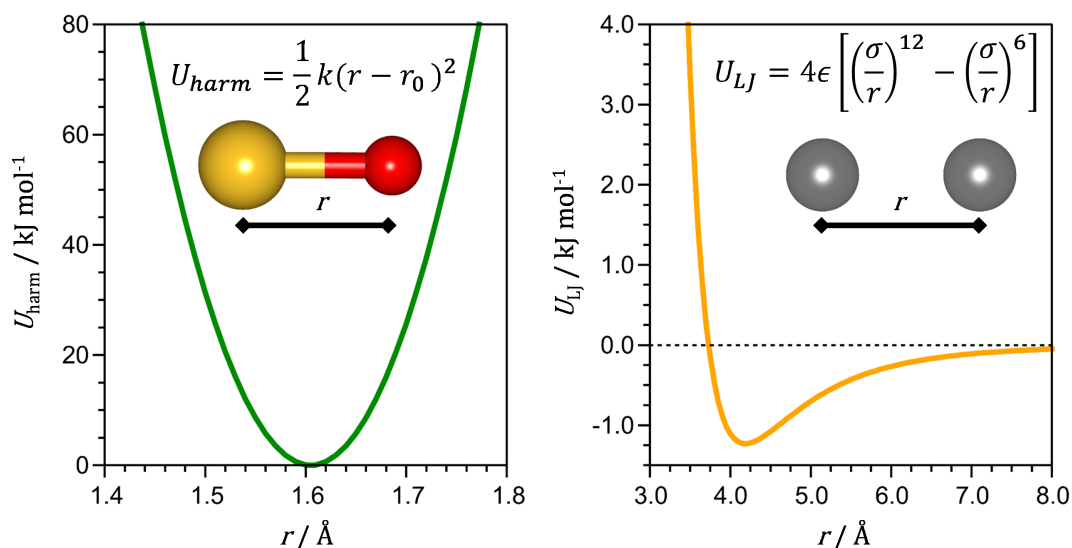


**Figure 1.8:** Typical potentials used in molecular mechanics force fields. **Left:** Harmonic potential used to represent bond stretching, example: Si–O bond. **Right:** Lennard-Jones potential used to represent short-range repulsion and long-range attraction between non-bonded species, example:  $\text{CH}_4 \cdots \text{CH}_4$  interactions.  $\text{CH}_4$  is modelled as a single interaction site (united atom model).

### 1.3.1.2 Applications of force field methods in zeolite science

**Zeolite structures and thermochemistry:** A portfolio of FF-based methods has been employed to study various aspects of zeolites, and review articles published over the past 20 years give an excellent overview of the state-of-the-art of computational zeolite research at different points in time (Fuchs and Cheetham, 2001; Smit and Maesen, 2008; Van Speybroeck et al., 2015; Abdelrasoul et al., 2017). The following account can only cover key fields of application and mention selected examples. With regard to zeolite structures, **structure optimisations** (= **energy minimisations**) have been employed in conjunction with diffraction experiments to probe the plausibility of structure models (Villaescusa et al., 1999; Greenaway et al., 2015), or to optimise the location of the OSDA molecules prior to a Rietveld refinement (Paillaud et al., 2007). Other applications include investigations of the energetically preferred Al/Ge positions in aluminosilicates and silicogermanates (Sastre et al., 2002, 2005a; Muraoka et al., 2016), preferred locations of framework protons (Schröder et al., 1992; Sastre et al., 2002), extra-framework cations (Higgins et al., 1997; Grey et al., 1999), and other extra-framework species (Lewis et al., 2002), as well as studies of defect-containing zeolite models (Bushuev and Sastre, 2009). The FF-based studies of fluoride anions in all-silica zeolites and silicogermanates by George and Catlow (1997), Sastre and Gale (2005), and Pulido et al. (2006a) are of particular relevance to this work, as they partly motivated the DFT-based investigations of these systems included in this thesis. They will be discussed in more detail in **Chapter 4**.

In addition to the optimisation of structural parameters, FF-based energy minimisations also allow for a comparison of the total energies of different phases with identical composition, enabling a prediction of their relative stability. Early FF development work already showed an inverse correlation between the framework density and the enthalpy of transition for all-silica zeolites and AlPOs (*i.e.*, lower-density frameworks tend to be less stable, so their enthalpies of transition with respect to the dense phases  $\alpha$ -quartz or  $\alpha$ -berlinite are larger; Kramer et al. (1991); de Vos Burchart et al. (1992b,a); Henson et al. (1994, 1996)), a trend that was later established in calorimetric experiments (Piccione et al., 2000; Navrotsky et al., 2009). Besides studies of the thermodynamic stability of known frameworks, FF-based calcula-

tions have also been widely used to predict the feasibility of "hypothetical zeolites", computer-generated zeolite-like frameworks (Foster et al., 2004; Zwijnenburg and Bell, 2008; Deem et al., 2009; Li et al., 2015). The literature contains several examples of zeolites that were first proposed as hypothetical phases and later synthesised (Li et al., 2015; Turrina et al., 2017).

**Molecular Dynamics (MD) simulations:** MD simulations model the evolution of a system as a function of time. Starting from an initial configuration, the forces on the constituent atoms are calculated using the FF representation of interatomic interactions. By solving Newton's equation of motion, the velocities and positions of the atoms can be calculated for the next time step (typical timesteps in atomistic MD simulations are on the order of femtoseconds:  $1 \text{ fs} = 10^{-15} \text{ s}$ ). Then, the force calculation is repeated to proceed to the next time step, and so forth (Frenkel and Smit, 2002). For each step (or every  $N$ -th step), atomic configurations ( $\pm$  velocities) and total energy are stored in the **trajectory**. After an **equilibration phase**, the **production part** of the trajectory can be used to calculate thermodynamic and/or transport properties. MD simulations can be carried out in different thermodynamic **ensembles**. For zeolites, the most relevant ensembles are the **canonical ensemble** ( $NVT$ , number of atoms, volume, temperature are constant) and the **isothermal-isobaric ensemble** ( $NpT$ , number of atoms, pressure, temperature are constant) ensembles. They require the use of a thermostat and (for  $NpT$  ensemble) barostat to control temperature and pressure, respectively (Berendsen, 2007). For typical zeolites, FF-based MD simulations covering several nanoseconds are routinely possible. In addition to simulating equilibrium conditions, nonequilibrium MD simulations can also be used, *e.g.*, to model the flux between different parts of the system.

As the diffusion properties of guest molecules play an important role for applications in catalysis and separation, a large number of FF-based MD studies investigating the diffusion of various guest molecules have been published (Smit and Maesen, 2008; Krishna, 2012). Fields of application include the diffusion of small molecules like  $\text{CO}_2$ ,  $\text{H}_2$ , or  $\text{CH}_4$  (Selassie et al., 2008; Krishna and van Baten, 2010; Kim et al., 2013), of  $\text{C}_8$  aromatics, important with regard to both the isomerisation and the separation of xylene isomers (Zhai et al., 2012; Toda et al., 2015), and of drug molecules, where the diffusion behaviour controls the efficacy of zeolites as hosts in drug delivery applications (Fatouros et al., 2011; Spanakis et al., 2014). In addition to the prediction of diffusion coefficients and derived quantities like diffusion selectivities, the simulations can also give insights into the underlying mechanisms. It has been pointed out that both the choice of the zeolite structure model (*e.g.*, experimental vs. FF-optimised) and the inclusion/omission of framework flexibility can have a significant impact on the computed diffusion coefficients (Zimmermann et al., 2011; Boulfelfel et al., 2015).

**Monte Carlo (MC) simulations:** In MC simulations, a statistical algorithm is used to generate an ensemble of configurations, where the probability of finding a particular configuration is given by the Boltzmann distribution (Allen and Tildesley, 2017; Smit and Maesen, 2008). Starting from a given configuration, for example, a zeolite pore containing a single guest molecule, a new configuration is generated through a **trial move**, for example, a displacement of this molecule. The FF energy difference between the new and old configuration is calculated. If the new configuration is energetically favoured, it is always accepted. If it is less favourable, it is only accepted with a certain probability, with the acceptance probability depending on both energy difference and external thermodynamic conditions. By choosing an appropriate set of trial moves and **acceptance criteria**, different thermodynamic ensembles can be modelled, and quantities of interest can be obtained by averaging over the ensemble of configurations (after equilibration).



Although MC simulations have been employed in different fields of zeolite science, *e.g.*, to generate different Al distributions in aluminosilicates (Muraoka et al., 2016), they are most frequently used in adsorption simulations. These are performed in the **grand-canonical (GC) ensemble**, where chemical potential  $\mu$ , volume, and temperature are constant. The number of guest molecules varies during the simulation, allowing to compute the equilibrium number of guest molecules for a given pressure (related to  $\mu$ ) and temperature. Because the basic GCMC insertion algorithm tries to insert the entire guest molecule, the acceptance probability will become very small for bulky molecules or at high loadings due to overlap with the framework or other guest molecules. In these cases, use of more advanced schemes like configurational-bias MC can significantly enhance the efficiency of simulations (Smit and Maesen, 2008). A particular advantage of MC simulations is the straightforward treatment of mixture adsorption.

GCMC simulations do not only give access to macroscopically accessible quantities like adsorption isotherms, heats of adsorption, Henry constants, and adsorption selectivities (for mixtures), but they also allow for atomic-level insights into the adsorption process through an analysis of the preferred adsorption sites/regions (**Figure 1.9**). As in the case of diffusion studies, the majority of GCMC studies of adsorption have dealt with relatively small guest molecules like CO<sub>2</sub>, N<sub>2</sub>, or small hydrocarbons. Examples range from in-depth studies of one or a few zeolites (Talu and Myers, 2001; Goj et al., 2002; Granato et al., 2007) to large-scale screening studies covering several 10,000 of systems (Lin et al., 2012; Kim et al., 2012, 2013). The adsorption of larger molecules, including linear and branched hydrocarbons (Dubbeldam et al., 2004; Luna-Triguero et al., 2017), aromatics (Lucena et al., 2008; Narasimhan et al., 2010), and emerging contaminants like pharmaceuticals (Fischer, 2020) has also been addressed. In the context of this thesis, GCMC studies of water adsorption in AlPOs and SAPOs, discussed in more depth in **Chapter 5**, are of particular interest (Pillai and Jasra, 2010; Henninger et al., 2011b; Fasano et al., 2019).

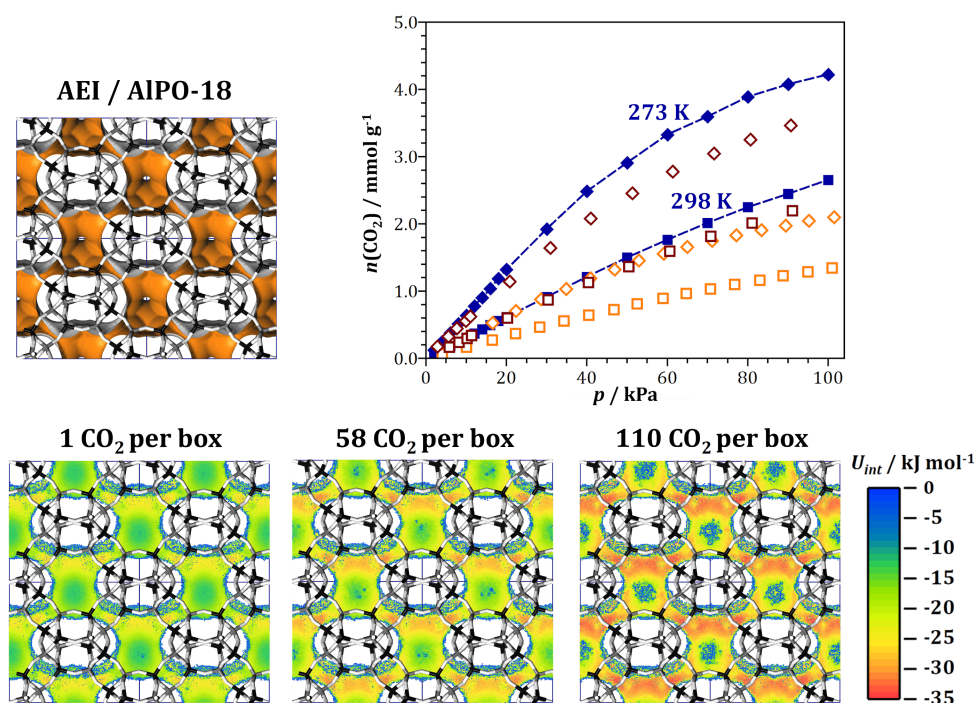


**Figure 1.9:** GCMC simulation results for CO<sub>2</sub> adsorption in AEL-type AlPO-18. **Top:** Pore topology and CO<sub>2</sub> adsorption isotherms (closed symbols = simulation, open symbols = experiment). **Bottom:** Interaction energy maps derived from GCMC simulations at different CO<sub>2</sub> loadings. Figure modified after Fischer (2017) and Fischer (2018).

Another issue that has received continued attention is the prediction of suitable OSDAs to synthesise a particular structure type. While simple, FF-based energy minimisations already allow for a calculation of the "stabilisation energy" of a given OSDA in different structures, or different OSDAs in one structure, MC simulations permit a more comprehensive sampling of different OSDA configurations in the zeolite pores (Cundy and Cox, 2003). Temperature effects can be accounted for by performing MD simulations for OSDA-containing zeolite models (Pophale et al., 2013). Using computational approaches to combine pre-defined organic fragments, it is even possible to design the OSDAs *de novo* (Lewis et al., 1996; Pophale et al., 2013). Starting with the synthesis of DAF-5, a CHA-type cobalt aluminophosphate (Lewis et al., 1997), there are now several examples in the literature where a computational prediction of the OSDA enabled the synthesis of known or new frameworks (Schmidt et al., 2014, 2015; Daeyaert and Deem, 2020). FF-based simulations have also been used to study the role of the OSDAs during the initial stages of zeolite synthesis, *i.e.*, the formation of zeolite precursors in the synthesis gel (Verstraelen et al., 2009).

GCMC simulations most typically employ rigid zeolite models. However, the accuracy of this approximation has come under some scrutiny, and recent work has shown that the inclusion of framework flexibility can be important in some cases, especially when there is a tight fit between zeolite pores and guest molecules, as is the case for some aromatics in MFI-type zeolites (Caro-Ortiz et al., 2020).

**The need for FF validation:** The empirical nature of FF-based methods implies a need to verify the suitability of the chosen potential parameters against experimental data and/or higher-level calculations. A comprehensive benchmarking of different FFs in predicting the structural, mechanical, and dynamical properties of all-silica zeolites was reported by Combariza et al. (2013). In adsorption and diffusion simulations, the validation procedure is often of an *ad hoc* nature, considering only experimental data (adsorption isotherms, diffusion coefficients) for the system(s) of interest. However, there have been numerous attempts to develop transferable FFs for adsorption simulations by making use of experimental data obtained for different zeolites and/or including information from DFT calculations (García-Sánchez et al., 2009; Fang et al., 2012; Fischer and Bell, 2012; Fang et al., 2013; Bai et al., 2013; Vujic and Lyubartsev, 2016). For example, GCMC simulations of CO<sub>2</sub> adsorption in various all-silica zeolites and AlPOs represented the framework atoms using a combination of DFT-derived charges and Lennard-Jones parameters that were fitted to reproduce experimental data (Fischer and Bell, 2012; Fischer, 2017, 2018). Exemplary results for AlPO-18 are shown in **Figure 1.9**.

### 1.3.2 Computational studies of zeolites II: Density functional theory

#### 1.3.2.1 Theoretical background and general considerations

The foundations of **density functional theory** (DFT) were laid by Hohenberg and Kohn (1964), who proved that the ground state properties of a many-electron system are unique functionals of the electron density. This implies that, rather than having to compute the wave function that gives the lowest total energy, as in **wave function theory** (WFT) methods, it is sufficient to determine the lowest-energy electron density to calculate ground state properties. As the electron density depends only on three spatial coordinates, whereas the wave function of an  $N$ -electron system depends on  $3N$  spatial coordinates, this results in a more favourable scaling behaviour upon increasing number of electrons, making DFT well suited for many-electron systems (large molecules, crystals) where high-quality WFT methods become prohibitively expensive (Sholl and Steckel, 2009). Kohn and Sham (1965) showed that the electron density of a system of interacting electrons can be generated using a set of one-electron wave



functions, the **Kohn-Sham (KS) orbitals**  $\psi$ . The Kohn-Sham equations, which need to be solved to find these orbitals, have the following form (Sholl and Steckel, 2009):

$$\left[ \frac{\hbar^2}{2m_e} \nabla^2 + V_{e-n}(\vec{r}) + V_{e-e}(\vec{r}) + V_{XC}(\vec{r}) \right] \psi_i(\vec{r}) = \epsilon_i \psi_i(\vec{r}) \quad (1.1)$$

Here,  $\hbar$  is Planck's constant,  $m_e$  is the electron mass,  $\vec{r}$  indicates a dependence on spatial coordinates,  $i$  is the orbital index, and  $\epsilon_i$  is the energy eigenvalue of orbital  $\psi_i$ . The first term in brackets corresponds to the kinetic energy of the electron, the second term gives the Coulomb attraction between the electron and all nuclei, and the third term (Hartree potential) represents Coulomb repulsion between a single electron and the total electron density (including spurious "self-interaction", which needs to be corrected); hence, it depends on the electron density. The final term  $V_{XC}$  represents the contributions of exchange and correlation.

The density dependence of the electron-electron and XC contributions in equation 1.1 implies that a practical implementation of DFT requires an iterative procedure: First, a trial electron density is defined. The one-electron wave functions are then determined by solving the KS equations, and the electron density is recalculated from these KS orbitals. The trial electron density is then updated by mixing the new and old densities, and the procedure is repeated until convergence is reached and the electron density does not change anymore. Although DFT was already in use in the solid state physics community in the 1970s, its appeal broadened in the 1990s, when methodological advances (**exchange-correlation functionals**) and increased computing power permitted the study of more complex systems (Perdew and Ruzsinszky, 2010). Today, DFT is by far the most widely used electronic structure method. Its tremendous impact can be illustrated by the fact that two key papers in the field, by Lee, Yang, and Parr (1988) and by Perdew, Burke, and Ernzerhof (1996), have been cited almost 100,000 times and more than 150,000 times, respectively (according to Google Scholar, August 2022).

**Exchange-correlation functionals:** Although the expression given in equation 1.1 is formally exact, the exact XC functional is unknown, and a suitable approximation needs to be made. The simplest such approximation is the **local density approximation (LDA)**, where  $V_{XC}(\vec{r})$  depends on the electron density at  $\rho(\vec{r})$ . LDA works reasonably well for metals, but gives poor results for molecules and ionic crystals (Haas et al., 2009; Perdew and Ruzsinszky, 2010). The XC functional can be improved by introducing a dependence on both the electron density and its gradient  $\nabla\rho(\vec{r})$ , which leads to the **generalised gradient approximation (GGA)**. A large number of GGA-type functionals have been proposed, among them the widely used PBE functional (as for many other functionals, this abbreviation derives from the authors of the original publication, Perdew, Burke, and Ernzerhof (1996)). More sophisticated (and computationally more expensive) XC functionals make use of the kinetic energy density (**meta-GGA functionals**), incorporate a fraction of exact Hartree-Fock exchange (**hybrid functionals**) or both Hartree-Fock exchange and perturbation theory correlation (**double-hybrid functionals**). Due to continuous developments, a vast number of XC functionals exist, with a recent benchmarking study on molecules comparing a total of 200 functionals (Mardirossian and Head-Gordon, 2017), and a work on periodic solids considering 38 functionals (Tran et al., 2016). The results from these and other studies clearly show that there is no "one size fits all" functional that performs well for every system and every quantity of interest. Therefore, an informed choice of the XC functional needs to be made prior to any DFT calculation.

**Basis sets:** In addition to the choice of XC functional, the size of the **basis set** (*i.e.*, the number of basis functions in which the KS orbitals are expanded) also affects the outcome of a calculation, and it should always be ensured that the basis set is large enough to give sufficiently converged results. Two different types of basis sets are important in this context: The **linear combination of atomic orbitals** (LCAO) approach uses atom-centered basis functions like Slater-type orbitals (STOs), Gaussian-type orbitals (GTOs), or numerical orbitals. Such basis sets are typically used in quantum chemistry codes developed for molecular calculations, but there are also several DFT codes that permit calculations on periodic systems within an LCAO approach, notably CRYSTAL (Dovesi et al., 2020) and DMol3 (Delley, 2000). An alternative to the use of atom-centered basis functions is the use of a **plane wave** (PW) basis set, as it follows from Bloch’s theorem that the electronic wave function in a periodic potential can be formulated as a sum of plane waves (Payne et al., 1992):

$$\psi_{i,\vec{k}}(\vec{r}) = \sum_{\vec{G}} c_{i,\vec{k}+\vec{G}} \exp \left[ i \left( \vec{k} + \vec{G} \right) \cdot \vec{r} \right] \quad (1.2)$$

In this equation,  $\vec{k}$  are the vectors in the first Brillouin zone at which the wave functions are calculated. While a fine sampling (many  $\vec{k}$  points) is required for metals, it is usually sufficient to sample only a few  $\vec{k}$  points for semiconductors or insulators, especially for systems with relatively large unit cells (= small first Brillouin zones). The vectors  $\vec{G}$  are reciprocal lattice vectors defined by  $\vec{G} \cdot \vec{L} = 2\pi m$ , where  $\vec{L}$  is a vector of the direct lattice and  $m$  is an integer. In principle, it would be necessary to expand the wave function in an infinite PW basis set (*i.e.*, include an infinite number of vectors  $\vec{G}$ ). As the coefficients  $c_{i,\vec{k}+\vec{G}}$  are larger for PWs with small kinetic energies  $E_{kin} = \frac{\hbar^2}{2m_e} |\vec{G}|^2$ , the PW expansion can be truncated at some **cutoff energy** value  $E_{cut}$ . By considering only reciprocal lattice vectors  $\vec{G}$  for which  $\frac{\hbar^2}{2m_e} |\vec{G}|^2 < E_{cut}$ , one arrives at a finite PW basis set. Both  $E_{cut}$  and the mesh of  $\vec{k}$  points need to be chosen appropriately to give converged results.

**Pseudopotentials:** The tightly bound, lower-lying electrons (core electrons) oscillate on short length scales in real space. This complicates the use of a PW basis set, as a very high cutoff energy, *i.e.*, a very large number of PWs, would be required to capture these oscillations (Sholl and Steckel, 2009). In order to reduce the computational cost, the core electrons can be described using a **pseudopotential** (PPT) representation. This approximation assumes that the core electrons are not affected by the chemical environment, and that it is hence sufficiently accurate to employ an environment-independent "frozen-core" representation, the pseudopotential, treating only the valence electrons explicitly with the PW basis. Different formalisms can be used to derive PPTs: Whereas ultrasoft PPTs are designed to give relatively accurate results at low cutoff energies, norm-conserving pseudopotentials are simpler in their derivation, but "harder", *i.e.*, they require a larger  $E_{cut}$  value (Garrity et al., 2014). At present, there are several openly accessible PPT libraries that can be used in conjunction with plane wave DFT codes like CASTEP (Clark et al., 2005), QuantumEspresso (Giannozzi et al., 2020), and CP2K (Kühne et al., 2020). CASTEP also contains a built-in function to generate PPTs "on the fly". In a more sophisticated development, the **projector augmented wave** (PAW) approach represents the core electrons with auxiliary wave functions that can be conveniently represented in a PW expansion. PAWs can be used, for example, in the VASP (Kresse and Furthmüller, 1996a,b; Kresse and Joubert, 1999) and QuantumEspresso codes. It has been shown that appropriately chosen state-of-the-art PPTs and PAWs can deliver excellent agreement with benchmark all-electron calculations (Garrity et al., 2014; Prandini et al., 2018).

**Dispersion interactions in DFT:** The semilocal nature of commonly used XC functionals (*i.e.*, their dominant or exclusive dependence on local quantities such as electron density and gradient) entails a poor description of long-range electron correlation effects. This causes large errors for systems where dispersion (vdW) interactions play a significant role (Dobson and Dinte, 1996; Grimme et al., 2016). This issue had already been widely recognised in the 1990s (Dobson and Dinte, 1996; Kohn et al., 1998), and key steps to improve upon this shortcoming were made in the early 2000s: First, Grimme (2004) proposed the first of the pairwise "Grimme-type" **DFT-D** dispersion correction schemes, in which an empirical term is added to the DFT energy *a posteriori*. For a pair of atoms *A* and *B*, the magnitude of this term depends on element-specific dispersion coefficients  $C_6^A$  and  $C_6^B$  and on the distance  $r_{AB}^{-6}$ , because dispersion interactions decay as  $r^{-6}$ . A short-range damping term is introduced to avoid artificial short-range interactions. Second, Dion et al. (2004) presented their **van der Waals density functional (vdW-DF)**, which provides a "seamless" description of both short-range and long-range interactions. The vdW-DF XC functional includes a nonlocal correlation contribution, calculated using a parameterised nonlocal kernel that depends on the electron density and its gradient. In addition to subsequent advances regarding the setup and parameterisation of the DFT-D and vdW-DF approaches (*e.g.*, DFT-D2: Grimme (2006); DFT-D3: Grimme et al. (2010); vdW-DF2: Lee et al. (2010)), numerous other flavours of dispersion-corrected DFT have been developed, which differ not only in the underlying physical description of dispersion interactions, but also in the computational overhead. One example is the TS correction scheme proposed by Tkatchenko and Scheffler (2009), which uses a pairwise description similar to the DFT-D methods, but introduces a scaling that depends on the effective atomic volume. Another, conceptually distinct approach is the use of dispersion-corrected atom-centered potentials, which are calibrated against reference data from high-level WFT calculations (von Lilienfeld et al., 2004). Comprehensive reviews on dispersion-corrected DFT methods are available (Grimme et al., 2016; Hermann et al., 2017), and numerous benchmarking studies have assessed the performance of different approaches, *e.g.*, for the description of molecular dimers (Mardirossian and Head-Gordon, 2017; Claudot et al., 2018) and for periodic systems (Tawfik et al., 2018; Tran et al., 2019a).

### 1.3.2.2 Applications of DFT calculations in zeolite science

Since the first reports of DFT studies on zeolites appeared in the early 1990s, tremendous methodological developments, together with increased computing power and a more and more facile use of DFT codes, have been pivotal to the widespread application of electronic structure calculations in zeolite science. Today, DFT calculations are almost routinely employed in some areas, often in close conjunction with experiments. The review by Van Speybroeck et al. (2015) provides a broad overview of different fields of zeolite-related uses of DFT methods (along with FF-based calculations). In the following, only those applications that are of direct or indirect relevance to the present work are summarised, mentioning representative examples without being exhaustive. The most noteworthy omission are computational studies related to the catalytic activity of zeolites. As electronic structure calculations – unlike FF methods using conventional (non-reactive) force fields – can model the bond breaking and formation during chemical reactions and give insights into reaction intermediates, this has been a particularly fruitful field for DFT methods (Li and Pidko, 2019; Chizallet, 2020). Moreover, the overview will concentrate on DFT calculations on periodic zeolite models, even though calculations employing either isolated cluster models or QM/MM schemes continue to be heavily used.

**Zeolite structures and thermochemistry:** Like FF-based methods, DFT calculations have been widely employed to study various aspects of the local structure of zeolites. For example, the energetically preferred Al distributions have been predicted computationally for MFI-type ZSM-5 (Ghorbanpour et al., 2014; Knott et al., 2018), CHA-type zeolites (Torres et al., 2008; Fletcher et al., 2017), and clinoptilolite (Uzunova and Mikosch, 2013). The distribution of Ge atoms has been investigated for BEC- and UTL-type silicogermanates (Kamakoti and Barckholtz, 2007; Odoh et al., 2014), and some authors have also studied zeolites containing other heteroatoms, such as titanium (Petkov et al., 2012). Starting from early work comparing different proton positions in CHA-type SSZ-13 and SAPO-34 (Shah et al., 1996; Jeanvoine et al., 1998a), many studies have used DFT to predict the energetically preferred proton and/or cation positions in various zeolites. Just two representative examples are mentioned here: First, the author of this thesis compared the stability of ten different cations at cation sites associated with six-membered rings (SII site) and eight-membered rings (SIII' site) in SAPO-34 (Figure 1.10; Fischer and Bell (2014)). As one would expect from the ionic radii, smaller cations are more stable at the 6MR site, whereas larger cations ( $d_{ion} > 1.2 \text{ \AA}$ ) preferably locate at the 8MR sites. Second, Jones and Iglesia (2015) compared the energetics of different proton locations in Si-rich models of the BEA, CHA, FAU, FER, MFI, and MOR frameworks, resulting in a total of 120 models for which the deprotonation energy was computed. The ability to study different possible arrangements comprehensively at the DFT level, even for (relatively) complex structures, can lead to insights into relationships between local environment and properties that are not accessible with any experimental method. Some authors have employed DFT calculations to study the structure of as-synthesised zeolites, investigating the local geometry of  $[\text{SiO}_4/2\text{F}]^-$  units in fluoride-containing all-silica zeolites (Attfield et al., 2001; Zicovich-Wilson et al., 2010a) and the location of OSDA molecules in the zeolite pores (Zicovich-Wilson et al., 2010a; Pulido et al., 2015), or to produce realistic models of local heterogeneities, such as "silicon islands" in SAPOs (Zokaie et al., 2012a) or defect sites produced through dealumination/desilication of aluminosilicates/SAPOs (Fjermestad et al., 2013).

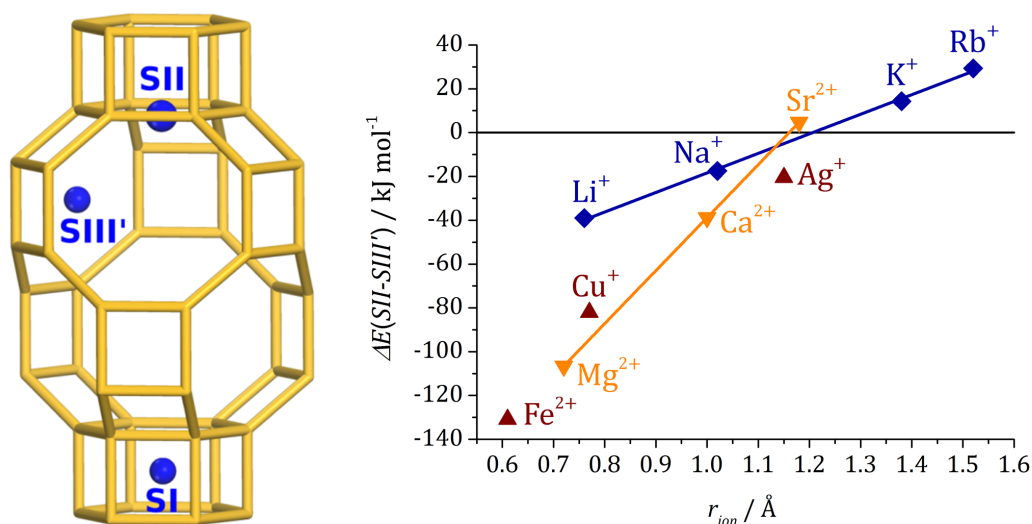


**Figure 1.10:** Left: Schematic visualisation of important cation sites in CHA-type structures. Right: DFT energy difference between SII and SIII' sites for ten different cations in SAPO-34, plotted against the ionic radius (Shannon, 1976). Negative values indicate that the SII location is favoured. Linear trends with different slope are found for alkali (blue) and alkaline earth cations (orange). Figure modified after Fischer and Bell (2014).

Early DFT-based studies of the relative energies of all-silica zeolites showed that different XC functionals can reproduce the inverse correlation between framework density and enthalpy of transition, but that calculations without dispersion correction are not able to make reasonably accurate quantitative predictions (Civalleri et al., 1998; Astala et al., 2004; Zwiijnenburg et al., 2007; Pedone et al., 2008). Notable improvements were reported in two papers that appeared in 2015, which can be seen as direct precursors to the investigations described in **Chapter 3** of this thesis: First, Román-Román and Zicovich-Wilson (2015) showed that dispersion-corrected DFT calculations with the PBE0-D functionals deliver a near-quantitative prediction of the enthalpy of transition across a set of 14 all-silica zeolites, despite a pronounced tendency to overestimate the unit cell volume by about 10%. Second, a study of different silica polymorphs including FAU- and FER-type zeolites by Hay et al. (2015) reported good agreement with experimental enthalpies of transition for both the PBE-D2 and PBE-TS functionals. Since these functionals overestimate Si–O bond lengths while simultaneously underestimating Si–O–Si angles, error compensation results in a fairly accurate prediction of the unit cell volumes (within 2% of experimental values).

The computation of the elastic constants of a system requires a series of calculations on structures with deformed unit cells (the number of required deformations depends on the symmetry). An early DFT-based prediction of the elastic constants of a few zeolites was reported in 2004 by Astala et al. (2004). A more recent large-scale investigation covered a total of 121 all-silica zeolites (Coudert, 2013). Intriguingly, some frameworks were found to exhibit unusual non-linear compressibility. The incorporation of pressure as an external variable into DFT calculations is straightforward, providing a convenient pathway to predict the structural evolution under pressure. This possibility has been exploited, for example, to study pressure-induced phase transitions and other phenomena such as "superhydration" in natrolite (NAT topology) exchanged with different cations (Kremleva et al., 2013, 2014).

**Calculation of vibrational and NMR spectra:** Whereas diffraction methods are employed to determine the long-range structure, vibrational spectroscopy and solid-state NMR spectroscopy can help to characterise the local environment. To interpret such spectra, the observed features (infrared-/Raman-active frequencies, NMR chemical shifts) need to be assigned to particular local environments. This assignment can, in many cases, be facilitated by combining the experiments with a DFT-based prediction of vibrational frequencies or chemical shifts. Consequently, a large number of combined experimental and DFT studies, as well as DFT-only investigations, have focussed on the spectroscopic properties of zeolites. Even the very early studies of protonated SSZ-13 and SAPO-34 included a prediction of the O–H stretching frequencies  $\nu(\text{O–H})$  of different sites, permitting a comparison to experimental infrared (IR) spectra (Shah et al., 1996; Jeanvoine et al., 1998a). Subsequent calculations of the  $\nu(\text{O–H})$  values were often motivated by a proposed correlation with the respective acid strength of the protons (Bordiga et al., 2015). However, comparative DFT studies of different zeolites showed that such a correlation does not exist (Otero Arean et al., 2014; Jones and Iglesia, 2015). DFT calculations also revealed that neither the shift in  $\nu(\text{O–H})$  upon adsorption of basic guest molecules nor the corresponding enthalpy of adsorption are completely reliable indicators of the acidity, as these quantities also depend on other interactions with the framework atoms, rather than being exclusively determined by the proton acidity (Otero Arean et al., 2014; Boronat and Corma, 2019). In addition to numerous studies of zeolites containing adsorbed guest molecules, reviewed by Bordiga et al. (2015), DFT-based predictions of vibrational spectra have also focussed on framework vibrations (Zicovich-Wilson et al., 2007; Wang et al., 2019), on the spectroscopic signature of cations (Mikuła et al., 2015), and on vibrational modes associated with encapsulated OSDA cations and fluoride anions (Zicovich-Wilson et al., 2007).

As the chemical shifts are often very sensitive to changes in the local environment, solid state NMR experiments have greatly contributed to the understanding of the local structure in zeolites and zeolite types (Brouwer et al., 2010). Although the assignment of resonances representing distinct coordination environments (*e.g.*, tetrahedral vs. octahedral Al atoms) is straightforward, it is more difficult to anticipate the impact of rather intricate changes in the local environment (*e.g.*, Al on different T sites) on the resulting chemical shifts. In such cases, a DFT-based prediction of the chemical shifts can be key to an unambiguous assignment. The theoretical framework of these calculations as well as numerous application examples (including zeolites) have been reviewed by Bonhomme et al. (2012) and by Ashbrook and McKay (2016), and only a few illustrative examples will be given in the following. In an investigation of as-synthesised and calcined AlPO-14 (AFN topology), a combination of DFT calculations and  $^{27}\text{Al}$ - $^{31}\text{P}$  magic angle spinning (MAS) NMR experiments was employed to further refine structures obtained from diffraction data (Ashbrook et al., 2008). Moreover, it was shown that a DFT optimisation of the structure is required to obtain reasonable agreement between computed and experimental chemical shifts. This issue was further explored in subsequent work covering several AlPOs, where a DFT-D optimisation prior to the NMR calculation was recommended as an approach that provides simultaneous agreement with experimental crystal structure data and chemical shifts (Sneddon et al., 2014). As shown for ZSM-5, among other systems, the combination of NMR experiments and DFT calculations permits conclusions regarding the preferred Al sites in aluminosilicate zeolites (Dib et al., 2018). However, such a procedure may fail if different local environments result in non-distinguishable NMR resonances, as observed for various arrangements of Si and Ge in a BEC-type silicogermanate (Whittleton et al., 2018). In fluoride-containing silicogermanates with  $d4r$  units, the  $^{19}\text{F}$ -NMR chemical shift stemming from the encapsulated fluoride anions varies depending on the number and arrangement of Ge atoms on the corners of the cage. Although a tentative assignment was already proposed on the basis of experimental data alone (Blasco et al., 2002), systematic DFT studies were pivotal to fully explain the observations (Sastre et al., 2005b; Pulido et al., 2006b). A combination of NMR experiments and DFT calculations has also been employed to explore the nature of the interactions between the tetramethylammonium OSDAs and the purely siliceous framework of octadecasil (Dib et al., 2017).

**Host-guest interactions:** DFT-based investigations of the interaction of various guest molecules with zeolites have been motivated by different reasons: On the one hand, *in-situ* spectroscopic studies of zeolites containing adsorbed probe molecules such as CO, NH<sub>3</sub>, or pyridine are an important characterisation technique, and many researchers have complemented the experiments with DFT computations (Bordiga et al., 2015). On the other hand, the (potential or actual) use of zeolites in adsorption-based separations constitutes a vast field of application for DFT methods: For example, calculations can be used to predict trends in affinity among different zeolites. Studies addressing the impact of cation exchange in typical adsorbents like zeolite Y have considered guest molecules of varying complexity, ranging from small molecules like CO<sub>2</sub> and H<sub>2</sub>O (Pirngruber et al., 2010; Hessou et al., 2018) to relatively bulky organic species like dibenzyl disulfide (Hessou et al., 2019). By studying different guest molecules within a consistent theoretical framework, qualitative predictions of the trends in selectivity can be made. For example, the author of this thesis investigated the affinity of cation-exchanged SAPO-34 towards five small hydrocarbons (ethane, ethene, ethyne, propane, propene), proposing Mg- and Sr-SAPO-34 as promising adsorbents for a selective adsorption of alkenes over alkanes, and Ag-SAPO-34 as best suited for ethyne/ethene separations (Fischer and Bell, 2014). A similar approach was employed by Shang et al. (2014) to study the potential of CHA-type aluminosilicates for CO<sub>2</sub>/CH<sub>4</sub> and CO<sub>2</sub>/N<sub>2</sub> separations.

In addition to predicting interaction energies, DFT calculations can also give detailed insights into the nature of the host-guest interactions. In many cases, adsorption is dominated by dispersion interactions, which, as noted above, are not well represented by standard XC functionals. The severity of this problem was studied in detail by Göttl, Hafner, and co-workers, who published a series of publications in which different "flavours" of dispersion-corrected DFT were used to predict the interaction of small hydrocarbons with CHA-type zeolites (Göttl and Hafner, 2011; Göttl et al., 2012; Göttl and Hafner, 2013). Altogether, these works convincingly showed that an inclusion of a dispersion correction is absolutely necessary to arrive at reasonable interaction energies and that the results exhibit significant scatter depending on the dispersion correction scheme employed. Recent benchmarking work covering various small guest molecules showed that accurate adsorption energies can be obtained in the framework of the random phase approximation (RPA) with singles correction scheme (Klimeš and Tew, 2019) and with hybrid MP2:DFT calculations (Rehak et al., 2020). DFT-D approaches exhibit a tendency to overestimate the interaction strength for many guest molecules, as shown for small hydrocarbons in protonated chabazite (H-CHA) in **Table 1.1**. Due to their computational expense, calculations at the RPA or MP2 level of theory are not (at present) routinely applicable for zeolites with large unit cells.

**Table 1.1:** Adsorption energies of methane, ethane, and propane adsorbed in H-CHA (all values in  $\text{kJ mol}^{-1}$ ). In addition to values computed with different DFT approaches, results obtained with the random phase approximation (RPA), MP2 perturbation theory (WFT), and a hybrid MP2:DFT scheme are included for comparison. Experimental reference adsorption energies were computed from measured adsorption enthalpies (Rehak et al., 2020).

Method	CH <sub>4</sub>	C <sub>2</sub> H <sub>6</sub>	C <sub>3</sub> H <sub>8</sub>	References
Experiment	-27.2	-33.5	-43.8	(Rehak et al., 2020)
PBE	-10.3	-12.8	-10.6	(Göttl and Hafner, 2013)
PBE-D2	-35.6	-46.8	-58.7	(Grimme, 2006; Rehak et al., 2020)
PBE-D3	-34.5	-48.4	-61.9	(Grimme et al., 2010; Rehak et al., 2020)
PBE-TS	-39.2	-56.6	-73.0	(Tkatchenko and Scheffler, 2009; Rehak et al., 2020)
PBE-MBD/FI	-30.0	-41.7	-53.6	(Gould et al., 2016; Rehak et al., 2020)
vdW-DF	-41.8	-59.1	-81.0	(Dion et al., 2004; Göttl and Hafner, 2013)
RPA	-26.4	-38.2	-48.8	(Klimeš et al., 2015; Klimeš and Tew, 2019)
MP2	-25.6	-37.0	-47.6	(Klimeš and Tew, 2019)
MP2:DFT	-25.3	-36.2	-46.7	(Piccini et al., 2015)

The water molecule is a particularly interesting guest molecule for various reasons: First, it plays a role in zeolite synthesis and in numerous applications. Second, it can act as both hydrogen bond donor and acceptor. Third, the affinity of zeolites and zeotypes towards water covers a wide range, from highly hydrophilic aluminosilicates to hydrophobic all-silica zeolites. As a consequence, periodic DFT calculations have been widely used to study the interaction between zeolites and adsorbed water molecules, starting from early work published in the second half of the 1990s (Nusterer et al., 1996; Jeanvoine et al., 1998b). Topics of study include the structure and hydrogen bonding of physisorbed water molecules in aluminosilicate zeolites (Larin et al., 2003; Vener et al., 2009; Fois and Tabacchi, 2019) and the organisation of water molecules in AIPOs (Poulet et al., 2002, 2005; Pillai and Jasra, 2010; Varlec et al., 2016). Where FF-based methods would require an elaborate parameterisation to include the coordination of

water molecules to framework atoms (*e.g.*, to Al atoms in AIPOs), such changes in the coordination environment can be studied directly with DFT calculations. Furthermore, the possibility to predict chemical reaction pathways has been exploited to analyse the role of water during zeolite dealumination (Silaghi et al., 2016; Stanciakova et al., 2019).

**DFT-based molecular dynamics:** A DFT structure optimisation delivers the (local) energy minimum at 0 K. Temperature effects can be included through a calculation of the vibrational modes in the framework of the harmonic approximation. An alternative approach that also accounts for anharmonic effects is available through DFT-based molecular dynamics simulations (also termed *ab initio* molecular dynamics – AIMD). They proceed in a largely analogous fashion to the FF-based MD simulations described in the previous subsection, the key difference being the calculation of total energy and forces using DFT, rather than a force field. This renders them computationally very demanding, and typical AIMD simulations of zeolites can only cover simulation times on the order of picoseconds.

Early applications of AIMD simulations on zeolites investigated the adsorption of H<sub>2</sub>O molecules in protonated zeolites, addressing the ability of individual molecules or small (H<sub>2</sub>O)<sub>n</sub> clusters to deprotonate the framework (Jeanvoine et al., 1998a). Due to the high mobility of the hydrogen atoms, a purely static treatment can give only limited insights in this regard. A comprehensive assessment was reported for the case of CHA-type H-SSZ-13, which showed that the protonated water tetramer (H<sub>3</sub>O)<sup>+</sup>(H<sub>2</sub>O)<sub>3</sub> is the smallest stable protonated cluster (Vener et al., 2009). Other works investigated the role of framework-H<sub>2</sub>O and H<sub>2</sub>O-H<sub>2</sub>O interactions on the collective behaviour of water molecules in one-dimensional zeolite channels of different size (Fois et al., 2001a,b, 2002), and on the structure and hydrogen bonding of water nanodroplets in zeolite pores of varying hydrophobicity (Coudert et al., 2009). A recent AIMD study contributed to the controversy regarding the stability of Al–O–Al linkages ("non-Löwenstein linkages"): Comparing AIMD simulations for anhydrous and hydrated models, Heard et al. (2019) showed that a configuration containing an Al–O–Al linkage is energetically preferred over configurations with no such linkages in the anhydrous form, but that hydration inverts the energetic order, leading to a preference for structures obeying Löwenstein's rule. The ubiquitous presence of water during zeolite formation might explain the observed absence of Al–O–Al linkages.

Sometimes, the DFT optimisation of a zeolite structure that starts from experimental data will deliver only a local minimum, rather than the global minimum structure. In such cases, an AIMD-based annealing can be employed to move out of the local minimum, as shown for all-silica zeolites and hydrated aluminosilicate zeolites (Hoffman et al., 2019; Abatal et al., 2020). AIMD calculations can also give insights into the instantaneous structure, which may deviate from the time-averaged crystal structure. Prominent examples are zeolites and zeotypes with linear or near-linear T–O–T linkages. The presence of such linkages is typically interpreted as a result of (static or dynamic) disorder of oxygen atoms around a higher-symmetry site. The highly dynamic behaviour of oxygen atoms associated with such linkages was indeed corroborated in AIMD simulations for AFI-type AIPO-5 (Cortie et al., 2017) and for the high-temperature phase of all-silica ferrierite (FER topology; Trudu et al. (2019)). Besides framework dynamics, the dynamic behaviour of cations has been studied with this method, for example to explain the impact of cation displacements on the diffusion of guest molecules through the 8MR windows of zeolite Na-RHO (Coudert and Kohen, 2017), and to investigate the role of the extra-framework content on the pressure-dependent behaviour of yugawaralite (YUG topology; Fois et al. (2005)) and gismondine (GIS topology; Betti et al. (2007)). A "potential of mean force" approach based on AIMD simulations has been proposed as a general framework to compute adsorption free energies, explicitly including different adsorption sites/configurations and temperature effects (Li et al., 2018).



## CHAPTER 2

### OVERVIEW AND CO-AUTHOR CONTRIBUTION INFORMATION

As demonstrated in the Introduction, computational methods are employed to investigate a diverse array of research topics in zeolite science. This thesis summarises the author's efforts in three distinct areas: **Chapter 3** compiles the results of "benchmarking" studies, in which DFT results obtained with different XC functionals and/or dispersion corrections were thoroughly validated against experimental structure data and, in some cases, other quantities. **Chapter 4** deals with fluoride-containing all-silica zeolites and other neutral-framework zeotypes, with particular emphasis on the dynamics of the fluoride anions encapsulated in small cages. Finally, **Chapter 5** compiles investigations that are broadly related to the adsorption of water in AIPOs and SAPOs. Although the questions addressed in these three chapters are essentially independent of each other, there are nevertheless various interconnections among them. For example, the benchmarking investigations were pivotal to choose suitable approaches for the work summarised in the two following chapters.

Every chapter starts with a thorough review of prior work before outlining the key questions that motivated the studies compiled in the respective chapter. A short summary of the content is then provided for each article. Key findings are illustrated in separate figures, and references to additional figures and tables in the respective articles (which constitute the **Appendix** of this thesis) are made where useful. Each chapter ends with a Conclusions section that summarises the key findings, and an Outlook providing perspectives for possible future work. The main part of this thesis ends with **Chapter 6**, entitled **Final Remarks**, which aims to put the main results in a broader context.

The following sections give a brief overview of the content of each chapter and list the individual research articles. Furthermore, co-author contribution statements are included for all articles having more than one author.

#### *2.1 Chapter 3: Benchmarking DFT Calculations against Zeolite Structure Data (and Other Quantities)*

This chapter compiles a total of five research articles that deal with the benchmarking of DFT calculations against experimental data for zeolites. **Article A1** focusses on the reproduction of crystal structure data, performing DFT optimisations with nine different approaches (six XC functionals without dispersion correction and three dispersion-corrected variants) for six hydrated natural zeolites. **Article A2** also puts most emphasis on crystal structures, but looks at neutral-framework zeotypes (ten all-silica zeolites, four AIPOs) as well as  $\alpha$ -quartz and  $\alpha$ -berlinite. It reports calculations with three pure-GGA and two dispersion-corrected GGA functionals. **Article A3** combines a benchmarking against structure data, which encompasses the same set of structures as **Article A2**, with a comparison of DFT-calculated relative energies against experimental enthalpies of transition for 16 all-silica zeolites and  $\alpha$ -cristobalite. Here, two dispersion-corrected variants of the PBEsol functional are used. **Article A4** represents the most comprehensive benchmarking study on neutral-framework zeotypes, as it compares the performance of a total of 14 dispersion-corrected DFT methods, along with two pure-GGA functionals. Using

the same set of reference structures as **Article A2**, an analysis of the optimisation results for all structures is augmented by an evaluation of computed relative energies and bulk moduli for those systems where experimental data are available. Finally, **Article A5**, which deals with fluoroaluminophosphates having the CHA topology, goes beyond a pure benchmarking study. In the first part of the article, it is assessed how well different approaches (two pure-GGA, four dispersion-corrected XC functionals) reproduce the structural parameters of four fluoroaluminophosphates containing different OSDAs, and the pressure-dependent behaviour of one of them. In the second part, it is predicted how the structural evolution under pressure varies as a function of the OSDA.

#### List of articles:

- A1** M. Fischer (2015): *Structure and Bonding of Water Molecules in Zeolite Hosts: Benchmarking Plane-Wave DFT against Crystal Structure Data*, Z. Kristallogr. 230, 325–336.
- A2** M. Fischer, F. O. Evers, F. Formalik, A. Olejniczak (2016): *Benchmarking DFT-GGA Calculations for the Structure Optimisation of Neutral-Framework Zeotypes*, Theor. Chem. Acc. 135, 257.
- A3** M. Fischer, R. J. Angel (2017): *Accurate Structures and Energetics of Neutral-Framework Zeotypes from Dispersion-Corrected DFT Calculations*, J. Chem. Phys. 146, 174111.
- A4** M. Fischer, W. J. Kim, M. Badawi, S. Lebègue (2019): *Benchmarking the Performance of Approximate van der Waals Methods for the Structural and Energetic Properties of SiO<sub>2</sub> and AlPO<sub>4</sub> Frameworks*, J. Chem. Phys. 150, 094102.
- A5** M. Fischer (2019): *Template Effects on the Pressure-Dependent Behavior of Chabazite-Type Fluoroaluminophosphates: A Computational Approach*, Phys. Chem. Minerals 46, 385–401.

#### Co-author contributions:

- The calculations on which **Article A2** is based were performed by Felix O. Evers in the context of a research project. Since Felix O. Evers' analysis remained rather preliminary, it was later redone and improved by MF, Filip Formalik, and Adam Olejniczak. The article was written by MF, with comments from Filip Formalik and Adam Olejniczak.
- The calculations reported in **Article A3** as well as the largest part of the analysis were done by MF. Ross J. Angel provided a code to compute the "Simple Rigid Body" correction of bond lengths, and assisted in the analysis of the effect of temperature. The article was written by MF, with input from Ross J. Angel.
- The results reported in **Article A4** were obtained in a large series of calculations that were set up by Won June Kim, the joint first author. The analysis and comparison to experimental data was largely done by MF. Both Michael Badawi and Sébastien Lebègue were constantly involved by providing thoughts and advice on both calculation setup and analysis. The larger part of the article was drafted by MF, with the exception of the Computational Methods section (section II), which was written by Won June Kim. All authors contributed to the finalisation of the article.

## 2.2 Chapter 4: Structure and Dynamics of Fluoride-Containing Zeolites and Zeotypes

This chapter encompasses five research articles that address the local environment and dynamic behaviour of fluoride anions in different zeolites and zeotypes. All of these works use a more or less identical methodology, combining DFT optimisations and DFT-based AIMD simulations. **Article B1** focusses on silicogermanates with the AST topology, where fluoride is encapsulated in *d4r* cages. After determining the energetically most favourable arrangements of Si and Ge at the corners of the cage for different Si/Ge ratios, AIMD simulations are employed to investigate the influence of the local environment on the dynamic behaviour of fluoride. In **Article B2**, the investigation on AST-type system is expanded to include  $\text{AlPO}_4$  and  $\text{GaPO}_4$  compositions, and to study the influence of the OSDA on the equilibrium position and dynamic behaviour of fluoride. Fluoride anions that are bonded to Si atoms in trigonal-bipyramidal  $[\text{SiO}_{4/2}\text{F}]^-$  units are at the core of the investigations reported in **Article B3** and **B4**. In the former article, the influence of the OSDA on the dynamic disorder of fluoride anions in MFI-type Silicalite-1 is studied using AIMD simulations. **Article B4** covers a total of five all-silica zeolites with different topologies, all of which contain  $[\text{SiO}_{4/2}\text{F}]^-$  units. While the first part of the study looks at the energetic ordering of different fluoride positions in the respective structures, the second part investigates qualitative differences in the dynamic behaviour of fluoride. Finally, **Article B5** concentrates on a single zeolite topology, investigating the preferred Ge distributions in ITQ-13 silicogermanates (ITH topology), which contain fluoride anions in two different cages. Besides a prediction of the energetic ordering of different configurations at a given Ge content, the influence of the local environment on the  $^{19}\text{F}$  chemical shifts, on the fluoride dynamics, and on the likely defluorination behaviour is evaluated for selected systems.

### List of articles:

- B1** M. Fischer (2019): *Local Environment and Dynamic Behavior of Fluoride Anions in Silicogermanate Zeolites: A Computational Study of the AST Framework*, J. Phys. Chem. C 123, 1852–1865.
- B2** M. Fischer, L. Freymann (2021): *Local Distortions in a Prototypical Zeolite Framework Containing Double Four-Ring Cages: The Role of Framework Composition and Organic Guests*, ChemPhysChem 22, 40–54.
- B3** M. Fischer (2020): *Influence of Organic Structure-Directing Agents on Fluoride Dynamics in As-Synthesized Silicalite-1*, J. Phys. Chem. C 124, 5690–5701.
- B4** M. Fischer (2021): *Fluoride Anions in All-Silica Zeolites: Studying Preferred Fluoride Sites and Dynamic Disorder with Density Functional Theory Calculations*, J. Phys. Chem. C 125, 8825–8839.
- B5** M. Fischer, C. Bornes, L. Mafra, J. Rocha (2022): *Elucidating the Germanium Distribution in ITQ-13 Zeolites by Density Functional Theory*, Chem. Eur. J. 28, e202104298.

### Co-author contributions:

- The calculations on which **Article B2** is based were partially run by Linus Freymann (student assistant), who also did a large part of the initial analysis of the AIMD trajectories. The article was written by MF, with comments from Linus Freymann.
- The calculations of the  $^{19}\text{F}$ -NMR chemical shifts reported in **Article B5** were carried out by Carlos Bornes. Carlos Bornes and his supervisors Luís Mafra and João Rocha all contributed to the discussions and the finalisation of the article.

## 2.3 Chapter 5: Interaction of (Silico)Aluminophosphates with Adsorbed Water Molecules

This chapter brings together five articles that deal with the adsorption of water in AlPOs and SAPOs. The first two articles use an analogous approach, employing DFT optimisations to study the interaction with water at different levels of hydration. While **Article C1** looks at models of CHA-type SAPO-34 that contain different silicon environments (isolated Si atoms, Si islands) or defects, **Article C2** compares a total of six different frameworks in AlPO and SAPO form. In **Article C3**, DFT calculations are used to study the structure and vibrational spectra of fully hydrated APC-type  $\text{AlPO}_4\text{-H3}$ , which contains  $[\text{AlO}_{4/2}(\text{H}_2\text{O})_2]$  octahedra, as well as its calcined counterpart. Moreover, AIMD simulations deliver insights into the dynamic behaviour of the adsorbed water molecules. **Article C4** focusses on ECR-40, an unusual MEI-type SAPO that contains corner-sharing  $\text{AlO}_4$  tetrahedra, thus violating Löwenstein's rule. After predicting the preferred locations and acidities of the framework protons with DFT calculations, AIMD simulations for different levels of hydration are employed to investigate the proton mobility, as well as hydration-induced structural changes. **Article C5** is rather loosely connected to the other studies, as it primarily deals with the structure and dynamics of calcined AlPO-11, especially the differences between the instantaneous and time-averaged structure. The preferred water adsorption sites are also predicted, forming a thematic link to the remaining articles in this chapter.

### List of articles:

- C1** M. Fischer (2015): *Water Adsorption in SAPO-34: Elucidating the Role of Local Heterogeneities and Defects Using Dispersion-Corrected DFT Calculations*, Phys. Chem. Chem. Phys. 17, 25260–25271.
- C2** M. Fischer (2016): M. Fischer: *Interaction of Water with (Silico)Aluminophosphate Zeotypes: A Comparative Investigation using Dispersion-Corrected DFT*, Phys. Chem. Chem. Phys. 18, 15738–15750.
- C3** M. Fischer (2019): *First-Principles Study of  $\text{AlPO}_4\text{-H3}$ , a Hydrated Aluminophosphate Zeotype Containing Two Different Types of Adsorbed Water Molecules*, Molecules 24, 922.
- C4** M. Fischer (2019): *Proton Acidity and Proton Mobility in ECR-40, a Silicoaluminophosphate that Violates Löwenstein's Rule*, Chem. Eur. J. 25, 13579–13590.
- C5** M. Fischer (2021): *Revisiting the Structure of Calcined and Hydrated AlPO-11 with DFT-Based Molecular Dynamics Simulations*, ChemPhysChem 22, 2063–2077.

## 2.4 Funding information

The investigations compiled in this thesis were carried out between 2014 and 2021 at the **University of Bremen**, funded by the **Central Research Development Funds** (Zentrale Forschungsförderung – ZF) of the University of Bremen from 2014 to 2018 (funding line "ZF 04 - Independent Projects for Postdocs", project title: *Computational studies of host-guest interactions in zeolites*) and by the **German Research Foundation** (Deutsche Forschungsgemeinschaft – DFG) from 2018 to 2021 (module "Temporary Positions for Principal Investigators", project title: *Beyond tetrahedral coordination in zeolite-type materials – A computational approach*, project no. 389577027). The thesis was completed while receiving funding through a DFG Heisenberg fellowship (project title: *Comparative, modelling-based investigations of pharmaceutical adsorption in zeolites*, project no. 455871835).

## CHAPTER 3

# BENCHMARKING DFT CALCULATIONS AGAINST ZEOLITE STRUCTURE DATA (AND OTHER QUANTITIES)

### 3.1 *Broader context and previous work*

#### 3.1.1 *Pitfalls in zeolite crystal structure determination*

Since the structure determination of the zeolite mineral analcime (ANA topology) by Taylor (1930), several 1,000s of zeolite crystal structures have been determined from X-ray, neutron, or electron diffraction data (Baur and Fischer, 2000 to 2017). Although very accurate structure determinations have been reported for some zeolite minerals and a few synthetic zeolites that can be produced as sizeable crystals, such as zeolite A (Fischer et al., 2012), typical zeolite syntheses deliver very small crystals that are not amenable to conventional single-crystal X-ray diffraction (sc-XRD). Structure refinements based on powder X-ray diffraction (PXRD) experiments usually require a reasonable starting model and are therefore unable to determine the structure from scratch. State-of-the-art three-dimensional electron diffraction allows to perform single-crystal diffraction experiments on very small crystals (Huang et al., 2021), however, this method is not (yet) as routinely applicable as conventional XRD experiments. Besides frequent limitations in terms of crystal size and quality, several other issues can complicate the crystal structure determination of zeolites and zeotypes:

- Si and Al are often disordered on the T sites, and the essentially identical scattering factors of  $\text{Si}^{4+}$  and  $\text{Al}^{3+}$  make it difficult to determine accurate occupancies from XRD data (Armbruster and Gunter, 2001).
- Static or dynamics disorder of framework oxygen atoms around higher-symmetry sites can result in "apparently straight" T–O–T angles, which may result in a shortening of the T–O distances to chemically implausible values (Trudu et al., 2019).
- In cation-exchanged zeolites, there are often several fractionally occupied cation positions that may lie in close proximity. The correlation between thermal displacement parameters and site occupancy factors complicates the refinement of accurate occupancies.
- For zeolites synthesised in the presence of organic cations, the localisation of OSDA molecules in the pores is often hampered by static or dynamic disorder.
- Hydrated zeolites pose a particular challenge, as the water molecules in the pores may be heavily disordered, especially in the absence of strong interactions with extra-framework cations. The positions of hydrogen atoms of water molecules can only be determined in favourable cases, usually by using neutron diffraction (although determinations from XRD data have also been reported; Pluth and Smith (1986)).

In the view of these pitfalls, it is not surprising that many published zeolite structures suffer from crystal-chemical "problems", such as unrealistic T–O bond distances (Dawson et al., 2017; Baur and Fischer, 2019). In such cases, computational structure optimisations can help to remove problematic

features in the crystal structure. For example, systematic investigations by Ashbrook's group on aluminophosphates showed that a DFT relaxation of the structure results in much better agreement of the calculated NMR parameters with experiment than a computation of these parameters using the experimental crystal structure (Ashbrook et al., 2008; Sneddon et al., 2014). As NMR shifts are sensitive to the local environment, this provides clear evidence that the optimisations cause adjustments towards more plausible local geometries.

A specific issue highlighted above is the experimental determination of the hydrogen positions of adsorbed water molecules. Larin et al. (2003) used periodic Hartree-Fock calculations to optimise the hydrogen positions of the water molecules in three hydrated zeolites prior to an analysis of cation-water interactions and hydrogen bonds. Subsequent work by the same group of authors employed both Hartree-Fock and DFT calculations to analyse the distortions of the adsorbed H<sub>2</sub>O molecules in the same set of zeolites (Larin et al., 2005).

### 3.1.2 Benchmarking DFT calculations for periodic solids

Due to the dependence of the outcome of a DFT calculation on the XC functional and – if included – the dispersion correction scheme, the "benchmarking" of DFT calculations has become a research field of its own. Studies on molecules and molecular complexes typically use reference data from high-level WFT calculations (Remya and Suresh, 2013; Mardirossian and Head-Gordon, 2017; Claudot et al., 2018). Because such high-level reference data are hardly available for periodic solids, benchmarking efforts on these systems typically rely on experimental data, such as crystal structures, cohesive energies, and/or bulk moduli. For example, Haas et al. (2009) studied the performance of the LDA, 5 GGA functionals, and one meta-GGA functional in reproducing lattice parameters and bulk moduli of simple cubic solids, as well as graphite and two noble gas crystals. The same group later expanded this work by considering about 35 GGA, meta-GGA, and hybrid XC functionals, as well as about 25 dispersion-corrected variants (Tran et al., 2016). This work showed that the inclusion of a dispersion correction is not only pivotal for the description of weakly bonded systems (rare gas crystals, layered systems), but that it may also improve the performance of GGA-type functionals for strongly bonded solids (metals, ionic solids), as the overestimation of unit cell dimensions that is typical for GGA can be alleviated. Demichelis et al. (2010a) investigated the performance of 12 different XC functionals (LDA, GGA, hybrids) to reproduce the structures and relative stabilities of Al<sub>2</sub>SiO<sub>5</sub>, Al(OOH), and Al(OH)<sub>3</sub> polymorphs. While GGA-type functionals performed rather well for Al<sub>2</sub>SiO<sub>5</sub> structures, only hybrid functionals could reproduce the structural parameters of layered aluminium hydroxides satisfactorily. A subsequent study by Tunega et al. (2012) showed that dispersion-corrected DFT approaches can afford an accurate prediction of the interlayer distance of sheet silicates, with typical errors in the lattice parameter *c* (normal to the sheets) falling below 1%. Due to the importance of intermolecular interactions in molecular crystals, it is not surprising that the inclusion of a dispersion correction is pivotal to arrive at reasonably accurate lattice parameters for these systems (Reilly and Tkatchenko, 2013; Binns et al., 2014; Carter and Rohl, 2014). Although most emphasis in the benchmarking studies summarised above was on structural parameters, the performance of DFT for other properties has also been investigated. This includes computational predictions of vibrational spectra (Demichelis et al., 2010b; De la Pierre et al., 2011), dielectric tensors (De la Pierre et al., 2011), band gaps (Tran and Blaha, 2017), or elastic constants (Råsander and Moram, 2015). Taking together results from these different benchmarking studies, it is clear that the choice of a suitable approach will strongly depend on the quantity in question.

### 3.1.3 Previous benchmarking works on zeolites: Structures and relative energies

A number of authors also assessed the performance of different XC functionals and, in the more recent studies, dispersion corrections in the calculation of equilibrium structures and/or relative energies of zeolites. With regard to neutral-framework zeolites, the earliest comparison was presented by Civaleri et al. (1998), who used the LDA, two GGA functionals (BLYP and PW91), and the hybrid B3LYP functional to predict the relative stability of all-silica zeolites and  $\beta$ -quartz with respect to  $\alpha$ -quartz. Although similar trends were found for all functionals, quantitative differences were far from negligible, with individual values varying, in some instances, by a factor of 2. These authors also noted a significant dependence on the basis set size for these LCAO calculations (CRYSTAL code). In a similar vein, Astala et al. (2004) compared the performance of the LDA and the GGA-type PW91 functional to reproduce structural parameters and relative stabilities of five all-silica zeolites,  $\alpha$ -quartz, and  $\alpha$ -cristobalite, using plane-wave DFT calculations with VASP. At variance with the work of Civalleri et al. (1998), these authors observed that the PW91 functional failed to reproduce the inverse correlation between framework density and relative energy that is known from experiment (Navrotsky et al., 2009). Moreover, it exhibited a systematic tendency to overestimate the lattice parameters, whereas LDA delivered parameters in reasonable agreement with experiment. The overestimation of the unit cell dimensions by the GGA-type PW91 and PBE functionals was also reported by Göttl and Hafner (2012) in a study of all-silica CHA. Observing much better agreement with experiment for the hybrid PBE0, HSE03, and HSE06 functionals, they also noted that the use of GGA functionals resulted in Si–O bond lengths that were somewhat longer than experimental (and hybrid DFT) values.

The importance of including dispersion interactions to arrive at accurate relative energies of all-silica zeolites was pointed out more recently by Román-Román and Zicovich-Wilson (2015). Using CRYSTAL, these authors compared the performance of the hybrid B3LYP functional and the dispersion-corrected hybrids B3LYP-D2, B3LYP-D\*, and PBE0-D2 in reproducing experimental enthalpies of transition of 14 all-silica zeolites (the reference point being  $\alpha$ -quartz; it is usually assumed that enthalpies of transition can be approximated using DFT energy differences, *i.e.*, relative energies). PBE0-D2 delivered fairly good agreement with experiment, B3LYP without dispersion correction underestimated the range of relative energies, and B3LYP-D2/D\* resulted in a too large energy difference between zeolites and  $\alpha$ -quartz (**Figure 3.1**). These findings were interpreted as clear evidence that dispersion interactions play a key role in stabilising  $\alpha$ -quartz over the less dense zeolite phases, and hence need to be accounted for in DFT calculations aiming at quantitative accuracy. A downside that was mentioned, although not emphasised in the work of Román-Román and Zicovich-Wilson (2015) was the severe overestimation of the molar volumes (*i.e.*, underestimation of the densities) by all tested approaches, with typical errors in the range of 10%. Hay et al. (2015) placed more emphasis on the reproduction of structural properties, employing the LDA and PBE functionals as well as different dispersion-corrected functionals (pairwise dispersion correction schemes: PBE-D2, PBE-TS; nonlocal vdW-DF approaches: vdW-DF2, rVV10) to optimise the structures of  $\alpha$ -quartz,  $\alpha$ -cristobalite, coesite, and two all-silica zeolites (faujasite and ferrierite), using a combination of CASTEP and QuantumEspresso. They found a good performance of dispersion-corrected DFT methods for relative energies, but, unlike Román-Román and Zicovich-Wilson (2015), also observed a relatively accurate reproduction of the lattice parameters. For example, the PBE-D2 and PBE-TS functionals delivered to unit cell volumes that agreed to within 2% with experimental values. Hay et al. (2015) noted that the dispersion-corrected GGA functionals (PBE-D2/Ts) tend to overestimate Si–O bond distances, but that the simultaneous underestimation of Si–O–Si angles results in an error compensation in the lattice parameters.



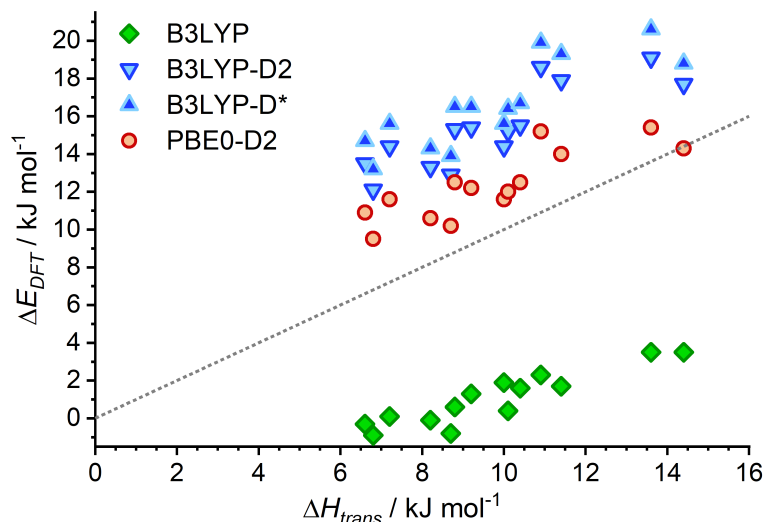


**Figure 3.1:** Plot of relative energies  $\Delta E_{DFT}$  computed with different XC functionals by Román-Román and Zicovich-Wilson (2015) against experimental enthalpies of transition  $\Delta H_{trans}$  (both per  $\text{SiO}_2$  formula unit). The D\* label represents a pairwise dispersion correction proposed by Jurečka et al. (2007).

Due to the frequent occurrence of disorder on T sites and/or cation positions, crystal structures of cation-exchanged zeolites are often less well suited for DFT benchmarking investigations, and few authors appear to have compared the performance of different XC functionals for these systems. One notable exception is the work of Kremleva et al. (2013), who considered the PBE and PBE-D2 functionals in their study of cation-exchanged natrolites (which have a fully ordered distribution of Si and Al). On the one hand, they observed an improved agreement with experimental lattice parameters when employing the D2 dispersion correction, agreeing with the previously mentioned studies on all-silica zeolites. On the other hand, unlike PBE, the use of the PBE-D2 functional resulted in qualitatively wrong trends when predicting the pressure-dependent behaviour of hydrated natrolite. The challenge of describing the interaction with adsorbed water molecules was also highlighted by Labat et al. (2010), who benchmarked different DFT approaches against high-level WFT calculations (MP2 perturbation theory) in an investigation of  $\text{H}_2\text{O}$  molecules interacting with small fragments taken from the structure of Silicalite-1. Of the different functionals tested, the GGA-type B97-D and the parameterised hybrid meta-GGA functional M05-2X delivered the best agreement in terms of equilibrium distances and interaction energies.






### 3.2 Key questions addressed in this chapter

The summary given in the previous section clarifies that significant knowledge gaps existed in the DFT literature on zeolites prior to the start of the investigations reported in **Articles A1 to A5**:

1. The performance of different XC functionals in reproducing crystal structures of cation-exchanged zeolites had remained largely unexplored.
2. Studies comparing different DFT approaches for all-silica zeolites either included only a few zeolite structures or focussed predominantly on relative energies, whereas detailed structural studies considering a larger set of frameworks were missing.

3. AlPOs or other neutral-framework zeotypes were hardly considered in benchmarking investigations, despite a wealth of experimental structure data.
4. Comparative investigations on OSDA-containing zeolite or zeotype structures were also missing.

While **Article A1** deals with the first point, **Articles A2, A3, and A4** address the second and third point. Finally, the issue of OSDA-containing zeotypes is touched upon in **Article A5**. **Figure 3.2** gives an overview of the zeolites and zeotypes studied, the XC functionals and dispersion correction schemes used, the DFT codes used in the calculations, and the quantities considered in the benchmarking (in several instances, not all quantities were available for all zeolites). It should be noted that, although many of the articles that are part of the subsequent chapters also contain a comparison of DFT-optimised structures to experimental data, they do not include a systematic comparison of different XC functionals and/or dispersion corrections.

Article	Materials	DFT methods	DFT code	Quantities
<b>A1</b>	Li-BIK, Ba-EDI, Ca-GIS, Ca-NAT, Na-NAT, Ca-YUG	LDA PW91, PBE, PBEsol, WC, RPBE PW91-OBS, PBE-D2, PBE-TS		<ul style="list-style-type: none"> <li>Atomic coordinates</li> </ul>
<b>A2</b>	$\alpha$ -quartz, $\alpha$ -berlinite ASZs: CHA, FAU, FER, IFR, LTA, RTE, SAS, TON (AST, SOD) AIPOs: AEN, CHA, ERI, EZT	PBE, PBEsol, WC PBE-D2, PBE-TS		<ul style="list-style-type: none"> <li>Lattice parameters</li> <li>T-O distances, T-O-T angles</li> <li>Relative energies (<i>some systems</i>)</li> </ul>
<b>A3</b>	Set 1: same as A2 Set 2: $\alpha$ -quartz, $\alpha$ -cristobalite, 16 ASZs	PBEsol-D2, PBEsol-TS		<p>Set 1:</p> <ul style="list-style-type: none"> <li>Lattice parameters</li> <li>T-O distances, T-O-T angles</li> </ul> <p>Set 2:</p> <ul style="list-style-type: none"> <li>Relative energies</li> </ul>
<b>A4</b>	qtz- and crs-type SiO <sub>2</sub> , and AlPO <sub>4</sub> ASZs: CHA, FAU, FER, IFR, LTA, RTE, SAS, TON AIPOs: AEN, CHA, ERI, EZT	PBE, PBEsol PBE-D2, -D3, -D3(BJ), PBE-TS, -TS/HI, -MBD, -MBD/FI vdW-DF, optPBE-vdW, optB88-vdW, optB86b-vdW, vdW-DF-cx, vdW-DF2, rev-vdW-DF2		<ul style="list-style-type: none"> <li>Lattice parameters</li> <li>T-O distances, T-O-T angles</li> <li>Relative energies (<i>some systems</i>)</li> <li>Bulk moduli (<i>some systems</i>)</li> </ul>
<b>A5</b>	4 CHA-type fluoroaluminophosphates containing different OSDAs	PBE, PBEsol PBE-D2, PBE-TS, PBEsol-D2, PBEsol-TS		<ul style="list-style-type: none"> <li>Unit cell volumes</li> <li>Interatomic distances &amp; angles</li> <li>Bulk modulus (<i>one system</i>)</li> </ul>

**Figure 3.2:** Overview of the materials, DFT methods and codes, and quantities that were considered in the benchmarking investigations reported in **Articles A1** to **A5**. ASZs = all-silica zeolites.

### 3.3 **Article A1:** Structure and Bonding of Water Molecules in Zeolite Hosts: Benchmarking Plane-Wave DFT against Crystal Structure Data

#### 3.3.1 Outline

In this article, DFT optimisations were performed for six hydrated, cation-exchanged zeolites, using a total of nine different DFT approaches, and the DFT-optimised structures were then compared against experimental structure data. The main criteria for the selection of zeolites were the availability of structure data obtained from single-crystal neutron diffraction experiments (which permit a reliable localisation of the hydrogen/deuterium atoms) and no, or only very limited, disorder in the crystal structure. This led to the selection of the following natural zeolites: Bikitaite (Li-BIK; Ståhl et al. (1989)), edingtonite (Ba-EDI; Belitsky et al. (1986)), gismondine (Ca-GIS; Artioli et al. (1986)), scolecite (Ca-NAT; Kvik and Ståhl (1985)), natrolite (Na-NAT; Artioli et al. (1984)), and yugawaralite (Ca-YUG; Kvik et al.

(1986)). As shown in **Figure 3.2**, the set of DFT approaches included one LDA and five GGA functionals as well as three dispersion-corrected variants of the GGA-type PW91 and PBE functionals. The calculations used the CASTEP code (Clark et al., 2005) with ultrasoft pseudopotentials (generally, only the most important aspects of the calculation settings are provided here, as detailed descriptions are supplied in the individual articles and the associated material).

It is worth noting that, unlike in all following articles, the lattice parameters were not optimised in this study. Previous works have shown that many XC functionals deliver systematic deviations in the unit cell dimensions (*e.g.*, GGA functionals like PBE tend to overestimate them). Therefore, it may often be the preferred option to use experimentally determined lattice parameters, for example when trying to improve the structural parameters determined from diffraction data, or in AIMD simulations in the *NVT* ensemble. As this work placed particular emphasis on the positions of water molecules, where the hydrogen positions are notoriously difficult to determine experimentally, the lattice parameters were fixed to their experimental values, and the error analysis focussed on the changes in atomic coordinates (and, as a result, interatomic distances and angles) that occur during the structure optimisation. The error was quantified by computing the arithmetic mean of the moduli of the difference vectors between experimental and DFT-optimised positions of all atoms, labelled average positional deviation *dev*.

### 3.3.2 Summary of results

An analysis of the deviations in atomic positions for all individual combinations of zeolites and XC functionals delivered average positional deviations *dev* between 0.022 Å and 0.230 Å (**A1**, Table 1). The PBE functional performed rather well, with no *dev* value exceeding 0.070 Å. Although some functionals gave smaller errors than PBE for individual zeolites, none of them showed a better performance across the board. This can be illustrated by dividing the *dev* values of other functionals by the *dev* values of PBE (*i.e.*,  $dev(PBE) \equiv 1$ ), as shown in **Figure 3.3**. Among the dispersion-corrected functionals, PBE-TS, which employs a volume-dependent scaling of the dispersion coefficients, resulted in significantly smaller deviations than the other two variants, which use generic coefficients. A separate calculation for different groups of atoms showed that the deviations are, generally, smallest for framework atoms, followed by extra-framework cations and O and H atoms of H<sub>2</sub>O molecules. In other words, atoms that participate in strong and directional bonds move only relatively slightly during the DFT optimisation, whereas the structural relaxation has a larger impact on the position of atoms that interact with their environment only through electrostatic interactions, dispersion, and (in some cases) hydrogen bonds. Moreover, it seems plausible to expect that the positions of the water molecules in the experimental crystal structures are associated with a larger uncertainty than those of framework atoms and cations. Having established the good performance of the PBE and PBE-TS functionals in reproducing crystal structure data, the zeolite structures optimised with these functionals were analysed in more detail, with focus on the geometry of the water molecules, on hydrogen bond distances, and on cation-oxygen distances. With regard to intramolecular O<sub>water</sub>-H bonds, the optimisation of the structure resulted in a narrower distribution of the bond lengths, and, overall, a slight expansion when compared to experiment (**Figure 3.3**). An increase of approximately the same magnitude is obtained when correcting the experimental results for thermal motion ("riding" correction; Busing and Levy (1964)). For hydrogen bonds, a modest, but systematic tendency towards shorter H ··· O distances was observed in the DFT-optimised structures (**A1**, Figure 4), in agreement with earlier findings (Ireta et al., 2004). The cation-oxygen distances mostly agreed with experiment to within a few 1/100 Å, with the exception of some rather pronounced changes in the barium coordination environment in Ba-EDI (**A1**, Figure 6).

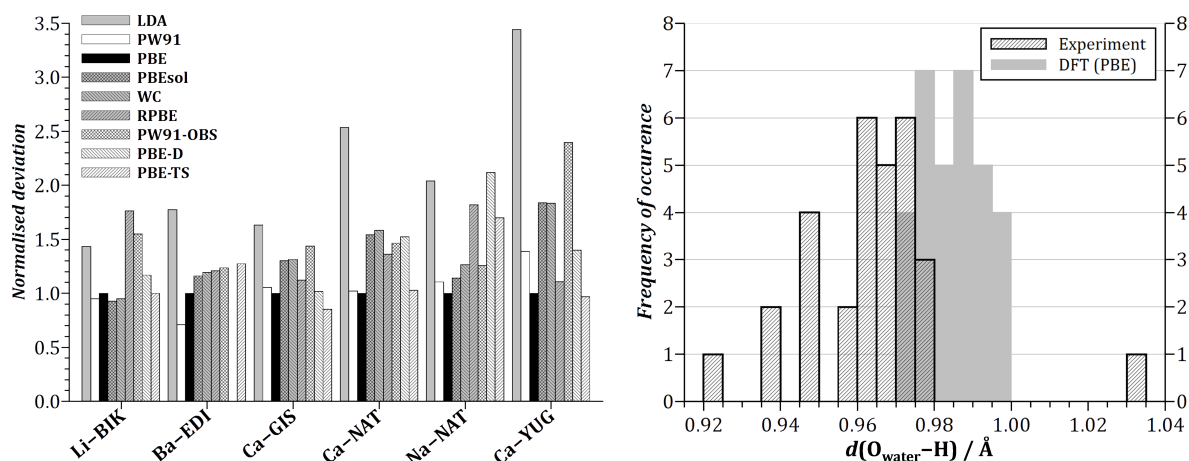


**Figure 3.3:** Left: Normalised positional deviation obtained with different functionals for individual zeolites. For a given functional  $X$ , the normalised (dimensionless) deviation was calculated as  $dev(X)/dev(PBE)$ . Right: Distribution of  $O_{\text{water}}-H$  bonds in experimental structures and DFT-optimised structures (PBE functional). Figure modified after **Article A1**.

In summary, the benchmarking against high-quality crystal structures determined from neutron diffraction experiments, which are available only for a handful of hydrated zeolites, showed that DFT optimisations using the PBE or PBE-TS functionals result in a fairly accurate reproduction of the experimental crystal structures. This indicates their suitability for computational studies of water-containing zeolites, *e.g.*, to "improve" crystal structures in cases where the experimental data do not allow for a reliable refinement of all atomic positions, or in DFT or AIMD studies of hydrated zeolites and zeotypes. Building on this result, the DFT calculations performed in the context of **Chapter 5** all used dispersion-corrected variants of the PBE functional (PBE-TS and PBE-D3).

### 3.4 **Article A2:** Benchmarking DFT-GGA Calculations for the Structure Optimisation of Neutral-Framework Zeotypes

#### 3.4.1 Outline

This investigation looked at the performance of five DFT approaches (three GGA functionals: PBE, WC, PBEsol; two dispersion-corrected approaches: PBE-D2, PBE-TS) in reproducing structural parameters (lattice parameters, T-O bond lengths, T-O-T angles) of neutral-framework zeotypes having  $\text{SiO}_2$  and  $\text{AlPO}_4$  compositions. A comprehensive evaluation of the available experimental crystal structure data, taken from the ZeoBase database compiled by Baur and Fischer (2010) (also published in book form; Baur and Fischer (2000 to 2017)), led to the definition of several selection criteria: For example, the crystal structure refinement should have been performed for a calcined sample of a pure  $\text{SiO}_2/\text{AlPO}_4$  system, there should be no signs of structural disorder, all T-O bond lengths should fall in a reasonable range, etc. On this basis, a total of eight all-silica zeolites and four AlPOs were identified (**Figure 3.4**).  $\alpha$ -quartz and  $\alpha$ -berlinite were included in the benchmarking as non-porous tetrahedral frameworks, and two additional all-silica zeolites (SOD and AST) were also optimised, but analysed separately due to the much larger errors in lattice parameters.

The overall deviations between DFT-optimised and experimental structures were evaluated by making use of the mean of signed errors (MSE) and the mean of absolute errors (MAE), as well as the root mean

square of relative errors (RMSE), which were computed for the quantities of interest (lattice parameters, T-O bonds, T-O-T angles). For comparison, an analogous analysis was performed on previously published structures optimised by Coudert (2013) using the B3LYP-D2 functional (structure data were kindly provided by Dr. F.-X. Coudert, Paris), and on structures optimised with two different force fields. Finally, relative energies were compared to experimental enthalpies of transition for four all-silica zeolites for which experimental data are available.

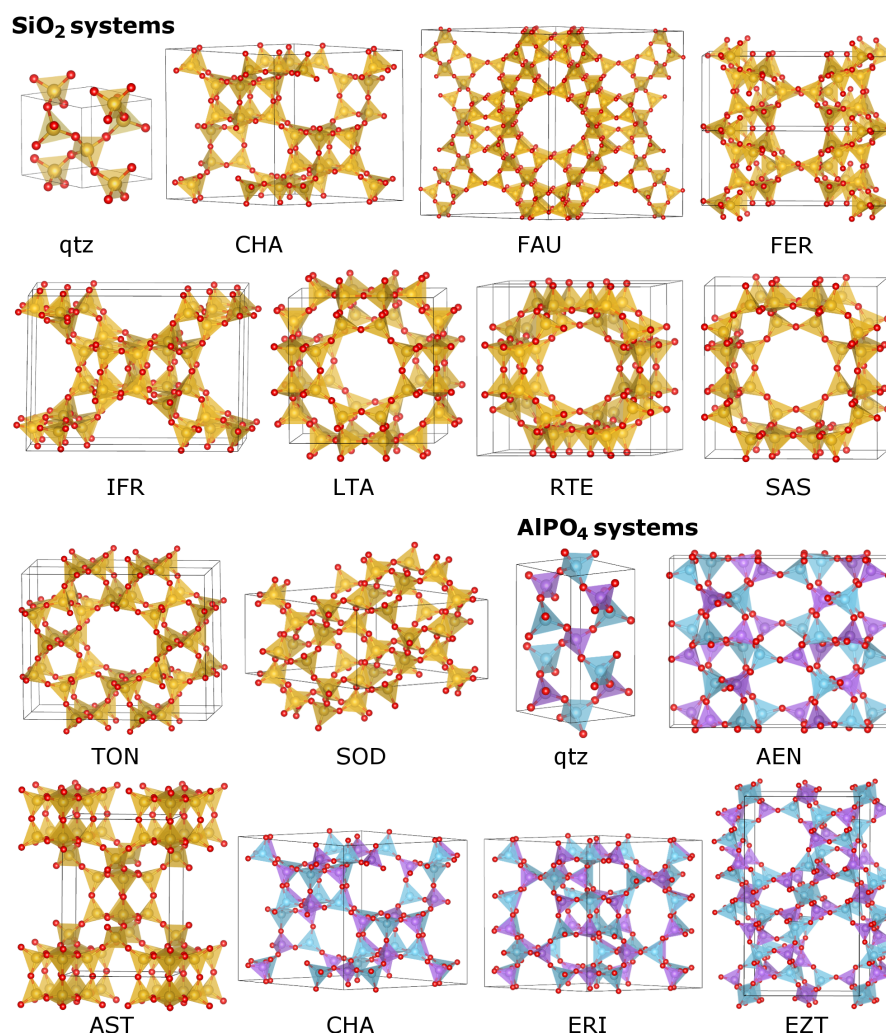


**Figure 3.4:** Crystal structure plots of SiO<sub>2</sub> and AlPO<sub>4</sub> systems used in the benchmarking against experimental structure data. Figure reproduced from **Article A2**.

### 3.4.2 Summary of results

A comparison of the optimised unit cell parameters to experimental data showed that all functionals exhibit a systematic tendency to overestimate the cell dimensions. An overview of the MSE and MAE values is shown in **Figure 3.5**. As expected, PBE performed worst. While PBEsol and WC reduced the overestimation, the dispersion-corrected variants performed even better, with a root mean square of relative errors of about 0.5% for PBE-TS. With regard to T-O bond lengths, all PBE-based approaches delivered somewhat too long Si-O and Al-O bonds, with typical errors on the order of 0.01 Å (**A2**, **Figure 4**). The PBEsol and WC functionals reduced the deviations for these bonds, but showed

a slight tendency to underestimate the P–O bond distances. Although the dispersion corrections had essentially no influence on the bond distances, they delivered systematically smaller T–O–T angles (A2, Table 4). This observation was attributed to an exaggerated attraction between the T atoms at opposite ends of the T–O–T linkages, resulting in the conclusion that more elaborate dispersion correction schemes might be needed to capture the balance between short-range and long-range interactions. This tendency was also corroborated for the two outliers, SOD and AST: Both of these structures contain relatively distorted 6MR windows. Whereas the functionals without dispersion correction delivered a reduced distortion when compared to the experimental structures, the dispersion-corrected functionals exaggerated the distortion (A2, Figure 8), presumably due to an overestimated attraction between atoms lying at opposite sides of the 6MR windows.

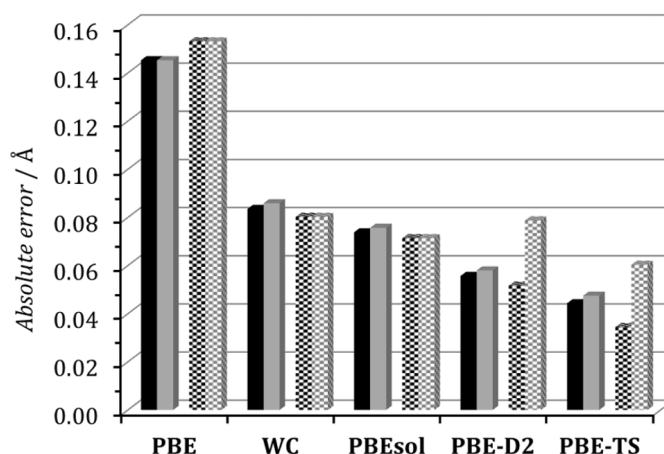


**Figure 3.5:** MSE and MAE in lattice parameters obtained with different functionals. For each functional, the bars from left to right represent: MSE (black, filled) and MAE (grey, filled) for SiO<sub>2</sub> systems, MSE (black, checkered) and MAE (grey, checkered) for AlPO<sub>4</sub> systems. Figure reproduced from **Article A2**.

The overall errors in the structures of all-silica zeolites previously optimised with the B3LYP-D2 functional were found to be significantly larger than for any of the functionals considered in the present study. The systematic tendency of this functional to deliver too large molar volumes, already pointed out by Román-Román and Zicovich-Wilson (2015), was attributed to a concurrent overestimation of Si–O bonds and Si–O–Si angles. Among the two force fields, the SLC FF (Sanders et al., 1984) resulted in an excellent prediction of structural parameters, essentially on par with PBE-TS, the best-performing DFT approach. In contrast, the ClayFF (Cygan et al., 2004) was found to combine an underestimation of Si–O bond lengths with an overestimation of Si–O–Si angles.

Since experimentally measured enthalpies of transition have been published for all-silica zeolites with the CHA, FAU, FER, and IFR topologies, the relative energies for these four systems could be compared to experiment. All functionals without dispersion correction showed a completely unsatisfactory performance, failing even to reproduce the trend in relative stability. PBE-D2 and PBE-TS gave much improved results, highlighting the importance of including dispersion corrections to predict reasonable relative energies. Among the two, the PBE-D2 functional gave relatively good quantitative agreement with experimental enthalpies of transition, whereas the PBE-TS functional overstabilised  $\alpha$ -quartz over the porous frameworks (A2, Table 7). The different behaviour of these two dispersion corrections in the prediction of relative stabilities was one of the key questions addressed in the following paper.



### 3.5 Article A3: Accurate Structures and Energetics of Neutral-Framework Zeotypes from Dispersion-Corrected DFT Calculations

#### 3.5.1 Outline

Motivated by the rather good agreement of the T–O bond distances observed for the PBEsol functional (Perdew et al., 2008) in the preceding study, the first part of this study investigated the performance of two dispersion-corrected variants of this functional, PBEsol-D2 (Csonka et al., 2008) and PBEsol-TS (Al-Saidi et al., 2012), in reproducing the structural parameters of neutral-framework zeotypes, looking at the same set of structures as in Article A2 (Figure 3.4). An aspect that was touched upon only briefly in the previous article, namely the degree to which temperature-dependent changes of lattice parameters and bond lengths might affect the agreement between DFT and experiment, was investigated in more depth, making use of low-temperature structure data and a bond length correction based on isotropic displacement parameters for some systems. The second part of this article looked at the relative stability of SiO<sub>2</sub> phases, performing calculations for  $\alpha$ -quartz,  $\alpha$ -cristobalite, and a total of 16 all-silica zeolites. Some of these structures were already part of the set of reference structures used for the benchmarking against experimental structure data, and the overlap between both sets is shown in Figure 3.6. The DFT relative energies  $\Delta E_{DFT}$  were then compared to enthalpies of transition  $\Delta H_{trans}$  obtained from solution calorimetry experiments (Navrotsky et al., 2009).

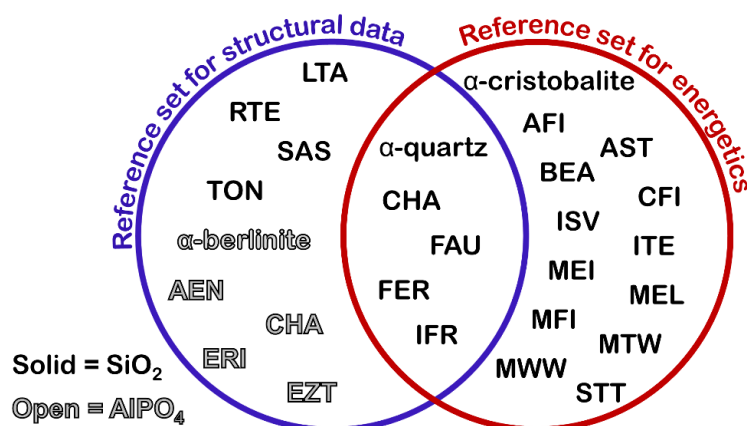


**Figure 3.6:** Overview of reference sets used for the benchmarking against crystal structure data (left circle) and against enthalpies of transition (right circle). Figure reproduced from Article A3.

#### 3.5.2 Summary of results

The error analysis of the lattice parameters, summarised in Figure 3.7, showed that both PBEsol-D2 and PBEsol-TS outperformed the best functional identified in Article A2, PBE-TS, with MAE values of 0.036 Å and 0.032 Å, respectively. While still detectable, the systematic tendency to overestimate the unit cell dimensions was also reduced. With regard to T–O bond distances, the dispersion-corrected variants gave essentially identical results as the uncorrected PBEsol functional, delivering somewhat too long Si–O and Al–O bonds and too short P–O bonds (A3, Table IV). The systematic underestimation of Si–O–Si angles was found to be less pronounced than for PBE-D2 and PBE-TS, whereas no clear trend could be identified for Al–O–P angles (A3, Table V). In contrast, the exaggerated distortion of 6MR windows in SOD and AST, attributed to an overestimation of dispersion interactions by the pairwise dispersion correction schemes in the preceding article, persisted when using the PBEsol-D2 and -TS approaches.

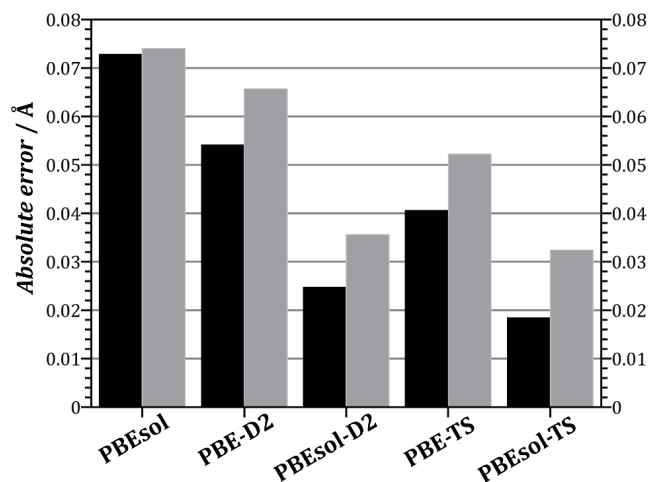


**Figure 3.7:** MSE and MAE in lattice parameters obtained with different functionals. Unlike in **Figure 3.5**, values computed for  $\text{SiO}_2$  and  $\text{AlPO}_4$  frameworks are not separated. Figure reproduced from **Article A3**.

When comparing DFT-optimised structures to experimental data, it has to be considered that the DFT calculations do not include any temperature effects, thus delivering the 0 K equilibrium structure. In contrast, most of the experimental reference structures were refined from room temperature (RT) data, and one should therefore expect that a part of the deviations between DFT and experiment can be attributed to this inherent difference. To elucidate the magnitude of this effect, the DFT-optimised cell parameters were compared to experimental values determined from data measured at cryogenic temperatures. Such data are available for four all-silica zeolites and two AlPOs, with measurement temperatures ranging from 18 K to 133 K. A calculation of the overall errors for these systems showed that the agreement with experiment became better when using low temperature data as reference, since the frequent negative thermal expansion of these framework materials tends to bring DFT and experimental values closer together (**A3**, Table VI). With regard to the T–O bond lengths, it has been established that the correlated motion of  $\text{TO}_4$  tetrahedra in tetrahedral frameworks leads to a shortening of the "apparent" T–O distance (*i.e.*, the experimentally measured distance) with respect to the true bond length (Busing and Levy, 1964; Downs et al., 1992). This effect can be approximated via the "simple rigid body" (SRB) correction proposed by Downs et al. (1992), which makes use of the isotropic displacement parameters to correct the bond distances. Although a meaningful SRB correction could only be performed for a subset of six structures, it was found that the expansion of the bonds caused by this correction reduces the differences between experimental and DFT-optimised values for Si–O and Al–O bond distances, while increasing the deviations for P–O bond lengths.

The relative energies  $\Delta E_{DFT}$  for all-silica zeolites and  $\alpha$ -cristobalite were computed directly from the DFT total energies, using the total energy of  $\alpha$ -quartz as reference. These values were then compared to experimental enthalpies of transition, as additional calculations for selected zeolites showed that the inclusion of zero-point vibrations and temperature effects for  $T = 298$  K would change the results by less than  $1 \text{ kJ mol}^{-1}$  per  $\text{SiO}_2$  formula unit. As shown in **Figure 3.8**, both functionals nicely reproduced the inverse correlation with the framework density. A direct plot against the experimental  $\Delta H_{trans}$  values, shown in the right panel of **Figure 3.8**, revealed excellent agreement for the PBEsol-D2 functional, with an MAE value of  $1.1 \text{ kJ mol}^{-1}$  that is only marginally larger than the experimental uncertainty (typically around  $1 \text{ kJ mol}^{-1}$ ; Navrotsky et al. (2009)). The PBEsol-TS functional exhibited a systematic tendency



to overstabilise  $\alpha$ -quartz, as observed for PBE-TS in **Article A2**, pointing to the dispersion correction scheme as the dominant factor determining the accuracy for energetics.

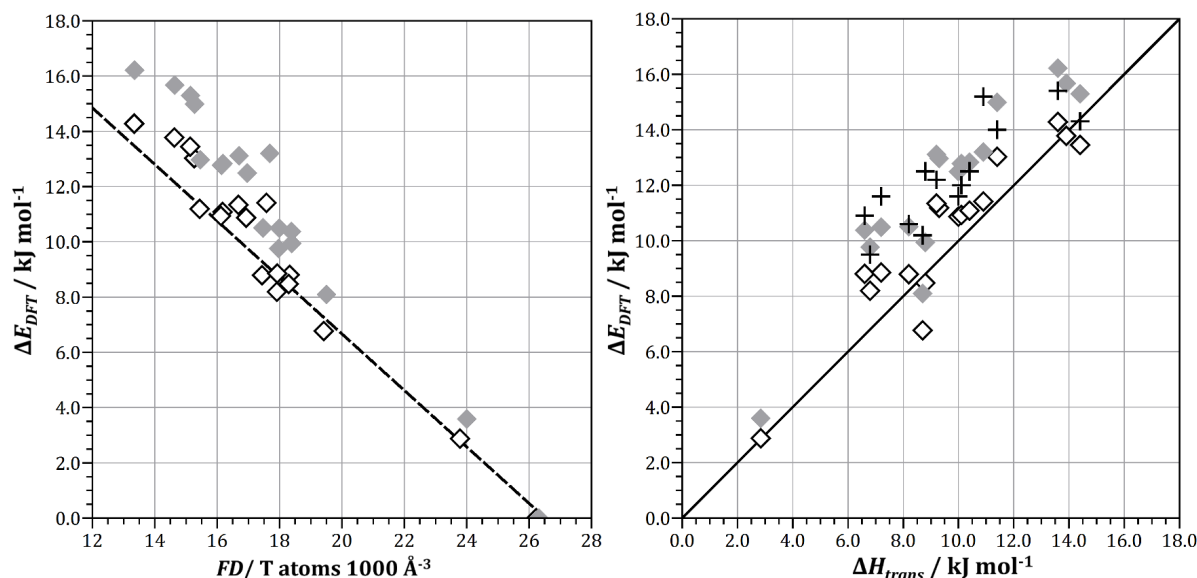


**Figure 3.8:** **Left:** Correlation between framework density  $FD$  and relative energy  $\Delta E_{DFT}$  as obtained from calculations with PBESol-D2 (open diamonds) and PBESol-TS (grey diamonds). The dashed line corresponds to the correlation between  $FD$  and  $\Delta H_{trans}$  calculated on the basis of experimental data (Navrotsky et al., 2009). **Right:** Plot of relative energy  $\Delta E_{DFT}$  against experimental enthalpy of transition  $\Delta H_{trans}$  for PBESol-D2 (open diamonds) and PBESol-TS (grey diamonds). Results from a previous computational study employing the PBE0-D2 functional (Román-Román and Zicovich-Wilson, 2015) are included for comparison (crosses). Figure reproduced from **Article A3**.

### 3.6 **Article A4:** Benchmarking the Performance of Approximate van der Waals Methods for the Structural and Energetic Properties of $\text{SiO}_2$ and $\text{AlPO}_4$ Frameworks

#### 3.6.1 Outline

Whereas all other articles compiled in this part reported calculations using the CASTEP code, the benchmarking study carried out in this work, done in collaboration with Won-June Kim, Michael Badawi and Sébastien Lebègue (Université de Lorraine), employed the VASP code (Kresse and Furthmüller, 1996a,b; Kresse and Joubert, 1999). The key advantage of the VASP code that was exploited here is the availability of a much larger range of dispersion-corrected DFT methods, including the Grimme-type D3 correction (Grimme et al., 2010), advanced pairwise schemes based on the Tkatchenko-Scheffler correction, *e.g.*, the PBE-TS/Hi (Bučko et al., 2013) and PBE-MBD/FI (Gould et al., 2016) approaches, as well as several nonlocal dispersion correction methods, *e.g.*, vdW-DF1 (Dion et al., 2004), vdW-DF2 (Lee et al., 2010), optPBE-vdW (Klimeš et al., 2010), and rev-vdW-DF2 (Hamada, 2014). Altogether, seven pairwise DFT-D methods and seven vdW-DF functionals were considered, together with the uncorrected PBE and PBESol functionals (**Figure 3.2**). The benchmarking against experimental structure data used essentially the same set of reference structures as in **Article A2** and the first part of **Article A3**, adding  $\alpha$ -cristobalite and cristobalite-type  $\text{AlPO}_4$ , but omitting SOD- and AST-type all-silica zeolites, which had been discussed separately in the previous studies. In addition to an analysis of lattice parameters, framework densities, T–O bonds, and T–O–T angles for the whole set of reference struc-

tures, agreement with experimental bulk moduli and enthalpies of transition was evaluated for those materials where such data were available. Experimental bulk moduli had been reported for five SiO<sub>2</sub> and two AlPO<sub>4</sub> systems (one of which was discarded during the analysis due to very large differences between the experimental bulk modulus and all DFT-computed values), and enthalpies of transition were considered for four all-silica zeolites and  $\alpha$ -cristobalite, using  $\alpha$ -quartz as reference.

### 3.6.2 Summary of results

The MAE and MSE values in lattice parameters are shown in **Figure 3.9**. MAEs in the range of 0.10 Å were found for several of the dispersion-corrected approaches. Among the pairwise DFT-D approaches, PBE-D3(BJ), PBE-TS, and PBE-MDB performed best, and a comparably good prediction of the lattice parameters was also provided by most of the nonlocal vdW-DF functionals, with vdW-DF1 and vdW-DF2 being notable exceptions. It is noteworthy that systematically larger MAEs were found when comparing the VASP results to CASTEP calculations from **Article A2**; however, the origin of these discrepancies could not be elucidated in the context of this study. As a consequence of the relatively accurate prediction of lattice parameters, the framework densities were also reproduced to within 0.5 T atoms per 1000 Å<sup>3</sup> by the majority of functionals. The systematic overestimation of T–O distances and concurrent underestimation of T–O–T angles were found to be essentially ubiquitous features, although the performance of individual functionals differed (**A4**, Figures 3 and 5). The very large overestimation of T–O distances by the vdW-DF1 and vdW-DF2 functionals and the relatively small errors in T–O–T angles provided by sophisticated DFT-D approaches like PBE-MBD stood out in this regard.

Concerning the bulk moduli, two DFT-D approaches using a Grimme-type correction, PBE-D2 and PBE-D3(BJ), as well as the rev-vdW-DF2 functional gave the smallest errors, with MAEs on the order of 2.5 GPa (**A4**, Figures 6). Whereas the poor performance of vdW-DF1 and vdW-DF2, which also exhibited large errors in structural parameters, was more or less expected, the significant systematic overestimation of the bulk moduli by the PBE-TS functional was rather surprising (MAE = MSE = 5.0 GPa), especially when viewing these results in the context of the results of **Article A5** (although **A5** was published a few months earlier than **Article A4**, it appears later in this chapter to emphasise the strong thematic link between **Articles A2**, **A3**, and **A4**). A rather complex picture emerged when looking at the relative stability of SiO<sub>2</sub> frameworks, where - as in previous work - relative energies were compared to experimental enthalpies of transition: Two of the advanced DFT-D schemes, PBE-TS/HI and PBE-MBD/FI, systematically underestimated the energy differences between the SiO<sub>2</sub> phases, whereas PBE-TS and some vdW-DF approaches strongly overestimated them. Three pairwise correction schemes (PBE-D2, -D3, -MBD) gave the most accurate results, with MAEs of about 1 kJ mol<sup>-1</sup>, closely followed by PBE-D3(BJ), vdW-DF2, and rev-vdW-DF2. **Figure 3.9** shows the correlation between framework density and  $\Delta E_{DFT}$  as obtained with five selected functionals. Assessing the performance across the board, PBE-MBD and rev-vdW-DF2 were identified as reasonable choices if all quantities were considered to be equally important. Moreover, PBE-D3 was identified as an inexpensive, widely applicable functional delivering robust results for equilibrium structures and energetics, justifying its use in many of the DFT and AIMD studies reported in **Chapter 4** and **Chapter 5**.

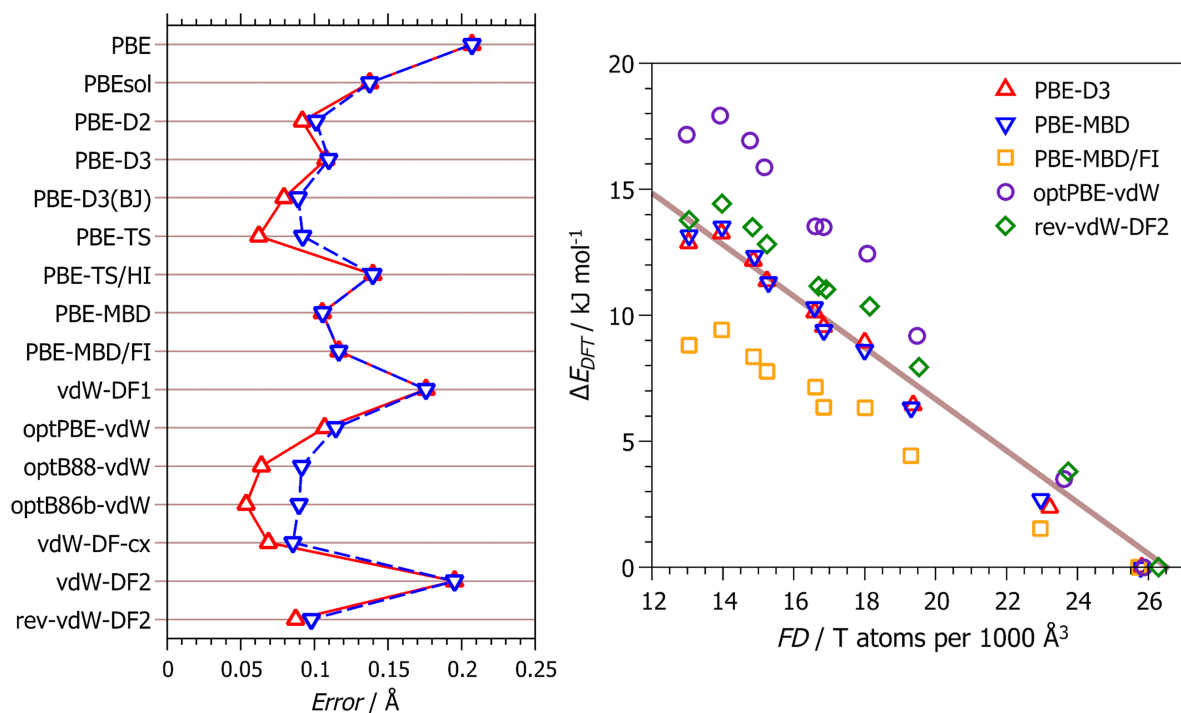


**Figure 3.9:** **Left:** MAE (blue) and MSE (red) in lattice parameters for all functionals considered in **Article A4**. **Right:** Correlation between framework density  $FD$  and relative energy  $\Delta E_{DFT}$  for selected functionals. The light brown line corresponds to the correlation between  $FD$  and  $\Delta H_{trans}$  calculated on the basis of experimental data (Navrotsky et al., 2009). Figure modified after **Article A4**.

### 3.7 **Article A5:** Template Effects on the Pressure-Dependent Behavior of Chabazite-Type Fluoroaluminophosphates: A Computational Approach

#### 3.7.1 Outline

In contrast to all other articles compiled in this chapter, which considered a set of zeolites and zeotypes with different topologies, this article focussed on one particular material, CHA-type fluoroaluminophosphate. The key point addressed in this study was the dependence of the pressure-dependent behaviour on the organic template occluded in the pores, comparing AIPO-CHA\_X materials containing four different OSDAs or "templates" X, morpholinium (morph), pyridinium (pyr), 1,3-dimethylimidazolium (DMI), and 1,2,3-trimethylimidazolium (TMI), shown in **Figure 3.10**. In the validation part of this study, DFT-optimised structural parameters obtained with the PBE and PBEsol functionals and their dispersion-corrected variants (D2 and TS dispersion correction schemes) were compared to experimental data. Furthermore, DFT-based predictions of the bulk modulus and the pressure-dependent evolution of the lattice parameters of AIPO-CHA\_morph were compared to results from the experimental *in situ* study by Leardini et al. (2012). In the second, predictive part of this article, PBE-TS calculations were employed to study the compressional behaviour of AIPO-CHA\_X systems in a pressure range up to 5.0 GPa.

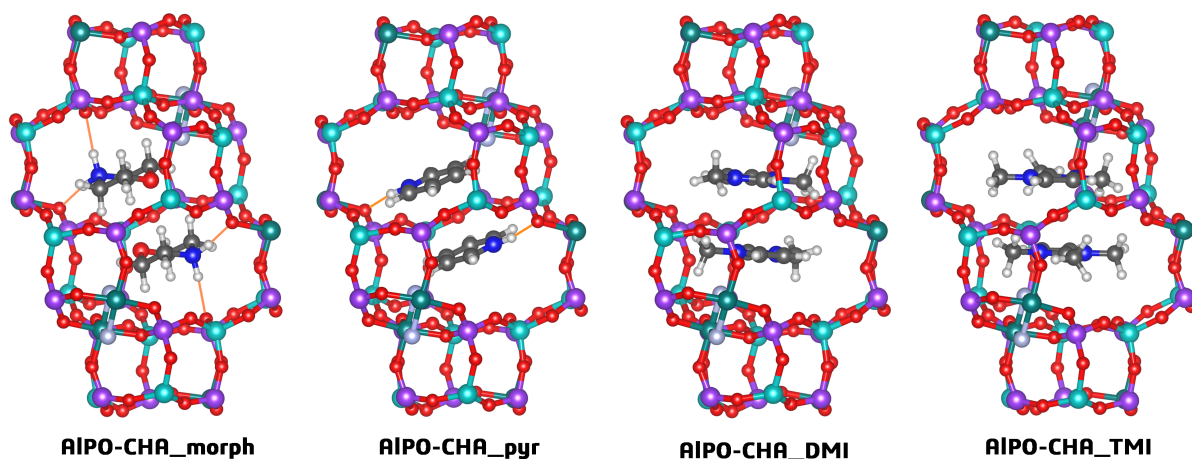


**Figure 3.10:** Visualisation of the CHA-type fluoroaluminophosphates systems studied in **Article A5**. For clarity, only a single *cha* cage is shown. Thin orange lines represent hydrogen bonds. The complete framework topology is visualised in Figure 1 of **A5** and the molecular structure of the OSDAs is emphasised in Figure 2 of **A5**.

### 3.7.2 Summary of results

An optimisation of the AlPO-CHA\_X systems using different functionals resulted in the well-known overestimation of the unit cell volumes by PBE. Whereas PBEsol, PBE-D2 and -TS gave relatively accurate volumes, with MAEs on the order of 4 to 6 Å<sup>3</sup> (corresponding to relative errors of less than 1%), dispersion-corrected variants of PBEsol delivered rather severely underestimated volumes (MAEs around 15 Å<sup>3</sup>). In the view of the good performance of these functionals for guest-free neutral-framework zeotypes, this result appears rather surprising. Furthermore, PBE-TS was identified as the only functional giving the correct order of the unit cell volumes among the four AlPOs. Along with the unit cell volumes, template-template distances and angles as well as template-framework distances were also compared to experimental data. Here, PBE without dispersion correction delivered the best overall agreement with experimental values, although the excellent performance of PBE-TS for template-framework distances was also noteworthy (**A5**, Table 3). PBE-TS also emerged as the functional giving the best prediction of the bulk modulus  $K_0$  of AlPO-CHA\_morph, with a computed value of 46 GPa, compared to the experimental value of  $54 \pm 3$  GPa (Leardini et al., 2012). All other functionals gave lower bulk moduli, with  $K_0$  values between 37 and 41 GPa. Due to the good performance of PBE-TS in terms of equilibrium volume and bulk modulus, this functional was used in all further calculations performed in the context of this study.

In the *in situ* study of the compressional behaviour of AlPO-CHA\_morph by Leardini et al. (2012), only the evolution of the lattice parameters with pressure could be refined, as the data quality precluded a complete structure refinement. The experimental results showed a phase transition at a pressure of about 3.1 GPa, which was associated with a contraction along the pseudo-hexagonal *a* axes and a concurrent expansion along the *c* axis (the structures of CHA-type fluoroaluminophosphates are triclinic, but they can be described using a pseudo-hexagonal metric). The DFT calculations reproduced this qualitative behaviour, but the transition pressure was shifted upwards, with the transition happening between 4.0 and 4.5 GPa (**A5**, Figure 6). An analysis of the optimised structures showed that the pressure-induced transition coincides with a reorientation of the morpholinium templates in the *cha* cages as well as a change in their hydrogen bonding pattern, resulting in an expansion of the cage along *c* (**Figure 3.11**). Calculations for the other three AlPO-CHA\_X compounds, which have not been studied

experimentally under pressure, provided no evidence for a phase transition in the pressure range up to 5.0 GPa. The bulk moduli showed a remarkable variation, ranging from 19 GPa in AIPO-CHA\_pyr to 51 GPa in AIPO-CHA\_TMI. Altogether, the qualitative and quantitative differences observed among the AIPO-CHA\_X systems provided clear evidence that the template molecules significantly affect the compressional behaviour. Both the degree of "space filling" provided by the template molecules and the different nature of template-framework interactions, specifically the presence/absence of hydrogen bonds, were identified as important factors in this context.

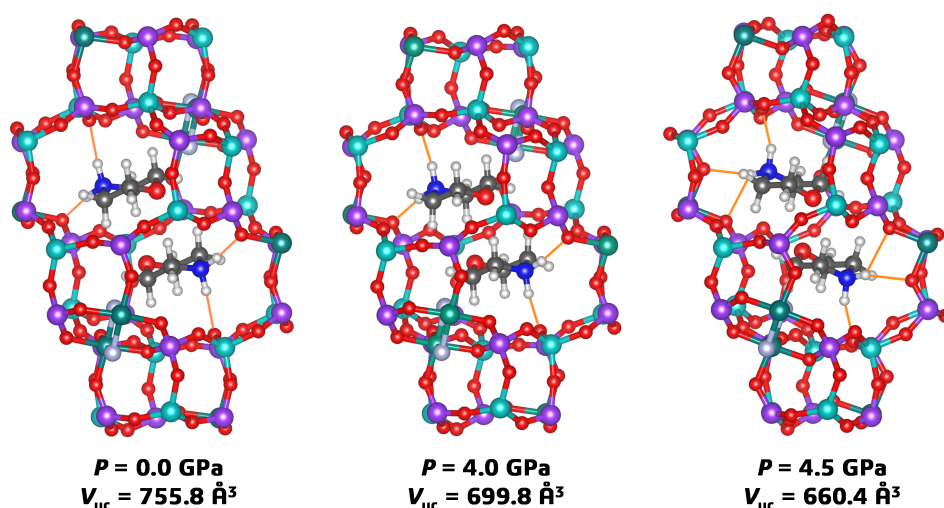


**Figure 3.11:** Visualisation of the *cha* cage in DFT-optimised structures of AIPO-CHA\_morph obtained for pressures of 0.0, 4.0, and 4.5 GPa. The rearrangement of the OSDA molecules, including a change in the hydrogen bonding pattern, and the concurrent expansion of the cage along the pseudohexagonal *c* axis occurring between 4.0 and 4.5 GPa are clearly visible. The DFT-optimised unit cell volume  $V_{uc}$  is also given.

### 3.8 Conclusions

The first conclusion that can be drawn from the body of results reported in **Article A1** to **A5** is that the inclusion of a dispersion correction is pivotal to arrive at reasonable structural parameters when aiming at a full structure optimisation of zeolites or zeotypes, at least as long as a semilocal GGA-type exchange-correlation functional is used (functionals from higher rungs of the "Jacob's ladder" like meta-GGA and hybrid functionals were not tested, as they are computationally more demanding). This finding is fully in line with the results of previous benchmarking studies on zeolites (Hay et al., 2015) and other materials (Tunega et al., 2012; Tran et al., 2016). It is also apparent that the inclusion of dispersion interactions is required to compute reasonable relative energies of all-silica zeolites, agreeing with the results of Román-Román and Zicovich-Wilson (2015). Beyond this, however, it became clear that the choice of an appropriate dispersion-corrected functional will depend both on the quantities of interest and the systems of study: On the one hand, a functional that performs well for one quantity may fail for others. On the other hand, the results also showed that the performance of a given functional can vary depending on whether the zeolite/zeotype(s) studied are guest-free or contain extra-framework species. An example for the former behaviour is the PBE-TS functional, which performs well for structural properties of guest-free, hydrated, and OSDA-containing zeolites and zeotypes, but fails for relative energies. An example falling in the latter category is the PBEsol-D2 functional, which gives accurate structural pa-

rameters for guest-free all-silica zeolites and AlPOs, but fails for OSDA-containing fluoroaluminophosphates. Of course, one question that needs to be considered when choosing a suitable functional for a task at hand is the magnitude of an "acceptable" error in a given quantity. For example, an error of 2% in a unit cell parameter will be unacceptable in many instances, whereas the typical experimental uncertainty of enthalpies of transition is already on the order of 10%.

Focussing on neutral-framework types, which are particularly relevant for the following two chapters, the PBE functional in conjunction with a Grimme-type correction (PBE-D2, PBE-D3) as well as the PBEsol-D2 and rev-vdW-DF2 functionals showed a rather robust behaviour, delivering a reasonable prediction of structural parameters and relative stabilities. On this basis, any of these functionals might appear as suitable choice for future investigations of these compounds. Indeed, several of the studies reported in the following chapter showed that PBE-D3 reproduces the unit cell parameters of OSDA-containing all-silica zeolites very well, often with relative errors below 1%. It has to be conceded, however, that error compensation, specifically an overestimation of T–O bond lengths and a concurrent underestimation of T–O–T angles, which had already been identified by Hay et al. (2015), is partially responsible for the rather accurate prediction of lattice parameters by these dispersion-corrected functionals.

The results from **Article A4** and **A5** show that the inclusion of the pressure-dependent behaviour further complicates the choice of the functional. It was particularly striking to observe that PBE-TS performed badly for guest-free neutral-framework zeotypes, but good for OSDA-containing fluoroaluminophosphates. While the latter observation was sufficient to make a reasonable *ad hoc* choice for the study of AlPO-CHA\_X compounds, a transferability to other compounds cannot be taken for granted. Altogether, it is clear that there is no generally applicable functional that could be used for any zeolite-related task in a "black box fashion", but that the chosen DFT approach should be validated against available experimental data whenever possible.

The surprisingly large differences between overall error values obtained when using the same functional, but different codes, could not be explored in the context of this work. Although it can be hypothesised that these differences are related to the choice of pseudopotentials (CASTEP) and projector augmented waves (VASP), a validation against high-level all-electron calculations would be required to quantify the effect of the different treatment of the core electrons. A PBE-TS study of CHA-type SAPO-34 delivered differences of up to 0.9% among optimised unit cell parameters when using different sets of built-in PPTs within CASTEP, indicating that the choice of PPTs does indeed have a non-negligible influence (Chieh-Min Hsieh: Research project "Computational prediction of preferred silicon distributions in the silicoaluminophosphate SAPO-34", completed at the University of Bremen in September 2019).

### 3.9 Outlook

Even though the benchmarking investigations compiled in this chapter aimed at a reasonably comprehensive assessment of the performance of dispersion-corrected GGA functionals for calculations on zeolites and zeotypes, it is also clear that various opportunities for future work remain:

- The study reported in **Article A1** did not include an optimisation of the lattice parameters. Given the importance of hydrated and dehydrated cation-exchanged zeolites in materials science and the geosciences, it would be worthwhile to perform full structure optimisations on a suitably chosen set of such compounds in order to benchmark the performance of different DFT approaches.

- As mentioned in the preceding section, the errors introduced by the use of PPTs/PAWs to represent core electrons have remained unexplored. They could be evaluated by performing reference all-electron calculations, following in the footsteps of the DeltaCodesDFT project (Lejaeghere et al., 2016), which concentrated on elemental structures. While the DeltaCodesDFT results provide an excellent starting point to estimate the importance of such errors, explicit reference calculations for zeolite/zeotype structures would be required to explore this in more depth.
- Clearly, it would be very useful to expand the choice of XC functionals beyond the GGA level of theory. Specifically, the meta-GGA SCAN (Sun et al., 2015) functional showed a very promising behaviour in calculations performed in the context of the study reported in **Article A4**. However, some SCAN results were apparently affected by numerical issues that have also been reported by other authors (Gould et al., 2018), which is why they were excluded from the analysis. As an improved numerical stability has been found for the more recently developed r<sup>2</sup>SCAN functional (Furness et al., 2020), this functional and its dispersion-corrected variants, as well as other recently proposed meta-GGA or hybrid functionals, could be very interesting choices for future investigations.
- Recent years have seen significant advances in the field of "low-cost quantum chemistry methods", which aim to deliver similar accuracy as DFT calculations at a fraction of the computational cost (Brandenburg et al., 2014). For one such method, dubbed HF-3c, Cutini et al. (2019) obtained relatively accurate unit cell volumes for a set of 14 all-silica zeolites. Although the HF-3c method performed poorly for relative stabilities, very good results were obtained when computing B3LYP-D energies for structures optimised with the "low-cost" method. Such computationally efficient methods could be especially interesting for zeolites with very large unit cells, or to screen a large number of heteroatom or cation distributions in charged-framework zeolites and zeotypes.
- A further reduction in computational cost could be achieved through the use of analytical potentials. Well-tested DFT methods that simultaneously reproduce structural parameters and relative energies could provide input data for the development of more accurate force fields, or the improvement of existing ones. Very interesting opportunities in this regard can arise from the use of machine learning approaches to "train" the interatomic potentials. Recent work by Erlebach et al. (2022) used calculations employing the PBE-D3 functional on a variety of all-silica zeolite structures, including hypothetical zeolites and deformed structures, to train a set of neural-network potentials, which were then used to evaluate the relative stability of a dataset containing more than 300,000 hypothetical zeolites.
- The analysis carried out in the context of **Article A3** pointed out the systematic shortcomings of comparing the results of DFT optimisations, which deliver the equilibrium structure at 0 K, to experimental structure data obtained at finite temperature. To this end, it would be very interesting to obtain a larger set of reference structure data refined from low-temperature measurements. From the side of the calculations, the effect of temperature could be accounted for by using AIMD simulations in  $NpT$  ensemble, as demonstrated for the case of AlPO-11 in **Article C5**. However, the computational expense of these calculations is orders of magnitude at higher than for structure optimisations, precluding their routine use for benchmarking purposes, at least when aiming at the coverage of a range of structures and functionals. The use of AIMD simulations would also enable the direct prediction of enthalpies of transition at finite temperature, obviating the need for phonon calculations to compute thermodynamic properties.



## CHAPTER 4

# STRUCTURE AND DYNAMICS OF FLUORIDE-CONTAINING ZEOLITES AND ZEOTYPES

### 4.1 Broader context and previous work

#### 4.1.1 The "fluoride route" of zeolite synthesis

The development of the "fluoride route" of zeolite synthesis, *i.e.* hydrothermal synthesis in the presence of fluoride anions, began with a patent that was granted to Edith Flanigen and Robert Patton of Union Carbide Corporation (Flanigen and Patton, 1978). In this patent, the authors disclosed that the addition of inorganic fluorides like HF, KF, or  $\text{NH}_4\text{F}$  to the reaction mixture resulted in sizeable single crystals of Silicalite-1 with sizes of up to  $200\ \mu\text{m}$  (conventional syntheses in hydroxide media typically deliver crystals with a size of a few  $\mu\text{m}$ ). Subsequently, this allowed the preparation of a Silicalite-1 crystal that was large enough for a structure determination using laboratory sc-XRD (Aubert et al., 2002). The addition of fluoride to the reaction mixture is also beneficial to obtain all-silica zeolite crystals with very few defects, because the positive charge of the OSDA cations is balanced through the  $\text{F}^-$  anions, which are incorporated in the crystal structure (Cambor and Villaescusa, 1999; Caullet et al., 2005; Schmidt et al., 2007). In contrast, the OSDA charge is largely balanced through framework defects in all-silica zeolites synthesised in hydroxide media (Koller et al., 1995; Shantz et al., 2000; Bruncklaus et al., 2016). Besides their beneficial impact on crystal size and defect content, fluoride anions can also play a structure-directing role. The systematic study of zeolite syntheses using a variety of OSDAs in fluoride-containing media has led to the discovery of several new all-silica zeolites (Cambor and Villaescusa, 1999; Burton et al., 2005; Caullet et al., 2005; Zones et al., 2005, 2007; Burton, 2018). Examples include octadecasil (AST topology; Caullet et al. (1991)), ITQ-3 (ITE; Cambor et al. (1997)), SSZ-23 (STT; Cambor et al. (1998b)), ITQ-4 (IFR; Barrett et al. (1998)),  $\text{SiO}_2$ -chabazite (CHA; Díaz-Cabañas et al. (1998)), ITQ-7 (ISV; Villaescusa et al. (1999)), ITQ-12 (ITW; Yang et al. (2004)), ITQ-13 (ITH; Corma et al. (2003)), ITQ-29 (LTA; Corma et al. (2004)), SSZ-73 (SAS; Wragg et al. (2007)), and HPM-1 (STW; Rojas and Cambor (2012)). Although some of these zeolites can also be synthesised in the absence of fluoride, many of them have (so far) been prepared exclusively in fluoride media. Specifically, it has been observed that the presence of fluoride anions tends to stabilise small rings, especially single 4MRs and  $d4r$  cages. The T–O–T angles in 4MRs are usually relatively small, around  $140^\circ$ , whereas the equilibrium Si–O–Si angle is closer to  $150^\circ$  (Sastre and Corma, 2010; Dawson et al., 2014). The incorporation of fluoride anions in the proximity of 4MRs, either at the centre of  $d4r$  units or in the form of  $[\text{Si}^{[5by]} \text{O}_{4/2} \text{F}]^-$  units, can relax the associated strain, enhancing the stability of zeolite frameworks containing such rings over competing phases (Zicovich-Wilson et al., 2010a).

Another possibility to stabilise small rings in zeolite structures is the incorporation of germanium on the T sites, as the equilibrium Ge–O–Ge angle is closer to  $130^\circ$  (Dawson et al., 2014). The structure-directing effects of Ge incorporation and fluoride addition can also be combined, and several silicogermanates with very large pores have been synthesised in fluoride media, such as IM-12 (UTL topology, contains 14MRs; Paillaud et al. (2004)), ITQ-33 (ITT, 18MRs; Corma et al. (2006)), ITQ-37 (-ITV, 30MRs;



Sun et al. (2009)), and ITQ-44 (IRR, 18MRs; Jiang et al. (2010)). While all four mentioned examples contain  $d4r$  units, the structure of ITQ-44 also possesses double three-rings ( $d3r$ ). This unusual, highly strained building unit occurs only in silicogermanates synthesised via the fluoride route (Baerlocher and McCusker, 2022).

In addition to all-silica zeolites and silicogermanates, the fluoride route has also been employed in the synthesis of other neutral-framework zeotypes, such as pure-GeO<sub>2</sub> frameworks like AST-type ASU-9 (Li and Yaghi, 1998), BEC-type FOS-5 (Conradsson et al., 2000) and UOZ-type IM-10 (Mathieu et al., 2004), aluminophosphates like the CHA-type fluoroaluminophosphates included in the previous chapter, AST-type AIPO-16 (Schott-Daric et al., 1994), and AIPO<sub>4</sub>-LTA (Sierra et al., 1994), as well as gallophosphates including the extra-large pore cloverite, which contains 20MRs (-CLO topology; Estermann et al. (1991)). Although the present chapter deals exclusively with neutral-framework zeolites and zeotypes, it should be noted that the presence of fluoride anions can also have a beneficial effect on the synthesis of charged-framework zeolites, such as high-silica alumino- and borosilicates (Burton et al., 2005; Caultet et al., 2005; Burton, 2018). Moreover, an OSDA-free synthesis of CHA-type low-silica zeolites also made use of a fluoride-containing reaction mixture (Liu et al., 2014).

#### 4.1.2 Experimental characterisation of fluoride environments

##### 4.1.2.1 Diffraction methods

Diffraction methods permit a localisation of fluoride anions in the crystal structures of as-synthesised zeolites (provided that sample and data quality are sufficient). As already discussed in the Introduction, two different environments can be distinguished in all-silica zeolites: First, the fluoride anions can be located at the centre of  $d4r$  cages. Second, they can be located in other small cages, where they form trigonal-bipyramidal  $[\text{Si}^{[5by]} \text{O}_{4/2} \text{F}]^-$  units. **Figure 4.1** shows examples of  $[\text{Si}^{[5by]} \text{O}_{4/2} \text{F}]^-$ -containing cages from different zeolite structures. Both types of environments coexist in the structure of ITQ-13 (Corma et al., 2003).

In structures containing  $[\text{Si}^{[5by]} \text{O}_{4/2} \text{F}]^-$  units, the fluoride anions are frequently disordered, resulting in two or more fractionally occupied fluoride positions. Different types of disorder can be distinguished, which are visualised in **Figure 4.1**: Whereas disorder over two sites that are equivalent by symmetry, but located in different cages, is found in nonasil (NON; van de Goor et al. (1995)), disorder over two symmetry-equivalent sites in the same cage occurs in Silicalite-1 (Aubert et al., 2002). A rather peculiar situation occurs in SSZ-23 (STT topology), where the fluoride anions are disordered over three non-equivalent sites within the same cage (Cambor et al., 1998b). The occurrence of disorder complicates an accurate determination of the F–Si distances: In a disordered structure, a Si atom in the vicinity of a fluoride anion has an "average" environment that lies between tetrahedral and trigonal-bipyramidal coordination, because the local coordination changes over time (in the case of dynamic disorder) or because images in different unit cells have different environments (in the case of static disorder). Diffraction methods can only probe this average environment, leading to F–Si distances in the range of 1.8 to 2.0 Å. In contrast, NMR methods deliver shorter distances around 1.75 Å (Wragg et al., 2008).

Silicogermanates, pure-GeO<sub>2</sub> zeotypes, AIPOs, and GaPOs often show a preference of the fluoride anions to locate in  $d4r$  cages, either at the centre of the cages or somewhat displaced towards one of the faces (in some AIPOs and GaPOs). In ITQ-13 silicogermanates, they are found both in  $d4r$  cages and in  $[4\cdot5^6]$  cages (Vidal-Moya et al., 2003), but this appears to be the exception rather than the rule. In some AIPOs and GaPOs, fluoride anions may also occur as terminal or bridging species, as in the CHA-type fluoroaluminophosphates that were at the core of the investigation reported in **Article A5**.

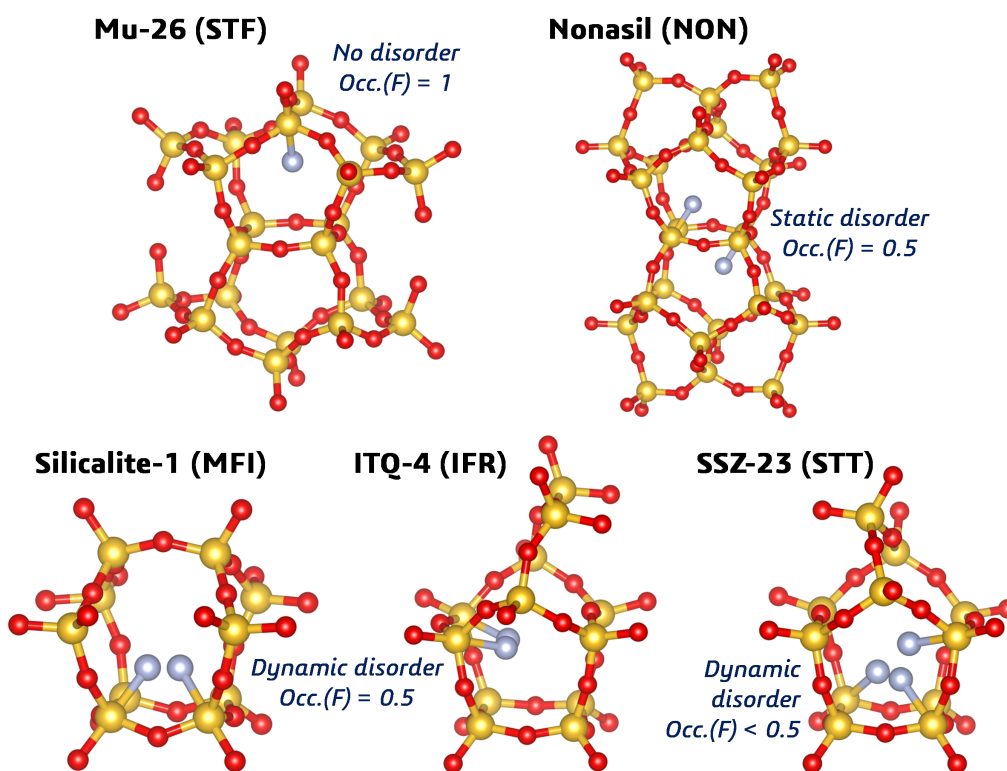


**Figure 4.1:** Environment of  $[\text{Si}^{[5by]} \text{O}_{4/2} \text{F}]^-$  units in zeolites that show qualitatively different types of disorder. In addition to the type of disorder, the occupancy of the F positions is also given in the figure. STT contains three non-equivalent F positions with occupancies of 0.32, 0.26, and 0.17.

#### 4.1.2.2 NMR and vibrational spectroscopy

Due to their sensitivity to the local environment, NMR methods are a very important tool to study fluoride-containing zeolites and zeotypes. By combining observations from solid-state NMR experiments with available information about the crystal structure, the characteristic  $^{19}\text{F}$  chemical shifts of fluoride anions in different bonding situations can be distinguished. For example, all-silica zeolites in which the fluoride anions are exclusively located in *d4r* cages show a single resonance at about  $\delta = -38$  ppm (reference:  $\text{CFCl}_3$ ; Caullet et al. (2005)). In contrast, the two distinct fluoride environments in purely siliceous ITQ-13 give rise to two resonances at  $\delta = -38$  ppm and  $-66$  ppm, respectively (Vidal-Moya et al., 2003). In ITQ-13 silicogermanates, additional resonances emerge, which can be explained as being due to *d4r* cages having different local arrangements of Si and Ge at the corners of the cage, as well as  $[4\cdot 5^6]$  units having a Ge atom in the basal 4MR plane.

The  $[\text{Si}^{[5by]} \text{O}_{4/2} \text{F}]^-$  units are also visible in  $^{29}\text{Si}$ -NMR spectra, where the five-coordinated silicon atoms give rise to a characteristic resonance at about  $-145$  ppm (reference:  $\text{Si}(\text{CH}_3)_4$ ; Koller et al. (1997)). In contrast, the resonances corresponding to  $\text{Si}^{[4t]}$  atoms are found in a chemical shift range of  $\delta = -104$  ppm to  $-116$  ppm. In addition to confirming the presence of trigonal-bipyramidal units and, through use of specialised NMR techniques and advanced analysis methods, the possibility to determine F-Si distances (demonstrated, for example, for STF-type SSZ-35 by Fyfe et al. (2002)),  $^{29}\text{Si}$ -NMR experiments can also provide insights into the nature of the fluoride disorder: If a sharp resonance at about  $-145$  ppm is observed, the local environment of the five-coordinated silicon atoms does not change on the timescale of the NMR experiments. On the other hand, a broad resonance centered at about  $-125$  ppm corresponds to an "averaged" resonance that is due to dynamic exchange between four- and five-coordinated

silicon atoms (Koller et al., 1997). This change in the coordination number over time is caused by a dynamic disorder of the fluoride anions, in other words, a "hopping" of fluoride between different Si atoms. Koller et al. (1997) were the first to distinguish static and dynamic disorder of fluoride anions by means of  $^{29}\text{Si}$ -NMR measurements, observing that fluoride anions are dynamically disordered in Silicalite-1, but not in nonasil. This appears plausible when considering that the partially occupied fluoride sites in Silicalite-1 are in close proximity, whereas the sites in nonasil are located in different cages, with no diffusion pathway between them (**Figure 4.1**). Koller et al. (1997) also showed that cooling of Silicalite-1 to  $T = 140\text{ K}$  "freezes" the dynamic disorder. Subsequent work by Koller et al. (1999) delivered evidence for dynamic disorder of fluoride anions in the all-silica zeolites ITQ-4 and SSZ-23, and for its absence in ITQ-3, ZSM-12 (MTW topology), and zeolite beta (\*BEA). More recent work by Brace et al. (2015) showed that the dynamic behaviour of fluoride anions in Silicalite-1 can be modulated through use of different OSDAs: Whereas samples synthesised with tetrapropylammonium ( $\text{TPA}^+$ ) exhibit dynamic disorder at room temperature, the use of methyltributylammonium ( $\text{MTBA}^+$ ) produces samples showing a sharp resonance at  $-146\text{ ppm}$ , indicating that there is no dynamic exchange between different sites.

Although vibrational spectroscopy has been relatively scarcely used to gain insights into the interactions of encapsulated fluoride anions with their environment, a characteristic mode that arises from the vibration of fluoride anions confined to the interior of  $d4r$  cages could be identified. This mode, which appears at a frequency of about  $500\text{ cm}^{-1}$ , was observed in the IR spectra of as-synthesised octadecasil, ITQ-7 (Villaescusa et al., 2002), and ITQ-12 (Zicovich-Wilson et al., 2007).

#### 4.1.3 Previous computational investigations of fluoride-containing zeolites

In the view of the important structure-directing role that fluoride anions can play during zeolite synthesis, it is not surprising that numerous researchers have employed computational chemistry methods to study the interaction of fluoride with zeolite frameworks, or fragments thereof. In the field of FF-based studies, an early contribution by George and Catlow (1997) looked at purely siliceous, fluoride-containing  $d4r$  units. The authors concluded that the fluoride anions act as an "anionic template" in the formation of these units, but that the framework structure is stable after fluoride removal. The latter point was later proven experimentally, as many  $d4r$ -containing all-silica zeolites like octadecasil (Villaescusa et al., 1998) can be calcined without destruction of the framework. Whereas George and Catlow (1997) used a combination of FF parameters from previous studies, a dedicated set of parameters for fluoride-containing silicates and germanates was developed in later work by Sastre and Gale (2005). This force field successfully reproduced the local environments of fluoride in all-silica zeolites containing  $d4r$  cages or  $[\text{Si}^{[5by]}\text{O}_{4/2}\text{F}]^-$  units. For ASU-9, an AST-type germanate, an off-centre location of fluoride within the  $d4r$  cage was predicted, with a F-Ge bond distance of  $2.16\text{ \AA}$ . This FF was subsequently used in a study of all-silica zeolites containing  $[\text{Si}^{[5by]}\text{O}_{4/2}\text{F}]^-$  units by Pulido et al. (2006a). These authors compared different possible fluoride locations in IFR-, ITH-, IWR-, STF-, and STT-type zeolites, and evaluated the role of different interactions. They concluded that the equilibrium position of fluoride is determined by an interplay of factors: Whereas electrostatic interactions with the cationic OSDAs control which cages are occupied by fluoride anions, local interactions determine the most favourable location for the formation of an  $[\text{Si}^{[5by]}\text{O}_{4/2}\text{F}]^-$  trigonal bipyramid. Another FF-based study that is worth mentioning in this context employed the CVFF parameters to investigate the interaction between fluoride anions incorporated in the  $[4\cdot 5^8]$  cages of EUO-1 and fluorobenzene moieties of the OSDAs (Arranz et al., 2005).

The incorporation of fluoride anions at the centre of *d4r* cages is not easily explained using classical chemical bonding concepts. For this reason, several researchers have employed electronic structure calculations to gain insights into the nature of the chemical bond. In an early DFT study using a cluster model of the *d4r* unit, George and Catlow (1995) observed a transfer of electron density from the fluoride anion to the surrounding silicon atoms, resulting in a decrease in the ionic character of the Si–O bonds. Bauzá et al. (2013) coined the term "tetrel bonding" for interactions of group IV atoms (tetrels), which act as electron acceptors (Lewis acids), with anions or other electron donors. These authors employed MP2 calculations to study the incorporation of fluoride into  $T_8O_{12}(OH)_8$  cages (with  $T = Si, Ge, Sn$ ) as showcase examples for such tetrel bonds. Observing a considerable stabilisation, with interaction energies in the range of  $-400 \text{ kJ mol}^{-1}$  per fluoride anion (about  $-50 \text{ kJ mol}^{-1}$  per  $T$  atom), they concluded that tetrel bonds are comparable in strength to hydrogen bonds. In their DFT study, Goesten et al. (2017) identified an interplay between hypervalent bonding and strain as being responsible for the high stability of the centre-of-cage position of fluoride in *d4r* cages. Based on DFT calculations for a larger cluster containing the complete environment of the  $[4^6 \cdot 6^{12}]$  (*ast*) cage of octadecasil, Dib et al. (2017) concluded that the tetrel bonding within the *d4r* cages promotes the formation of C–H  $\cdots$  O hydrogen bonds with the tetramethylammonium ( $TMA^+$ ) cations incorporated in the *ast* cages. These hydrogen bonds restrict the motion of the  $TMA^+$  cations, explaining the high  $^{14}N$  quadrupolar coupling parameters observed in NMR measurements (unhindered rotation should lead to quadrupolar coupling parameters close to zero). DFT calculations on cluster models also helped the interpretation of vibrational spectra of *d4r*-containing all-silica zeolites (Villaescusa et al., 2002).

In silicogermanates, cages with different distributions of Si and Ge at the corners give rise to distinct resonances in  $^{19}F$ -NMR spectra (Vidal-Moya et al., 2003; Wang et al., 2003). While the experiments alone can thus provide qualitative evidence for the presence of different cages, it is not clear which resonance corresponds to which kind of cage. Sastre et al. (2005b) and Pulido et al. (2006b) used DFT calculations on fluoride-containing  $Si_{8-x}Ge_xO_{12}(OH)_8$  cages to predict the  $^{19}F$  chemical shifts corresponding to different arrangements of Si and Ge. These calculations permitted an assignment of previously measured NMR shifts to different types of local environments. In particular, it could be established that the  $^{19}F$ -NMR shifts are primarily influenced by the surroundings of the Ge atom to which fluoride is bonded, *i.e.*, the number of Si and Ge atoms in the direct neighbourhood, but not so much by the total number of Si and Ge atoms at the corners of the cage. An analogous approach based on periodic DFT calculations was used more recently by Rigo et al. (2018) in an investigation of a series of STW-type silicogermanates. These authors could distinguish four groups of *d4r* cages according to their  $^{19}F$ -NMR shifts: (1) purely siliceous cages, (2) cages containing isolated Ge atoms, (3) cages containing at least one Ge–O–Ge linkage, but no Ge atom participating in three Ge–O–Ge linkages ( $Ge(Ge)_3$ ), (4) cages containing (at least) one  $Ge(Ge)_3$  atom (**Figure 4.2**). The DFT-based assignment agreed very well with experimental observations.

Periodic DFT calculations were also employed to investigate the chemical bonding in *d4r*-containing zeolites. In their study of ITQ-12, Zicovich-Wilson et al. (2007) optimised the structure of the as-synthesised form, predicted the vibrational spectrum, and computed partial charges to analyse the chemical bonding. They observed that the incorporation of fluoride in the *d4r* cages led to a more ionic character of the Si–O bonds, thereby enhancing flexibility and facilitating the formation of the strained *d4r* units. Interestingly, this interpretation is opposed to that put forward by George and Catlow (1995), who proposed a more covalent/less ionic character of the Si–O bonds upon fluoride inclusion. However, the more recent interpretation was corroborated in a subsequent, combined experimental and theoretical study (Rojas et al., 2012): In that work, it was shown that the OSDA that favoured ITQ-12

most strongly over the competing TON-type phase (without  $d4r$  units) resulted in the highest partial charges on the framework atoms, in other words, the most ionic Si–O bonds. The reaction pathway of the removal of fluoride anions from  $d4r$  cages was also investigated by means of periodic DFT calculations (Zicovich-Wilson et al., 2010b).

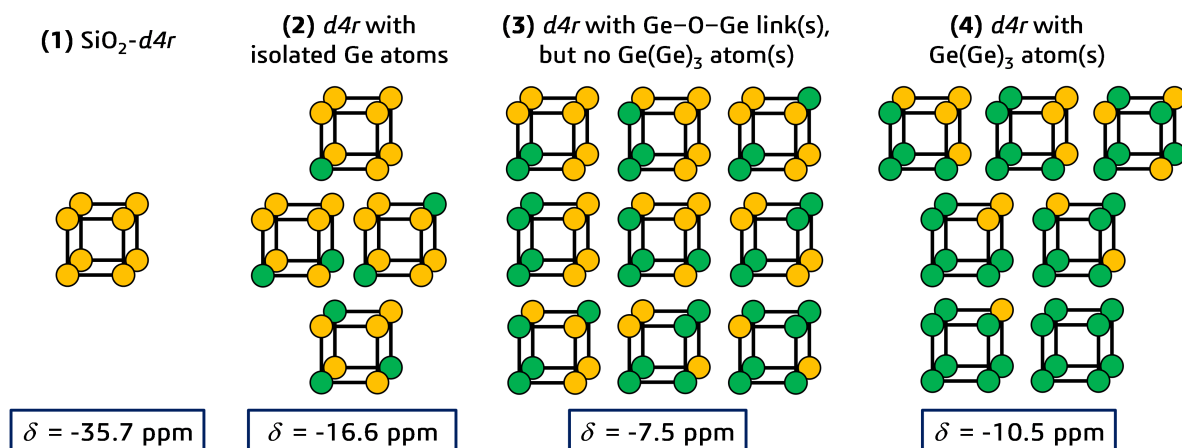


**Figure 4.2:** Silicogermanate  $d4r$  units with different distributions of Si (yellow) and Ge (green) studied by Rigo et al. (2018). The experimentally observed  $^{19}\text{F}$  chemical shifts, which were assigned to the four groups of cages on the basis of DFT calculations, are given below each group. The schematic representation of the  $d4r$  cages does not include the occluded fluoride anions.

Zeolites containing  $[\text{Si}^{[5by]}\text{O}_{4/2}\text{F}]^-$  units were less frequently investigated with electronic structure calculations than those with  $d4r$  units. Attfield et al. (2001) used DFT optimisations on fluoride-containing models of sodalite and ferrierite to establish that the geometry of the  $[\text{SiO}_{4/2}\text{F}]^-$  units corresponds to a relatively regular trigonal bipyramid: The  $\text{Si}^{[5by]}\text{--O}$  bonds are elongated to about 1.7 Å (compared to about 1.6 Å in  $\text{SiO}_4$  tetrahedra), and the  $\text{F--Si}^{[5by]}$  bond has a length of about 1.75 Å (for reasons discussed above, this value is significantly shorter than typical values obtained from diffraction), with the  $\text{O--Si}^{[5by]}\text{--O}/\text{O--Si}^{[5by]}\text{--F}$  angles also being close to their ideal values. A DFT-based comparison of ITQ-12 (with  $d4r$  cages) and a competing TON-type phase (with  $[\text{Si}^{[5by]}\text{O}_{4/2}\text{F}]^-$  units) showed that the presence of fluoride in  $d4r$  units results in an extended negative polarisation of the framework, whereas the negative polarisation induced by  $[\text{Si}^{[5by]}\text{O}_{4/2}\text{F}]^-$  environments is of a more local character (Zicovich-Wilson et al., 2010a). This qualitative difference affords stronger electrostatic interactions of ITQ-12 with the 1,3,4-trimethylimidazolium OSDA, which, together with a better fit of the OSDA molecules into the pores, is sufficient to overcome the energetic penalty associated with the lower framework density. After the successful preparation of pure-silica MWW in fluoride media, Lu et al. (2019) employed DFT calculations to predict the most stable fluoride locations, and to compute the associated  $^{19}\text{F}$  chemical shifts. The chemical shifts obtained for the two lowest-energy positions agreed rather well with the experimentally observed resonances, pointing to the presence of fluoride in  $[4\cdot 5^2\cdot 6^2]$  cages and in double six-ring ( $d6r$ ) cages. Finally, Mineva et al. (2020) performed DFT-based MD simulations on as-synthesised Silicalite-1 to study the presence of weak  $\text{C--H}\cdots\text{O}$  hydrogen bonds between the OSDA and framework oxygen atoms. They found that the shortest of these bonds were formed to oxygen atoms belonging to the fluoride-containing  $[4\cdot 5^2\cdot 6^2]$  cages, indicating stabilising interactions between the positively charged OSDA and this negatively polarised part of the framework that could play an important role during zeolite formation.

## 4.2 Key questions addressed in this chapter

The investigations on zeolites and zeotypes containing fluoride in  $d4r$  cages aimed to address the following points:

1. There was notable disagreement between diffraction investigations, which typically located fluoride at the centre of the  $d4r$  cages of (silico)germanates, and the prediction of a formation of F–Ge bonds in FF-based calculations. DFT structure optimisations of  $d4r$ -containing silicogermanates cages having different amounts of Ge atoms at the corners appeared as a promising route to resolve this issue.
2. The previous point can be extended to AlPO and GaPO zeotypes, where both centre-of-cage positions and off-centre locations of fluoride had been observed.
3. Earlier studies predicting preferred Ge distributions in  $d4r$ -containing zeolites typically used bare-framework models, ignoring the presence of fluoride anions and OSDA cations in as-synthesised samples. A more realistic assessment of the energetically preferred arrangements of Si and Ge at the corners of the cage should include these species, as interactions with them might affect the lowest-energy Ge locations.
4. The dynamic behaviour of fluoride anions encapsulated in  $d4r$  cages had not been studied so far. Therefore, it remained unclear whether the fluoride anions only oscillate about their equilibrium position, or whether they approach surrounding T sites to form short-lived bonds. Investigations of the impact of the cage composition on the dynamic behaviour were also lacking.

**Article B1** deals with the first, third, and fourth point, focussing on silicogermanates with the AST topology. The study of AST-type systems was expanded to AlPO and GaPO systems in **Article B2**, which, besides addressing the second and fourth point, also looks at the role of the OSDA in stabilising the equilibrium location of fluoride.

With regard to all-silica zeolites containing trigonal-bipyramidal  $[\text{Si}^{[5by]} \text{O}_{4/2} \text{F}]^-$  units, the following points motivated the investigations:

5. Pulido et al. (2006a) showed that interactions with the OSDA determine in which cage the fluoride anions reside, but it remained unclear how the local environment determines the specific location within the cage. An improved understanding of the energetic ordering of different possible fluoride sites could potentially result in the development of crystal-chemical "rules" that might allow to forecast the most likely locations on the basis of the framework topology.
6. While the dynamic disorder of fluoride anions in some zeolites had been established on the basis of experiments, it had not yet been assessed whether the dynamic behaviour could be reproduced in DFT-based AIMD simulations. If successful, the calculations could help to understand the impact of the local environment (geometry of the cage) and interactions with the OSDA on the occurrence of dynamic disorder.

**Article B3** primarily addresses point 6, reproducing the experimentally observed dynamic disorder of Silicalite-1 and studying the influence of the OSDA. Both point 5 and 6 are included in **Article B4**, which compares five different all-silica zeolites. Finally, the study reported in **Article B5** addresses various points from the above lists, as ITQ-13 contains fluoride in both  $d4r$  cages and in  $[\text{T}^{[5by]} \text{O}_{4/2} \text{F}]^-$  ( $\text{T} =$

Si, Ge) environments. Key aims of this study were to evaluate the energetically most favourable distribution of Ge among the different building units (expanding upon point 3) and the dynamic behaviour of fluoride in different environments (point 4 and point 6).

### 4.3 **Article B1:** *Local Environment and Dynamic Behavior of Fluoride Anions in Silicogermanate Zeolites: A Computational Study of the AST Framework*

#### 4.3.1 *Outline*

In the first place, this study aimed to predict the equilibrium positions of fluoride anions incorporated in silicogermanate *d4r* cages for the whole range of compositions (from pure SiO<sub>2</sub> to pure GeO<sub>2</sub>). Second, the impact of fluoride on the relative stability of different arrangements of Si and Ge at fixed composition was evaluated. Finally, it was investigated how the local environment, *i.e.*, the arrangement of Si and Ge at the corners of the cage, affects the dynamic behaviour. To address these points, a combination of DFT optimisations and DFT-based AIMD simulations (*NVT* ensemble,  $T = 298$  K) were performed with the CP2K code (Kühne et al., 2020), employing the PBE-D3 functional (Perdew et al., 1996; Grimme et al., 2010). With regard to the choice of model system, the AST framework is ideally suited for various reasons: To start with, it is a relatively simple framework, with only two non-equivalent T sites in the aristotype, where the T1 sites form the corners of the *d4r* cages and the T2 sites connect these cages, with T1 and T2 sites together forming the larger [4<sup>6</sup>.6<sup>12</sup>] (*ast*) cages, which host the OSDAs (**Figure 4.3**). Moreover, AST-type silicogermanates had been synthesised across the whole range of Si<sub>1-x</sub>Ge<sub>x</sub>O<sub>2</sub> compositions (Wang et al., 2003; Tang, 2005), including the pure end members (Caullet et al., 1991; Li and Yaghi, 1998). A crystal structure of SiO<sub>2</sub>-AST containing disordered TMA<sup>+</sup> cations in the *ast* cages had been refined from PXRD data by Yang (2006), providing a suitable starting point to generate fully ordered models for the calculations.

The DFT optimisations considered all possible arrangements of Si and Ge at the corners of the *d4r* cages, making the simplifying assumption that both cages in the unit cell have the same arrangement. An additional occupation of the T2 site by Ge was considered for higher Ge contents. The equilibrium structures were analysed in detail, and the relative energies were calculated for sets of configurations having the same composition. AIMD simulations were then carried out for selected low-energy configurations. The F-Si/Ge radial distribution functions (RDFs) and root mean square displacements (RMSDs) of different atomic species were analysed using the VMD code (Humphrey et al., 1996).

#### 4.3.2 *Summary of results*

The optimisation of the pure end members, SiO<sub>2</sub>-AST and GeO<sub>2</sub>-AST, showed that the fluoride anions are located at the centre of the *d4r* cages. This centre-of-cage location agrees with the experimental crystal structures (Caullet et al., 1991; Wang et al., 2003), but disagrees with the computational prediction of a F-Ge bond made by Sastre and Gale (2005). Such F-Ge bonds did appear, however, in AST-type systems having a mixed occupancy of the corners by Si and Ge. Relatively short F-Ge bonds on the order of 2.2 Å occurred in a system containing a single Ge atom (7Si, 1Ge) and in a (4Si, 4Ge) model where one Ge atom is surrounded by three Ge-O-Ge linkages (**Figure 4.3**). Conversely, the fluoride anions were found closer to the cage centre in models with a distributed arrangement of Ge (*i.e.*, without Ge-O-Ge linkages) and in Ge-rich systems (6 or more Ge atoms at the corners). When looking at the relative energies, a clear trend to maximise the number of Ge-O-Ge linkages along the corners of the *d4r* cage could be established, corroborating the results from a previous DFT study of BEC-type silicogermanates by



Kamakoti and Barckholtz (2007). Exactly the opposite trend, an avoidance of Ge–O–Ge links, was observed in an FF-based study by Pulido et al. (2006b), which might point to inherent limitations of their force field (Sastre and Gale (2003) used simple interpolation to obtain the parameters for oxygen atoms in Si–O–Ge links). Interestingly, the preference for arrangements maximising the number of Ge–O–Ge linkages was no longer visible when performing calculations for AST models without fluoride anions and OSDA molecules. This indicates that computations on such bare-framework models may be of limited use to predict energetically preferred local environments, as the local structure of a real sample will be determined during the synthesis, when fluoride and OSDA are present.

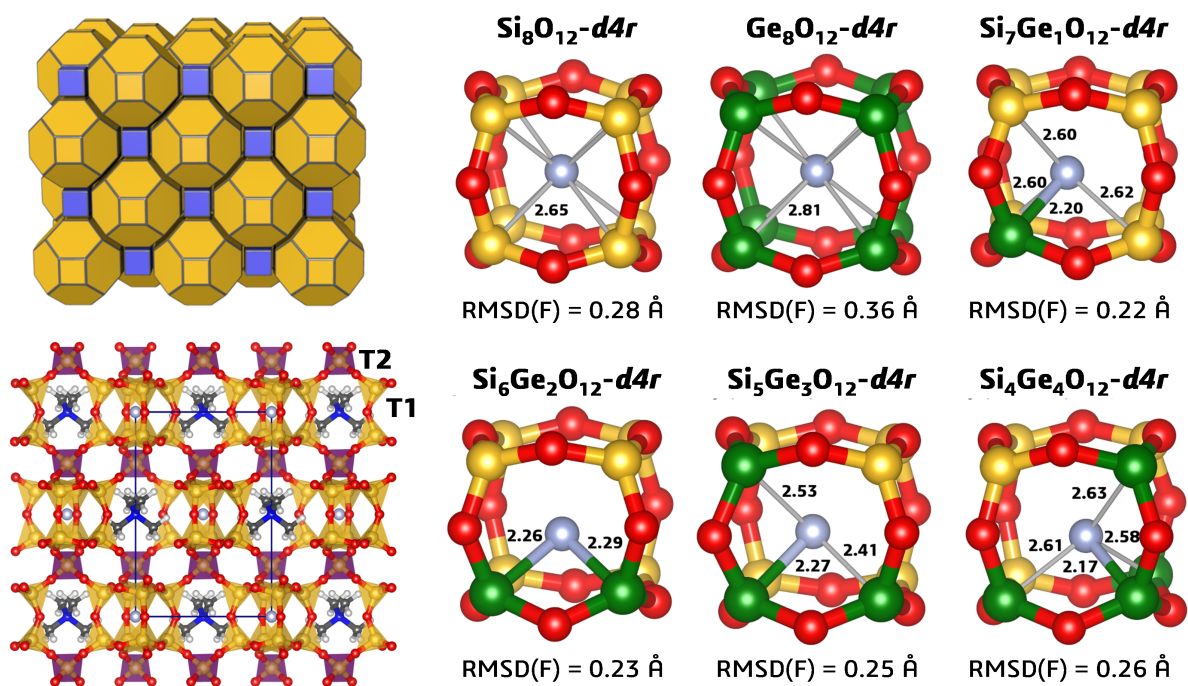


**Figure 4.3:** **Top left:** Natural tiling representation of the AST framework, showing *d4r* cages (blue) and *ast* cages (yellow). **Bottom left:** Structure of as-synthesised  $\text{SiO}_2$ -AST, with fluoride anions occupying the *d4r* cages, and  $\text{TMA}^+$  cations occupying the *ast* cages. T1 tetrahedra are shown in yellow and T2 tetrahedra are shown in purple. **Right:** *d4r* cages taken from DFT-optimised structures. Relevant F–T distances are given in Å. The RMSDs of fluoride as obtained from the AIMD simulations are also given. Figure modified after **Article B1**

An analysis of the RMSDs and RDFs obtained from the AIMD simulations showed that fluoride anions incorporated in purely siliceous *d4r* cages possess a relatively large freedom of motion due to the absence of any localised F–Si bond. This freedom of motion is increased further in  $\text{GeO}_2$ -AST due to the larger dimensions of the *d4r* cage. These AIMD results were complemented by a calculation of the potential energy curves (**B1**, Figure 6), which delivered shallow, symmetric potential wells, without any secondary local minima in the vicinity of the T atoms. A qualitatively different picture emerged for a model containing a single Ge atom at one corner: Here, the movement of fluoride is drastically reduced due to the presence of the localised F–Ge bond, and the potential well is asymmetric. Upon increasing the Ge content, the fluoride anions tend to form short-lived contacts to different Ge atoms over the time of the AIMD simulations (which amounted to 7.5 picoseconds for each individual trajectory), resulting in an increase of the RMSDs. Even for high Ge contents, a distinct tendency of fluoride to locate closer to the Ge atoms than to the corners occupied by Si atoms was detectable.



## 4.4 **Article B2:** Local Distortions in a Prototypical Zeolite Framework Containing Double Four-Ring Cages: The Role of Framework Composition and Organic Guests

### 4.4.1 Outline

The study reported in this article built directly on the investigation of AST-type silicogermanates described above. The focus was, again, on AST-type systems, and the computational protocol was essentially the same. The three new aspects addressed in this study were the following: First, SiO<sub>2</sub>-AST and GeO<sub>2</sub>-AST were compared to the alumino- and gallophosphate analogues, AlPO<sub>4</sub>-AST and GaPO<sub>4</sub>-AST. While the AlPO<sub>4</sub> form is synthetically accessible (the framework type code AST derives from the reference material **AlPO-SixTeen**; Bennett and Kirchner (1991)), GaPO<sub>4</sub>-AST is a hypothetical system. However, several other *d4r*-containing gallophosphates are known (Estermann et al., 1991; Simmen et al., 1993). Second, the role of the OSDA was investigated by comparing models containing two different cations, TMA<sup>+</sup> and quinuclidinium (QNU<sup>+</sup>). QNU<sup>+</sup> cations were used in the synthesis of AlPO-16 (Bennett and Kirchner, 1991), whereas both TMA<sup>+</sup> and QNU<sup>+</sup> can act as OSDAs in the preparation of SiO<sub>2</sub>-AST (octadecasil; Caulet et al. (1991)). Finally, three different temperatures were considered, performing AIMD simulations in the *NVT* ensemble for 150, 298, and 573 K.

The analysis also proceeded in a largely analogous fashion to the preceding article. Most attention was directed towards the impact of variations in framework composition and OSDA on the equilibrium position of fluoride anions inside the cage, and on their dynamic behaviour. Findings from DFT optimisations and AIMD simulations were compared, revealing, in some instances, rather significant discrepancies that were critically discussed.

### 4.4.2 Summary of results

The DFT structure optimisations predicted a centre-of-cage position of the fluoride anions for all eight systems considered (four framework compositions, two OSDAs). The TMA<sup>+</sup> cations were found to form H···O contacts in the range of 2.4 to 2.7 Å. As these distances are somewhat shorter than the sum of the vdW radii of H and O of 2.7 Å (Alvarez, 2013), it is debatable whether these contacts should be interpreted as weak C–H···O hydrogen bonds (Mineva et al., 2020). The picture is more clear-cut for the QNU<sup>+</sup>-containing systems, where H···O distances of 1.7 to 2.0 Å indicate the presence of a N–H···O hydrogen bond (**B2**, Figure 3). The shortest hydrogen bond occurs in GeO<sub>2</sub>-AST\_QNU, which also shows an unusual "pyritohedron-like" distortion of the *d4r* cages. Such a distortion had been described previously by Attfield et al. (2009) in a sc-XRD study of the germanate zeolite ASU-7.

The analysis of F–T RDFs and time-averaged structures obtained from the AIMD trajectories revealed qualitative differences in the local structure depending on the framework composition (**Figure 4.4**): In SiO<sub>2</sub>-AST, the fluoride anions were found to oscillate around their equilibrium position at the cage centre, and the *d4r* cages showed no significant distortion from their ideal cube-like shape. In GeO<sub>2</sub>-AST, the fluoride anions also oscillated around the cage centre, but the cages exhibited a pronounced pyritohedron-like distortion, regardless of whether TMA<sup>+</sup> or QNU<sup>+</sup> cations were included as OSDA. A displacement of the fluoride anions from the cage centre was observed for AlPO<sub>4</sub>-AST, where one of the Al atoms assumes a trigonal-bipyramidal coordination with a F–Al bond length of about 1.9 Å. A comparison of the RDFs and individual trajectories computed for different temperatures showed that the fluoride anions largely remain bonded to the same Al atoms on the simulation timescale at 150 K, but that dynamic exchanges between different Al sites can occur at 298 K and, most prominently, at 573 K. Finally, GaPO<sub>4</sub>-AST combines the two features observed in the GeO<sub>2</sub> and AlPO<sub>4</sub> systems,

namely a pyritohedral distortion of the  $d4r$  cages and the displacement of the fluoride anions from the cage centre, either towards a single Ga atom or towards one of the faces of the cage, with fluoride in a "bridging" mode between two Ga atoms (B2, Figure 11).

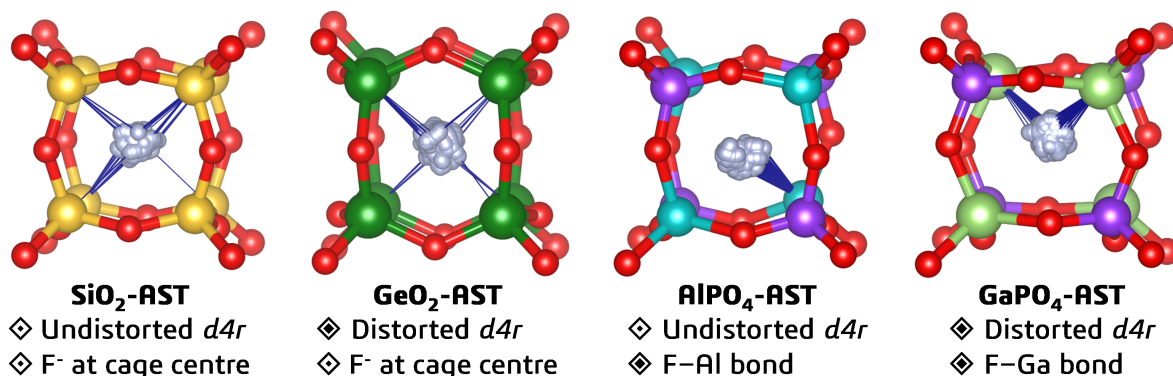


**Figure 4.4:** Representative trajectories of individual fluoride anions computed for  $T = 298$  K. Positions of the T and O atoms are taken from the respective average structures. Thin blue lines are used to represent F-T contacts below 2.3 Å for SiO<sub>2</sub>- and GeO<sub>2</sub>-AST, and below 2.0 Å for AlPO<sub>4</sub>- and GaPO<sub>4</sub>-AST. Figure modified after **Article B2**.

When looking beyond the local structure of the individual  $d4r$  cages, a remarkable influence of the OSDA became apparent: In the TMA<sup>+</sup>-containing systems, the local distortions in the form of pyritohedral distortions and/or off-centre displacements of fluoride occurred essentially at random. Due to the stronger interaction of the QNU<sup>+</sup> cations with the framework, the ordered arrangement of these cations induced an ordering of the framework distortions. This ordering, which was most pronounced at 150 K, is illustrated in **Figure 4.5**. Although this effect may not occur in real samples, where the OSDA cations are unlikely to be as well ordered as in the models used for the calculations, these findings point to the theoretical possibility to trigger ordered framework distortions through a judicious choice of the OSDA. In the view of the previous suggestion of weak hydrogen bonds in SiO<sub>2</sub>-AST\_TMA by Dib et al. (2017), the analysis of the AIMD trajectories also covered the H-O RDFs, with most emphasis on their evolution with temperature. A qualitatively different behaviour was found for the two cations considered: In QNU<sup>+</sup>-containing systems, the first maximum in the H-O RDF decreased with increasing temperature, an observation that can be interpreted as a weakening/breaking of the N-H ··· O hydrogen bonds due to increased thermal motion. In contrast, the left flank of the first maximum in the RDF shifted towards lower distances at higher temperatures in TMA<sup>+</sup>-containing systems. The more frequent occurrence of shorter H ··· O contacts upon increasing thermal motion did not corroborate the existence of hydrogen bonds proposed by Dib et al. (2017), but rather indicated that non-directional interactions dominate for this OSDA.

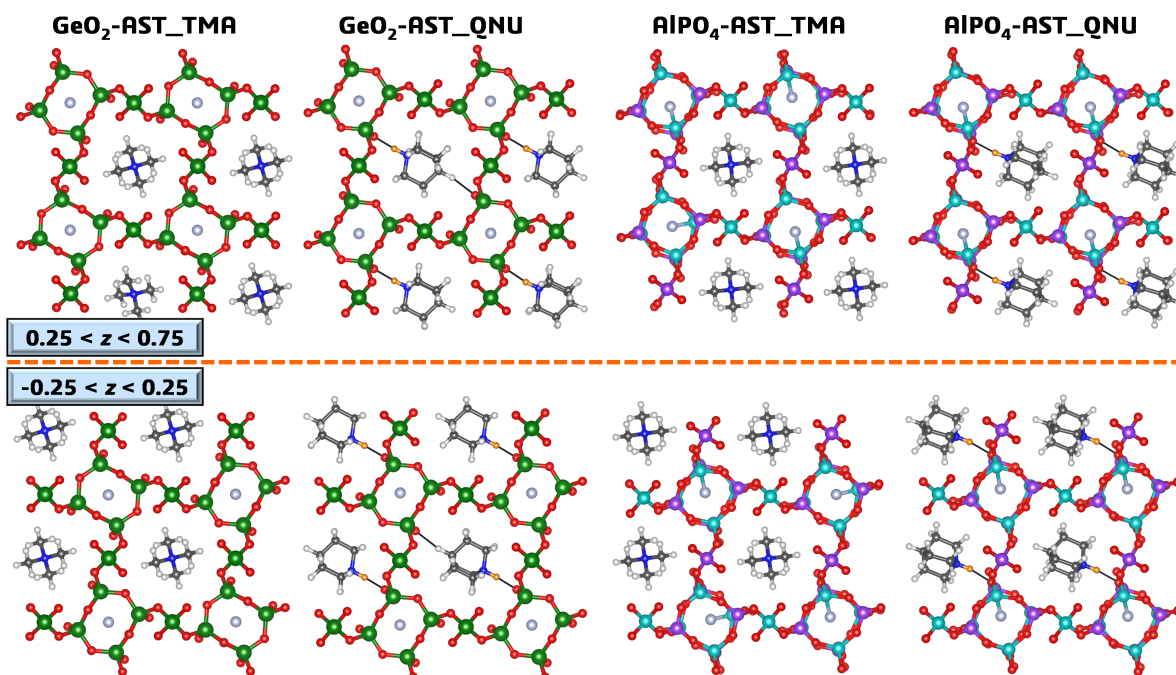


**Figure 4.5:** Representative average structures of GeO<sub>2</sub>-AST\_TMA/\_QNU and AlPO<sub>4</sub>-AST\_TMA/\_QNU obtained from AIMD trajectories computed for  $T = 150$  K. For clarity, different sections perpendicular to  $c$  are visualised separately. Hydrogen atoms of the QNU<sup>+</sup> N-H moieties are highlighted in orange. Figure modified after **Article B2**.

## 4.5 **Article B3:** Influence of Organic Structure-Directing Agents on Fluoride Dynamics in As-Synthesized Silicalite-1

### 4.5.1 Outline

Silicalite-1 was the first all-silica zeolite for which a dynamic disorder of fluoride anions was established on the basis of <sup>29</sup>Si-NMR experiments (Koller et al., 1997). While it is easily rationalised that the dynamic disorder disappears upon cooling to cryogenic temperatures, the strong variation of the dynamic behaviour as a function of the choice of OSDA reported by Brace et al. (2015) was a more surprising finding. These authors attributed the lack of dynamic disorder in a sample synthesised using MTBA<sup>+</sup> to shorter contacts between the fluoride anions and the positively polarised nitrogen atoms of the OSDA molecules, resulting in stronger electrostatic interactions. In order to elucidate this behaviour, DFT-based AIMD simulations were performed for Silicalite-1 models containing different OSDAs in this work: On the one hand, four tetra-X-ammonium OSDAs with X = methyl, ethyl, propyl, butyl were considered (TMA<sup>+</sup>, TEA<sup>+</sup>, TPA<sup>+</sup>, TBA<sup>+</sup>). On the other hand, four "asymmetric" OSDAs having one shorter and three longer alkyl chains were included: X-tributylammonium where X = methyl, ethyl, propyl (MTBA<sup>+</sup>, ETBA<sup>+</sup>, PTBA<sup>+</sup>), as well as methyl-tripropylammonium (MTPA<sup>+</sup>).

The AIMD simulations, which used a similar protocol as in the preceding articles (CP2K code; Kühne et al. (2020); PBE-D3 functional; Perdew et al. (1996); Grimme et al. (2010)), were carried out in the *NVT* ensemble for three different temperatures (298, 373, and 473 K). In the first place, it was evaluated whether the dynamic disorder of the fluoride anions could be observed on the picosecond timescale that is accessible with the simulations. In the following, OSDA-dependent variations of the dynamic

behaviour were evaluated, and it was attempted to rationalise the observed influence of the OSDA on the dynamic disorder.

#### 4.5.2 Summary of results

As  $\text{TPA}^+$  is the prototypical OSDA employed in the synthesis of Silicalite-1,  $\text{MFI}(\text{TPA}^+, \text{F}^-)$  was taken as starting point for the analysis of fluoride dynamics. A plot of the RMSDs against temperature showed a large increase of the F-RMSD across the range of temperatures studied (**B3**, Figure 2). This was rationalised by looking at the time evolution of the coordinates of individual fluoride anions: With increasing temperature, "jumps" of fluoride anions between different silicon atoms become increasingly likely (**Figure 4.6**). In addition to causing a significant increase in the F-RMSDs, these "dynamic events" were also visible in the F–Si RDFs, where a non-zero  $g(r)$  value between the first and second maximum indicated a dynamic exchange between different Si sites (**B3**, Figure 4).

Comparing the four models with OSDAs having chains of equal length, between 5 and 8 dynamic events occurred in the 22.5 ps sampled by AIMD simulations for  $T = 373$  K. Among the four systems, a decreasing number of dynamic events with increasing chain length was apparent, which correlates with a reduced freedom of motion of the increasingly bulky OSDAs occupying the channels. Contrary to the hypothesis of Brace et al. (2015), the shortest F–N contacts were found for the models containing smaller OSDAs, despite the larger number of dynamic events. The total number of dynamic events at 298 K was too small to identify any trends. For 473 K, all systems showed a similar dynamic behaviour, indicating that the increased thermal motion supersedes any OSDA-related variation at this temperature.

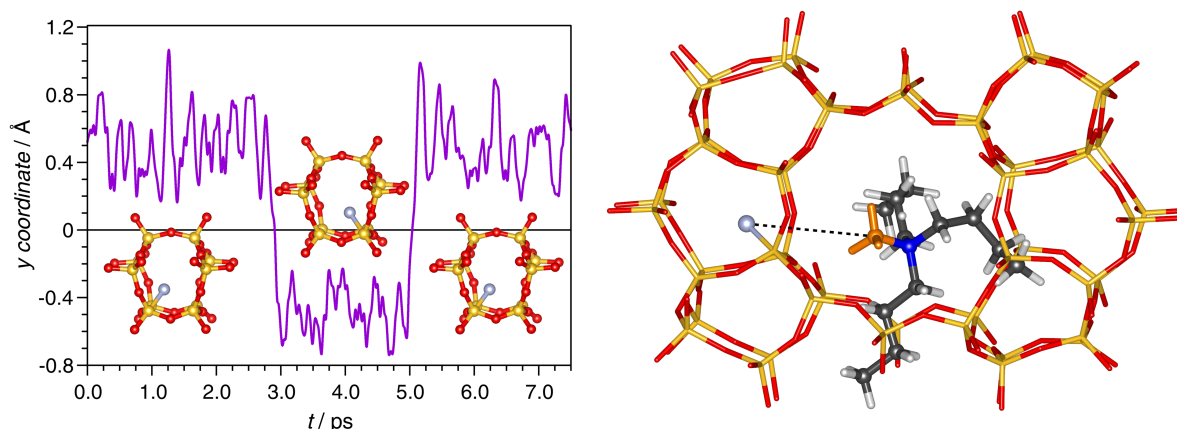


**Figure 4.6:** **Left:** Evolution of the  $y$  coordinate of one fluoride anion in  $\text{MFI}(\text{TPA}^+, \text{F}^-)$  obtained from an AIMD trajectory computed for  $T = 373$  K. Dynamic events occur after about 3 and 5 ps. **Right:** Local environment of  $\text{MTBA}^+$  cation in  $\text{MFI}(\text{MTBA}^+, \text{F}^-)$ , highlighting the relatively short distance between the methyl group of  $\text{MTBA}^+$  (orange) and the fluoride anion ( $d(\text{F}-\text{C}_{\text{methyl}}) = 4.85$  Å). Figure modified after **Article B3**.

Looking at the models with asymmetric OSDAs, a drastic reduction of the number of dynamic events was observed for  $\text{MFI}(\text{MTBA}^+, \text{F}^-)$  and  $\text{MFI}(\text{ETBA}^+, \text{F}^-)$ . This finding is in qualitative agreement with the experimentally observed behaviour, as Brace et al. (2015) observed a complete freezing of the dynamic disorder at room temperature in the former system, and a pronounced reduction in comparison to  $\text{MFI}(\text{TPA}^+, \text{F}^-)$  in the latter case. An analysis of the RMSDs and N–F RDFs, together with a visualisation of the electrostatic potential of the OSDAs, allowed the identification of two crucial factors whose interplay is responsible for the suppression of dynamic disorder: First, the presence of one short chain

and three long chains results in a more heterogeneous electrostatic potential, with a positively polarised short chain. This leads to enhanced electrostatic interactions with the fluoride anions, increasing the energetic penalty for their movement to another Si atom. Second, the three butyl chains reduce the overall freedom of motion of the OSDA, keeping the positively polarised part confined to the channel intersections (**Figure 4.6**). Despite short F–N contacts, OSDAs without long chains like TMA<sup>+</sup> do not suppress the dynamic disorder, as their vigorous motion will, on average, weaken the electrostatic interaction.

## 4.6 **Article B4:** *Fluoride Anions in All-Silica Zeolites: Studying Preferred Fluoride Sites and Dynamic Disorder with Density Functional Theory Calculations*

### 4.6.1 *Outline*

The NMR investigations by Koller et al. (1997, 1999) revealed qualitative differences in the occurrence of dynamic disorder of fluoride anions in different all-silica zeolites containing  $[\text{Si}^{[5by]} \text{O}_{4/2} \text{F}]^-$  units. It was the central aim of this study to investigate these differences by comparing a set of different zeolites on an equal theoretical footing, employing DFT-based AIMD calculations and analysing them along the same lines as in the preceding article. In connection with this, the relative stabilities of different possible fluoride sites within one cage were also predicted in order to test whether common features determining the most stable position could be identified. This part of the study is similar in spirit to the previous work of Pulido et al. (2006a), however, using a higher-level computational method (DFT instead of FF calculations) and more realistic model systems, including the OSDA molecules contained in the pores and the same amount of fluoride anions per unit cell as in the experimental samples.

A total of five all-silica zeolites were considered in the calculations. For all of them, the location of fluoride had been determined using XRD methods, and experimental information about the dynamic disorder was available for four of them. Specifically, nonasil (NON topology; van de Goor et al. (1995)), Mu-26 (STF; Paillaud et al. (2007)), ITQ-4 (IFR; Bull et al. (2000)), SSZ-23 (STT; Cambor et al. (1998a)), and SiO<sub>2</sub>-CHA (Villaescusa et al., 2003) were included. Whereas the fluoride anions in as-synthesised NON- and STF-type zeolites do not exhibit dynamic disorder at room temperature (Koller et al., 1997; Paillaud et al., 2007), they are dynamically disordered over two symmetry-equivalent sites in ITQ-4 (Koller et al., 1999; Bull et al., 2000), and over three non-equivalent sites in SSZ-23 (Cambor et al., 1998a; Koller et al., 1999). The fluoride environments in these four zeolites are visualised in **Figure 4.1**. NMR investigations on SiO<sub>2</sub>-CHA permitted no conclusions regarding the occurrence or absence of dynamic disorder in this zeolite (Villaescusa et al., 2003). The computational approach was largely analogous to that of the previous study on Silicalite-1, combining DFT optimisations and AIMD simulations (NVT ensemble,  $T = 298, 373, 473$  K). In addition to a detailed analysis of the DFT-optimised structures and a calculation of RDFs, RMSDs, and average structures from the AIMD trajectories, the trajectories of individual fluoride anions undergoing dynamic events were also visualised, allowing for an intuitive understanding of the dynamic behaviour.

### 4.6.2 *Summary of results*

A comparison of the relative stability of different fluoride positions in the respective cages gave excellent agreement with experiment for NON, IFR, and STT. It was particularly noteworthy that the three positions over which fluoride is disordered in STT were very close in energy (with an energy difference  $\Delta E_{rel}$  of less than 3 kJ mol<sup>-1</sup>), whereas all other sites were distinctly higher in energy (**Figure 4.7**). For STF, one position associated with a 4MR (coloured green in **Figure 4.7**) was predicted to be lower in

energy than the experimentally observed site. No such assessment could be made for CHA, as the fluoride anions are disordered over all twelve sites in the *d6r* cages in the experimental structure. Different factors determining the lowest-energy siting of fluoride in a given cage could be identified: Besides a general preference for sites associated with 4MRs, a tendency to maximise the distance between individual  $[\text{Si}^{[5by]}\text{O}_{4/2}\text{F}]^-$  units was observed in one case. Moreover, interactions with different parts of the OSDA molecules were also found to play a role. Altogether, it was concluded that the energetically favoured fluoride location(s) in a given structure are determined by a complex interplay of factors, precluding the definition of simple crystal-chemical "rules" that would allow for a prediction without additional information from experiment and/or calculations.

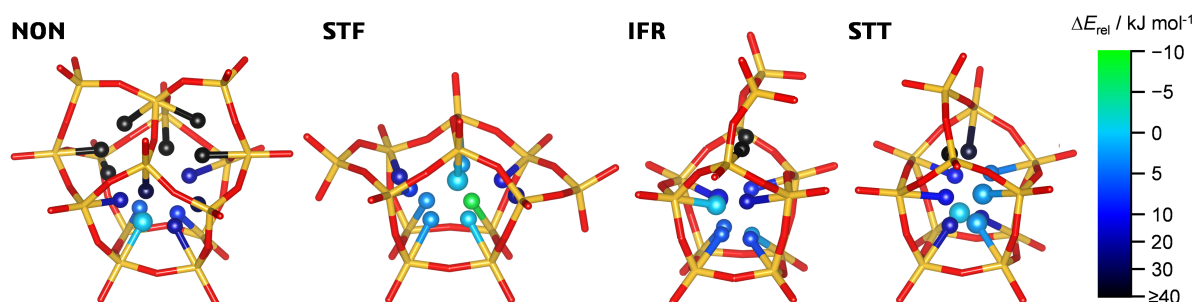


**Figure 4.7:** Visualisation of all fluoride positions considered in zeolites NON, STF, IFR, and STT. The fluoride sites are coloured according to their relative energy with respect to the experimental position having the lowest energy, which is set as zero point on the energy scale (light blue colour). Experimentally observed sites are visualised using larger spheres than other sites. Figure modified after **Article B4**.

In the AIMD simulations, dynamic jumps of the fluoride anions occurred in both IFR and STT at all temperatures considered, in agreement with experimental observations (Koller et al., 1999). Moreover, an analysis of the trajectories showed that these dynamic events involve exactly those fluoride locations that were found in the crystal structure refinements, even in the complex case of STT (**Figure 4.8**). For NON, no dynamic events were observed up to 473 K. A somehow intermediate picture emerged for STF and CHA: While no dynamic events occurred in the simulations for 298 K, a few dynamic jumps were found at 373 K and 473 K. Although the absence of dynamic disorder in STF at room temperature agrees with experiment, the relatively short timespan covered by the simulations puts some limitations on the interpretation of these results, as it cannot be ruled out that significantly longer simulations might predict dynamic disorder even for 298 K. In any event, a distinction could be made between pronounced dynamic disorder in IFR and STT, an intermediate behaviour of STF and CHA, with a likely onset of dynamic disorder at elevated temperatures, and the absence of any dynamic disorder in NON.

Beyond the reproduction of experimental observations, it was also attempted to develop a microscopic explanation for the qualitatively different dynamic behaviour of the fluoride anions in these zeolites. It was found that "secondary"  $\text{F} \cdots \text{Si}$  contacts play a very important role in this regard: In IFR and STT, relatively short distances, typically below  $2.7 \text{ \AA}$ , were found between the fluoride anion and at least one Si atom in addition to the primary bonding partner (**B4**, Table 2). Such short distances were not encountered in NON and STF. The occurrence of dynamic disorder in the former systems was explained as being due to these secondary interactions, which weaken the primary F–Si bond and enhance the probability of a dynamic motion towards another Si atom. In other words, the local environment, specifically the  $\text{F} \cdots \text{Si}$  distances, determine whether dynamic disorder occurs or not. The examples of CHA and of the previously studied MFI-type systems showed that the cage geometry is not the only contributing factor: In the case of a relatively strong attractive interaction between fluoride anions and OSDA



cations (which is present in CHA and MFI<sub>(MTBA<sup>+</sup>,F<sup>-</sup>)</sub>), the dynamic disorder may be suppressed. This explains why the fluoride anions in CHA show no dynamic disorder at room temperature, despite a relatively short secondary F...Si contact. The findings discussed here on the basis of the interatomic distances were corroborated by a detailed analysis of the F–Si and F–N RDFs (B4, Figures 9 and 10).

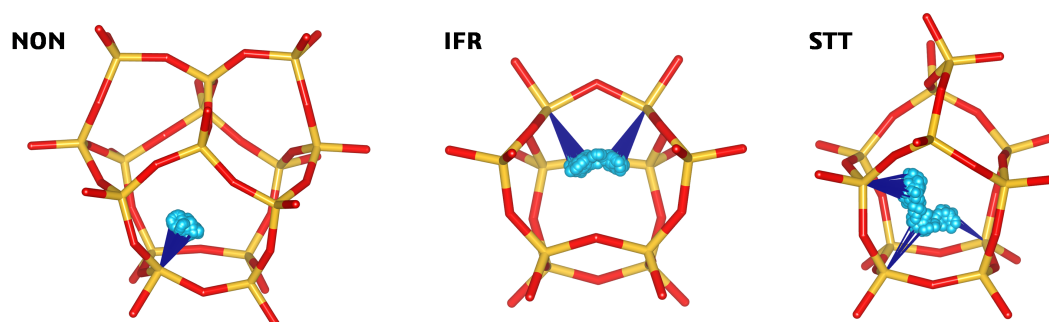


**Figure 4.8:** Representative trajectories of individual fluoride anions in NON, IFR, and STT, plotted into the average structure of the surrounding cages. While the fluoride anion in NON oscillates about its equilibrium position, those in IFR and STT undergo dynamic events that involve the experimentally observed fluoride sites. Thin blue lines are used to represent F–Si contacts below 1.9 Å. In the IFR visualisation, two Si atoms and one O atom are omitted from the cage visualisation to improve the visibility of the fluoride trajectory. Figure modified after **Article B4**.

## 4.7 **Article B5:** *Elucidating the Germanium Distribution in ITQ-13 Zeolites by Density Functional Theory*

### 4.7.1 Outline

The ITH-type zeolite ITQ-13 is a particularly interesting system for various reasons: First of all, it contains fluoride in two different environments, namely in *d4r* cages and in [4·5<sup>6</sup>] cages (Corma et al., 2003). Second, it is available both in all-silica form (Corma et al., 2003) and as silicogermanate across a wide range of Ge contents, down to Si/Ge ratios as low as 2.5 (Shamzhy et al., 2014). Finally, ITQ-13 also shows promising performance in catalytic applications, *e.g.*, as co-catalyst in the cracking of vacuum gasoil when aiming at the production of propene-rich feeds (Castañeda et al., 2006).

In this article, ITQ-13 was studied using a similar methodological approach as employed in **Article B1** for AST-type systems, but accounting for the significantly higher structural complexity of this zeolite. Specifically, ITQ-13 models with different Ge distributions were constructed for six Si/Ge ratios ranging from 55 to 6. On the basis of DFT structure optimisations, the energetically favoured Ge distributions were determined, and the results were correlated to experimental observations. These calculations were supplemented by NMR calculations for discrete building units. For ten selected models containing different amounts of Ge, AIMD simulations for room temperature and for a typical synthesis temperature (408 K) were used to investigate the impact of the Ge distribution on the dynamic behaviour of the fluoride anions. Since experimental investigations by Liu et al. (2011a,b) point to a selective defluorination of ITQ-13 zeolites upon alkaline treatment, where fluoride anions are preferentially removed from the [4·5<sup>6</sup>] cages, DFT optimisations were carried out for partially defluorinated models in order to evaluate whether the experimentally observed behaviour can be understood on the basis of the computed relative stabilities.

#### 4.7.2 Summary of results

DFT optimisations of ITQ-13 models containing one Ge atom per unit cell in different positions revealed a strong energetic preference for the two non-equivalent T sites at the corners of the  $d4r$  cages (T2 and T5 sites according to Corma et al. (2003)) and for the T7 site forming the basal 4MR plane of the  $[4\cdot5^6]$  cages, in perfect agreement with experimental observations (Vidal-Moya et al., 2003). As a consequence, only these three positions were considered in calculations for higher Ge contents, which considered between 18 and 48 distinct configurations. The energetic preference to incorporate Ge at the T2, T5, and T7 sites was not clear-cut in calculations for bare-framework models, corroborating the finding from **Article B1** that the inclusion of fluoride anions and OSDA cations has a significant impact on the results. Calculations for models containing 2, 3, 4, 6, and 8 Ge atoms per unit cell showed a tendency to distribute the Ge atoms relatively evenly among the available building units (two  $d4r$  and two  $[4\cdot5^6]$  cages per unit cell). The prediction of an even distribution of Ge agrees with the pronounced intensity decrease of the  $^{19}\text{F}$ -NMR resonances stemming from fluoride in purely siliceous  $d4r$  and  $[4\cdot5^6]$  cages upon increasing Ge content (Vidal-Moya et al., 2003; Liu et al., 2011b). At the highest Ge content, a model containing  $[4\cdot5^6]_{2\text{Ge,pair}}$  cages (two Ge atoms at adjacent corners) was found to be the lowest-energy case. While it had been established by Vidal-Moya et al. (2003) that  $[4\cdot5^6]_{1\text{Ge}}$  cages give rise to a distinct resonance in the  $^{19}\text{F}$ -NMR spectrum at  $-55$  ppm,  $[4\cdot5^6]$  cages with more than one Ge atom had not yet been discussed, and there is no unassigned resonance in the experimental spectra, even for Ge-rich samples. A DFT-based prediction of the  $^{19}\text{F}$  chemical shifts gave good agreement with experiment for those building units where the corresponding isotropic shifts had already been assigned ( $d4r$  cages with 0, 1, 2 Ge atoms and  $[4\cdot5^6]$  cages with no or one Ge atom), with typical deviations on the order of 3 to 4 ppm (**B5**, Table 2). The resonance stemming from fluoride in  $[4\cdot5^6]_{2\text{Ge,pair}}$  cage was predicted to lie at about  $-16$  ppm, between the two main peaks associated with fluoride in  $d4r$  cages where a Ge atom occupies at least one corner ( $-8$  and  $-20$  ppm). As especially the peak at  $-8$  ppm is very broad, it cannot be ruled out that the contribution from  $[4\cdot5^6]_{2\text{Ge,pair}}$  cages was so far overlooked in the analysis of experimental spectra.

AIMD simulations carried out for  $T = 298$  K delivered no evidence for dynamic disorder of the fluoride anions in  $[4\cdot5^6]$  cages. Upon increasing the number of Ge atoms at the corners of the cage, the RMSD of the fluoride anions also increased, an observation that was attributed to the higher flexibility of F–Ge bonds compared to F–Si bonds and, for the specific case of  $[4\cdot5^6]_{2\text{Ge,pair}}$  cages, to oscillations of the fluoride anions between the two Ge atoms. In simulations for 408 K, dynamic events occurred in models containing purely siliceous  $[4\cdot5^6]$  cages, analogously to the observations made for STF (which contains the same cage) in **Article B4**, whereas only short-lived ( $< 1$  ps) displacements towards one of the Si atoms were observed in  $[4\cdot5^6]_{1\text{Ge}}$  cages (**Figure 4.9**). The trends in the freedom of motion of fluoride anions in  $d4r$  cages were essentially identical to those observed in **Article B1**.

Calculations for partially defluorinated models of the all-silica zeolite ITQ-13, in which the fluoride anions were removed either from the  $d4r$  cages or from the  $[4\cdot5^6]$  cages, predicted a higher stability of fluoride incorporated in the former type of cage, in line with the experimentally observed selective removal from  $[4\cdot5^6]$  cages (Liu et al., 2011a). Incorporation of Ge into the structure further stabilised the fluoride anions, retaining the preference for  $d4r$  over  $[4\cdot5^6]$  cages at equal Ge content. Altogether, it was concluded that the high thermodynamic stability of fluoride anions in  $d4r$  cages is a key factor in the selective defluorination behaviour of ITQ-13, although it cannot be ruled out that kinetic effects also play a role.



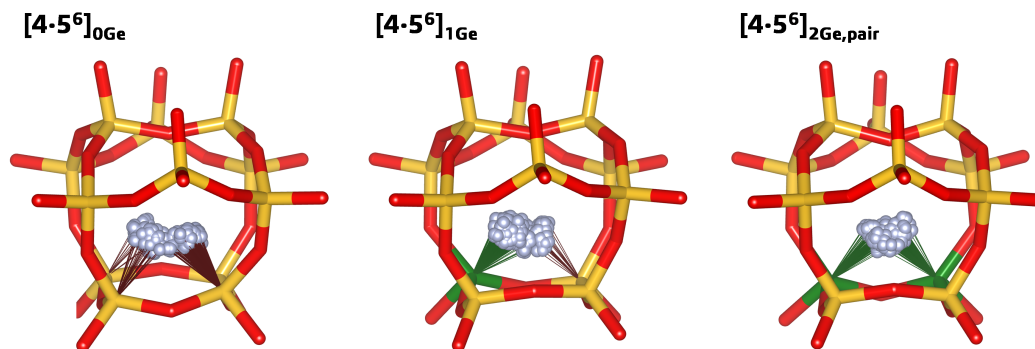


**Figure 4.9:** Representative trajectories of individual fluoride anions in  $[4 \cdot 5^6]$  cages of ITQ-13 systems, obtained from AIMD simulations performed for  $T = 408$  K. Coordinates of atoms forming the cages were taken from average structures. Thin lines are used to represent F–T contacts below 2.0 Å. Figure modified after **Article B5**.

## 4.8 Conclusions

In **Articles B1, B4, and B5**, DFT optimisations were employed to compare zeolite models with different local structures (different Ge distributions or fluoride positions) in order to identify the most stable configurations. This led to the establishment of some relatively clear trends, such as a tendency to maximise the number of Ge–O–Ge linkages in *d4r*-containing silicogermanates, and, for the case of  $[\text{Si}^{[5by]} \text{O}_{4/2} \text{F}]^-$  trigonal bipyramids, a preference of fluoride anions to bond to Si atoms that are part of 4MRs. However, it also became clear that such simple trends are not able to explain the full set of results: In several zeolites, a large spread of the relative energies was observed for distinct fluoride positions associated with 4MRs, despite essentially identical local environments (as is visible, for example, for NON in **Figure 4.7**). Similarly, ITQ-13 models containing exactly the same type of constituent building units in different orientations with respect to each other had, in some cases, rather different total energies. This clearly implies that there are a variety of factors beyond the local environment that determine the total energy, whose individual contributions are far from trivial to discern. Hence, it appears advisable to carry out a reasonably comprehensive computational screening of relevant models, rather than trying to extrapolate trends from calculations for a limited set of configurations. As demonstrated for silicogermanate zeolites, there is convincing evidence that the inclusion of extra-framework species (fluoride anions, OSDAs) is required to arrive at a realistic energetic ordering. This aspect should be taken into account in future DFT studies of these systems.

There are also a few caveats associated with the interpretation of the DFT optimisations: First of all, temperature effects are not included in the calculations, so the analysis of the relative stabilities refers to 0 K. Although an inclusion of temperature using phonon calculations or AIMD simulations might be warranted in special cases, it is not expected that this would affect the qualitative findings. The second issue is potentially more significant, and definitely harder to resolve: Calculations on periodic zeolite structures give only the relative thermodynamic stability of the end product of zeolite synthesis, whereas the actual atomic arrangement will be determined during zeolite formation, where kinetics will also play an important role. It is, however, clear that an atomistic simulation approach to zeolite synthesis that covers both the formation of small building units as well as their assembly to periodic zeolite structures would have to be extremely complex and computationally demanding. A third issue became apparent in the comparison of DFT optimisations and AIMD simulations in **Article B2**, where DFT optimisations delivered a qualitatively different local structure than AIMD simulations for some

of the AST-type zeotypes. While AIMD simulations can sample several local minima, DFT optimisations will always converge to the nearest local minimum. The usefulness of AIMD simulations to find low-energy zeolite structures has been highlighted recently by Hoffman et al. (2019) and by Abatal et al. (2020).

All articles compiled in this chapter employed AIMD simulations to investigate the dynamic behaviour. While most emphasis was placed on the fluoride anions, the dynamics of the zeolite framework and of the OSDA molecules were also analysed where relevant. Although AIMD simulations had previously been employed to study various aspects of zeolites and zeotypes, there were no prior works focussing on fluoride dynamics. The studies of *d4r*-containing systems clearly demonstrated the important influence of the local environment on the freedom of motion of the encapsulated fluoride anions: In cases where the fluoride anions are relatively strongly bonded to a T atom, their RMSDs are similar to those of framework atoms. If such bonds are absent, the RMSDs are significantly increased, because the potential energy surface inside the cage is relatively shallow. In silicogermanates, the strongest F–Ge bonds occur if there is only a single Ge atom at one corner of the *d4r* cage, whereas interactions with multiple Ge atoms result in larger F–Ge distances and increased fluoride motion. A rather unexpected finding was the ordering of local distortions induced by ordered, hydrogen-bonded OSDAs in GeO<sub>2</sub>-, AlPO<sub>4</sub>- and GaPO<sub>4</sub>-AST. If realised in actual zeolite samples, such ordered distortions could affect the material properties, *e.g.*, dielectric properties. This could be relevant for applications, especially if the properties can be "tuned" through a variation of composition or external conditions (temperature).

The calculations for zeolites containing [Si<sup>[5by]</sup>O<sub>4/2</sub>F]<sup>-</sup> units showed that the dynamic disorder of fluoride anions can be predicted rather reliably using AIMD simulations covering relatively short time-scales on the order of 10 ps. However, it was also noted that the number of dynamic events at room temperature was very small. As a consequence, the interpretation had to remain purely qualitative. An increase of the simulation temperature, *e.g.*, to 373 K, also increased the number of events, facilitating the analysis of the structural changes associated with the dynamic behaviour. The local environment of the fluoride anion, specifically the presence of relatively short contacts (typically below 2.7 Å) to "secondary" Si atoms, was identified as key factor determining whether a dynamic motion between different Si atoms is possible. Attractive interactions with the OSDA can also play a role, as they can suppress dynamic behaviour in cases where the local environment should, in principle, enable a dynamic motion of fluoride between different Si atoms. The detailed investigation of MFI-type zeolites containing different OSDAs showed that both the charge distribution of the OSDA and its size play a role: While the former governs the strength of the electrostatic interactions, the latter affects the mobility of the OSDA. Small OSDAs, which have a larger freedom of motion, are less effective in suppressing dynamic disorder than larger molecules that are more strongly confined.

## 4.9 Outlook

First of all, there are some methodological issues and developments that should be considered in future work on comparable systems:

- All calculations reported in this chapter used the PBE-D3 functional. On the one hand, comparisons to experimental structure data gave satisfactory results, and the accurate prediction of relative energies of all-silica zeolites presented in the previous chapter gives reason to be confident in the predictions for Ge-containing systems. On the other hand, it must be conceded that

a comparison of relative energies to experimental enthalpies of transition was not attempted. Although calorimetry data are available for a few silicogermanates (Li et al., 2003, 2004), the various ways to distribute the Ge atoms in the structures would render a meaningful comparison very challenging. A more promising benchmarking strategy might involve DFT and higher-level WFT calculations on small clusters, such as *d4r* cages.

- The DFT results from this work could form the basis for force field development work, *e.g.*, to derive FFs that give a more accurate description of the relative stability of silicogermanates. Due to the much lower computational cost, such FFs could be employed for large-scale studies comparing a vast number of zeolite models with different Ge distributions, as even calculations covering 1,000s of structures should be feasible at a rather modest computational cost for typical zeolites. Even though FF parameters for silicogermanates exist, the parameters developed by Sastre and Gale (2003) predict an avoidance of Ge–O–Ge linkages, disagreeing with the DFT results. As highlighted in the previous chapter, the use of machine learning techniques could render the FF development much more efficient.
- In a similar vein, the data from DFT calculations and AIMD simulations could be employed to develop a new FF for use in classical MD simulations of fluoride-containing zeolites or zeotypes. This would enable an extension to much longer simulation times, well into the nanosecond timescale. An additional challenge in this regard would be the development of a potential model that covers the breaking and re-formation of F–Si bonds in the spirit of a "reactive" force field (Senftle et al., 2016).
- The AIMD investigations that were carried out to study the dynamic disorder of fluoride anions in  $[\text{Si}^{[5by]}\text{O}_{4/2}\text{F}]^-$  units employed essentially a "brute force" technique, running unconstrained AIMD simulations for given conditions and a certain, computationally feasible number of picoseconds. In many instances, the extraction of more quantitative information would require impractically long AIMD simulations, *e.g.*, to achieve statistics that would be sufficient to compute free energy barriers. Constrained AIMD simulations, which have been used, for example, to investigate the diffusion of guest molecules through 8MR windows of zeolite Na-RHO (Coudert and Kohen, 2017), are better suited to study rare events that are too infrequently observed in unconstrained AIMD simulations. They should hence constitute a more elegant and computationally efficient approach to investigate the dynamics of fluoride anions in a more quantitative fashion.
- Even though the different bonding scenarios were discussed in several instances, no detailed attempts were made to elucidate the nature of the chemical bonding, *e.g.*, to quantify the importance of covalent and ionic contributions. In principle, electronic structure methods provide many possibilities to analyse the chemical bonding, which could be exploited in future work.

Beyond these methodological aspects, extensions in several other directions could be envisaged:

- With the exception of the study of ITQ-13 silicogermanates, the investigations of *d4r*-containing systems dealt with AST-type frameworks. Due to the absence of any accessible porosity, AST-type materials are of little interest for most applications. It would therefore be interesting to expand the work to other zeolite topologies. In the field of silicogermanates, the preferred Ge locations in zeolites that can be disassembled using the assembly-disassembly-organisation-reassembly (ADOR) mechanism are of particular interest, as the Ge distribution determines the disassembly behaviour

(Shamzhy et al., 2014). While DFT calculations have already been employed to study some frameworks that could be interesting starting points for the ADOR mechanism, they typically ignored the presence of OSDA cations and fluoride anions (Odoh et al., 2014), an approximation that appears to be of questionable validity in the view of the present findings.

- Correspondingly, future studies of *d4r*-containing AlPOs might look at materials that are of interest for applications in thermal energy storage, such as AlPO<sub>4</sub>-LTA (Krajnc et al., 2017). A better understanding of the structure-directing role of fluoride might aid the development of new synthesis routes and potentially even towards fluoride-free synthesis, which would be attractive in the view of the hazard potential and corrosiveness of hydrofluoric acid.
- Whereas the calculations predicted localised F–T bonds for several *d4r*-containing zeotypes, diffraction methods are rarely able to establish the occurrence of such bonds: Taking the example of an AlPO zeotype, one can anticipate a disorder of fluoride over four positions with an occupancy of 0.25. It will be difficult to distinguish this scenario from a fully occupied centre-of-cage position, especially when only powder samples are available. In the view of these limitations of diffraction methods, one could employ advanced vibrational or NMR-spectroscopic methods to gather experimental evidence for the presence of localised F–T bonds, potentially in conjunction with a computational prediction of the IR/Raman bands or NMR shifts.
- The observation of ordered framework distortions in AST zeotypes induced by an ordering of the hydrogen-bonded QNU<sup>+</sup> molecules was one of the most surprising results reported in this chapter. It would be interesting to investigate whether such ordered distortions could be stabilised in real samples. Given that zeolites/zeotypes are typically synthesised at temperatures between 400 and 500 K, it can be anticipated that asymmetric, strongly hydrogen-bonded OSDAs would be required to achieve an ordering at such temperatures. Further calculations could be employed to predict which OSDAs might stabilise framework distortions, either in AST-type systems or in other zeotypes of interest. Besides, it could also be insightful to predict the influence of these distortions on dielectric and other properties.
- As already mentioned in the Conclusions, the actual Ge distribution in silicogermanates is determined during zeolite synthesis, when building units form and assemble. To this end, DFT-based calculations could be employed to study the stability of such isolated building units, ideally accounting for solvent effects and potentially also for the presence of OSDAs in the vicinity. Such calculations could be complemented using *in situ* NMR experiments.
- In the view of the reliable prediction of the preferred location of [Si<sup>[5by]</sup>O<sub>4/2</sub>F]<sup>−</sup> units in different zeolites, it appears straightforward to perform analogous calculations in a rather routine fashion in cases where the fluoride locations cannot be determined unambiguously with diffraction methods. As interactions with the organic cations can be expected play a non-negligible role in determining the lowest-energy position, the OSDAs should be included in such calculations. The determination of the most probable orientation of the OSDAs in the larger cavities may be the largest challenge in many instances, because they are often heavily disordered.
- The AIMD simulations on zeolites containing fluoride anions and OSDA cations could form a starting point for computational investigations of the phase selectivity in zeolite synthesis. In a pioneering study, Zicovich-Wilson et al. (2010a) employed DFT calculations to investigate the competition between TON- and ITW-type all-silica zeolites, showing that the better fit of the OSDA

into the pores, together with the structure-directing effect of fluoride towards the formation of *d4r* units, is responsible for the formation of the ITW-type phase, in spite of the higher thermodynamic stability of the TON framework in the absence of OSDA and fluoride (which is related to the higher framework density of TON). While these calculations employed vibrational calculations in the framework of the harmonic approximation to account for the effect of temperature, AIMD simulations can be applied for conditions where the harmonic approximation is no longer valid. Hence, AIMD studies of competing zeolite phases (*i.e.*, different frameworks that form in the presence of the same OSDA, *e.g.*, ITW/TON or CHA/STT) could be used to predict the synthesis outcome and the effect of temperature on the phase selectivity. They could also help to identify key factors driving the phase selectivity. However, in many instances, the different stoichiometries of the competing phases, specifically different OSDA:SiO<sub>2</sub> ratios, complicate the calculation of the relative stability, as additional calculations for auxiliary reference systems are required.

- Finally, an aspect that has been touched upon in the last article is the removal of fluoride from zeolite cages. While the optimisations performed in the context of that work gave insights into the relative stability of different fluoride sites in ITQ-13, they did not elucidate the actual mechanism of fluoride removal. Prior work by Zicovich-Wilson et al. (2010b) has shown that a temporary breaking of Si–O bonds is required to remove fluoride from *d4r* cages, but only the interaction with acid media was considered in that work. During calcination, either thermal motion alone or interactions with reactive fragments formed during OSDA decomposition might be responsible for such a bond breaking, and the role of these factors could be studied using AIMD simulations for relevant temperatures. The role of alkaline media in promoting the selective removal from [4·5<sup>6</sup>] cages could also be addressed.

## CHAPTER 5

# INTERACTION OF (SILICO)ALUMINOPHOSPHATES WITH ADSORBED WATER MOLECULES

### 5.1 Broader context and previous work

#### 5.1.1 Interaction of water with AlPOs and AlPO-based zeotypes

The interaction of water with AlPOs and heteratom-containing AlPO-based zeotypes (SAPOs, MeAPOs) is relevant in various contexts: First of all, these materials are usually synthesised in aqueous media, and the presence of water will play a role during crystallisation. Some AlPO zeotypes like VFI-type  $\text{AlPO}_4\text{-H1}$  and APC-type  $\text{AlPO}_4\text{-H3}$  can even be synthesised in the absence of any organic species, pointing to a structure-directing role of water (D'Yvoire, 1961; Duncan et al., 1990; Kunii et al., 2001). Second, water adsorption is often used as a characterisation method. The seminal paper on AlPO zeotypes by a research team from Union Carbide Corporation, which started off intense research activities in this area, already reported pore volumes determined from  $\text{H}_2\text{O}$  adsorption experiments (Wilson et al., 1982). Third, as already mentioned in the Introduction, adsorption-based heat transformations often use water as working fluid, and AlPOs have been widely studied as adsorbents for this purpose. Even for other applications, such as catalysis or separation, the interaction with water plays an important role, *e.g.*, when using steaming to regenerate SAPO catalysts in methanol-to-olefin processes (Tian et al., 2015). Finally, the hydration stability of different materials varies widely: Whereas some AlPO-based adsorbents were found to be stable over several 10s of adsorption-desorption cycles without appreciable loss of capacity (Ristić et al., 2012; Krajnc et al., 2017), the MEI-type SAPO ECR-40 becomes amorphous upon calcination of the hydrated form (Lee et al., 2015).

In the following, an overview of experimental studies aimed at heat transformation applications of AlPOs will be given, as this use motivated several of the investigations reported in this chapter. Afterwards, previous experimental and computational studies that addressed the interaction between AlPOs and adsorbed water molecules will be summarised, with particular emphasis on investigations looking at the coordination of  $\text{H}_2\text{O}$  molecules to framework Al atoms.

#### 5.1.2 AlPOs and related zeotypes in adsorption-based heat transformations

The basic principle of adsorption-based thermal energy storage is illustrated in **Figure 1.7**. As stated in the Introduction, water has received most attention as working fluid, and studies of water adsorption will be the sole focus here. AlPOs exhibit an intermediate affinity towards water, being less hydrophilic than low-silica zeolites while still possessing considerable adsorption capacity (Ng and Mintova, 2008). In addition to the pore size and pore volume, other factors such as the concentration of defect hydroxyl groups affect the hydrophilicity. As SAPOs and most MeAPOs carry a framework charge, balanced by framework protons or extra-framework cations, a higher affinity towards water in comparison to neutral-framework AlPOs should be expected. This has indeed been observed in some studies, for example, in a direct comparison of AFI-type AlPO-5 and SAPO-5 by Basina et al. (2018). On the other hand, not all investigations showed a clear increase in hydrophilicity in heteroatom-containing systems

(Kornatowski et al., 1999), highlighting that other factors like increased pore blocking may outweigh the potential benefits of heteroatom substitution.

In a very early work evaluating the potential of AlPO-based adsorbents for adsorption refrigeration, Bobonich et al. (2001) studied AlPO-5, AlPO-18 (AEI topology), and SAPO-34 (CHA topology), reporting especially promising results for the latter two systems, with fast adsorption kinetics (complete uptake within 2 hours) and high loading spreads exceeding 200 g(H<sub>2</sub>O) per kg of adsorbent. In this context, it is important to note that the "loading spread" corresponds to the difference between the water uptakes at adsorption and desorption conditions. As different authors have considered different conditions (temperature, relative humidity), depending on the target application, loading spreads are not necessarily comparable across studies, and only some representative values are mentioned here. Whereas the paper by Bobonich et al. (2001), originally published in Russian, apparently received relatively little attention (it accumulated only 9 citations until 2022 according to Google Scholar), subsequent work by Jänchen et al. (2005) that considered the same three adsorbents plus AlPO-17 was apparently much more widely read (>140 citations). The reported heats of water adsorption of the three AlPOs were in the range of 55 kJ mol<sup>-1</sup>, indicating mild hydrophilicity. For SAPO-34, a much higher value of about 90 kJ mol<sup>-1</sup> was obtained for low water coverages (below 50 g(H<sub>2</sub>O) per kg(adsorbent)), which decreased to about 60 kJ mol<sup>-1</sup> at higher loadings. This points to a stronger, specific interaction of the initially adsorbed H<sub>2</sub>O molecules with the framework protons, whereas the subsequently adsorbed molecules interact more weakly. Jänchen et al. (2005) highlighted the beneficial features of AlPO-based adsorbents for heat transformation applications, specifically, their relatively low desorption temperatures, with near-complete desorption achieved at about 100 °C, as well as medium energy densities and temperature lifts (corresponding to the temperature increase upon water adsorption). At about the same time, researchers at Mitsubishi Chemicals investigated AlPO-based materials with AFI and CHA topologies. These results were summarised by Shimooka et al. (2007), who reported essentially perfectly S-shaped water adsorption isotherms for AFI-type adsorbents. Such S-shaped isotherms are favourable for applications because a large change in loading, corresponding to a large heat effect, can be achieved upon a modest change in pressure. Subsequently, Mitsubishi Chemicals commercialised three adsorbents for use in adsorption chillers and desiccant wheels (de Lange et al., 2015): AQSOA-Z01, an AFI-type FeAPO, AQSOA-Z02, a CHA-type SAPO, and AQSOA-5, an AFI-type AlPO.

In more recent academic research, CHA-type materials like SAPO-34 and a triclinic form of AlPO-34 dubbed AlPO-tric were investigated in a number of studies (Bauer et al., 2009; Henninger et al., 2010, 2011a; Ristić et al., 2012; Jänchen and Stach, 2014; Freni et al., 2015; Kohler et al., 2017; Brancato and Frazzica, 2018; Mal et al., 2021). A peculiar feature of SAPO-34 is the dependence of the water adsorption properties on the sample preparation route: When synthesising SAPO-34 using morpholinium as OSDA, the water adsorption capacity deteriorates quickly over repeated water adsorption-desorption cycles, whereas use of other (in some cases unspecified) OSDAs produces samples that exhibit only negligible loss of capacity (Bauer et al., 2009; Henninger et al., 2010, 2011a). This observation appears to be linked to the different distribution of silicon in the framework: While samples synthesised using morpholinium primarily contain isolated Si atoms, samples prepared with tetraethylammonium as OSDA contain a larger amount of "silicon islands", areas in which silicon atoms occupy several adjacent T sites (Vomscheid et al., 1994), avoiding Si–O–P linkages (Flanigen et al., 1988; Sastre et al., 1996). Several studies also addressed AEI-type AlPO-18 and SAPO-18 adsorbents, often together with CHA-type materials (Bauer et al., 2009; van Heyden et al., 2009; Henninger et al., 2010, 2011a; Ristić et al., 2012; Kohler et al., 2017; Brancato and Frazzica, 2018). The CHA and AEI frameworks are rather similar, both having medium-sized cages connected by 8MR windows (**Figure 5.1**). Typical loading spreads are on the order

of 300 g(H<sub>2</sub>O) per kg(adsorbent), and heats of H<sub>2</sub>O adsorption of the AlPO forms are in the range of 55 kJ mol<sup>-1</sup> (Ristić et al., 2012). Krajnc et al. (2017) showed that AlPO<sub>4</sub>-LTA (also labelled AlPO-42, **Figure 5.1**) exhibits an even superior performance, with a loading spread of 370 g(H<sub>2</sub>O) per kg(adsorbent), essentially complete desorption at a low temperature of about 60 °C, and excellent stability over 40 adsorption-desorption cycles, outperforming not only AlPO-34, but also two hydrophilic, water-stable metal-organic frameworks (MOF-801, MIL-160). Two recently prepared AlPOs of the ABC-6 family (frameworks that can be constructed by stacking layers of 6MRs; Baerlocher and McCusker (2022)), AlPO-78 and AlPO-91 (AVE and ANO topologies), were shown to possess promising H<sub>2</sub>O adsorption properties, especially in terms of volumetric storage density (Yuhás et al., 2018, 2021). As a last remark, it should be noted that a use of powdered adsorbents in heat exchangers results in poor heat transfer efficiency. An improved performance can be achieved by coating the adsorbent material onto the lamellae of the heat exchanger, as demonstrated, among other systems, for SAPO-34 on aluminium substrates (Bauer et al., 2009; Freni et al., 2015).

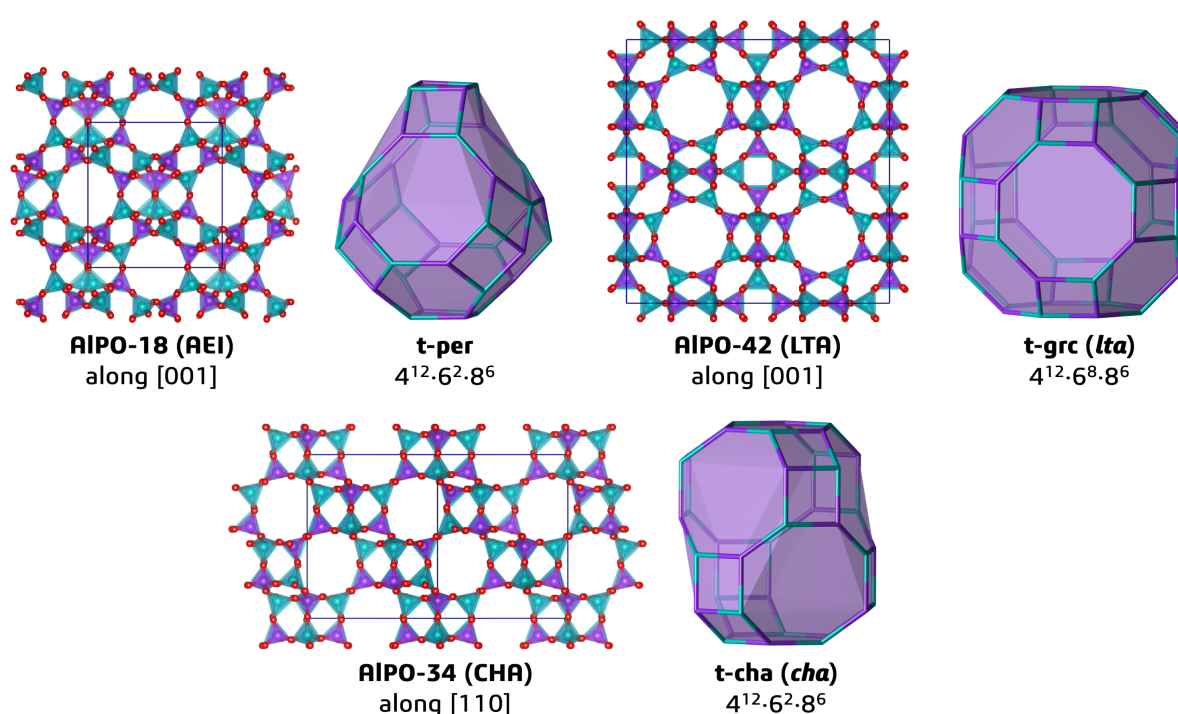


**Figure 5.1:** Crystal structures of AlPO-18, AlPO-42, and AlPO-34 in their guest-free forms. Real samples may, in some instances, exhibit lower symmetry than depicted here, as is the case for the triclinic form of AlPO-34 dubbed AlPO-tric (Ristić et al., 2012). The visualisation of the main cage of each structure is accompanied by the tile designator and face symbol.

### 5.1.3 Experimental investigations of host-guest interactions in hydrated AlPOs and SAPOs

With regard to applications in adsorption-based heat transformations, the macroscopically measurable adsorption behaviour is most relevant. As water adsorption is also used as a basic characterisation method of the pore volume, the literature contains a vast amount of H<sub>2</sub>O adsorption data, either reporting full isotherms or at least saturation uptakes. The review article by Ng and Mintova (2008) already compiled water uptakes for more than 30 AlPOs, SAPOs, and MeAPOs, and a number of additional AlPO-based materials have been characterised since then. However, such measurements give only



very limited insights into the nature of the interactions, because they do not provide any information on the atomic level. More detailed insights can be obtained using crystallographic and spectroscopic methods, as described in the following.

### 5.1.3.1 Diffraction methods

The common lack of sizeable crystals and the frequent disorder of the H<sub>2</sub>O molecules complicate the crystal structure determination of hydrated AlPOs. Prior to works on synthetic aluminophosphates, the crystal structures of variscite and metavariscite, two AlPO<sub>4</sub> · n H<sub>2</sub>O minerals, were fully determined (*i.e.*, including H atom positions) from sc-XRD data (Kniep and Mootz, 1973; Kniep et al., 1977), giving direct evidence for the formation of [Al<sup>[6o]</sup>O<sub>4/2</sub>(H<sub>2</sub>O)<sub>2</sub>] octahedra through coordination of water molecules to Al atoms as well as providing insights into the hydrogen bonding pattern. With regard to synthetic aluminophosphates, several early sc-XRD studies also showed a coordination of water molecules and/or hydroxyl groups to framework Al atoms, *e.g.*, for as-synthesised AIPO-21 (AWO topology) and AIPO-17 (ERI), which contain trigonal-bipyramidal [Al<sup>[5by]</sup>O<sub>4/2</sub>(OH)]<sup>-</sup> units (Bennett et al., 1985; Pluth et al., 1986), and for as-synthesised AIPO<sub>4</sub>-H3, which contains [Al<sup>[6o]</sup>O<sub>4/2</sub>(H<sub>2</sub>O)<sub>2</sub>] octahedra (Pluth and Smith, 1985, 1986). The structure of the latter system, visualised in **Figure 5.2**, contains both Al-coordinated H<sub>2</sub>O molecules and non-coordinated water molecules residing in the channels. Although a network of hydrogen bonds could be inferred from the interatomic distances, the position of the H atoms of the non-coordinated H<sub>2</sub>O molecules could not be determined due to disorder.

With further advances in the analysis of powder data, the refinement of the H<sub>2</sub>O positions from PXRD or powder neutron diffraction data became feasible, at least in favourable cases. An early attempt in this direction was made by Khouzami et al. (1990), who used Rietveld refinement and Fourier difference maps to localise the water molecules in the channels of AEL-type AIPO-11. As discussed in more detail in **Article C5**, the obtained structure appears implausible, with one of the O<sub>water</sub> atoms lying in close proximity of a framework oxygen atom. A more coherent result was obtained by McCusker et al. (1991) with synchrotron powder diffraction, who investigated hydrated VPI-5 (VFI topology), also using Rietveld refinement and Fourier difference maps. The refined structure, visualised in **Figure 5.2**, contains [Al<sup>[6o]</sup>O<sub>4/2</sub>(H<sub>2</sub>O)<sub>2</sub>] octahedra as well as an ordered triple-helix arrangement of water molecules in the 18MR channels. Several more recent studies have looked at AIPOs that are of interest for heat transformation applications, including AIPO-34 (Tuel et al., 2000; Varlec et al., 2016), AIPO-17 (Tuel et al., 2005), and AIPO-18 (Poulet et al., 2005). All of these investigations showed a coordination of water molecules to specific Al sites, as well as revealing the positions of non-coordinated molecules. In fully hydrated AIPO-34, which contains 12 H<sub>2</sub>O molecules per unit cell, 2 of the 6 Al atoms in the unit cell are octahedrally coordinated, and a third one assumes trigonal-bipyramidal coordination (**Figure 5.2**). This system is also interesting as the dehydration does not occur in one step, but two intermediate phases with 11 and 10 H<sub>2</sub>O molecules per unit cell appeared at slightly elevated temperatures in an *in situ* investigation (Varlec et al., 2016). These intermediate phases contain only six-coordinated, but no five-coordinated Al atoms, indicating a higher stability of the former environment. In hydrated AIPO-17, one third of the Al atoms are octahedrally coordinated, with the others remaining in tetrahedral coordination (Tuel et al., 2005). The investigation of AIPO-18 used only a partial Rietveld refinement to determine the positions of framework atoms, and obtained the H<sub>2</sub>O positions from computational modelling that was further informed by NMR experiments (Poulet et al., 2005). In the resulting structure, 6 out of 12 Al atoms in the unit cell are octahedrally coordinated.

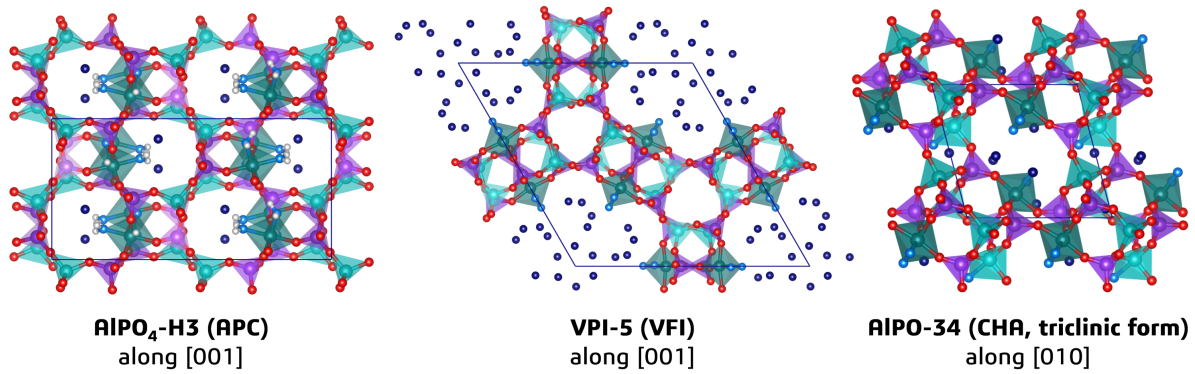


**Figure 5.2:** Crystal structures of AlPO<sub>4</sub>-H3 (Pluth and Smith, 1986), VPI-5 (McCusker et al., 1991), and AlPO-34 (Tuel et al., 2000) in their hydrated forms. Oxygen atoms of Al-coordinated H<sub>2</sub>O molecules are shown in light blue, whereas those of non-coordinated molecules are shown in dark blue. [Al<sup>[60]</sup>O<sub>4/2</sub>(H<sub>2</sub>O)<sub>2</sub>] octahedra and [Al<sup>[5by]</sup>O<sub>4/2</sub>(H<sub>2</sub>O)] trigonal bipyramids are shown in different shades of green than [Al<sup>[4f]</sup>O<sub>4/2</sub>] tetrahedra.

Taking together findings from these and other crystallographic studies of hydrated AlPOs, the following points can be noted:

- In fully hydrated AlPOs, [Al<sup>[60]</sup>O<sub>4/2</sub>(H<sub>2</sub>O)<sub>2</sub>] octahedra appear much more frequently than trigonal-bipyramidal [Al<sup>[5by]</sup>O<sub>4/2</sub>(H<sub>2</sub>O)] units.
- The coordination of water molecules to framework Al typically results in a reduction of symmetry with respect to the guest-free (calcined) AlPO, because Al sites become inequivalent upon hydration.
- Al–O<sub>water</sub> bond distances usually fall in a range of 1.95 to 2.1 Å, being significantly larger than Al–O<sub>framework</sub> distances, where typical values are 1.85 Å for Al<sup>[60]</sup> atoms and 1.75 Å for Al<sup>[4f]</sup> atoms.
- Hydrogen positions cannot be determined from PXRD data, and the uncertainty of the positions of non-coordinated O<sub>water</sub> atoms is usually fairly large. Hence, some caution must be exercised when trying to analyse hydrogen bonding patterns.

Besides studies that aimed to elucidate the structure of hydrated AlPOs at ambient or near-ambient conditions, other investigations have looked at their temperature- or pressure-dependent behaviour, studying, for example, the freezing behaviour of water confined to the 18MR channels of VFI-type AlPO-54 (Alabarse et al., 2012) and the pressure-induced amorphisation of the same material (Alabarse et al., 2014). While one third of the Al atoms are octahedrally coordinated at ambient pressure, the formation of additional [Al<sup>[60]</sup>O<sub>4/2</sub>(H<sub>2</sub>O)<sub>2</sub>] octahedra upon pressure increase destabilises the structure, resulting in a loss of long-range order that is complete at 5 GPa.

Due to the disordered distribution of silicon over the T sites in the large majority of SAPOs (the MEL-type ECR-40, shown in **Figure 5.3** is a noteworthy exception; Afeworki et al. (2004)), diffraction methods cannot fully elucidate all aspects of the local structure. In favourable cases, however, a comparison of the T–O bond distances to those in pure AlPO<sub>4</sub> systems can show whether Si is incorporated only at P sites or also at Al sites. For the case of ATO-type SAPO-31, the observation of somewhat expanded P–O bond lengths, but unaffected Al–O distances confirmed that Si only substitutes for P atoms at isolated sites (Baur et al., 1994).

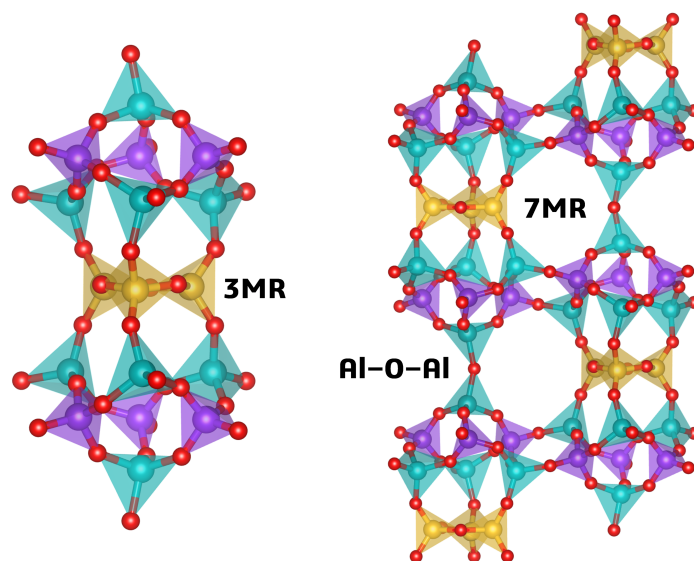


**Figure 5.3:** **Left:** Building unit of 17 T atoms that forms the basis of the ECR-40 structure. The distribution of Al, P, and Si is fully ordered, with Si atoms located in the central 3MR. **Right:** Fragment of the ECR-40 structure showing the connection of the 17 T atom units via Al–O–Al linkages.

With regard to hydrated SAPOs, a seminal study was published by Smith et al. (1996b): These authors investigated hydrated SAPO-34 using neutron diffraction experiments, observing a coexistence of  $\text{H}_3\text{O}^+$  ions and  $\text{H}_2\text{O}$  molecules that were hydrogen-bonded to framework protons. Whereas the protonated species were found inside the 8MRs, the hydrogen-bonded water molecules resided above the 6MRs, indicating a different acidity of protons associated with different rings. It had already been postulated in an earlier IR spectroscopic study that the interaction with adsorbed water molecules causes a removal of the framework protons, resulting in the formation of hydronium ions in the pores (Marchese et al., 1993). However, the extent of this phenomenon and its dependence on the hydration level have remained the matter of considerable debate (Bordiga et al., 2005). A more recent *in situ* diffraction study of SAPO-34 by Wragg et al. (2010) looked at the adsorption-induced deformation: While water adsorption caused a considerable contraction of the framework (volume change of  $-2\%$ ), methanol adsorption resulted in a slight expansion (volume change of  $+0.5\%$ ), indicating a weaker interaction of the latter species, in agreement with earlier thermochemical and IR spectroscopic investigations. A slight contraction of the unit cell also occurred upon steaming at  $700^\circ\text{C}$ , which was attributed to a rearrangement of the Si atoms to form silicon-rich aggregates, probably in extra-framework locations (Arstad et al., 2016). The specific evidence for the presence of these aggregates was gathered from solid-state NMR, rather than diffraction experiments.

As mentioned above, ECR-40 is an unusual SAPOs as it contains Si atoms in well-defined locations, forming the 3MRs of the MEI-type framework (note that odd-membered rings do not normally occur in AlPO zeotypes due to the avoidance of Al–O–Al and P–O–P links). Moreover, it contains Al atoms on neighbouring T sites (**Figure 5.3**). In the as-synthesised form, hydroxyl oxygen atoms of the OSDA molecules are bonded to these Al atoms, resulting in pairs of face-sharing  $[\text{Al}^{[6\text{o}]} \text{O}_6]$  octahedra (Lee et al., 2015). Upon OSDA removal, the Al atoms assume tetrahedral coordination, but remain connected via a common oxygen atom, in violation of Löwenstein’s rule. Hydration leads to a return of these Al atoms to octahedral coordination, indicating a limited stability of these linkages. While crystallinity is retained in the hydrated form, a recalcination of hydrated ECR-40 results in complete amorphisation.

### 5.1.3.2 NMR spectroscopy

Shortly after the first paper reporting AIPO zeotypes by Wilson et al. (1982), Blackwell and Patton (1984) published the first solid-state MAS-NMR study of four of these novel porous materials. They reported  $^{27}\text{Al}$  as well as  $^{31}\text{P}$  chemical shifts for AIPO-5, AIPO-11, AIPO-17, and AIPO-31, both in the as-synthesised and hydrated forms (a dehydrated sample of AIPO-17 was also studied). Whereas  $^{31}\text{P}$  chemical shifts in the range of  $\delta = -19$  ppm to  $-30$  ppm (reference:  $\text{H}_3\text{PO}_4$ ) corroborated the tetrahedral coordination of phosphorus, the observed  $^{27}\text{Al}$  chemical shifts indicated the presence of both tetrahedrally and octahedrally coordinated Al atoms, which give rise to resonances at about  $\delta = 30$  ppm to 45 ppm and at about  $\delta = -15$  ppm, respectively (reference: aqueous  $\text{Al}(\text{NO}_3)_3$ ). Hence, this NMR study already provided clear indications for the coordination of OSDAs (in as-synthesised samples) or water molecules (in hydrated samples) to framework Al atoms, prior to any crystal structure determinations of as-synthesised or hydrated AIPOs. For the case of as-synthesised AIPO-17, an additional resonance at about  $\delta = 15$  ppm was observed, which was later attributed to five-coordinated Al atoms on the basis of their occurrence in the crystal structure (Pluth et al., 1986). The relative intensity of the signals depends on the amount of Al atoms in different coordination environments. For example, the resonance at about  $-18$  ppm in the  $^{27}\text{Al}$ -NMR spectrum of AIPO-5 grows at the expense of the resonance at about 30 ppm when increasing the amount of adsorbed water, consistent with the formation of  $[\text{Al}^{[60]}\text{O}_{4/2}(\text{H}_2\text{O})_2]$  octahedra upon hydration (Meinhold and Tapp, 1990).

Typically, the  $^{27}\text{Al}$ -NMR resonances are fairly broad, complicating a deconvolution into contributions from non-equivalent Al atoms having the same coordination number. However, if the crystal structure is known, a simulation of the spectrum can take the number of inequivalent T sites as starting point, and attempt to model the observed spectrum as a sum of the corresponding number of individual peaks. This was done for the case of calcined and hydrated AIPO-11 by Peeters et al. (1993): Three peaks with intensity ratios of 2:2:1 could model the spectrum of the calcined form, in agreement with the multiplicity of the three Al sites in the crystal structure (8:8:4). The spectrum of the hydrated form could be represented using 4 peaks corresponding to  $\text{Al}^{[4f]}$  atoms and one peak corresponding to  $\text{Al}^{[60]}$  atoms, all of them with equal intensity, indicating a reduction in symmetry with respect to the calcined form as well as coordination of water to 20% of the Al sites. This example shows how an analysis of the  $^{27}\text{Al}$ -NMR spectrum can provide information on the relative amount of Al atoms in different coordination environments. This can be further illustrated for the three systems shown in **Figure 5.2**: For hydrated VPI-5, Grobet et al. (1989) determined an  $\text{Al}^{[60]}:\text{Al}^{[4f]}$  ratio of 1:2 from NMR experiments prior to the crystal structure determination by McCusker et al. (1991). The  $^{27}\text{Al}$ -NMR spectrum of  $\text{AlPO}_4\text{-H3}$  confirmed the 1:1 ratio of  $\text{Al}^{[60]}$  sites to  $\text{Al}^{[4f]}$  sites known from the crystal structure (Knops-Gerrits et al., 2000). In the study of hydrated AIPO-34 by Tuel et al. (2000), the  $^{27}\text{Al}$ -NMR investigation indicated the presence of  $\text{Al}^{[60]}$ ,  $\text{Al}^{[5by]}$ , and  $\text{Al}^{[4f]}$  sites in the ratio of 2:1:3. This information was taken into account to develop a starting model for the Rietveld refinement, the result of which is shown in **Figure 5.2**.

Even in the absence of a crystal structure model of the hydrated form, the use of sophisticated NMR techniques can provide some information about the location of different types of Al coordination polyhedra: Combining two-dimensional  $^{27}\text{Al} \rightarrow ^{31}\text{P}$  correlation NMR spectroscopy and  $^1\text{H} \rightarrow ^{31}\text{P}$  cross-polarisation MAS-NMR spectroscopy, Caldarelli et al. (1999) determined that the  $[\text{Al}^{[60]}\text{O}_{4/2}(\text{H}_2\text{O})_2]$  octahedra in AIPO-41 (AFO topology) are located at the Al1 site, where the curvature of the 10MR channels is maximal. Generally, most NMR investigations point to a formation of six-coordinated (or, less frequently, five-coordinated Al atoms) at well defined sites in the structure, rather than randomly, indicating that non-equivalent Al sites in the structure have a different propensity to expand their co-

ordination number beyond four. It is also worth noting that different AIPO frameworks show a rather large variation in the amount of octahedrally coordinated Al sites, from 20% in AIPO-11 and AIPO-41 to 50% in AIPO<sub>4</sub>-H3 and AIPO-18.

In the more recent NMR literature on hydrated AIPOs, there has been a certain shift from the fundamental characterisation of the local structure towards *in situ* studies aimed at an understanding of the hydration or dehydration behaviour, motivated by potential applications in thermal energy storage. In addition to the combined XRD and NMR investigation of AIPO-34 by Varlec et al. (2016), already summarised in the previous subsection, Krajnc et al. (2017) employed *in situ* <sup>27</sup>Al-NMR experiments to study the hydration behaviour of AIPO<sub>4</sub>-LTA. While the hydration occurred over a period of several hours, the peaks corresponding to Al<sup>[6o]</sup> and Al<sup>[4f]</sup> increased simultaneously, maintaining a constant intensity ratio of 1:2. This was interpreted as evidence for a one-step hydration mechanism, in which unit cell after unit cell is filled completely at once, rather than layer-by-layer (the relative amounts of different types of Al atoms should vary over time in such a hypothetical multistep process). This recent example clearly shows the value of *in situ* NMR methods in application-related investigations of hydrated AIPOs. In addition to providing information on the local environment of the T sites, NMR techniques can also give information about the dynamics of adsorbed water molecules. For example, Goldfarb et al. (1992) used an analysis of the <sup>2</sup>H-NMR lineshapes across a range of temperatures to deduce the dynamic behaviour of D<sub>2</sub>O molecules adsorbed in AIPO-5 and VPI-5. They were able to distinguish two types of D<sub>2</sub>O molecules, framework-bound species exhibiting only local, rotational motions about an essentially fixed axis and "free" molecules undergoing fast and isotropic reorientations. In a similar vein, Yang et al. (2005) used a combination of <sup>27</sup>Al-NMR spectroscopy and incoherent inelastic neutron scattering (IINS) to study hydrated AIPO-14 (AFN topology). Distinct, sharp librational bands in the IINS spectra indicated the presence of two different types of water molecules, more tightly bound species bonded to framework Al atoms and more loosely bound species occupying the channels, interacting with each other through hydrogen bonds.

Since diffraction methods cannot elucidate the local structure of SAPOs, solid-state NMR spectroscopic methods have been established as a valuable tool to distinguish different local environments. More specifically, the localisation of Si at non-equivalent T sites gives rise to different <sup>29</sup>Si chemical shifts. In their study of SAPO-17, Zibrowius and Lohse (1992) observed two separate <sup>29</sup>Si-NMR resonances at  $\delta = -93.1$  ppm and  $-97.4$  ppm in the spectrum of the calcined material, which were assigned to Si at the T1 and T2 sites of the crystal structure. While the multiplicity ratio of the sites is 2:1, the intensity ratio of the resonances was 1.4:1, indicating a certain preference for Si at the T2 site.

Generally, the signals of isolated Si atoms that substitute for phosphorus (*i.e.*, Si(OAl)<sub>4</sub> atoms) mostly fall in a range from  $\delta = -90$  ppm to  $-95$  ppm (Blackwell and Patton, 1988). The chemical shift progressively moves to more negative values upon increasing number of Si atoms on the neighbouring T sites, and resonances at about  $\delta = -110$  ppm are indicative for Si(OSi)<sub>4</sub> environments that occur in Si-rich regions in the framework (silicon islands) or in unreacted silica (Man et al., 1991). Based on this assignment, Vomscheid et al. (1994) investigated the silicon environments across a series of SAPO-34 samples synthesised with different amounts of Si and different OSDAs. In samples synthesised with morpholinium as OSDA, Si(OSi)<sub>4</sub> environments were found only for relatively high Si contents. In contrast, samples synthesised with tetraethylammonium hydroxide (TEAOH) contained Si-rich regions (silicon islands and domains with Si–Al–Si environments) even at low Si contents (Si/(Si+Al+P) ratio of about 0.1). This difference also impacts the hydration stability, with samples containing a larger amount of silicon islands being more stable towards hydration (Briend et al., 1995). Using *in situ* <sup>1</sup>H- and <sup>27</sup>Al-MAS-NMR

spectroscopy, Buchholz et al. (2003) investigated SAPO-34 and SAPO-37 (FAU topology) at different levels of hydration. They could show that the hydration consists of two steps, the first being an adsorption of water molecules at framework protons associated with Si–O–Al linkages, and the second being a coordination of water to framework Al atoms, as discussed above in detail for AlPOs. At variance with earlier interpretations, they concluded that the hydrolysis of SAPO-37 is primarily caused by a breaking of Al–O–P, rather than Si–O–Al linkages.

Although the initial distribution of silicon in the framework is governed by the synthesis parameters, it can be modified through a post-synthetic treatment. Buchholz et al. (2002) showed that a heat treatment of different SAPOs (SAPO-11, -18, -31, and -34) causes a concurrent dehydroxylation and desilication of the framework. The Si atoms migrate to vacant T sites in the framework, resulting in an increase of the number of Si(OAl)<sub>n</sub> ( $n < 4$ ) sites, whereas the vacancies appearing through desilication are "healed" through a concurrent migration of phosphorus atoms. In other words, the treatment leads to the formation of silicon islands or other Si-enriched areas, despite no apparent changes in the crystallinity as observed with XRD methods. More recent work combining multinuclear MAS-NMR spectroscopy with a portfolio of other characterisation methods showed that steaming at temperatures between 873 and 1023 K also triggers a redistribution of silicon to form Si islands, resulting in a reduction of the number of catalytically active Brønsted acid sites while retaining the porosity (Minova et al., 2021).

Different types of such Brønsted acid sites in SAPOs can be distinguished using <sup>1</sup>H-NMR experiments, sometimes in conjunction with probe molecule adsorption and vibrational spectroscopy. Resonances at  $\delta = 3.8$  ppm and 4.8 ppm, which are observed in different SAPOs, were assigned to protons pointing into larger pores and to protons associated with 6MRs, which interact with other framework oxygen atoms (Zibrowius et al., 1992; Buchholz et al., 2002). In some systems, such as SAPO-5, different types of Brønsted acid sites are found, even though there is only one type of T site, indicating that the framework protons are located at different oxygen atoms (Zibrowius et al., 1992). In the unusual SAPO ECR-40, the two resonances at  $\delta = 3.3$  ppm and 4.3 ppm were attributed to protons associated with Si–O–Al and Al–O–Al links, respectively (Afeworki et al., 2004).

### 5.1.3.3 Vibrational spectroscopy

IR and Raman spectroscopy experiments have been employed to study different aspects of the structure and bonding in AlPOs, SAPOs, and related compounds, often in conjunction with NMR spectroscopy and/or diffraction. Broadly, the following vibrations may be of interest:

- Bands in the frequency range up to about 1,500 cm<sup>-1</sup> primarily correspond to framework vibrations (such as Al–O and P–O stretching modes or tetrahedral bending modes). Librational modes of water molecules in hydrated systems fall between 600 and 900 cm<sup>-1</sup> (Frost et al., 2004).
- For the free water molecule, the H<sub>water</sub>–O<sub>water</sub>–H<sub>water</sub> bending vibration gives rise to a band at 1,595 cm<sup>-1</sup>, and symmetric and asymmetric O<sub>water</sub>–H<sub>water</sub> stretching modes are observed at 3,657 and 3,756 cm<sup>-1</sup>, respectively (Johnson, 2022). Because the formation of hydrogen bonds in the adsorbed state results in a red-shift of the O–H stretching frequencies, vibrational spectroscopy can provide information on the bonding of adsorbed water molecules.
- In SAPOs, O<sub>framework</sub>–H<sub>framework</sub> stretching vibrations are typically observed at about 3,600 cm<sup>-1</sup>, whereas higher- and lower-frequency modes have been attributed to isolated and hydrogen-bonded silanol groups, respectively (Bordiga et al., 2005). Because the interaction of the Brønsted acid sites with probe molecules such as water, carbon monoxide, or methanol affects the vibra-

tions of framework protons and probe molecules, *in situ* spectroscopy can be used for a detailed characterisation of the acid sites (Bordiga et al., 2005; Martins et al., 2007).

- In as-synthesised zeotypes, vibrational spectroscopy can be used to characterise the host-guest interactions between the framework and the occluded OSDA molecules, as well as guest-guest interactions between neighbouring OSDA species (Marchese et al., 1999).

It has been shown that the position and intensity of the framework modes can be used as "fingerprint" to distinguish different hydrated phosphate minerals like variscite, metavariscite, and strengite ( $\text{FePO}_4 \cdot 2\text{H}_2\text{O}$ ; Frost et al. (2004)). Relatively little emphasis appears to have been placed on these modes in spectroscopic investigations of synthetic aluminophosphate zeotypes, although they have sometimes been used to follow the crystallisation, especially during the initial stages where the samples are X-ray amorphous (Tan et al., 2002; Ahn et al., 2017).

A detailed Raman spectroscopy study focusing on the  $\text{O}_{\text{water}}\text{-H}_{\text{water}}$  stretching vibrations has been carried out for hydrated aluminophosphates by Knops-Gerrits et al. (2000). Whereas series of relatively sharp bands were observed for metavariscite and  $\text{AlPO}_4\text{-H3}$ , the Raman spectra of VPI-5 and  $\text{AlPO}_8$  (AET topology) showed only broad maxima. This observation is consistent with the relatively ordered pattern of the hydrogen bonds in the former two systems that is evident from the crystal structures, as opposed to a disordered arrangement of the water molecules in the large pores of VPI-5 and  $\text{AlPO}_8$ .

As the framework protons in SAPOs are responsible for their catalytic activity, a large number of IR spectroscopic investigations have looked at the  $\text{O}_{\text{framework}}\text{-H}_{\text{framework}}$  stretching vibrations. A common finding of many of these studies was the observation of two separate bands being about  $30\text{ cm}^{-1}$  apart (Zibrowius et al., 1992; Marchese et al., 1993; Chen et al., 1994). The higher-frequency band, typically at about  $3630\text{ cm}^{-1}$ , was attributed to unperturbed framework protons, whereas the lower-frequency band was assigned to protons participating in weak hydrogen bonds to other framework oxygen atoms, typically across 6MRs, thus mirroring the results from  $^1\text{H-NMR}$  spectroscopy mentioned above. For the specific case of SAPO-34, neutron diffraction experiments confirmed the coexistence of two proton locations, one of which is associated with 6MRs, corroborating this interpretation of the vibrational spectrum (Smith et al., 1996a). In more recent work on SAPO-34 samples having  $\text{Si}/(\text{Si}+\text{Al}+\text{P})$  ratios above 0.1, a third band at  $3615\text{ cm}^{-1}$  was observed (Martins et al., 2007). *In situ* experiments using CO as probe molecule indicated that the protons that give rise to this band have a higher acidity than the other framework protons, resembling protons in aluminosilicate zeolites. It was hence concluded that these framework protons are associated with silicon islands or aluminosilicate domains.

In an early study, Marchese et al. (1993) interpreted the changes in the IR spectrum upon exposition of a dehydrated SAPO-34 sample to ambient air in a way that the adsorption of  $\text{H}_2\text{O}$  molecules leads to a stoichiometric formation of hydronium ions, in other words, a complete deprotonation of the framework. The subsequent, combined neutron diffraction and IR spectroscopic study of the same material by Smith et al. (1996b) indicated that hydronium ions form only in the vicinity of the framework protons associated with 8MRs, whereas the protons pointing across 6MRs form hydrogen bonds to water molecules. However, more recent studies that considered different levels of hydration concluded that a framework deprotonation due to the formation of  $\text{H}_3\text{O}^+$  ions occurs only to a very minor extent (Bordiga et al., 2005). The key piece of evidence was the presence of an ABC triplet of bands that is characteristic for  $\text{H}_2\text{O}$  molecules that are hydrogen-bonded to framework protons. As this band remained prominent at all levels of hydration studied, it was concluded that hydronium ions form only

to a minor extent. In contrast, hydronium ion formation was found to be much more significant in the structurally analogous CHA-type aluminosilicate SSZ-13, which was attributed to its higher acidity.

#### 5.1.4 Computational studies

##### 5.1.4.1 Force field calculations

Early applications of FF-based methods in the field of AlPOs, which used the Born model of ionic solids, mainly concerned the optimisation of crystal structures and the calculation of their relative stability (de Vos Burchart et al., 1992a; Henson et al., 1996). In addition to establishing that the inverse correlation between framework density and relative stability holds not only for all-silica zeolites, but also for AlPOs, the calculations also predicted more stable structures having lower symmetry than observed experimentally for several AlPO frameworks. Examples include AlPO-5, for which structures in space groups  $P6$  and  $P3c$  were proposed (experimental symmetry:  $P6cc$ ; Bennett et al. (1983)), AlPO-8, where the calculations pointed to  $P2_1$  or  $Pmn2_1$  symmetry (experiment:  $Cmc2_1$ ; Poojary and Clearfield (1993)), and AlPO-11, for which both de Vos Burchart et al. (1992a) and Henson et al. (1996) obtained lower-energy structures in space group  $P2$  (experimental symmetry:  $Ima2$ ; Richardson et al. (1988)). For all three AlPOs, subsequent diffraction investigations revealed pronounced diffuse scattering that is indicative of local, instantaneous deviations from the average symmetry at room temperature (AlPO-5: Liu et al. (2003); AlPO-8: Withers and Liu (2005); AlPO-11: Liu and Withers (2003)). As a consequence, cooling might result in transitions to ordered lower-symmetry structures or to locally disordered phases. The latter situation was observed in a recent low-temperature investigation of AlPO-5 (Cortie et al., 2017). Altogether, the good correspondence between FF-based calculations and subsequent experimental studies demonstrates the capabilities of the computations, which are especially impressive when considering the simplifications made when using a Born model to represent interatomic interactions. In more recent work, Praprotnik et al. (2008) developed a molecular mechanics FF to model the structure and dynamics of a CHA-type fluoroaluminophosphate in its as-synthesised form. The structure parameters, isotropic displacement parameters, and the IR spectrum computed with this force field agreed well with experimental data. Even though water molecules were included in the simulations, the FF-based MD simulations with these parameters would not be able to model a coordination of  $H_2O$  to framework Al atoms, as this would require a reactive FF that allows the formation of new bonds. Despite this evident shortcoming of any conventional (non-reactive) FF in the description of hydrated AlPOs, FF-based calculations have been used with considerable success to model the adsorption of water in these materials. Pillai and Jasra (2010) carried out MC simulations at fixed water loadings to predict the most likely water locations in AlPO-5 and AlPO-11. Aiming at more application-related predictions, Henninger et al. (2011b) used GCMC simulations to compute water adsorption isobars in AlPO-18, resulting in semi-quantitative agreement with experimental measurements. These authors employed the simple point charge (SPC) model for water (Berendsen et al., 1987) together with the augmented CVFF parameter set (Hill et al., 2000) to represent the framework atoms. In a very recent "screening" study of a large number of synthesiseable and hypothetical AlPOs, Shi et al. (2022) also employed an MC-based approach to model water adsorption, using the SPC water model, but framework parameters developed by Ghysels et al. (2015). Validation simulations accurately reproduced the experimental  $H_2O$  saturation uptake of AlPO-18 and AlPO-78, as well as giving reasonable agreement with full adsorption isotherms. The same set of framework parameters was used in a combined experimental-simulation study of water adsorption in SAPO-34 (Fasano et al., 2019). These authors slightly adjusted the charges on framework oxygen atoms in order to improve the agreement with ex-



perimental adsorption isotherms. They also performed MD simulations to investigate the temperature dependence of the self-diffusivity. Similar MD investigations have been reported for some AIPOs, addressing, for example, the influence of the water content on the diffusivity in the channels of AIPO-5 (Demontis et al., 2012). Looking beyond water adsorption, FF-based simulations have been frequently used to study the adsorption or diffusion of other guest molecules in AIPOs. Examples include GCMC investigations of CO<sub>2</sub>/N<sub>2</sub>, CO<sub>2</sub>/CH<sub>4</sub>, and CH<sub>4</sub>/N<sub>2</sub> mixture adsorption in about 50 different AIPOs by the author of this thesis (Fischer, 2017, 2018), a GCMC study of the separation of xylene isomers in AIPO-11 (Lucena et al., 2008), and an MD study of iodine diffusion in AIPO-11 (Hu et al., 2010).

Compared to AIPOs, SAPOs have been less frequently studied using FF-based simulations, presumably because some assumptions on the positions of Si atoms and charge-balancing species must be made. The ability to predict preferred local environments by means of FF-based energy minimisations was exploited by Sastre et al. (1996), who used a Born model to compute the total energies of different Si substitution patterns in SAPO-5. They found that substitutions resulting in the formation of Si–O–P linkages are unfavourable, in accordance with experiment. As a consequence, the smallest stable silicon island consists of 5 Si atoms (1 replacing Al, 4 replacing P), and the second smallest of 8 Si atoms (2 replacing Al, 6 replacing P). The same energetic trends as for SAPO-5 were found in subsequent work for SAPO-34 (Sastre et al., 1997). These works also investigated the most likely proton positions in the vicinity of the silicon islands. A fairly comprehensive investigation of the preferred proton locations in the vicinity of a 5-atom silicon island in SAPO-34 was carried out by Zokaie et al. (2012a), who validated their FF-based calculations against DFT calculations for selected models. The most stable configuration obtained in that work, which was used in **Article C1**, is shown in **Figure 5.4**. The same group of authors also compared the total energies of SAPO-34 models having different distributions of isolated Si atoms, with Si–Si distances varying from about 4.5 to above 16 Å (Zokaie et al., 2012b). They observed a tendency towards the formation of next-nearest neighbour pairs, *i.e.*, a separation of two Si sites by a single Al atom. It is, however, worth noting that these calculations did not include any OSDA, which can be expected to affect the distribution of the silicon atoms in the framework during SAPO synthesis.

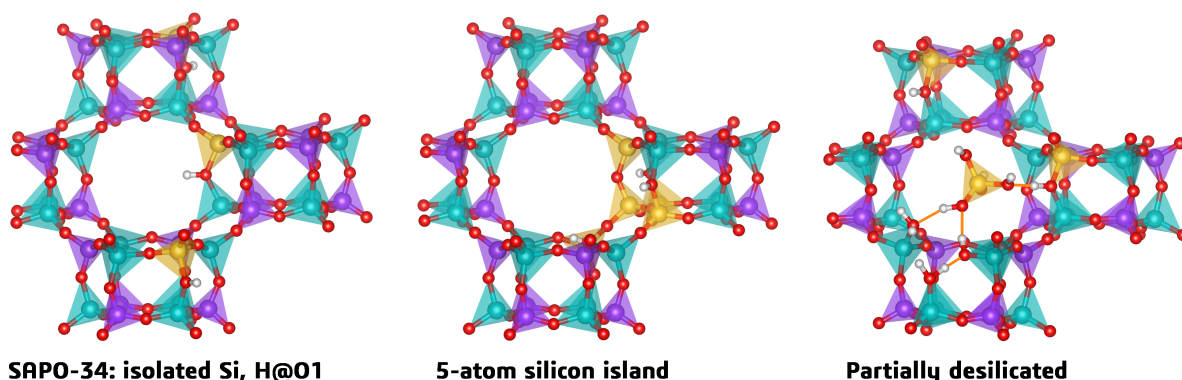


**Figure 5.4:** **Left:** Fragment of an ordered model of SAPO-34 with isolated Si atoms. The framework protons are bonded to the O1 atoms, corresponding to one of the two experimentally observed positions (Smith et al., 1996b). **Centre:** Fragment of a SAPO-34 model containing a 5-atom silicon island. Model based on the work of Zokaie et al. (2012a). **Right:** Fragment of a partially desilicated SAPO-34 model containing a silicic acid molecule in the pore. Model based on the work of Fjermestad et al. (2013).

#### 5.1.4.2 DFT calculations

In an early application of electronic structure calculations to AlPO zeotypes, Prasad et al. (1992) employed semiempirical calculations to predict the most favourable water adsorption sites in AlPO-11, predicting a coordination to the Al3 sites. More recently, different authors used DFT-based approaches to study the structure and bonding of water molecules in the pores of AlPO frameworks. For example, Poulet et al. (2002, 2005) supplemented their XRD and NMR investigations of AlPO-34 and AlPO-18 with static and dynamic DFT calculations. In the first of these works, they observed that DFT structure optimisations of fully hydrated AlPO-34 converged to different local minima with different positions of the water molecules. A more realistic picture was obtained in DFT-based AIMD simulations, which can account for the thermal motion of the H<sub>2</sub>O molecules at room temperature. Therefore, a combination of AIMD simulations and diffraction was suggested to obtain an accurate picture of the local structure of hydrated AlPOs. For the fully hydrated phase with 12 H<sub>2</sub>O molecules per unit cell, Poulet et al. (2002) obtained an interaction energy of  $-53 \text{ kJ mol}^{-1}$  per molecule, in excellent correspondence with more recently measured adsorption enthalpies (Ristić et al., 2012). For a model containing only 6 Al-coordinated H<sub>2</sub>O molecules per unit cell, a much less negative interaction energy of  $-30 \text{ kJ mol}^{-1}$  per H<sub>2</sub>O was computed, indicating that such a "half-hydrated" phase does not correspond to a thermodynamically stable scenario. In recent studies of the same system, DFT optimisations also showed that the fully hydrated phase was the most stable form. As these calculations refer to 0 K, the experimental observation of partially hydrated AlPO-34 forms at elevated temperatures does not disagree with this finding (Varlec et al., 2016; Krajnc et al., 2017). For AlPO-18, the use of AIMD simulations was crucial to obtain a realistic structure model of the hydrated form, although it was noted by the authors that some discrepancies between calculated and experimental XRD pattern remained (Poulet et al., 2005). Later work by Ashbrook et al. (2008) and Sneddon et al. (2014) on different as-synthesised and calcined AlPOs showed the usefulness of DFT-D optimisations to arrive at structure models that deliver agreement with experimental NMR chemical shifts and XRD data at the same time.

While the investigations mentioned in the preceding paragraph used the DFT calculations primarily to complement experimental work, other authors have focussed on the understanding of the bonding and dynamics of adsorbed water molecules. Notably, an early AIMD study by Fois et al. (2002) addressed the triple-helix of water molecules in the channels of VPI-5. Their simulations showed that the water molecules forming the helix undergo significant oscillations at room temperature, with hydrogen bonds between them breaking and re-forming at the picosecond timescale. As a consequence, the helical arrangement that is apparent in the average structure is not necessarily recognisable in the instantaneous configurations. They emphasised the importance of the Al-coordinated water molecules at the pore walls as a driving factor for the formation of the helical chains in the channels. Al-coordinated and non-coordinated water molecules were found to differ significantly in terms of their isotropic displacement parameters and their contribution to the IR spectrum, a difference that was attributed to the higher mobility of the latter species. No diffusion of the non-coordinated H<sub>2</sub>O molecule was observed on the timescale of the simulations. A different approach to studying Al-coordinated water molecules in AlPOs was taken by Herrera-Perez et al. (2007): These authors carried out DFT optimisations for partially hydrated models of AlPO-11 with water molecules coordinated to non-equivalent Al atoms. Assuming a formation of Al<sup>[6o]</sup> atoms upon hydration, they predicted the Al1 site as the most stable water adsorption site. In addition to noting the difference to the earlier semiempirical study of Prasad et al. (1992) mentioned above, it is worth pointing out that these authors did not take the experimentally observed symmetry lowering of AlPO-11 upon hydration into account (Khouzami et al., 1990). Another

DFT study of hydrated AIPO-5 and AIPO-11 did not consider the coordination of water molecules to framework Al atoms, despite ample experimental evidence (Pillai and Jasra, 2010).

With regard to SAPOs, it has already been mentioned that the FF-based calculations in the work of Zokaie et al. (2012a) and Zokaie et al. (2012b) on silicon islands and Si distribution in SAPO-34 were validated against DFT calculations for a subset of models. In subsequent work, the same group studied the formation of silicon islands in this system, arriving a complete DFT free energy profile for this complex process (Fjermestad et al., 2015a). As early as 1998, DFT calculations were used to assess the Brønsted acidity of different possible proton positions, again focussing on SAPO-34, which is particularly amenable to DFT calculations due to the small size of the (primitive) unit cell (Jeanvoine et al., 1998a). More recently, Suzuki et al. (2011) used DFT calculations in conjunction with temperature-programmed desorption of ammonia (analysed *in situ* using IR and mass spectroscopy) to distinguish Brønsted acid sites associated with isolated Si atoms and with Si islands in SAPO-34. A comparison across a set of topologically distinct aluminosilicates and their SAPO analogues was reported by Katada et al. (2011). In comparison to the rather large number of DFT studies of preferred Al sites in aluminosilicate zeolites (Ghorbanpour et al., 2014; Jones and Iglesia, 2015; Knott et al., 2018), analogous works on SAPOs are comparatively rare. A few relatively recent works have looked at the energetically preferred locations of the Si atoms and associated protons in SAPO-11 (Sierraalta et al., 2018; Grenev et al., 2021), and in four different SAPOs (SAPO-5, -11, -34, -41; Sierraalta et al. (2020)). The impact of the Si/proton locations on the acidity and on the interaction with guest molecules was also investigated in these studies. The interaction of SAPOs with water had already been the topic of early applications of DFT-based AIMD simulations (Termath et al., 1998; Jeanvoine et al., 1998b). In these works, which contributed to the ongoing discussion on the occurrence of framework deprotonation of SAPO-34 upon hydration, it was observed that the interaction with a single H<sub>2</sub>O molecule is not sufficient to remove the proton, but that a cluster of two or three H<sub>2</sub>O molecules will be protonated when interacting with the framework. A more recent AIMD study investigated the adsorption of water and methanol in SAPO-34 in order to elucidate the degree of proton mobility and adsorption-induced deformations (De Wispelaere et al., 2015). Here, it was found that at least six H<sub>2</sub>O molecules per acid site are required for a significant degree of framework deprotonation. The detailed analysis of the AIMD trajectories showed that framework deprotonation is a highly dynamical process, with fast transitions between protonated and deprotonated states of the framework. Subsequently, AIMD simulations were combined with *in situ* microspectroscopy to investigate the influence of water on methanol-to-olefin transformation reactions in SAPO-34 (De Wispelaere et al., 2016).

In the past decade, the stability of SAPOs in the presence of steam has received particular attention in DFT-based investigations, as the steaming treatment used in catalyst regeneration may result in irreversible structural changes that can affect the catalyst performance. Specifically, Fjermestad et al. (2013) and Fjermestad et al. (2015b) investigated the desilication pathway of SAPO-34, and compared it to the dealumination of SSZ-13, employing DFT-based predictions of the reaction path using the nudged elastic band method. The coordination of water molecules to an Al atom neighbouring the Si site was found to lower the activation energy towards desilication, highlighting that interactions between H<sub>2</sub>O molecules and framework Al atoms play a crucial role in determining the hydrothermal stability of SAPOs. Moreover, these authors also reported an atomistic model of partially desilicated SAPO-34 containing a silicic acid (Si(OH)<sub>4</sub>) molecule in the pores, which was used in the context of **Article C1** (**Figure 5.4**). Similar investigations on aluminosilicate zeolites showed that a coordination of water to framework Al atoms also happens during the initial stages of zeolite dealumination (Silaghi et al.,

2016; Stanciakova et al., 2019). Kalantzopoulos et al. (2020) employed DFT calculations in a combined experimental-computational study of SAPO-37, which is much more susceptible to hydrolysis than SAPO-34 (Buchholz et al., 2003). They observed a high affinity towards water in the smaller cavities of the FAU-type structure (*d6r* and *sod* cages). The accumulation of water molecules in these cavities enhances the mechanical strain, which, together with the formation of hydronium ions upon interaction with the Brønsted acid sites, promotes the destruction of the framework.

## 5.2 Key questions addressed in this chapter

The articles compiled in this chapter addressed a variety of questions pertaining, in one way or another, to the affinity of AlPOs and SAPOs towards water, and to the local structure of hydrated AlPOs/SAPOs. Although the thematic links between the individual articles are not as strong as in the other two chapters, it is still useful to summarise the key questions that motivated the individual investigations:

1. Because a complete experimental elucidation of the local structure of SAPOs is challenging, the impact of local heterogeneities on the affinity towards water is difficult to assess. To study this aspect using a DFT-based approach, SAPO-34 models with isolated Si atoms were compared to a model with a 5-atom silicon island in **Article C1**, looking at the interaction strength at low and high water loadings. In order to investigate the role of defects, defect-containing models of SAPO-34 were included in the same article, and AlPO-34 was used as a reference system without any local heterogeneities.
2. Even though water uptakes at saturation conditions have been reported for many AlPO-based zeotypes, more detailed experimental investigations comparing the adsorption properties of materials with different topologies remain limited to a few systems. Moreover, structural defects can play a particularly important role in the early stages of adsorption, rendering it difficult to draw conclusions regarding the impact of framework topology on the affinity towards water on the basis of experimental data alone. In **Article C2**, six AlPOs with different topologies and different pore sizes were studied, using a DFT-based approach that is essentially analogous to that used in the preceding article. In addition, SAPO models of these six frameworks were also included, comparing different possible positions of silicon for those frameworks that have more than one distinct T site, and always assuming substitution at isolated sites. Both **Article C1** and **C2** also assess changes in the local structure upon adsorption, especially the coordination of water molecules to framework Al atoms (AlPOs and SAPOs) and hydration-induced framework deprotonation (SAPOs only).
3. On the basis of experimental investigations and prior computational studies of AlPO-34 and AlPO-18, it was concluded that the main hydration of these AlPOs occurs in a single step, without any intermediate partially hydrated forms that contain only Al-coordinated H<sub>2</sub>O molecules. Given the narrow channels of AlPO<sub>4</sub>-H3 and the fact that 2/3 of the water molecules in the structure are coordinated to Al atoms (**Figure 5.2**), it could be a good candidate for a structure where a partially hydrated form might be stable. This AlPO is at the centre of the study reported in **Article C3**, in which DFT adsorption enthalpies were compared for fully and partially hydrated forms. Moreover, a detailed analysis of the DFT-calculated vibrational spectra was used to identify "fingerprint" modes stemming from H<sub>2</sub>O molecules in different environments, and the dynamic behaviour of adsorbed molecules was studied with AIMD simulations.

4. The computational studies of the potential stability of "non-Löwenstein" Al–O–Al linkages by Fletcher et al. (2017) and the subsequent work by Heard et al. (2019), which looked at the role of water, exclusively investigated computer-generated models of aluminosilicate zeolites, without considering the fact that the SAPO ECR-40 is a synthesiseable zeotype that contains such linkages. **Article C4** addresses the stability of the Al–O–Al linkages in this system in the presence of water molecules, employing AIMD simulations for guest-free, partially hydrated, and fully hydrated models. Besides, the acidity and mobility of protons associated with Al–O–Al and Si–O–Al linkages were also evaluated.
5. Due to the implausibility of some bond lengths and angles in the published crystal structure of AlPO-11 (Richardson et al., 1988) and the experimental evidence for dynamic, local deviations from the average structure (Liu and Withers, 2003), this system appeared as a particular suitable subject for a case study that employs AIMD simulations to investigate the local, instantaneous structure. The computational investigation of this zeotype reported in **Article C5** has a somewhat different emphasis than the other articles included in this chapter, as it primarily deals with the calcined form. However, partially hydrated AlPO-11 models in which the  $[\text{Al}^{(60)}\text{O}_{4/2}(\text{H}_2\text{O})_2]$  octahedra are located at different T sites were also considered in the context of this study, attempting to improve understanding of the factors that determine which Al atoms assume octahedral coordination upon hydration.

### 5.3 **Article C1:** *Water Adsorption in SAPO-34: Elucidating the Role of Local Heterogeneities and Defects using Dispersion-Corrected DFT Calculations*

#### 5.3.1 *Outline*

As outlined above, SAPO-34 is the silicoaluminophosphate zeotype that has been most widely investigated for adsorption-based heat transformation applications. In this context, some authors pointed out the dependence of the cycling stability on the choice of OSDA during SAPO-34 synthesis, which was attributed to differences in the silicon distribution (Bauer et al., 2009; Henninger et al., 2010, 2011a). Moreover, the propensity of SAPO-34 towards desilication in the presence of water at higher temperatures had also been established experimentally (Buchholz et al., 2002). The investigation reported in this article aimed to assess to what extent variations in the local structure and structural defects influence the affinity towards water. For this purpose, DFT calculations on periodic SAPO-34 models were performed with the CASTEP code (Clark et al., 2005), employing the PBE-TS functional (Perdew et al., 1996; Tkatchenko and Scheffler, 2009). Several defect-free SAPO-34 models were constructed, which contained isolated Si atoms, a 5-atom silicon island, or an aluminosilicate domain (central Al atom surrounded by four Si atoms). In addition, two defect-containing models were included. In the partially desilicated model, only one of the three Si atoms in the unit cell was removed from the framework, and retained in the pore in the form of a silicic acid molecule (**Figure 5.4**). In the fully desilicated model, all Si atoms were removed, creating "hydroxyl nests" in which three hydroxyl groups and one H<sub>2</sub>O molecule complete the coordination environment of the surrounding Al atoms (Fjermestad et al., 2013). The DFT calculations were carried out for both low and high water contents, corresponding to 1 and 30 H<sub>2</sub>O molecules per unit cell, respectively. Whereas only adsorption of the water molecule at accessible protons was considered for the low-loading case, the calculations for high loadings in each SAPO-34 model included five different snapshots from fixed-loading GCMC simulations to improve the statistics. AlPO-34 was also included for the high-loading scenario as a both silicon-free and defect-

free reference system. In addition to computing and comparing interaction energies, the bonding of the water molecules to the framework, and – at high loadings – to each other was also analysed on the basis of the DFT-optimised structures.

### 5.3.2 Summary of results

An optimisation of guest-free SAPO-34 models with isolated Si atoms and framework protons bonded to different oxygen atoms delivered the H@O1 case, shown in **Figure 5.4**, as the most favourable scenario. The H@O3 case, where the proton forms a hydrogen bond across the 6MR, was predicted to be second-lowest in energy. An estimation of the  $O_{\text{framework}}-H_{\text{framework}}$  stretching frequencies on the basis of the DFT-optimised bond distances for these two proton positions resulted in two distinct bands separated by approximately  $30\text{ cm}^{-1}$ , in agreement with experiment (Zibrowius et al., 1992; Marchese et al., 1993; Chen et al., 1994). On the other hand, analogous estimations for the SAPO-34\_Si\_island and SAPO-34\_SiAl\_domain models did not provide an explanation for the additional band at  $3615\text{ cm}^{-1}$  that had been attributed to silicon islands or aluminosilicate domains by Martins et al. (2007). With regard to the interaction with water at low loadings, the position of the protons in SAPO-34 with isolated Si atoms had only a minimal influence on the interaction energy, with all values falling between  $-90$  and  $-93\text{ kJ mol}^{-1}$  per  $\text{H}_2\text{O}$  molecule (in the following, DFT interaction energies are always given per water molecule). In the view of the number of approximations made, these results agree very well with the experimentally measured heat of adsorption at low coverages of about  $85\text{ kJ mol}^{-1}$  (Jänchen and Stach, 2014). For the SAPO-34\_Si\_island and SAPO-34\_SiAl\_domain models, a certain increase of the affinity towards water was observed, although a rather strong dependence on the local environment of the framework proton at which the  $\text{H}_2\text{O}$  molecule is adsorbed was apparent for the aluminosilicate domain model (**Figure 5.5**). These differences became insignificant at high water loadings, where the average interaction energies amounted to about  $-70\text{ kJ mol}^{-1}$  for all defect-free SAPO-34 models, again agreeing rather well with experimental heats of adsorption ( $62$  to  $65\text{ kJ mol}^{-1}$ ).

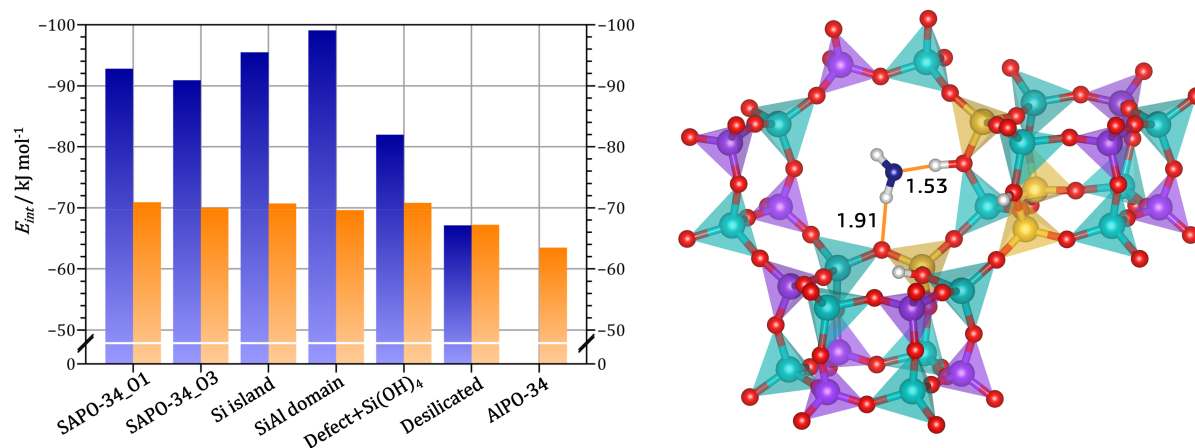


**Figure 5.5:** **Left:** DFT interaction energies computed for low water loadings (blue columns) and high water loadings (orange columns) for SAPO-34 models and AlPO-34. In models containing local heterogeneities or defects, an adsorption at different protons was considered for the low-loading case. Only the most negative value is shown. **Right:** Lowest-energy configuration of a single  $\text{H}_2\text{O}$  molecule adsorbed at a framework proton in SAPO-34\_SiAl\_domain. Hydrogen bond distances are given in Å. Figure modified after **Article C1**.

The DFT calculations for low water loadings delivered a distinctly weaker interaction for defect-containing as compared to defect-free models, regardless of the environment of the proton at which water is adsorbed. This weakening of the interaction was more pronounced in the fully desilicated model in comparison to the partially desilicated model. In contrast, the impact at high water loadings was barely statistically significant, with a modest reduction by about 3 to 4 kJ mol<sup>-1</sup> in the fully desilicated model. An analysis of the DFT-optimised structures showed a partial deprotonation of the framework at high water loadings for the defect-free SAPO-34 models. No deprotonation occurred at low water loadings, and hydroxyl groups in defect-containing models also remained unaffected. A coordination of water molecules to framework Al atoms was observed in models with isolated Si atoms, but not in those with a silicon island or an aluminosilicate domain (C1, Figure 7). Although this finding had to be interpreted with caution due to the limited number of snapshots considered in the calculation, it might reflect the higher hydration stability of SAPO-34 samples containing silicon islands or aluminosilicate domains, in agreement with experiment (Briend et al., 1995).

#### 5.4 **Article C2:** *Interaction of Water with (Silico)Aluminophosphate Zeotypes: A Comparative Investigation Using Dispersion-Corrected DFT*

##### 5.4.1 *Outline*

Whereas the study reported in **Article C1** looked exclusively at CHA-type structures, concentrating on the role of local heterogeneities and defects, this investigation addressed the influence of framework topology on the affinity of AlPOs and SAPOs towards water. For this purpose, six different frameworks were studied, all of which have been reported in AlPO and/or SAPO form: On the one hand, the CHA (AlPO/SAPO-34), ERI (AlPO/SAPO-17), and AFX (SAPO-56) topologies were considered. These three frameworks belong to the ABC-6 family, possessing elongated cages whose vertical dimension increases in the order CHA → ERI → AFX (C2 Figure 1). On the other hand, three frameworks having more or less isometric cages of different size were included: GIS (AlPO-GIS/SAPO-43), AEI (AlPO/SAPO-18), and RHO (SAPO-RHO). Of these frameworks, CHA, GIS, and RHO have only one type of T site, so only different proton positions were considered in initial optimisations of the guest-free SAPO models. For the other frameworks, two (ERI/AFX) or three (AEI) Si positions as well as all relevant proton sites were compared. Calculations for water-loaded models considered different Si positions, but only the energetically most favourable proton location for each framework model.

The computational approach to compute the interaction strength with water was largely analogous to that of **Article C1**, using DFT optimisations for models containing low and high amounts of water. Low amounts of one H<sub>2</sub>O molecule per cell were considered only for the SAPO models, where an initial adsorption at the framework protons can be expected. In contrast, no such preferential adsorption sites are evident for AlPOs. For high water loadings, the amount of H<sub>2</sub>O molecules per unit cell corresponding to near-saturation conditions was determined from preliminary GCMC simulations. Five distinct snapshots from fixed-loading MC simulations were then DFT-optimised for each AlPO and each SAPO, and the results were analysed both in terms of interaction energies and equilibrium structures.

##### 5.4.2 *Summary of results*

For the AlPOs, the saturation uptakes determined from the preliminary MC simulations amounted to between 29 and 58 H<sub>2</sub>O per unit cell, corresponding to between 290 to 370 g(H<sub>2</sub>O) per kg(adsorbent). The computed interaction energies were very similar for all six frameworks, falling in a range from

–64 to –66 kJ mol<sup>-1</sup> (**Table 5.1**). Experimental observations also indicate that heats of H<sub>2</sub>O adsorption of different AIPOs tend to be similar, in the range of 55 kJ mol<sup>-1</sup> (Ristić et al., 2012). The systematic difference was explained with the neglect of vibrational contributions in the DFT calculations. For SAPOs, a large variation in the interaction energy from about –75 to –100 kJ mol<sup>-1</sup> was observed for low water loadings (**Table 5.1**). An analysis of the optimised structures showed that the interaction is particularly strong when the H<sub>2</sub>O molecule is adsorbed near the centre of an 8MR (**C2**, Figure 3). This variation is lost at high water loadings, where the interaction energies obtained for all SAPO models fall in a range from –69 to –73 kJ mol<sup>-1</sup>, without any evident correlation to the size of the cages. Altogether, the results indicate that there is limited scope for a "tuning" of the affinity towards water through using AIPO or SAPO adsorbents with different topologies. As a consequence, the reachable energy density will be largely determined by the amount of water that can be adsorbed. For SAPOs, a slight effect of the number of Si atoms and charge-balancing protons was observed, which appears plausible as a more highly charged framework should afford a stronger interaction with adsorbed water molecules.

**Table 5.1:** DFT interaction energies obtained for water interacting with AIPOs (high loadings only) and SAPOs (low and high loadings). SAPO labels include the Si positions (where relevant) and the oxygen sites to which the framework protons are bonded. It is also indicated whether the protons points into a 6MR or into an 8MR.

AIPOs	Near saturation	SAPOs	1 H <sub>2</sub> O per cell	Near saturation
	$E_{int} / \text{kJ mol}^{-1}$		$E_{int} / \text{kJ mol}^{-1}$	$E_{int} / \text{kJ mol}^{-1}$
AIPO-34	–65.3	SAPO-34_O1 (8MR)	–93.4	–72.6
AIPO-17	–64.0	SAPO-17_Si1_O3 (6MR)	–74.2	–69.7
		SAPO-17_Si2_O5 (6MR)	–78.1	–72.0
AIPO-AFX	–66.0	SAPO-56_Si1_O5 (6MR)	–88.7	–69.9
		SAPO-56_Si2_O4 (8MR)	–97.1	–69.2
AIPO-GIS	–65.2	SAPO-43_O12 (8MR)	–101.5	–71.1
AIPO-18	–66.0	SAPO-18_Si1_O12 (8MR)	–97.5	–73.0
		SAPO-18_Si2_O11 (8MR)	–98.5	–72.5
		SAPO-18_Si3_O31 (6MR)	–89.2	–73.3
AIPO-RHO	–64.8	SAPO-RHO_Si11 (8MR)	–89.4	–70.7

When looking at the structural changes upon interaction with large amounts of water, significant differences were observed between those AIPO/SAPOs containing *d6r* units (CHA, ERI, AFX, AEI) and the remaining frameworks. In the *d6r*-containing frameworks, the unit cells contracted only slightly, and five-coordinated Al atoms were found relatively rarely in the DFT-optimised structures. In contrast, significant structural distortions, together with a more frequent formation of Al<sup>[5by]</sup> or even Al<sup>[6o]</sup> atoms, occurred in GIS and RHO (**C2**, Figure 2). These observations were taken as an indicator for a reduced hydration stability of these frameworks, although it was pointed out that further investigations would be required to substantiate this hypothesis. Whereas framework deprotonation of SAPOs did not occur upon interaction with a single H<sub>2</sub>O molecule, the formation of H<sub>3</sub>O<sup>+</sup> ions in the pores was frequently observed at near-saturation conditions.



## 5.5 **Article C3: First-Principles Study of $\text{AlPO}_4\text{-H3}$ , a Hydrated Aluminophosphate Zeotype Containing Two Different Types of Adsorbed Water Molecules**

### 5.5.1 Outline

Unlike the previous article, this study concentrated on a single aluminophosphate, namely the APC-type  $\text{AlPO}_4\text{-H3}$ . This AlPO constitutes a particularly suitable model system due to the availability of a nearly complete crystal structure of the hydrated form, where only the hydrogen atoms of the non-coordinated water molecules could not be localised (**Figure 5.2**; Pluth and Smith (1986)). In addition, thermogravimetric experiments showed that the dehydration occurs in a single step (Lagno and Demopoulos, 2005), and an experimental Raman spectrum in the  $\text{O}_{\text{water}}\text{-H}_{\text{water}}$  stretching frequency range had been reported (Knops-Gerrits et al., 2000), providing further possibilities to validate the computational predictions beyond a comparison to structure data.

While considering only a single AlPO, this investigation had a broader focus in terms of calculated quantities: In addition to analysing the interaction energy and equilibrium structures of both fully hydrated  $\text{AlPO}_4\text{-H3}$  and partially hydrated forms, phonon calculations were carried out to predict the vibrational spectra, with the aim of identifying "fingerprint" modes that are indicative for water molecules in different bonding situations. The isotropic displacement parameters were also obtained from these calculations, and compared to values computed from DFT-based AIMD simulations. These AIMD simulations were also used to compare the dynamic behaviour of Al-coordinated and non-coordinated  $\text{H}_2\text{O}$  molecules. Whereas the structure optimisations and calculations of the vibrational properties employed the CASTEP code (Clark et al., 2005), again using the PBE-TS functional (Perdew et al., 1996; Tkatchenko and Scheffler, 2009), the AIMD simulations used the CP2K code (Kühne et al., 2020) and the PBE-D3 functional (Perdew et al., 1996; Grimme et al., 2010).

### 5.5.2 Summary of results

In the first place, the DFT-optimised structural parameters of  $\text{AlPO}_4\text{-H3}$  and  $\text{AlPO}_4\text{-C}$ , its dehydrated form, were compared to experimental data (Pluth and Smith, 1986; Keller et al., 1990). Altogether, reasonable agreement was found for unit cell parameters and intra-framework bond distances, with only a slight tendency to overestimate the T-O bond distances that is in accordance with the results of benchmarking studies summarised in **Chapter 3**. Larger differences were observed for the  $\text{O}_{\text{framework}}\cdots\text{H}_2\text{O}$  and  $\text{H}_2\text{O}\cdots\text{H}_2\text{O}$  hydrogen bond distances in  $\text{AlPO}_4\text{-H3}$ , especially for the non-coordinated water molecules. The DFT-computed Raman spectrum in the frequency range from  $2900\text{ cm}^{-1}$  to  $3700\text{ cm}^{-1}$  showed excellent qualitative agreement with the experimental spectrum reported by Knops-Gerrits et al. (2000). However, scaling by a factor of about 1.04 was required to achieve quantitative agreement in the peak positions. Use of a scaling factor of this magnitude is not uncommon for PBE-based calculations (Alecú et al., 2010). An analysis of the atomic displacement patterns associated with the individual modes confirmed an inverse correlation between hydrogen bond length and stretching frequency: For H atoms participating in short, strong hydrogen bonds, the  $\text{O}_{\text{water}}\text{-H}_{\text{water}}$  bond is significantly elongated, resulting in a red-shift of the frequency (**Figure 5.6**). While the vibrational spectra can thus deliver information on the hydrogen bonding environment of the water molecules, they do not permit a distinction between Al-coordinated and non-coordinated  $\text{H}_2\text{O}$  molecules, because both groups can participate in short or long hydrogen bonds.

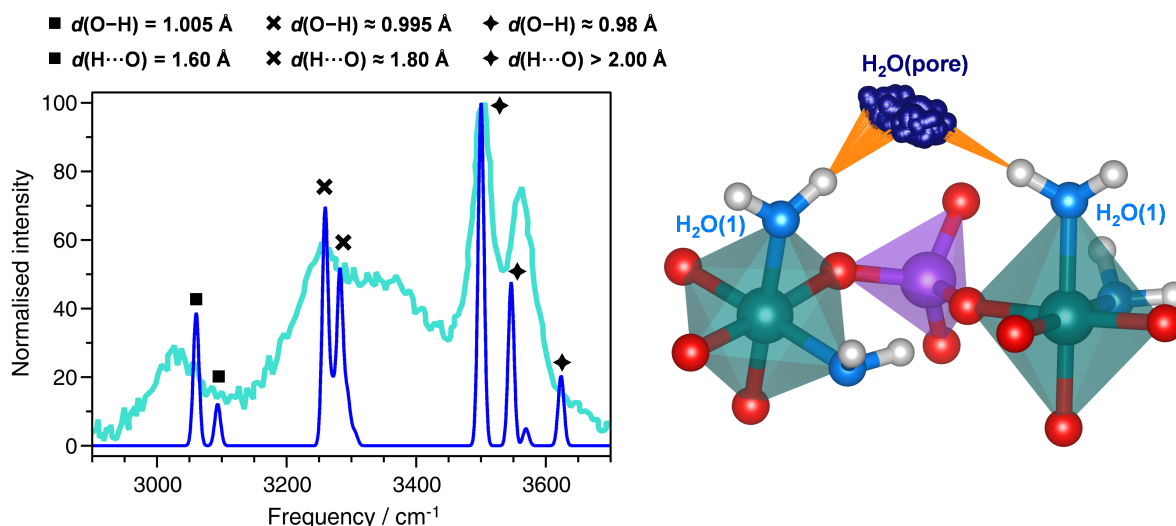


**Figure 5.6:** Left: Dark blue line: DFT-calculated, scaled Raman spectrum of  $\text{AlPO}_4\text{-H3}$ . Turquoise line: Experimental spectrum reported by Knops-Gerrits et al. (2000). Symbols are used to distinguish peaks stemming from water molecules in different hydrogen bonding situations. Right: Typical trajectory of the oxygen atom of a non-coordinated ("pore") water molecule in  $\text{AlPO}_4\text{-H3}$  obtained from AIMD simulations. Orange lines indicate  $\text{H}\cdots\text{O}$  distances from the Al-coordinated  $\text{H}_2\text{O}$  molecules below 1.65 Å. Figure modified after Article C3.

Since optimisations followed by vibrational calculations were carried out for fully hydrated  $\text{AlPO}_4\text{-H3}$  and for different partially hydrated models, adsorption enthalpies for  $T = 298\text{ K}$  could be derived in addition to interaction energies. The adsorption enthalpy for  $\text{AlPO}_4\text{-H3}$  amounted to  $-67\text{ kJ mol}^{-1}$ . The corresponding values after removal of different types of water molecules were always less negative, indicating that there are no stable partially hydrated phases (C3, Table 3). In particular, a phase containing Al-coordinated water molecules is less stable than the fully hydrated phase, highlighting the stabilising role of hydrogen bonds to non-coordinated water molecules. These results can be correlated with experimental observations made by Lagno and Demopoulos (2005): First, the instability of partially hydrated phases agrees with the observation of a single dehydration step in the thermogravimetry curve. Second, the relatively strong interaction predicted in the DFT calculations agrees with the comparatively high dehydration temperature, which exceeds  $100\text{ }^\circ\text{C}$ .

An analysis of the vibrational spectra in the frequency range of framework vibrations (up to  $1,200\text{ cm}^{-1}$ ) was carried out in order to identify potential "fingerprint" modes that are primarily due to deformations of the  $[\text{Al}^{[6\text{o}]} \text{O}_{4/2}(\text{H}_2\text{O})_2]$  octahedra (C3, Figure 6). Isotropic displacement parameters were obtained via two different computational routes, both from phonon calculations and from AIMD simulations for 298 K. While the AIMD simulations gave better quantitative agreement with experimental  $U_{iso}$  values for the framework atoms, both approaches delivered satisfactory results. An analysis of the displacements of the water molecules showed only modest oscillations about the equilibrium position for the Al-coordinated  $\text{H}_2\text{O}$  molecules. In contrast, much larger displacements were observed for the non-coordinated  $\text{H}_2\text{O}$  molecules, for which significant motions between the two nearest Al-coordinated molecules occurred (Figure 5.6). The large mobility of these molecules was identified as the reason for the deviation between the experimentally observed position, which corresponds to the time-averaged location at room temperature, and the DFT-optimised equilibrium position.

## 5.6 **Article C4:** Proton Acidity and Proton Mobility in ECR-40, a Silicoaluminophosphate that Violates Löwenstein's Rule

### 5.6.1 Outline

As visualised in **Figure 5.3**, the MEI-type SAPO ECR-40 is an unusual zeotype for two reasons: First, it has a fully ordered distribution of the Si atoms. Second, it contains Al–O–Al linkages, violating Löwenstein's Rule (Loewenstein, 1954). Although the proton positions could not be determined from diffraction experiments,  $^1\text{H-NMR}$  experiments showed two resonances that were approximately one ppm apart, which were assigned to protons at Si–O–Al and Al–O–Al linkages (Afeworki et al., 2004). It was assumed that the protons associated with the Al–O–Al linkages would exhibit a higher acidity, resulting in enhanced catalytic activity. In contrast, a recent AIMD study of aluminosilicates with such linkages pointed to a reduced acidity of protons at non-Löwenstein linkages (Heard et al., 2019). Other interesting features of ECR-40 are the octahedral coordination of the Al atoms participating in the Al–O–Al linkages in the fully hydrated form, and its instability towards recalcination (Lee et al., 2015). In the view of these prior experimental findings, and the lack of any computational investigation of ECR-40, it appeared warranted to study this zeotype using a combination of DFT calculations (which used the CASTEP code and the PBE-TS functional, as in the previous articles) and DFT-based AIMD simulations (which, like **Article C3** and the studies presented in **Chapter 4**, employed the CP2K code and the PBE-D3 functional). To start with, two ECR-40 models with different proton distributions were compared in terms of total energies and agreement with experimental unit cell parameters and  $^1\text{H-NMR}$  chemical shifts. The acidity of protons associated with different linkages was then evaluated through a calculation of deprotonation energies, which were compared to interaction energies computed for different probe molecules (CO, H<sub>2</sub>O, NH<sub>3</sub>). Finally, the mobility of the framework protons in the presence of small and large amounts of water was studied with AIMD simulations, which were also used to investigate changes in the local environment upon hydration.

### 5.6.2 Summary of results

The comparison of proton distributions considered two models: In the ECR-40(2H[O6],2H[O10]) structure, 2 protons per unit cell are associated with Al–O–Al linkages (oxygen atom labelled O6 in the crystal structure, **Figure 5.7**), and another 2 protons are located at Si–O–Al linkages (O10). Correspondingly, the ECR-40(4H[O10]) model contains only protons associated with Si–O–Al linkages. According to the DFT structure optimisations, the former of these models is favoured by about 32 kJ mol<sup>-1</sup>. Moreover, its unit cell parameter *c* is in better agreement with the experimental value than that of the second model (the values of *a* are essentially identical). Calculations of the  $^1\text{H-NMR}$  chemical shifts delivered two distinct resonances that differed by 1.0 ppm for the first model, in perfect agreement with experiment. In contrast, only one resonance was predicted for the second model, where all protons have the same environment. It was concluded that the Al–O–Al linkages in ECR-40 are fully protonated, and the ECR-40(2H[O6],2H[O10]) model was used in all further calculations.

Calculations of the deprotonation energy of the protons at Al–O–Al and Si–O–Al linkages delivered a higher deprotonation energy for the former group of protons, indicating a lower acidity (**Figure 5.7**). Whereas the trends in CO adsorption enthalpies and red-shifts of the C–O stretching frequency corroborated this finding, the opposite trends were found for H<sub>2</sub>O and NH<sub>3</sub> adsorption enthalpies, confirming the previous notion that these probe molecules are not suited to measure acidity in zeolites because different interactions, not just the interaction with the acid site, determine the overall adsorp-

tion enthalpy (Boronat and Corma, 2019). The AIMD simulations showed that the framework protons oscillate only about their equilibrium position in guest-free ECR-40, and that the adsorption of 1 H<sub>2</sub>O molecule per acid site is not sufficient for the formation of stable H<sub>3</sub>O<sup>+</sup> species in the pores (C4, Figure 6). At near-saturation conditions (38 H<sub>2</sub>O per unit cell), the Si–O–Al linkages were found to be fully deprotonated, whereas only a partial deprotonation of the Al–O–Al linkages occurred, with about three quarters of the protons at these linkages remaining attached to the framework, at least on the timescale of the AIMD simulations (Figure 5.7). It was also observed that a coordination of water molecules to Al atoms participating in the Al–O–Al linkages occurred, resulting in a trigonal-bipyramidal and, in one instance, even octahedral coordination of these atoms, typically with one or several water molecule(s) in a bridging position between the two Al atoms (C4, Figure 9). These profound structural changes were interpreted as first steps towards an irreversible transformation towards a structure containing face-sharing [Al<sup>[6o]</sup>O<sub>3/2</sub>(H<sub>2</sub>O)<sub>3</sub>] octahedra, which are present in the crystal structure of the hydrated form (Lee et al., 2015). As the water molecules of these octahedra are stabilised through hydrogen bonds to non-coordinated water molecules, it appears plausible to anticipate that the Al–O–Al linkages cannot be restored upon dehydration, resulting in amorphisation.

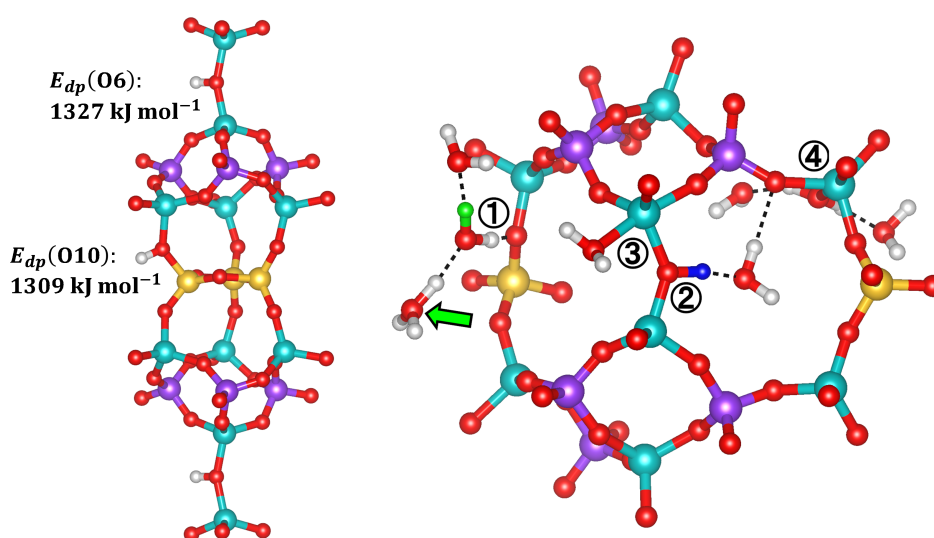


**Figure 5.7:** **Left:** Visualisation of the distinct proton positions in ECR-40. The DFT deprotonation energies are included as insets. **Right:** Schematic representation of various phenomena observed in AIMD simulations of fully hydrated ECR-40: (1) Deprotonation of Si–O–Al linkage, formation of H<sub>3</sub>O<sup>+</sup> ion in the vicinity. (2) No deprotonation of Al–O–Al linkage. (3) and (4) Formation of five-coordinated Al atoms upon water adsorption at Al–O–Al and Si–O–Al linkages. Figure modified after **Article C4**.

## 5.7 **Article C5:** Revisiting the Structure of Calcined and Hydrated AlPO-11 with DFT-Based Molecular Dynamics Simulations

### 5.7.1 Outline

Like the two preceding articles, this investigation was also aimed at one particular zeotype, AEL-type AlPO-11. In the calcined form of this AlPO, the presence of unrealistically short Al–O and P–O bond lengths and near-linear Al–O–P angles as well as the observation of diffuse scattering indicate local, instantaneous deviations from the reported *Ima2* symmetry (Richardson et al., 1988; Liu and Withers, 2003). To study the local structure of guest-free AlPO-11 on the timescale of picoseconds, AIMD simu-

lations in the  $NpT$  ensemble were carried out, again using the CP2K code and the PBE-D3 functional. These calculations considered three different temperatures ( $T = 100, 300, 500$  K) and ambient pressure. With regard to the hydrated form, a structure refinement of the isostructural SAPO-11 reported rather implausible positions of the water molecules (Khouzami et al., 1990), with no Al-coordinated  $H_2O$  molecules, disagreeing with subsequently reported NMR results that indicated a formation of octahedrally coordinated Al atoms at 20% of the available sites (Peeters et al., 1993). A prior DFT study of hydrated AlPO-11 did not take the experimentally observed amount of  $Al^{[6o]}$  atoms into account (Herrera-Perez et al., 2007). Taking the symmetry reduction to space group  $Pna2_1$  observed by Khouzami et al. (1990) as starting point, models of partially hydrated AlPO-11 with water molecules coordinated to different non-equivalent Al atoms were optimised using DFT. In the following, AIMD simulations for a temperature of 300 K were carried out to confirm the stability of Al-coordinated water molecules.

### 5.7.2 Summary of results

An initial optimisation of the structure of calcined AlPO-11 resulted in a massive overestimation of the unit cell dimensions with respect to experimental values. As the PBE-D3 functional had been found to give a rather accurate prediction of the unit cell parameters in previous work (especially **Article A4**), it was concluded that this deviation was caused by an adjustment of the T–O bond lengths to realistic values, while at the same time retaining some near-linear Al–O–P linkages. This systematic error disappeared when computing the unit cell parameters as average values over the AIMD trajectories, where excellent agreement with experiment was observed for the 300 K results (**C5**, Figure 3). A symmetry search on the AIMD average structures computed from the 100 K trajectories delivered two monoclinic structures (space groups  $Pn11$  and  $P112$ ), indicating a likely transition to a lower-symmetry phase upon cooling to cryogenic temperatures. A closer analysis of the structures showed a rotation of some tetrahedra belonging to the *afi* cages (face symbol  $6^5$ ) with respect to the *Ima2* phase that resulted in a disappearance of the near-linear angles. The  $Pn11$  and  $P112$  structures were found to differ only in the relative arrangement of neighbouring columns of stacked pairs of *afi* cages (**C5**, Figure 6), and their total energies were very close. As a consequence, it could not be inferred whether either of these phases corresponds to the "true" low-temperature phase of AlPO-11, or whether a phase with a disordered arrangement of these columns might be more likely.

Symmetry searches on the average structures computed from 300 and 500 K trajectories delivered evidence for instantaneous deviations from *Ima2* symmetry, which were more pronounced at 300 K. However, there were no indications for the stability of a lower-symmetry phase over extended periods of time. A comparison of the T–O bond distances and Al–O–P angles in the AIMD average structures to the radial and angle distribution functions computed over the whole trajectories using the TRAVIS code (Brehm et al., 2020) revealed systematic deviations (**C5**, Figure 2 and 7), showing that the instantaneous structure of AlPO-11 at these temperatures differs distinctly from the time-averaged structure. Through a close inspection of the trajectories of individual oxygen atoms, it was established that these atoms undergo precession-like motions (**Figure 5.8**). As a consequence, their average positions on the picosecond timescale lie closer to the respective Al–P connection lines than typical instantaneous positions, resulting in shortened "apparent" bond lengths and larger Al–O–P angles in the average structures. On the basis of these observations, it was concluded that the occurrence of unrealistically short bond distances and near-linear angles in the experimental crystal structure of calcined AlPO-11 is due to the peculiar dynamic behaviour of some oxygen atoms. Because these movements are frozen in at 100 K, a reduction in symmetry occurs upon cooling.

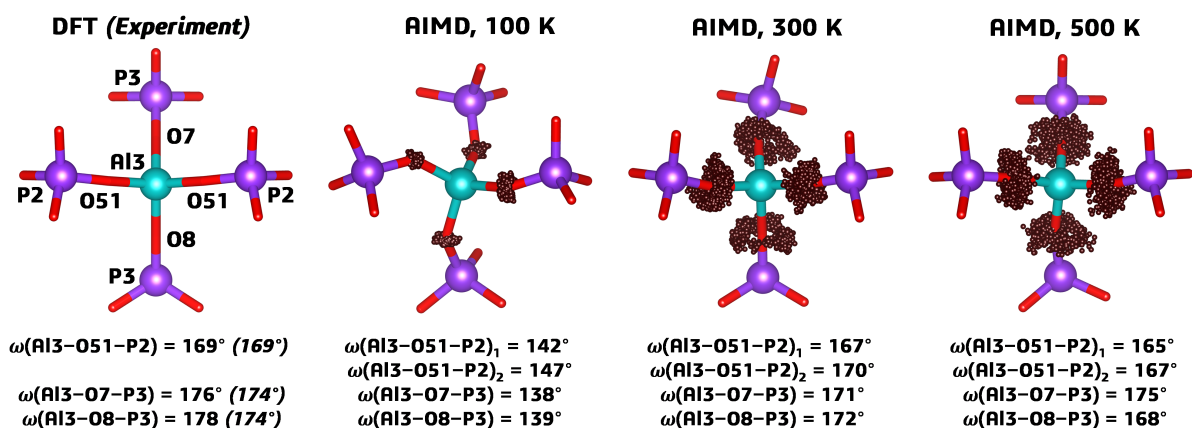


**Figure 5.8:** Environment of one Al3 atom in the DFT-optimised structure of AlPO-11 (left panel) and in selected AIMD average structures (other panels), with Al–O–P angles given below the structure figures. Al–O–P angles from the experimental structure are given below the left panel (*italicised*). For the AIMD average structures, the trajectories of the oxygen atoms over the course of 15 ps are shown as small, dark red spheres. Figure modified after **Article C5**.

For the study of hydrated AlPO-11, three models having  $Pna2_1$  symmetry were considered, in which the water molecules were coordinated to 50% of the Al1 or Al2 atoms (labelled Al11/Al21 in the  $Pna2_1$  phase) or to all Al3 atoms (**C5**, Figure 9). The formation of  $[\text{Al}^{[6\text{o}]} \text{O}_{4/2}(\text{H}_2\text{O})_2]$  octahedra at the Al11 sites emerged as the energetically most favourable scenario. Moreover, the DFT-optimised unit cell parameters of this model also agreed most closely with the experimental values reported by Khouzami et al. (1990). AIMD simulations confirmed the stability of Al-coordinated water molecules at these sites. Unlike for the calcined form of AlPO-11, there were no indications for systematic differences between the time-averaged and instantaneous structures of hydrated AlPO-11 at 300 K, presumably because the formation of octahedrally coordinated Al atoms and of hydrogen bonds between water molecules and framework oxygen atoms suppress the precession-like motion of oxygen atoms.

## 5.8 Conclusions

The articles included in this chapter dealt with a variety of questions related to the adsorption of water in AlPOs and SAPOs. Whereas the first two articles compared different frameworks, the remaining three looked at particular features of individual systems. The DFT results reported in **Article C1** and **Article C2** showed that the interaction energy at high water loadings, *i.e.*, at near-saturation conditions, is only slightly affected by the framework topology or – for SAPOs – by different silicon distributions. This puts limitations on the possibility to "tune" the attainable energy density, which is important for thermal energy storage applications, through a judicious choice of topology, or via preparation of SAPOs having a particular Si distribution (*e.g.*, favouring silicon islands). As the energy density also depends on the total water uptake capacity, which is determined by the accessible pore volume, the accessible porosity of the AlPO/SAPO emerges as a more important factor than the topology in this regard. However, it has to be emphasised that the calculations for near-saturation conditions did not provide any information on the pressure/temperature range in which the water adsorption isotherm/isobar would show the strongest rise, thereby defining the optimal operation conditions. For AlPOs, a dependence on pore size can be expected, with pore filling happening at lower relative pressures/lower temperatures for systems with smaller pores. Although it can be expected that this effect can be studied on a qualitative

level with GCMC simulations employing generic force fields, a quantitative treatment would require the development of FF parameters that can capture the formation of Al–O<sub>water</sub> bonds (or costly DFT-based MC simulations). For SAPOs, the onset pressure/temperature of water adsorption will largely depend on the strength of the interaction between adsorbed water molecules and framework protons, which act as initial adsorption sites. Here, the calculations showed that the interaction energy varies considerably, depending on the environment of the framework proton and on the presence of local heterogeneities or defects. Theoretically, the affinity of a SAPO towards water and, hence, the region of the steepest rise of the adsorption isotherm/isobar could therefore be tuned through targeted introduction of particular environments. It has to be conceded, however, that such manipulations, straightforwardly introduced in computational modelling, are often difficult to achieve in actual SAPO syntheses.

The investigation of AlPO<sub>4</sub>-H3 in **Article C3** corroborated that partially hydrated AlPOs are not thermodynamically stable intermediate phases, and that the water adsorption and desorption will therefore occur by filling/emptying the pores in one step. In particular, the calculations showed that Al-coordinated H<sub>2</sub>O molecules are significantly stabilised through hydrogen bonds to non-coordinated molecules in the pores/channels. Although these calculations considered only one AlPO framework, the findings tie in well with earlier computational investigations and experimental findings, and it appears therefore highly unlikely that a partially hydrated phase containing only Al-coordinated water molecules could be stabilised for any porous AlPO zeotype. The calculations for fully hydrated AlPO and SAPO models carried out in various articles of this chapter showed that the coordination of water molecules to framework Al atoms is a practically ubiquitous phenomenon. It is clear that the use of DFT optimisations, which ignore the role of temperature and can only converge to the nearest local minimum, could not give quantitative insights into the extent of the formation of Al<sup>[6o]</sup> or Al<sup>[5by]</sup> atoms in actual hydrated phases at room temperature, although it was speculated in **Article C2** that the observation of pronounced structural changes in DFT-optimised fully hydrated models could indicate a reduced hydration stability. While IR and Raman spectroscopy can be useful to distinguish different types of framework protons, and to analyse the hydrogen bonding environment of adsorbed water molecules, it remains unclear whether the "fingerprint" framework modes that were identified in the computational study of AlPO<sub>4</sub>-H3 could be of any practical use to detect [Al<sup>[6o]</sup>O<sub>4/2</sub>(H<sub>2</sub>O)<sub>2</sub>] octahedra using vibrational spectroscopy.

The DFT optimisations of fully hydrated SAPOs frequently resulted in Si–O–Al linkages that were deprotonated upon interaction with water, in agreement with earlier findings. Even though these protons may show a certain variation in their acidity, depending on the local environment, it can be expected that such linkages will typically be fully deprotonated upon hydration. Deprotonation of the Si–O–Al linkages was indeed observed in the AIMD study of ECR-40 (**Article C4**), with the protons exhibiting a considerable mobility. In contrast, the Al–O–Al linkages remained largely protonated. As calculations of the deprotonation energy also indicated a lower acidity of the protons associated with the latter type of links, it is unlikely that these protons are responsible for the high catalytic activity of ECR-40 that had been observed experimentally. It therefore appears at least debatable whether the introduction of non-Löwenstein linkages could be a promising strategy to obtain SAPOs with enhanced catalytic activity. Moreover, the preferred coordination of H<sub>2</sub>O molecules to the Al atoms of these linkages pointed to irreversible structural changes upon hydration, explaining the amorphisation of ECR-40 upon recalcination. Previous computational work has shown that non-Löwenstein linkages are thermodynamically unstable in the presence of water (Heard et al., 2019). Even if zeolite or zeotype materials having such linkages can be synthesised, as is the case for ECR-40, their usefulness for real-world applications will probably remain limited due to a lack of hydrothermal stability.

The investigation on AlPO-11 reported in **Article C5** stands apart from all other studies compiled in this chapter, as the computational prediction of the preferred water adsorption sites was only a secondary objective. The main focus of this work was the local structure of the calcined form, paying particular attention to the differences between the time-averaged and instantaneous structures. The AIMD simulations permitted a comprehensive understanding of these differences, thereby also providing an explanation for some implausible features in the experimental crystal structure. It is worth noting that AlPO-11 is by no means unique in this regard, as the crystal structures of many zeolites and zeotypes contain linear or near-linear T–O–T angles and shortened T–O bond distances. To this end, the investigation of AlPO-11, together with earlier work on AlPO-5 (Cortie et al., 2017) and all-silica ferrierite (Trudu et al., 2019), can be seen as "proof of principle" studies highlighting the possibilities of using DFT-based MD simulations to obtain detailed insights into the local, instantaneous structure of zeolite-like frameworks.

## 5.9 Outlook

The investigations compiled in the present chapter could constitute a starting point for future work going in various directions, both in terms of purely computational research and with regard to joint experimental-computational studies:

- Some AlPOs that are of particular interest to thermal energy storage, such as AlPO<sub>4</sub>-LTA and AlPO-78, were not included in the comparative DFT investigation. As it was observed that the computed interaction energies do not show a significant dependence on the framework topology, an extension of the same approach to these materials is likely to deliver limited new insights. However, DFT-based AIMD simulations at different water loadings could give some insights into the pore filling behaviour. Potentially, even DFT-based MC simulations (Fetisov et al., 2018), which have recently been used to study the adsorption of water in zeolites (Bai et al., 2021), could be used for this purpose, provided that sufficient computational resources are available.
- As such DFT-based MC simulations are not yet routinely applicable, at least for "screening" purposes, the FF-based modelling of water adsorption properties under relevant conditions will, for the foreseeable future, remain a key method in the computational identification of promising adsorbents for thermal energy storage. For the case of AlPOs and AlPO-based zeotypes, the frequent coordination of H<sub>2</sub>O molecules to framework Al atoms means that standard FFs that do not take such changes in the coordination environment into account cannot provide an accurate description of the adsorption process. The development of reactive FFs, possibly on the basis of DFT/AIMD results, and of MC algorithms that allow the formation and breaking of Al–O<sub>water</sub> bonds during the simulation would be crucial steps in this direction.
- On a more fundamental level, the calculations provided some insights into the preferred Si locations in SAPOs. In a few instances, these results could be compared to prior observations from NMR experiments: For example, the fact that the T1 and T2 sites are very close in energy for SAPO-17 agrees with the experimental observation of an occupation of both sites (however, with a certain preference for T2) in an NMR study (Zibrowius and Lohse, 1992). Such calculations could be straightforwardly extended to other SAPOs. They could also consider more complex environments such as larger Si islands in order to obtain realistic structure models that could then be used in subsequent DFT studies, *e.g.*, to understand adsorption or catalytic properties. It is, however, worth noting that the presence of the OSDA is likely to affect the preferred Si locations



(as observed for Ge locations in the previous chapter). They should therefore be included in the calculations. Another aspect that is relevant for applications, but more difficult to treat computationally is the possibility of a redistribution of the Si atoms upon post-synthesis treatments like steaming (Minova et al., 2021).

- While the works compiled in this chapter did not focus on the DFT-based prediction of NMR chemical shifts, it is clear that the combination of DFT and NMR constitutes a key tool to gather information about the local environments. With increasing possibilities to treat larger systems, more and more complex local environments can be addressed in such studies, *e.g.*, by going beyond perfect crystal structures to investigate the contribution of structural defects to the NMR spectra.
- Besides AlPOs, only protonated SAPOs were considered as charged-framework zeotypes. Both the incorporation of metal cations in SAPOs through cation exchange and the synthesis of AlPO-based zeotypes containing metal cations on some T sites (MeAPOs) could constitute promising strategies to "tune" the affinity towards water. DFT calculations could be a convenient method to predict how cation exchange or incorporation of metal cations into the framework would affect the interaction strength, permitting to identify particularly interesting systems which could then be synthesised and characterised experimentally.
- Although the study of the vibrational spectra of AlPO<sub>4</sub>-H3 delivered some framework modes that could serve as "fingerprints" for the presence of five- or six-coordinated Al atoms, it remains to be seen to what extent these modes are transferable among different AlPO structures, and whether they can be distinguished from other modes in spectroscopic experiments. Future combined experimental-computational work would be needed to look into this. Since NMR spectroscopy is already a well-established method permitting the distinction of different Al coordination environments, which can also be applied for non-crystalline materials, there may be limited scope for such research.
- The investigation of ECR-40, together with other AIMD studies of hydrated aluminosilicates containing non-Löwenstein linkages, corroborated the instability of Al–O–Al linkages in the presence of water. For this reason, future computational studies of hypothetical systems appear to be of limited usefulness, unless they specifically address the conditions under which such links could be stabilised (Fant et al., 2021). For the specific case of hydrated ECR-40, it could be interesting to run longer AIMD simulations to test whether an equilibrium state in which face-sharing [Al<sup>[6o]</sup>O<sub>3/2</sub>(H<sub>2</sub>O)<sub>3</sub>] octahedra have formed at all Al–O–Al linkages could be reached on the timescale that is accessible with such simulations. Starting from this form, partially dehydrated models could be generated by removing non-coordinated molecules. Further AIMD simulations on these models could potentially give insights into the structural changes that happen upon recalcination of the dehydrated form.
- The AIMD approach employed for AlPO-11 in **Article C5** could straightforwardly be extended to other zeolites or zeotypes with linear or near-linear T–O–T linkages. On the one hand, the computations can provide insights into the local, instantaneous structure, which could be validated experimentally through an analysis of the pair distribution function obtained from diffraction experiments, which gives access to the instantaneous interatomic distances (White et al., 2010). On the other hand, the calculations for AlPO-11 resulted in the prediction of lower-symmetry phases.

The existence of such phases could be probed experimentally by means of *in situ* diffraction experiments at low temperatures. As discussed for AlPO-11, the calculations alone do not allow for conclusions whether one of the computationally predicted, ordered phases is stable at low temperature, or whether a disordered phase having the same local structural features occurs. To investigate this, a combined analysis of diffraction data that takes both Bragg scattering and diffuse scattering into account would be warranted (Campbell et al., 2004). As the lack of sufficiently sized single crystals will, in many cases, put limitations on the applicability of X-ray/synchrotron diffraction experiments, electron diffraction investigations should be particularly promising.

- Finally, the presence of five- or six-coordinated Al atoms plays a big role during topotactic transformations of AlPOs, as demonstrated for the transformation from PST-5, a zeotype with a 2D pore system, to PSI-type PST-6, which has 1D channels (Huang et al., 2020): Due to the longer Al–O bonds around these sites, they correspond to "built-in weaknesses" in the structure which change their bonding pattern upon calcination, resulting in the breaking and re-formation of T–O bonds that is associated with the structural transformation. In this field, computational studies cannot only help to rationalise the experimentally observed behaviour, as shown in the work of Huang et al. (2020), but they could also be used to predict which AlPO structures might be susceptible to topotactic transformations.

## CHAPTER 6

### FINAL REMARKS

Each of the preceding chapters ended with a Conclusions section summarising the key findings of the respective studies, and with an Outlook section that compiled ideas for future work, including both purely computational investigations and possibilities to combine the calculations with experimental studies. It is not the aim of this chapter to reprise the content of these sections, although some repetitions are inevitable. The idea is rather to highlight the most significant contributions that the present work has made to the field of computational studies of zeolites and zeotypes. Given the multitude of scientific questions that are being addressed in this area, and the vast number of researchers working on them, the contribution of an individual may appear minuscule. This impression could be amplified by the fact that some of the topics that were addressed here, such as the dynamics of fluoride anions in all-silica zeolites or the hydration of a SAPO with Al–O–Al linkages, are fairly "exotic" in comparison to more widely studied aspects, such as catalytic properties or carbon dioxide capture. It is therefore gratifying to see that the articles compiled in this thesis have received considerable attention within the scientific community, being rather well cited and forming the basis for follow-up investigations by other researchers. To mention just one example, a recent benchmarking study on zeolites by Trachta et al. (2022) was heavily influenced by the studies reported in **Articles A2, A3, and A4**.

Altogether, the results have shown that structural properties of neutral-framework zeotypes can be computed fairly reliably using dispersion-corrected DFT methods, even at the GGA level, provided that a suitable combination of XC functional and dispersion correction is chosen. This result, established in benchmarking studies on guest-free all-silica zeolites and AlPOs (**A2, A3, A4**) appears to be transferable to as-synthesised systems, as shown in studies addressing all-silica zeolites containing OSDA molecules in the pores and charge-balancing fluoride anions (**B3, B4**). Even the energetically preferred fluoride locations in a given cage, which depend rather intricately on the local environment, were (mostly) successfully reproduced in calculations employing the PBE-D3 functional, a fairly inexpensive dispersion-corrected DFT approach that can also be applied in AIMD simulations (as shown throughout **Chapter 4**) or when studying zeolite structures with large unit cells. Even though there remains space for improvement in various ways, *e.g.*, with regard to the description of the interaction between T atoms at opposite ends of a T–O–T linkage, the body of results showed that dispersion-corrected DFT methods can, in most instances, deliver a fairly accurate representation of the equilibrium structure of guest-free and OSDA-containing neutral-framework zeolites and zeotypes. As observed for the case of AlPO-11 in **Article C5**, large deviations between DFT-optimised structures and experimental data may not necessarily be due to failures of the dispersion-corrected DFT approach. If there are local, instantaneous deviations from the time-averaged structure, use of a standard structure optimisation procedure that does not account for the dynamic behaviour of the system is bound to fail, even in the absence of any inherent errors of the electronic structure method. Similarly, as shown in the study on fluoride-containing AST-type systems (**B2**), it can be necessary to perturb the initial symmetry to avoid a trapping in local minima. These findings highlight that there are cases where an accurate description of the (seemingly "static") equilibrium structure cannot be achieved without the inclusion of dynamic effects.

Although the pressure-dependent behaviour of zeolites and zeotypes was not a major focus of this work, the results obtained in **Article A4** and **A5** point to a considerably larger sensitivity of the results to the choice of the dispersion-corrected DFT approach than for ambient-pressure equilibrium structures. It hence appears that an accurate reproduction of the pressure response is more challenging to achieve, and that further validation efforts should be undertaken in order to identify a suitable DFT approach for this purpose.

Going beyond crystal structures, a number of other DFT-derived quantities were analysed in various contexts. Relative energies of all-silica zeolites obtained with several dispersion-corrected DFT approaches were found to be in near-quantitative agreement with experimental enthalpies of transition (**A3**, **A4**). The comparison of different germanium distributions in silicogermanates also relied heavily on the relative energies (**B1**, **B5**). As a direct validation against experimental enthalpy data was not possible in these cases, only indirect connections to other experimental observations (especially  $^{19}\text{F}$ -NMR chemical shifts) could be drawn to confirm the soundness of the DFT results. A point of crucial importance with regard to follow-up studies is the impact of OSDA cations and fluoride anions on the energetic ordering of different Ge distributions, which was firmly established. It can be anticipated that this issue is not unique to fluoride-containing silicogermanates, but that it can be stated more generally that extra-framework species will influence the preferred locations of heteroatoms in zeolites and zeotypes. Besides relative energies, adsorption energies were also computed in several of the studies of water adsorption in AlPOs and SAPOs (**Chapter 5**). In the view of the known sensitivity of adsorption energies to the DFT setup and the poor performance of typical dispersion-corrected DFT approaches for many zeolite guest-combinations (**Chapter 1**), the good agreement between PBE-TS interaction energies and experimental adsorption enthalpies is rather surprising, and it is likely that a degree of error cancellation came into play here. Nevertheless, it appears reasonable to expect that results for individual systems should be affected in a similar way, giving some confidence in the qualitative trends that were identified on the basis of the calculations. Although there were some instances where vibrational or NMR spectra were computed in this work, it was not attempted to validate different DFT approaches. However, it was at least ensured that DFT-based predictions were in reasonable agreement with experiment. In the specific case of ITQ-13 silicogermanates, the calculation of  $^{19}\text{F}$ -NMR chemical shifts could show that previously undetected building units which were predicted to be stable by the DFT calculations are challenging to identify experimentally.

Although the application of DFT-based AIMD simulations to zeolites and related materials is far from new, recent developments in terms of algorithms and hardware have been pivotal to render such simulations feasible for zeolite unit cells of "typical" size, on the order of 100 to 1,000 atoms. Whereas a number of AIMD studies have addressed adsorption phenomena and catalytic reactions, the dynamic behaviour of as-synthesised zeolites had been explored to a much lesser extent. Prior to the publication of **Article B1**, there had been no AIMD studies investigating the dynamic behaviour of fluoride anions encapsulated in small cages of all-silica zeolites or other neutral-framework zeotypes. It is, however, worth noting that a parallel investigation of Silicalite-1 with a somewhat different emphasis (focussing on hydrogen bonding patterns, rather than fluoride dynamics) was published a few months before **Article B3**, underlining the timeliness of this direction of research (Mineva et al., 2020). The first impressive result of these calculations is the surprisingly good reproduction of the dynamic disorder of fluoride anions in different zeolites containing  $[\text{Si}^{[5by]}\text{O}_{4/2}\text{F}]^-$  units, despite the limitation to simulation runs covering only a few picoseconds. Beyond the reproduction of experimental observations, the cal-

culations also allowed a more comprehensive understanding of the influence of local environment and OSDA on the dynamic behaviour. These insights are particularly valuable as the required temporal and spatial resolution limits the ability of experimental techniques to probe such effects. The same is true for fluoride anions encapsulated in *d4r* cages, where the amount of information that can be inferred from diffraction or NMR experiments is limited. While it was established that the local environment plays the most important role in determining the equilibrium position of the fluoride anions and their dynamic behaviour, the simulations also showed a non-negligible influence of longer-range interactions with the OSDA molecules. Even though it might be far-fetched to expect that an OSDA-induced ordering of the fluoride displacements, observed in the AIMD simulation results, could be realised in any actual zeolite/zeotype sample, this example shows how the interplay of various interactions in these complex systems can trigger unexpected phenomena. For many systems, an MD-based approach is of key importance to arrive at a realistic description of the instantaneous structure. This became apparent not only in the studies of fluoride-containing zeolites, but also in the work investigating AlPO-11 (C5), where it could be shown that near-linear Al–O–P angles observed in the time-averaged structure are actually an artefact of the dynamic motion of oxygen atoms.

Rather than targeting specific application-related quantities, the AIMD investigations carried out in the context of the present work were largely aimed at a fundamental understanding of the dynamic behaviour. Although similar calculations could, in the future, aid the computational design of OSDAs for a targeted synthesis of particular zeolites, this possibility was not explored. Arguably the most "practical" application of AIMD simulations in the present work was the investigation of hydrated ECR-40 (C4), where the simulations could elucidate the difference in acidity among framework protons in different environments as well as the hydration-induced structural changes that are responsible for the instability towards recalcination. Comparable investigations could be envisaged in the context of a modelling-guided identification of zeolites/zeotypes having suitable acidity and sufficient stability for specific catalytic reactions.

Altogether, this work expanded the range of research questions in zeolite science that have been treated with electronic structure methods, especially with regard to the AIMD studies of fluoride-containing zeolites and zeotypes. The fact that such complex structures could be investigated with dispersion-corrected DFT calculations reflects the ever-increasing ability to treat larger systems (or longer timescales) with reasonably accurate electronic structure methods through the use of state-of-the-art codes and computing architectures. As these developments will continue, it can be anticipated that more and more complex systems and phenomena can be investigated at comparable levels of theory in the future. Potential topics of study include, but are not limited to, electronic structure investigations of hierarchical zeolites or of interfaces between zeolites and other materials (larger system sizes), AIMD-based studies of diffusion phenomena (longer timescales), or of zeolite stability under realistic geologic conditions (increased overall system complexity). Since parallel developments in terms of novel synthesis routes and advanced characterisation methods will without doubt lead to new and exciting research questions, it is not a bold prediction to state that computational zeolite science will continue to thrive.



## BIBLIOGRAPHY

- M. Abatal, A. R. Ruiz-Salvador, and N. C. Hernández. A DFT-based simulated annealing method for the optimization of global energy in zeolite framework systems: Application to natrolite, chabazite and clinoptilolite. *Microporous Mesoporous Mater.*, 294:109885, 2020. DOI: 10.1016/j.micromeso.2019.109885.
- A. Abdelrasoul, H. Zhang, C.-H. Cheng, and H. Doan. Applications of molecular simulations for separation and adsorption in zeolites. *Microporous Mesoporous Mater.*, 242:294–348, 2017. DOI: 10.1016/j.micromeso.2017.01.038.
- M. Afeworki, D. Dorset, G. Kennedy, and K. Strohmaier. Synthesis and structure of ECR-40: An ordered SAPO having the MEI framework. *Stud. Surf. Sci. Catal.*, 154:1274–1281, 2004. DOI: 10.1016/S0167-2991(04)80639-6.
- S. H. Ahn, H. Lee, and S. B. Hong. Crystallization Mechanism of Cage-Based, Small-Pore Molecular Sieves: A Case Study of CHA and LEV Structures. *Chem. Mater.*, 29:5583–5590, 2017. DOI: 10.1021/acs.chemmater.7b00980.
- W. A. Al-Saidi, V. K. Voora, and K. D. Jordan. An Assessment of the vdW-TS Method for Extended Systems. *J. Chem. Theory Comput.*, 8:1503–1513, 2012. DOI: 10.1021/ct200618b.
- F. G. Alabarse, J. Haines, O. Cambon, C. Levelut, D. Bourgogne, A. Haidoux, D. Granier, and B. Coasne. Freezing of water confined at the nanoscale. *Phys. Rev. Lett.*, 109:035701, 2012. DOI: 10.1103/PhysRevLett.109.035701.
- F. G. Alabarse, G. Silly, A. Haidoux, C. Levelut, D. Bourgogne, A.-M. Flank, P. Lagarde, A. S. Pereira, J.-I. Bantignies, O. Cambon, and J. Haines. Effect of H<sub>2</sub>O on the Pressure-Induced Amorphization of AlPO<sub>4</sub>-54 · x H<sub>2</sub>O. *J. Phys. Chem. C*, 118:3651–3663, 2014. DOI: 10.1021/jp412181f.
- I. M. Alecu, J. Zheng, Y. Zhao, and D. G. Truhlar. Computational Thermochemistry: Scale Factor Databases and Scale Factors for Vibrational Frequencies Obtained from Electronic Model Chemistries. *J. Chem. Theory Comput.*, 6:2872–2887, 2010. DOI: 10.1021/ct100326h.
- M. P. Allen and D. J. Tildesley. *Computer Simulation of Liquids*. Oxford University Press, Oxford, UK, 2nd edition, 2017. DOI: 10.1093/oso/9780198803195.001.0001.
- N. L. Allinger. *Molecular Structure*. John Wiley & Sons, Inc., Hoboken, NJ, USA, 2010. DOI: 10.1002/9780470608852.
- S. Alvarez. A cartography of the van der Waals territories. *Dalton Trans.*, 42:8617–8636, 2013. DOI: 10.1039/c3dt50599e.
- N. A. Anurova, V. A. Blatov, G. D. Ilyushin, and D. M. Proserpio. Natural Tilings for Zeolite-Type Frameworks. *J. Phys. Chem. C*, 114:10160–10170, 2010. DOI: 10.1021/jp1030027.
- Y. I. Aristov. Challenging offers of material science for adsorption heat transformation: A review. *Appl. Therm. Eng.*, 50:1610–1618, 2013. DOI: 10.1016/j.applthermaleng.2011.09.003.
- T. Armbruster and M. E. Gunter. Crystal Structures of Natural Zeolites. *Rev. Mineral. Geochem.*, 45:1–67, 2001. DOI: 10.2138/rmg.2001.45.1.
- M. Arranz, J. Pérez-Pariente, P. A. Wright, A. M. Z. Slawin, T. Blasco, L. Gómez-Hortigüela, and F. Cora. Cooperative structure-directing effect of fluorine-containing organic molecules and fluoride anions in the synthesis of zeolites. *Chem. Mater.*, 17:4374–4385, 2005. DOI: 10.1021/cm050971j.
- B. Arstad, A. Lind, J. H. Cavka, K. Thorshaug, D. Akporiaye, D. Wragg, H. Fjellvåg, A. Grønvold, and T. Fuglerud. Structural changes in SAPO-34 due to hydrothermal treatment. A NMR, XRD, and DRIFTS study. *Microporous Mesoporous Mater.*, 225:421–431, 2016. DOI: 10.1016/j.micromeso.2016.01.024.
- G. Artioli, J. V. Smith, and Å. Kvik. Neutron diffraction study of natrolite, Na<sub>2</sub>Al<sub>2</sub>Si<sub>3</sub>O<sub>10</sub> · 2H<sub>2</sub>O, at 20 K. *Acta Cryst. C*, 40:1658–1662, 1984. DOI: 10.1107/S0108270184009070.

- G. Artioli, R. Rinaldi, Å. Kvik, and J. Smith. Neutron diffraction structure refinement of the zeolite gismondine at 15 K. *Zeolites*, 6:361–366, 1986. DOI: 10.1016/0144-2449(86)90063-1.
- S. E. Ashbrook and D. McKay. Combining solid-state NMR spectroscopy with first-principles calculations – a guide to NMR crystallography. *Chem. Commun.*, 52:7186–7204, 2016. DOI: 10.1039/C6CC02542K.
- S. E. Ashbrook, M. Cutajar, C. J. Pickard, R. I. Walton, and S. Wimperis. Structure and NMR assignment in calcined and as-synthesized forms of AlPO-14: a combined study by first-principles calculations and high-resolution  $^{27}\text{Al}$ - $^{31}\text{P}$  MAS NMR correlation. *Phys. Chem. Chem. Phys.*, 10:5754–5764, 2008. DOI: 10.1039/b805681a.
- R. Astala, S. M. Auerbach, and P. A. Monson. Density Functional Theory Study of Silica Zeolite Structures: Stabilities and Mechanical Properties of SOD, LTA, CHA, MOR, and MFI. *J. Phys. Chem. B*, 108:9208–9215, 2004. DOI: 10.1021/jp0493733.
- M. P. Attfield, C. R. A. Catlow, and A. A. Sokol. True Structure of Trigonal Bipyramidal  $\text{SiO}_4\text{F}^-$  Species in Siliceous Zeolites. *Chem. Mater.*, 13:4708–4713, 2001. DOI: 10.1021/cm011141i.
- M. P. Attfield, F. Al-Otaibi, and Y. Al-Ebini. Revisiting the structure of the germanate zeotype ASU-7 (ASV). *Microporous Mesoporous Mater.*, 118:508–512, 2009. DOI: 10.1016/j.micromeso.2008.08.052.
- E. Aubert, F. Porcher, M. Souhassou, V. Petříček, and C. Lecomte. Location of fluoride counterion in as-synthesized Silicalite-1 by single crystal X-ray diffraction. *J. Phys. Chem. B*, 106:1110–1117, 2002. DOI: 10.1021/jp012231d.
- C. Baerlocher and L. McCusker. Database of Zeolite Structures, 2022.  
URL: <http://www.iza-structure.org/databases/>.
- C. Baerlocher, L. B. McCusker, and D. H. Olson. *Atlas of Zeolite Framework Types*. Elsevier B.V., Amsterdam, NL, 6th edition, 2007.
- P. Bai, M. Tsapatsis, and J. I. Siepmann. TraPPE-zeo: Transferable Potentials for Phase Equilibria Force Field for All-Silica Zeolites. *J. Phys. Chem. C*, 117:24375–24387, 2013. DOI: 10.1021/jp4074224.
- P. Bai, M. Neurock, and J. I. Siepmann. First-Principles Grand-Canonical Simulations of Water Adsorption in Proton-Exchanged Zeolites. *J. Phys. Chem. C*, 125:6090–6098, 2021. DOI: 10.1021/acs.jpcc.0c10104.
- R. M. Barrer. Fractionation of mixtures of hydrocarbons, US Patent 2306610, 1942.  
URL: <https://www.freepatentsonline.com/2306610.html>.
- R. M. Barrer. Synthesis of a zeolitic mineral with chabazite-like sorptive properties. *J. Chem. Soc.*, pages 127–132, 1948a. DOI: 10.1039/jr9480000127.
- R. M. Barrer. Syntheses and reactions of mordenite. *J. Chem. Soc.*, pages 2158–2163, 1948b.  
DOI: 10.1039/jr9480002158.
- P. A. Barrett, M. A. Camblor, A. Corma, R. H. Jones, and L. A. Villaescusa. Synthesis and Structure of As-Prepared ITQ-4, A Large Pore Pure Silica Zeolite: The Role and Location of Fluoride Anions and Organic Cations. *J. Phys. Chem. B*, 102:4147–4155, 1998. DOI: 10.1021/jp980735e.
- G. Basina, D. AlShami, K. Polychronopoulou, V. Tzitzios, V. Balasubramanian, F. Dawaymeh, G. N. Karanikolos, and Y. Al Wahedi. Hierarchical AlPO<sub>4</sub>-5 and SAPO-5 microporous molecular sieves with mesoporous connectivity for water sorption applications. *Surf. Coat. Technol.*, 353:378–386, 2018.  
DOI: 10.1016/j.surfcoat.2018.08.083.
- J. Bauer, R. Herrmann, W. Mittelbach, and W. Schwieger. Zeolite/aluminum composite adsorbents for application in adsorption refrigeration. *Int. J. Energy Res.*, 33:1233–1249, 2009. DOI: 10.1002/er.1611.
- W. H. Baur and R. X. Fischer. Zeolite-type crystal structures and their chemistry. In W. H. Baur and R. X. Fischer, editors, *Landolt-Börnstein - Group IV Physical Chemistry · Volumes 14B to 14H: Microporous and other Framework Materials with Zeolite-Type Structures*. Springer-Verlag Berlin Heidelberg, 2000 to 2017.



- W. H. Baur and R. X. Fischer. ZeoBase, a new kind of crystal structure database. In A. De Frede, editor, *Proc. 16th Int. Zeolite Conf.*, page 457, Sorrento, Italy, 2010.
- W. H. Baur and R. X. Fischer. The Floppiness of It All: Bond Lengths Change with Atomic Displacement Parameters and the Flexibility of Various Coordination Tetrahedra in Zeolitic Frameworks. An Empirical Structural Study of Bond Lengths and Angles. *Chem. Mater.*, 31:2401–2420, 2019. DOI: 10.1021/acs.chemmater.8b04919.
- W. H. Baur, W. Joswig, D. Kassner, J. Kornatowski, and G. Finger. Structure of SAPO-31 Refined from Single-Crystal Diffraction Data: Substitution of P by Si Established by Diffraction Methods. *Acta Cryst. B*, 50: 290–294, 1994. DOI: 10.1107/S0108768193012625.
- A. Bauzá, T. J. Mooibroek, and A. Frontera. Tetrel-Bonding Interaction: Rediscovered Supramolecular Force? *Angew. Chem. Int. Ed.*, 52:12317–12321, 2013. DOI: 10.1002/anie.201306501.
- I. A. Belitsky, S. P. Gabuda, W. Joswig, and H. Fuess. Study of the structure and dynamics of the water in the zeolite edingtonite at low temperature by neutron diffraction and NMR-spectroscopy. *N. Jahrb. f. Mineral., Monatsh.*, 12:541–551, 1986.
- J. M. Bennett and R. M. Kirchner. The structure of as-synthesized AlPO<sub>4</sub>-16 determined by a new framework modeling method and Rietveld refinement of synchrotron powder diffraction data. *Zeolites*, 11:502–506, 1991. DOI: 10.1016/S0144-2449(05)80125-3.
- J. M. Bennett, J. P. Cohen, E. M. Flanigen, J. J. Pluth, and J. V. Smith. Crystal Structure of Tetrapropylammonium Hydroxide-Aluminum Phosphate Number 5. *ACS Symp. Ser. Am. Chem. Soc.*, 218:109–118, 1983. DOI: 10.1021/bk-1983-0218.ch006.
- J. M. Bennett, J. M. Cohen, G. Artioli, J. J. Pluth, and J. V. Smith. Crystal structure of AlPO<sub>4</sub>-21, a framework aluminophosphate containing tetrahedral phosphorus and both tetrahedral and trigonal-bipyramidal aluminum in 3-, 4-, 5-, and 8-rings. *Inorg. Chem.*, 24:188–193, 1985. DOI: 10.1021/ic00196a014.
- H. J. C. Berendsen. *Simulating the Physical World - Hierarchical Modeling from Quantum Mechanics to Fluid Dynamics*. Cambridge University Press, Cambridge, UK, 2007. DOI: 10.1017/CBO9780511815348.
- H. J. C. Berendsen, J. R. Grigera, and T. P. Straatsma. The Missing Term in Effective Pair Potentials. *J. Phys. Chem.*, 91:6269–6271, 1987. DOI: 10.1021/j100308a038.
- C. Betti, E. Fois, E. Mazzucato, C. Medici, S. Quartieri, G. Tabacchi, G. Vezzalini, and V. Dmitriev. Gismondine under HP: Deformation mechanism and re-organization of the extra-framework species. *Microporous Mesoporous Mater.*, 103:190–209, 2007. DOI: 10.1016/j.micromeso.2007.01.051.
- J. Binns, M. R. Healy, S. Parsons, and C. A. Morrison. Assessing the performance of density functional theory in optimizing molecular crystal structure parameters. *Acta Cryst. B*, 70:259–267, 2014. DOI: 10.1107/S205252061303268X.
- C. S. Blackwell and R. L. Patton. Aluminum-27 and Phosphorus-31 Nuclear Magnetic Resonance Studies of Aluminophosphate Molecular Sieves. *J. Phys. Chem.*, 88:6135–6139, 1984. DOI: 10.1021/j150669a016.
- C. S. Blackwell and R. L. Patton. Solid-state NMR of silicoaluminophosphate molecular sieves and aluminophosphate materials. *J. Phys. Chem.*, 92:3965–3970, 1988. DOI: 10.1021/j100324a055.
- T. Blasco, A. Corma, M. J. Díaz-Cabañas, F. Rey, J. A. Vidal-Moya, and C. M. Zicovich-Wilson. Preferential location of Ge in the double four-membered ring units of ITQ-7 zolite. *J. Phys. Chem. B*, 106:2634–2642, 2002. DOI: 10.1021/jp013302b.
- V. A. Blatov, O. Delgado-Friedrichs, M. O’Keeffe, and D. M. Proserpio. Three-periodic nets and tilings: natural tilings for nets. *Acta Cryst. A*, 63:418–425, 2007. DOI: 10.1107/S0108767307038287.
- O. A. Blatova, A. A. Golov, and V. A. Blatov. Natural tilings and free space in zeolites: Models, statistics, correlations, prediction. *Z. Kristallogr. - Cryst. Mater.*, 234:421–436, 2019. DOI: 10.1515/zkri-2018-2143.

- F. M. Bobonich, V. N. Solomakha, and L. A. Chubirka. The Relation between the Efficiency of an Adsorbent in a Refrigeration System and its Hydration Isotherm. *Theor. Exp. Chem.*, 37:116–120, 2001. DOI: 10.1023/A:1010461611025.
- C. Bonhomme, C. Gervais, F. Babonneau, C. Coelho, F. Pourpoint, T. Azaïs, S. E. Ashbrook, J. M. Griffin, J. R. Yates, F. Mauri, and C. J. Pickard. First-Principles Calculation of NMR Parameters Using the Gauge Including Projector Augmented Wave Method: A Chemist's Point of View. *Chem. Rev.*, 112:5733–5779, 2012. DOI: 10.1021/cr300108a.
- S. Bordiga, L. Regli, C. Lamberti, A. Zecchina, M. Bjørgen, and K. P. Lillerud. FTIR adsorption studies of H<sub>2</sub>O and CH<sub>3</sub>OH in the isostructural H-SSZ-13 and H-SAPO-34: Formation of H-bonded adducts and protonated clusters. *J. Phys. Chem. B*, 109:7724–7732, 2005. DOI: 10.1021/jp044324b.
- S. Bordiga, C. Lamberti, F. Bonino, A. Travert, and F. Thibault-Starzyk. Probing zeolites by vibrational spectroscopies. *Chem. Soc. Rev.*, 44:7262–7341, 2015. DOI: 10.1039/C5CS00396B.
- M. Boronat and A. Corma. What Is Measured When Measuring Acidity in Zeolites with Probe Molecules? *ACS Catal.*, 9:1539–1548, 2019. DOI: 10.1021/acscatal.8b04317.
- S. E. Boulfelfel, P. I. Ravikovitch, and D. S. Sholl. Modeling Diffusion of Linear Hydrocarbons in Silica Zeolite LTA Using Transition Path Sampling. *J. Phys. Chem. C*, 119:15643–15653, 2015. DOI: 10.1021/acs.jpcc.5b01633.
- S. L. Brace, P. Wormald, and R. J. Darton. The effect of structure directing agents on the ordering of fluoride ions in pure silica MFI. *Phys. Chem. Chem. Phys.*, 17:11950–11953, 2015. DOI: 10.1039/C5CP00834D.
- V. Brancato and A. Frazzica. Characterisation and comparative analysis of zeotype water adsorbents for heat transformation applications. *Sol. Energy Mater. Sol. Cells*, 180:91–102, 2018. DOI: 10.1016/j.solmat.2018.02.035.
- J. G. Brandenburg, M. Hochheim, T. Bredow, and S. Grimme. Low-Cost Quantum Chemical Methods for Noncovalent Interactions. *J. Phys. Chem. Lett.*, 5:4275–4284, 2014. DOI: 10.1021/jz5021313.
- D. Breck, W. Eversole, R. Milton, T. Reed, and T. Thomas. Crystalline zeolites. I. The properties of a new synthetic zeolite, type A. *J. Am. Chem. Soc.*, 78:5963–5972, 1956. DOI: 10.1021/ja01604a001.
- M. Brehm, M. Thomas, S. Gehrke, and B. Kirchner. TRAVIS – A free analyzer for trajectories from molecular simulation. *J. Chem. Phys.*, 152:164105, 2020. DOI: 10.1063/5.0005078.
- M. Briend, R. Vomscheid, M. J. Peltre, P. P. Man, and D. Barthomeuf. Influence of the Choice of the Template on the Short- and Long-Term Stability of SAPO-34 Zeolite. *J. Phys. Chem.*, 99:8270–8276, 1995. DOI: 10.1021/j100020a060.
- D. H. Brouwer, I. L. Moudrakovski, R. J. Darton, and R. E. Morris. Comparing quantum-chemical calculation methods for structural investigation of zeolite crystal structures by solid-state NMR spectroscopy. *Magn. Reson. Chem.*, 48:S113–S121, 2010. DOI: 10.1002/mrc.2642.
- G. Brunklaus, H. Koller, and S. I. Zones. Defect Models of As-Made High-Silica Zeolites: Clusters of Hydrogen-Bonds and Their Interaction with the Organic Structure-Directing Agents Determined from <sup>1</sup>H Double and Triple Quantum NMR Spectroscopy. *Angew. Chem. Int. Ed.*, 55:14459–14463, 2016. DOI: 10.1002/anie.201607428.
- A. Buchholz, W. Wang, M. Xu, A. Arnold, and M. Hunger. Thermal stability and dehydroxylation of Brønsted acid sites in silicoaluminophosphates H-SAPO-11, H-SAPO-18, H-SAPO-31, and H-SAPO-34 investigated by multi-nuclear solid-state NMR spectroscopy. *Microporous Mesoporous Mater.*, 56:267–278, 2002. DOI: 10.1016/S1387-1811(02)00491-2.
- A. Buchholz, W. Wang, A. Arnold, M. Xu, and M. Hunger. Successive steps of hydration and dehydration of silicoaluminophosphates H-SAPO-34 and H-SAPO-37 investigated by in situ CF MAS NMR spectroscopy. *Microporous Mesoporous Mater.*, 57:157–168, 2003. DOI: 10.1016/S1387-1811(02)00562-0.

- T. Bučko, S. Lebègue, J. Hafner, and J. G. Ángyán. Improved Density Dependent Correction for the Description of London Dispersion Forces. *J. Chem. Theory Comput.*, 9:4293–4299, 2013. DOI: 10.1021/ct400694h.
- I. Bull, L. A. Villaescusa, S. J. Teat, M. A. Camblor, P. A. Wright, P. Lightfoot, and R. E. Morris. Imposition of Polarity on a Centrosymmetric Zeolite Host: The Effect of Fluoride Ions on Template Ordering in Zeolite IFR. *J. Am. Chem. Soc.*, 122:7128–7129, 2000. DOI: 10.1021/ja000885e.
- A. Burton. Recent trends in the synthesis of high-silica zeolites. *Catal. Rev.*, 60:132–175, 2018. DOI: 10.1080/01614940.2017.1389112.
- A. W. Burton, S. I. Zones, and S. Elomari. The chemistry of phase selectivity in the synthesis of high-silica zeolites. *Curr. Opin. Colloid Interface Sci.*, 10:211–219, 2005. DOI: 10.1016/j.cocis.2005.08.005.
- Y. G. Bushuev and G. Sastre. Atomistic Simulations of Structural Defects and Water Occluded in SSZ-74 Zeolite. *J. Phys. Chem. C*, 113:10877–10886, 2009. DOI: 10.1021/jp9013306.
- W. R. Busing and H. A. Levy. The effect of thermal motion on the estimation of bond lengths from diffraction measurements. *Acta Cryst.*, 17:142–146, 1964. DOI: 10.1107/S0365110X64000408.
- S. Caldarelli, A. Meden, and A. Tuel. Solid-State Nuclear Magnetic Resonance Study of the Microporous Aluminophosphate AlPO<sub>4</sub>-41. *J. Phys. Chem. B*, 103:5477–5487, 1999. DOI: 10.1021/jp990667b.
- M. A. Camblor and L. A. Villaescusa. Synthesis of all-silica and high-silica molecular sieves in fluoride media. *Top. Catal.*, 9:59–76, 1999. DOI: 10.1023/A:1019154304344.
- M. A. Camblor, A. Corma, P. Lightfoot, L. A. Villaescusa, and P. A. Wright. Synthesis and Structure of ITQ-3, the First Pure Silica Polymorph with a Two-Dimensional System of Straight Eight-Ring Channels. *Angew. Chem. Int. Ed.*, 36:2659–2661, 1997. DOI: 10.1002/anie.199726591.
- M. A. Camblor, A. Corma, M.-J. Díaz-Cabañas, and C. Baerlocher. Synthesis and structural characterization of MWW type zeolite ITQ-1, the pure silica analog of MCM-22 and SSZ-25. *J. Phys. Chem. B*, 102:44–51, 1998a. DOI: 10.1021/JP972319K.
- M. A. Camblor, M.-J. Díaz-Cabañas, J. Perez-Pariente, S. J. Teat, W. Clegg, I. J. Shannon, P. Lightfoot, P. A. Wright, and R. E. Morris. SSZ-23: An Odd Zeolite with Pore Openings of Seven and Nine Tetrahedral Atoms. *Angew. Chem. Int. Ed.*, 37:2122–2126, 1998b. DOI: 10.1002/(SICI)1521-3773(19980817)37:15<2122::AID-ANIE2122>3.0.CO;2-6.
- B. J. Campbell, T. R. Welberry, R. W. Broach, H. Hong, and A. K. Cheetham. Elucidation of zeolite microstructure by synchrotron X-ray diffuse scattering. *J. Appl. Crystallogr.*, 37:187–192, 2004. DOI: 10.1107/S0021889803028048.
- S. Caro-Ortiz, E. Zuidema, D. Dekker, M. Rigutto, D. Dubbeldam, and T. J. Vlugt. Adsorption of Aromatics in MFI-Type Zeolites: Experiments and Framework Flexibility in Monte Carlo Simulations. *J. Phys. Chem. C*, 124:21782–21797, 2020. DOI: 10.1021/acs.jpcc.0c06096.
- D. J. Carter and A. L. Rohl. Benchmarking Calculated Lattice Parameters and Energies of Molecular Crystals Using van der Waals Density Functionals. *J. Chem. Theory Comput.*, 10:3423–3437, 2014. DOI: 10.1021/ct500335b.
- R. Castañeda, A. Corma, V. Fornés, J. Martínez-Triguero, and S. Valencia. Direct synthesis of a 9 × 10 member ring zeolite (Al-ITQ-13): A highly shape-selective catalyst for catalytic cracking. *J. Catal.*, 238:79–87, 2006. DOI: 10.1016/j.jcat.2005.11.038.
- C. R. A. Catlow. *Computer Modeling in Inorganic Crystallography*. Academic Press, Cambridge, MA, USA, 1997. DOI: 10.1016/B978-0-12-164135-1.X5000-X.
- P. Caullet, J. L. Guth, J. Hazm, J. M. Lamblin, and H. Gies. Synthesis, characterization and crystal structure of the new clathrasil phase octadecasil. *Eur. J. Solid State Inorg. Chem.*, 28:345–361, 1991.
- P. Caullet, J.-I. Paillaud, A. Simon-Masseron, M. Soulard, and J. Patarin. The fluoride route: a strategy to crystalline porous materials. *C. R. Chim.*, 8:245–266, 2005. DOI: 10.1016/j.crci.2005.02.001.

- J. Chen, P. A. Wright, J. M. Thomas, S. Natarajan, L. Marchese, S. M. Bradley, G. Sankar, C. R. A. Catlow, and P. L. Gai-Boyes. SAPO-18 Catalysts and Their Brønsted Acid Sites. *J. Phys. Chem.*, 98:10216–10224, 1994. DOI: 10.1021/j100091a042.
- C. Chizallet. Toward the Atomic Scale Simulation of Intricate Acidic Aluminosilicate Catalysts. *ACS Catal.*, 10: 5579–5601, 2020. DOI: 10.1021/acscatal.0c01136.
- P. Cieplak, F.-Y. Dupradeau, Y. Duan, and J. Wang. Polarization effects in molecular mechanical force fields. *J. Phys. Condens. Matter*, 21:333102, 2009. DOI: 10.1088/0953-8984/21/33/333102.
- B. Civalleri, C. M. Zicovich-Wilson, P. Ugliengo, V. R. Saunders, and R. Dovesi. A periodic ab initio study of the structure and relative stability of silica polymorphs. *Chem. Phys. Lett.*, 292:394–402, 1998. DOI: 10.1016/S0009-2614(98)00749-0.
- S. J. Clark, M. D. Segall, C. J. Pickard, P. J. Hasnip, M. I. J. Probert, K. Refson, and M. C. Payne. First principles methods using CASTEP. *Z. Kristallogr.*, 220:567–570, 2005. DOI: 10.1524/zkri.220.5.567.65075.
- J. Claudot, W. J. Kim, A. Dixit, H. Kim, T. Gould, D. Rocca, and S. Lebègue. Benchmarking several van der Waals dispersion approaches for the description of intermolecular interactions. *J. Chem. Phys.*, 148:064112, 2018. DOI: 10.1063/1.5018818.
- C. Colella and A. F. Gualtieri. Cronstedt's zeolite. *Microporous Mesoporous Mater.*, 105:213–221, 2007. DOI: 10.1016/j.micromeso.2007.04.056.
- A. F. Combariza, D. A. Gomez, and G. Sastre. Simulating the properties of small pore silica zeolites using interatomic potentials. *Chem. Soc. Rev.*, 42:114–127, 2013. DOI: 10.1039/c2cs35243e.
- T. Conradsson, M. Dadachov, and X. Zou. Synthesis and structure of  $(\text{Me}_3\text{N})_6[\text{Ge}_{32}\text{O}_{64}](\text{H}_2\text{O})_{4.5}$ , a thermally stable novel zeotype with 3D interconnected 12-ring channels. *Microporous Mesoporous Mater.*, 41:183–191, 2000. DOI: 10.1016/S1387-1811(00)00288-2.
- D. S. Coombs, A. Alberti, T. Armbruster, G. Artioli, C. Colella, E. Galli, J. D. Grice, F. Liebau, J. A. Mandarino, H. Minato, E. H. Nickel, E. Passaglia, D. R. Peacor, S. Quartieri, R. Rinaldi, M. Ross, R. A. Sheppard, E. Tillmanns, and G. Vezzalini. Recommended nomenclature for zeolite minerals: report of the subcommittee on zeolites of the International Mineralogical Association, Commission on new Minerals and Mineral names. *Canad. Miner.*, 35:1571–1606, 1997. DOI: 10.1180/002646198547800.
- A. Corma, M. Puche, F. Rey, G. Sankar, and S. J. Teat. A zeolite structure (ITQ-13) with three sets of medium-pore crossing channels formed by 9- and 10-rings. *Angew. Chem. Int. Ed.*, 42:1156–1159, 2003. DOI: 10.1002/anie.200390304.
- A. Corma, F. Rey, J. Rius, M. J. Sabater, and S. Valencia. Supramolecular self-assembled molecules as organic directing agent for synthesis of zeolites. *Nature*, 431:287–290, 2004. DOI: 10.1038/nature02909.
- A. Corma, M. J. Díaz-Cabañas, J. L. Jordá, C. Martínez, and M. Moliner. High-throughput synthesis and catalytic properties of a molecular sieve with 18- and 10-member rings. *Nature*, 443:842–845, 2006. DOI: 10.1038/nature05238.
- D. L. Cortie, B. R. McBride, N. Narayanan, N. R. de Souza, M. Avdeev, R. A. Mole, G. J. McIntyre, G. J. Kearley, R. Withers, D. H. Yu, and Y. Liu. Time-Disordered Crystal Structure of  $\text{AlPO}_4\text{-5}$ . *J. Phys. Chem. C*, 121: 18762–18770, 2017. DOI: 10.1021/acs.jpcc.7b06415.
- F.-X. Coudert. Systematic investigation of the mechanical properties of pure silica zeolites: stiffness, anisotropy, and negative linear compressibility. *Phys. Chem. Chem. Phys.*, 15:16012–16018, 2013. DOI: 10.1039/c3cp51817e.
- F.-X. Coudert and D. Kohen. Molecular Insight into  $\text{CO}_2$  "Trapdoor" Adsorption in Zeolite Na-RHO. *Chem. Mater.*, 29:2724–2730, 2017. DOI: 10.1021/acs.chemmater.6b03837.
- F.-X. Coudert, F. Cailliez, R. Vuilleumier, A. H. Fuchs, and A. Boutin. Water nanodroplets confined in zeolite pores. *Faraday Discuss.*, 141:377–389, 2009. DOI: 10.1039/b804992k.

- A. F. Cronstedt. RÖN och BESKRIFNING Om en oberkant barg art, som kallas Zeolites. *Kongl. Vet. Acad. Handl. Stockholm*, 17:120, 1756.
- G. I. Csonka, A. Ruzsinszky, J. P. Perdew, and S. Grimme. Improved description of stereoelectronic effects in hydrocarbons using semilocal density functional theory. *J. Chem. Theory Comput.*, 4:888–891, 2008. DOI: 10.1021/ct800003n.
- C. S. Cundy and P. A. Cox. The Hydrothermal Synthesis of Zeolites: History and Development from the Earliest Days to the Present Time. *Chem. Rev.*, 103:663–702, 2003. DOI: 10.1021/cr020060i.
- M. Cutini, B. Civalleri, and P. Ugliengo. Cost-Effective Quantum Mechanical Approach for Predicting Thermodynamic and Mechanical Stability of Pure-Silica Zeolites. *ACS Omega*, 4:1838–1846, 2019. DOI: 10.1021/acsomega.8b03135.
- R. T. Cygan, J.-J. Liang, and A. G. Kalinichev. Molecular Models of Hydroxide, Oxyhydroxide, and Clay Phases and the Development of a General Force Field. *J. Phys. Chem. B*, 108:1255–1266, 2004. DOI: 10.1021/jp0363287.
- F. Daeyaert and M. W. Deem. Design of Organic Structure-Directing Agents for the Controlled Synthesis of Zeolites for Use in Carbon Dioxide/Methane Membrane Separations. *ChemPlusChem*, 85:277–284, 2020. DOI: 10.1002/cplu.201900679.
- P. Dauber-Osguthorpe, V. A. Roberts, D. J. Osguthorpe, J. Wolff, M. Genest, and A. T. Hagler. Structure and energetics of ligand binding to proteins: Escherichia coli dihydrofolate reductase-trimethoprim, a drug-receptor system. *Proteins*, 4:31–47, 1988. DOI: 10.1002/prot.340040106.
- C. J. Dawson, R. Sanchez-Smith, P. Rez, M. O’Keeffe, and M. M. J. Treacy. Ab Initio Calculations of the Energy Dependence of Si–O–Si Angles in Silica and Ge–O–Ge Angles in Germania Crystalline Systems. *Chem. Mater.*, 26:1523–1527, 2014. DOI: 10.1021/cm402814v.
- D. M. Dawson, R. F. Moran, and S. E. Ashbrook. An NMR Crystallographic Investigation of the Relationships between the Crystal Structure and <sup>29</sup>Si Isotropic Chemical Shift in Silica Zeolites. *J. Phys. Chem. C*, 121:15198–15210, 2017. DOI: 10.1021/acs.jpcc.7b03730.
- M. De la Pierre, R. Orlando, L. Maschio, K. Doll, P. Ugliengo, and R. Dovesi. Performance of six functionals (LDA, PBE, PBESOL, B3LYP, PBE0, and WC1LYP) in the simulation of vibrational and dielectric properties of crystalline compounds. The case of forsterite Mg<sub>2</sub>SiO<sub>4</sub>. *J. Comput. Chem.*, 32:1775–1784, 2011. DOI: 10.1002/jcc.21750.
- M. F. de Lange, K. J. F. M. Verouden, T. J. H. Vlugt, J. Gascon, and F. Kapteijn. Adsorption-Driven Heat Pumps: The Potential of Metal–Organic Frameworks. *Chem. Rev.*, 115:12205–12250, 2015. DOI: 10.1021/acs.chemrev.5b00059.
- D. J. De Ridder, J. Q. Verberk, S. G. Heijman, G. L. Amy, and J. C. Van Dijk. Zeolites for nitrosamine and pharmaceutical removal from demineralised and surface water: Mechanisms and efficacy. *Separ. Purif. Technol.*, 89:71–77, 2012. DOI: 10.1016/j.seppur.2012.01.025.
- E. de Vos Burchart, H. van Bekkum, B. van de Graaf, and E. T. C. Vogt. A consistent molecular mechanics force field for aluminophosphates. *J. Chem. Soc. Faraday Trans.*, 88:2761–2769, 1992a. DOI: 10.1039/ft9928802761.
- E. de Vos Burchart, V. Verheij, H. van Bekkum, and B. van de Graaf. A consistent molecular mechanics force field for all-silica zeolites. *Zeolites*, 12:183–189, 1992b. DOI: 10.1016/0144-2449(92)90082-Z.
- K. De Wispelaere, B. Ensing, A. Ghysels, E. J. Meijer, and V. Van Speybroeck. Complex Reaction Environments and Competing Reaction Mechanisms in Zeolite Catalysis: Insights from Advanced Molecular Dynamics. *Chem. Eur. J.*, 21:9385–9396, 2015. DOI: 10.1002/chem.201500473.
- K. De Wispelaere, C. S. Wondergem, B. Ensing, K. Hemelsoet, E. J. Meijer, B. M. Weckhuysen, V. V. Speybroeck, and J. Ruiz-Martínez. Insight into the Effect of Water on the Methanol-to-Olefins Conversion in H- SAPO-34

- from Molecular Simulations and in Situ Microspectroscopy. *ACS Catal.*, 6:1991–2002, 2016. DOI: 10.1021/acscatal.5b02139.
- M. W. Deem, R. Pophale, P. A. Cheeseman, and D. J. Earl. Computational Discovery of New Zeolite-Like Materials. *J. Phys. Chem. C*, 113:21353–21360, 2009. DOI: 10.1021/jp906984z.
- B. Delley. From molecules to solids with the DMol<sup>3</sup> approach. *J. Chem. Phys.*, 113:7756–7764, 2000. DOI: 10.1063/1.1316015.
- R. Demichelis, B. Civalleri, P. D’Arco, and R. Dovesi. Performance of 12 DFT functionals in the study of crystal systems: Al<sub>2</sub>SiO<sub>5</sub> orthosilicates and Al hydroxides as a case study. *Int. J. Quantum Chem.*, 110:2260–2273, 2010a. DOI: 10.1002/qua.22574.
- R. Demichelis, B. Civalleri, M. Ferrabone, and R. Dovesi. On the performance of eleven DFT functionals in the description of the vibrational properties of aluminosilicates. *Int. J. Quantum Chem.*, 110:406–415, 2010b. DOI: 10.1002/qua.22301.
- P. Demontis, J. Gulín-González, and G. B. Suffritti. Water Adsorbed in AlPO<sub>4</sub>-5 and SSZ-24 Studied by Molecular Dynamics Simulation. *J. Phys. Chem. C*, 116:11100–11109, 2012. DOI: 10.1021/jp3020782.
- M.-J. Díaz-Cabañas, P. A. Barrett, and M. A. Cambor. Synthesis and structure of pure SiO<sub>2</sub> chabazite: the SiO<sub>2</sub> polymorph with the lowest framework density. *Chem. Commun.*, pages 1881–1882, 1998. DOI: 10.1039/a804800b.
- E. Dib, M. Freire, V. Pralong, T. Mineva, and B. Alonso. Intermolecular interactions in AST zeolites through <sup>14</sup>N NMR and DFT calculations. *Acta Cryst. C*, 73:202–207, 2017. DOI: 10.1107/S2053229616017022.
- E. Dib, T. Mineva, E. Veron, V. Sarou-Kanian, F. Fayon, and B. Alonso. ZSM-5 Zeolite: Complete Al Bond Connectivity and Implications on Structure Formation from Solid-State NMR and Quantum Chemistry Calculations. *J. Phys. Chem. Lett.*, 9:19–24, 2018. DOI: 10.1021/acs.jpcllett.7b03050.
- M. Dion, H. Rydberg, E. Schroder, D. C. Langreth, and B. I. Lundqvist. Van der Waals density functional for general geometries. *Phys. Rev. Lett.*, 92:246401, 2004. DOI: 10.1103/PhysRevLett.92.246401.
- J. Dobson and B. Dinte. Constraint satisfaction in local and gradient susceptibility approximations: Application to a van der Waals density functional. *Phys. Rev. Lett.*, 76:1780–1783, 1996. DOI: 10.1103/PhysRevLett.76.1780.
- R. Dovesi, F. Pascale, B. Civalleri, K. Doll, N. M. Harrison, I. Bush, P. D’Arco, Y. Noël, M. Rérat, P. Carbonnière, M. Causà, S. Salustro, V. Lacivita, B. Kirtman, A. M. Ferrari, F. S. Gentile, J. Baima, M. Ferrero, R. Demichelis, and M. De La Pierre. The CRYSTAL code, 1976–2020 and beyond, a long story. *J. Chem. Phys.*, 152:204111, 2020. DOI: 10.1063/5.0004892.
- R. T. Downs, G. V. Gibbs, K. L. Bartelmehs, and M. B. Boisen. Variations of bond lengths and volumes of silicate tetrahedra with temperature. *Am. Miner.*, 77:751–757, 1992.
- D. Dubbeldam, S. Calero, T. J. H. Vlugt, R. Krishna, T. L. M. Maesen, E. Beerdsen, and B. Smit. Force Field Parametrization through Fitting on Inflection Points in Isotherms. *Phys. Rev. Lett.*, 93:088302, 2004. DOI: 10.1103/PhysRevLett.93.088302.
- B. Duncan, R. Szostak, K. Sorby, and J. G. Ulan. Organic-free VPI-5: Synthesis and characterization of AlPO<sub>4</sub>-H1. *Catal. Lett.*, 7:367–375, 1990. DOI: 10.1007/BF00764926.
- F. D’Yvoire. Étude des phosphates d’aluminium et de fer trivalent. I. L’orthophosphate neutre d’aluminium. *Bull. Soc. Chim. Fr.*, pages 1762–1776, 1961.
- T. Ennaert, J. Van Aelst, J. Dijkmans, R. De Clercq, W. Schutyser, M. Dusselier, D. Verboekend, and B. F. Sels. Potential and challenges of zeolite chemistry in the catalytic conversion of biomass. *Chem. Soc. Rev.*, 45:584–611, 2016. DOI: 10.1039/c5cs00859j.

- A. Erlebach, P. Nachtigall, and L. Grajciar. Accurate large-scale simulations of siliceous zeolites by neural network potentials. *npj Comput. Mater.*, 8:174, 2022. DOI: 10.1038/s41524-022-00865-w.
- M. Estermann, L. B. McCusker, C. Baerlocher, A. Merrouche, and H. Kessler. A synthetic gallophosphate molecular sieve with a 20-tetrahedral-atom pore opening. *Nature*, 352:320–323, 1991. DOI: 10.1038/352320a0.
- H. Fang, P. Kamakoti, J. Zang, S. Cundy, C. Paur, P. I. Ravikovitch, and D. S. Sholl. Prediction of CO<sub>2</sub> Adsorption Properties in Zeolites Using Force Fields Derived from Periodic Dispersion-Corrected DFT Calculations. *J. Phys. Chem. C*, 116:10692–10701, 2012. DOI: 10.1021/jp302433b.
- H. Fang, P. Kamakoti, P. I. Ravikovitch, M. Aronson, C. Paur, and D. S. Sholl. First principles derived, transferable force fields for CO<sub>2</sub> adsorption in Na-exchanged cationic zeolites. *Phys. Chem. Chem. Phys.*, 15:12882–12894, 2013. DOI: 10.1039/c3cp52246f.
- M. Fant, M. Ångqvist, A. Hellman, and P. Erhart. To Every Rule There is an Exception: A Rational Extension of Loewenstein’s Rule. *Angew. Chem. - Int. Ed.*, 60:5132–5135, 2021. DOI: 10.1002/anie.202013256.
- M. Fasano, G. Falciani, V. Brancato, V. Palomba, P. Asinari, E. Chiavazzo, and A. Frazzica. Atomistic modelling of water transport and adsorption mechanisms in silicoaluminophosphate for thermal energy storage. *Appl. Therm. Eng.*, 160:114075, 2019. DOI: 10.1016/j.applthermaleng.2019.114075.
- D. G. Fatouros, D. Douroumis, V. Nikolakis, S. Ntais, A. M. Moschovi, V. Trivedi, B. Khima, M. Roldo, H. Nazar, and P. A. Cox. In vitro and in silico investigations of drug delivery via zeolite BEA. *J. Mater. Chem.*, 21:7789–7794, 2011. DOI: 10.1039/c1jm10204d.
- M. Fauth, H. Jerg, K. Paintner, A. Reiter, and R. Rieger. Method for operating a dishwasher, German patent DE102008043548A1, 2008. URL: <https://patents.google.com/patent/DE102008043548A1/en>.
- E. O. Fetisov, M. S. Shah, J. R. Long, M. Tsapatsis, and J. I. Siepmann. First principles Monte Carlo simulations of unary and binary adsorption: CO<sub>2</sub>, N<sub>2</sub>, and H<sub>2</sub>O in Mg-MOF-74. *Chem. Comm.*, 54:10816–10819, 2018. DOI: 10.1039/C8CC06178E.
- M. Fischer. Computational evaluation of aluminophosphate zeotypes for CO<sub>2</sub>/N<sub>2</sub> separation. *Phys. Chem. Chem. Phys.*, 19:22801–22812, 2017. DOI: 10.1039/C7CP03841K.
- M. Fischer. Porous aluminophosphates as adsorbents for the separation of CO<sub>2</sub>/CH<sub>4</sub> and CH<sub>4</sub>/N<sub>2</sub> mixtures – a Monte Carlo simulation study. *Sustain. Energy & Fuels*, 2:1749–1763, 2018. DOI: 10.1039/C8SE00173A.
- M. Fischer. Simulation-based evaluation of zeolite adsorbents for the removal of emerging contaminants. *Mater. Adv.*, 1:86–98, 2020. DOI: 10.1039/D0MA00025F.
- M. Fischer and R. G. Bell. Influence of Zeolite Topology on CO<sub>2</sub>/N<sub>2</sub> Separation Behavior: Force-Field Simulations using a DFT-Derived Charge Model. *J. Phys. Chem. C*, 116:26449–26463, 2012. DOI: 10.1021/jp3099768.
- M. Fischer and R. G. Bell. Cation-exchanged SAPO-34 for adsorption-based hydrocarbon separations: Predictions from dispersion-corrected DFT calculations. *Phys. Chem. Chem. Phys.*, 16:21062–21072, 2014. DOI: 10.1039/C4CP01049C.
- R. X. Fischer, M. Sehovic, W. H. Baur, C. Paulmann, and T. M. Gesing. Crystal structure and morphology of fully hydrated zeolite Na-A. *Z. Kristallogr.*, 227:438–445, 2012. DOI: 10.1524/zkri.2012.1501.
- T. Fjermestad, S. Svelle, and O. Swang. Mechanistic Comparison of the Dealumination in SSZ-13 and the Desilication in SAPO-34. *J. Phys. Chem. C*, 117:13442–13451, 2013. DOI: 10.1021/jp4028468.
- T. Fjermestad, S. Svelle, and O. Swang. Mechanism of Si Island Formation in SAPO-34. *J. Phys. Chem. C*, 119:2086–2095, 2015a. DOI: 10.1021/jp510845z.
- T. Fjermestad, S. Svelle, and O. Swang. Desilication of SAPO-34: Reaction Mechanisms from Periodic DFT Calculations. *J. Phys. Chem. C*, 119:2073–2085, 2015b. DOI: 10.1021/jp510844v.
- E. M. Flanigen and R. L. Patton. Silica polymorph and process for preparing same, US Patent 4073865 A, 1978.

- E. M. Flanigen, R. L. Patton, and S. T. Wilson. Structural, Synthetic and Physicochemical Concepts in Aluminophosphate-Based Molecular Sieves. *Stud. Surf. Sci. Catal.*, 37:13–27, 1988. DOI: 10.1016/S0167-2991(09)60578-4.
- R. E. Fletcher, S. Ling, and B. Slater. Violations of Löwenstein's rule in zeolites. *Chem. Sci.*, 8:7483–7491, 2017. DOI: 10.1039/C7SC02531A.
- E. Fois and G. Tabacchi. Water in zeolite L and its MOF mimic. *Z. Kristallogr. - Cryst. Mater.*, 234:495–511, 2019. DOI: 10.1515/zkri-2018-2153.
- E. Fois, A. Gamba, G. Tabacchi, S. Quartieri, and G. Vezzalini. Water Molecules in Single File: First-Principles Studies of One-Dimensional Water Chains in Zeolites. *J. Phys. Chem. B*, 105:3012–3016, 2001a. DOI: 10.1021/jp002752l.
- E. Fois, A. Gamba, G. Tabacchi, S. Quartieri, and G. Vezzalini. On the collective properties of water molecules in one-dimensional zeolitic channels. *Phys. Chem. Chem. Phys.*, 3:4158–4163, 2001b. DOI: 10.1039/b102231h.
- E. Fois, A. Gamba, and A. Tilocca. Structure and Dynamics of the Flexible Triple Helix of Water inside VPI-5 Molecular Sieves. *J. Phys. Chem. B*, 106:4806–4812, 2002. DOI: 10.1021/jp014276k.
- E. Fois, A. Gamba, G. Tabacchi, R. Arletti, S. Quartieri, and G. Vezzalini. The "template" effect of the extra-framework content on zeolite compression: The case of yugawaralite. *Am. Miner.*, 90:28–35, 2005. DOI: 10.2138/am.2005.1653.
- M. D. Foster, A. Simperler, R. G. Bell, O. D. Friedrichs, F. A. A. Paz, and J. Klinowski. Chemically feasible hypothetical crystalline networks. *Nature Mater.*, 3:234–238, 2004. DOI: 10.1038/nmat1090.
- A. Freni, L. Bonaccorsi, L. Calabrese, A. Capri, A. Frazzica, and A. Sapienza. SAPO-34 coated adsorbent heat exchanger for adsorption chillers. *Appl. Therm. Eng.*, 82:1–7, 2015. DOI: 10.1016/j.applthermaleng.2015.02.052.
- D. Frenkel and B. Smit. *Understanding Molecular Simulation: From Algorithms to Applications*. Academic Press, San Diego, CA, USA, 2nd edition, 2002. DOI: 10.1016/B978-0-12-267351-1.X5000-7.
- R. L. Frost, M. L. Weier, K. L. Erickson, O. Carmody, and S. J. Mills. Raman spectroscopy of phosphates of the variscite mineral group. *J. Raman Spectr.*, 35:1047–1055, 2004. DOI: 10.1002/jrs.1251.
- A. H. Fuchs and A. K. Cheetham. Adsorption of Guest Molecules in Zeolitic Materials: Computational Aspects. *J. Phys. Chem. B*, 105:7375–7383, 2001. DOI: 10.1021/jp010702q.
- J. W. Furness, A. D. Kaplan, J. Ning, J. P. Perdew, and J. Sun. Accurate and Numerically Efficient  $r^2$ SCAN Meta-Generalized Gradient Approximation. *J. Phys. Chem. Lett.*, 11:8208–8215, 2020. DOI: 10.1021/acs.jpcclett.0c02405.
- C. A. Fyfe, D. H. Brouwer, A. R. Lewis, L. A. Villaescusa, and R. E. Morris. Combined solid state NMR and X-ray diffraction investigation of the local structure of the five-coordinate silicon in fluoride-containing as-synthesized STF zeolite. *J. Am. Chem. Soc.*, 124:7770–7778, 2002. DOI: 10.1021/ja012558s.
- J. D. Gale and N. J. Henson. Derivation of interatomic potentials for microporous aluminophosphates from the structure and properties of berlinite. *J. Chem. Soc. Faraday Trans.*, 90:3175–3179, 1994. DOI: 10.1039/ft9949003175.
- A. García-Sánchez, C. O. Ania, J. B. Parra, D. Dubbeldam, T. J. H. Vlugt, R. Krishna, and S. Calero. Transferable Force Field for Carbon Dioxide Adsorption in Zeolites. *J. Phys. Chem. C*, 113:8814–8820, 2009. DOI: 10.1021/jp810871f.
- K. F. Garrity, J. W. Bennett, K. M. Rabe, and D. Vanderbilt. Pseudopotentials for high-throughput DFT calculations. *Comput. Mater. Sci.*, 81:446–452, 2014. DOI: 10.1016/j.commatsci.2013.08.053.
- A. R. George and C. R. A. Catlow. An investigation into the effects of ion incorporation on the electronic structure of silicate fragments via ab initio computational techniques. *Chem. Phys. Lett.*, 247:408–417, 1995. DOI: 10.1016/S0009-2614(95)01141-2.



- A. R. George and C. R. A. Catlow. A computational study of the role of F<sup>-</sup> ions in the octadecasil structure. *Zeolites*, 18:67–70, 1997. DOI: 10.1016/S0144-2449(96)00113-3.
- A. Ghorbanpour, J. D. Rimer, and L. C. Grabow. Periodic, vdW-corrected density functional theory investigation of the effect of Al siting in H-ZSM-5 on chemisorption properties and site-specific acidity. *Catal. Commun.*, 52: 98–102, 2014. DOI: 10.1016/j.catcom.2014.04.005.
- A. Ghysels, S. L. Moors, K. Hemelsoet, K. De Wispelaere, M. Waroquier, G. Sastre, and V. Van Speybroeck. Shape-Selective Diffusion of Olefins in 8-Ring Solid Acid Microporous Zeolites. *J. Phys. Chem. C*, 119: 23721–23734, 2015. DOI: 10.1021/acs.jpcc.5b06010.
- P. Giannozzi, O. Barone, P. Bonfà, D. Brunato, R. Car, I. Carnimeo, C. Cavazzoni, S. de Gironcoli, P. Delugas, F. Ferrari Ruffino, A. Ferretti, N. Marzari, I. Timrov, A. Urru, and S. Baroni. QuantumESPRESSO toward the exascale. *J. Chem. Phys.*, 152:154105, 2020. DOI: 10.1063/5.0005082.
- M. G. Goesten, R. Hoffmann, F. M. Bickelhaupt, and E. J. M. Hensen. Eight-coordinate fluoride in a silicate double-four-ring. *Proc. Natl. Acad. Sci. U.S.A.*, 114:828–833, 2017. DOI: 10.1073/pnas.1615742114.
- A. Goj, D. S. Sholl, E. D. Akten, and D. Kohen. Atomistic Simulations of CO<sub>2</sub> and N<sub>2</sub> Adsorption in Silica Zeolites: The Impact of Pore Size and Shape. *J. Phys. Chem. B*, 106:8367–8375, 2002. DOI: 10.1021/jp025895b.
- D. Goldfarb, H. X. Li, and M. E. Davis. Dynamics of water molecules in VPI-5 and AlPO<sub>4</sub>-5 studied by deuterium NMR spectroscopy. *J. Am. Chem. Soc.*, 114:3690–3697, 1992. DOI: 10.1021/ja00036a018.
- F. Göttl and J. Hafner. Alkane adsorption in Na-exchanged chabazite: The influence of dispersion forces. *J. Chem. Phys.*, 134:064102, 2011. DOI: 10.1063/1.3549815.
- F. Göttl and J. Hafner. Structure and properties of metal-exchanged zeolites studied using gradient-corrected and hybrid functionals. I. Structure and energetics. *J. Chem. Phys.*, 136:064501, 2012. DOI: 10.1063/1.3676408.
- F. Göttl and J. Hafner. Modelling the adsorption of short alkanes in protonated chabazite: The impact of dispersion forces and temperature. *Microporous Mesoporous Mater.*, 166:176–184, 2013. DOI: 10.1016/j.micromeso.2012.04.052.
- F. Göttl, A. Grüneis, T. Bučko, and J. Hafner. Van der Waals interactions between hydrocarbon molecules and zeolites: Periodic calculations at different levels of theory, from density functional theory to the random phase approximation and Moller-Plesset perturbation theory. *J. Chem. Phys.*, 137:114111, 2012. DOI: 10.1063/1.4750979.
- T. Gould, S. Lebègue, J. G. Ángyán, and T. Bučko. A Fractionally Ionic Approach to Polarizability and van der Waals Many-Body Dispersion Calculations. *J. Chem. Theory Comput.*, 12:5920–5930, 2016. DOI: 10.1021/acs.jctc.6b00925.
- T. Gould, E. R. Johnson, and S. A. Tawfik. Are dispersion corrections accurate outside equilibrium? A case study on benzene. *Beilstein J. Org. Chem.*, 14:1181–1191, 2018. DOI: 10.3762/bjoc.14.99.
- M. A. Granato, T. J. H. Vlught, and A. E. Rodrigues. Molecular Simulation of Propane-Propylene Binary Adsorption Equilibrium in Zeolite 13X. *Ind. Eng. Chem. Res.*, 46:7239–7245, 2007. DOI: 10.1021/ie0705655.
- A. G. Greenaway, J. Shin, P. A. Cox, E. Shiko, S. P. Thompson, S. Brandani, S. B. Hong, and P. A. Wright. Structural changes of synthetic paulingite (Na,H-ECR-18) upon dehydration and CO<sub>2</sub> adsorption. *Z. Kristallogr. - Cryst. Mater.*, 230:223–231, 2015. DOI: 10.1515/zkri-2014-1824.
- I. V. Grenev, N. D. Klimkin, I. A. Shamanaeva, A. A. Shubin, I. A. Chetyrin, and V. Y. Gavrilov. A novel adsorption-based method for revealing the Si distribution in SAPO molecular sieves: The case of SAPO-11. *Microporous Mesoporous Mater.*, 328:111503, 2021. DOI: 10.1016/j.micromeso.2021.111503.
- T. Grey, J. Gale, D. Nicholson, and B. Peterson. A computational study of calcium cation locations and diffusion in chabazite. *Microporous Mesoporous Mater.*, 31:45–59, 1999. DOI: 10.1016/S1387-1811(99)00056-6.

- S. Grimme. Accurate description of van der Waals complexes by density functional theory including empirical corrections. *J. Comput. Chem.*, 25:1463–1473, 2004. DOI: 10.1002/jcc.20078.
- S. Grimme. Semiempirical GGA-type density functional constructed with a long-range dispersion correction. *J. Comput. Chem.*, 27:1787–1799, 2006. DOI: 10.1002/jcc.20495.
- S. Grimme, J. Antony, S. Ehrlich, and H. Krieg. A consistent and accurate ab initio parametrization of density functional dispersion correction (DFT-D) for the 94 elements H-Pu. *J. Chem. Phys.*, 132:154104, 2010. DOI: 10.1063/1.3382344.
- S. Grimme, A. Hansen, J. G. Brandenburg, and C. Bannwarth. Dispersion-Corrected Mean-Field Electronic Structure Methods. *Chem. Rev.*, 116:5105–5154, 2016. DOI: 10.1021/acs.chemrev.5b00533.
- P. J. Grobet, J. A. Martens, I. Balakrishnan, M. Mertens, and P. A. Jacobs. The very large pore molecular sieve VPI-5: An aluminophosphate-hydrate! *Appl. Catal.*, 56:L21–L27, 1989. DOI: 10.1016/S0166-9834(00)80152-9.
- P. Haas, F. Tran, and P. Blaha. Calculation of the lattice constant of solids with semilocal functionals. *Phys. Rev. B*, 79:085104, 2009. DOI: 10.1103/PhysRevB.79.085104.
- I. Hamada. van der Waals density functional made accurate. *Phys. Rev. B*, 89:121103, 2014. DOI: 10.1103/PhysRevB.89.121103.
- M. M. Harding and B. M. Kariuki. Microcrystal structure determination of AlPO<sub>4</sub>-CHA using synchrotron radiation. *Acta Cryst. C*, 50:852–854, 1994. DOI: 10.1107/S0108270194000326.
- A. Hauer and F. Fischer. Open Adsorption System for an Energy Efficient Dishwasher. *Chem. Ing. Tech.*, 83:61–66, 2011. DOI: 10.1002/cite.201000197.
- H. Hay, G. Ferlat, M. Casula, A. P. Seitsonen, and F. Mauri. Dispersion effects in SiO<sub>2</sub> polymorphs: An *ab initio* study. *Phys. Rev. B*, 92:144111, 2015. DOI: 10.1103/PhysRevB.92.144111.
- C. J. Heard, L. Grajciar, and P. Nachtigall. The effect of water on the validity of Löwenstein’s rule. *Chem. Sci.*, 10: 5705–5711, 2019. DOI: 10.1039/C9SC00725C.
- S. Henninger, F. Schmidt, and H.-M. Henning. Water adsorption characteristics of novel materials for heat transformation applications. *Appl. Therm. Eng.*, 30:1692–1702, 2010. DOI: 10.1016/j.applthermaleng.2010.03.028.
- S. Henninger, G. Munz, K.-F. Ratzsch, and P. Schossig. Cycle stability of sorption materials and composites for the use in heat pumps and cooling machines. *Renewable Energy*, 36:3043–3049, 2011a. DOI: 10.1016/j.renene.2011.03.032.
- S. K. Henninger, F. P. Schmidt, and H.-M. Henning. Characterisation and improvement of sorption materials with molecular modeling for the use in heat transformation applications. *Adsorption*, 17:833–843, 2011b. DOI: 10.1007/s10450-011-9342-6.
- S. K. Henninger, F. Jeremias, H. Kummer, P. Schossig, and H.-M. Henning. Novel Sorption Materials for Solar Heating and Cooling. *Energy Procedia*, 30:279–288, 2012. DOI: 10.1016/j.egypro.2012.11.033.
- N. J. Henson, A. K. Cheetham, and J. D. Gale. Theoretical Calculations on Silica Frameworks and Their Correlation with Experiment. *Chem. Mater.*, 6:1647–1650, 1994. DOI: 10.1021/cm00046a015.
- N. J. Henson, A. K. Cheetham, and J. D. Gale. Computational studies of aluminum phosphate polymorphs. *Chem. Mater.*, 8:664–670, 1996. DOI: 10.1021/cm9503238.
- J. Hermann, R. A. DiStasio, and A. Tkatchenko. First-Principles Models for van der Waals Interactions in Molecules and Materials: Concepts, Theory, and Applications. *Chem. Rev.*, 117:4714–4758, 2017. DOI: 10.1021/acs.chemrev.6b00446.
- A. J. Hernández-Maldonado and R. T. Yang. Desulfurization of transportation fuels by adsorption. *Catal. Rev. Sci. Eng.*, 46:111–150, 2004. DOI: 10.1081/CR-200032697.

- G. Herrera-Perez, C. Zicovich-Wilson, and A. Ramirez-Solis. Periodic DFT Studies of AlPO-11: The Role of Hydration on Structural Properties. *J. Phys. Chem. C*, 111:9664–9670, 2007. DOI: 10.1021/jp072004x.
- E. P. Hessou, W. G. Kanhounon, D. Rocca, H. Monnier, C. Vallières, S. Lebègue, and M. Badawi. Adsorption of NO, NO<sub>2</sub>, CO, H<sub>2</sub>O and CO<sub>2</sub> over isolated monovalent cations in faujasite zeolite: a periodic DFT investigation. *Theor. Chem. Acc.*, 137:161, 2018. DOI: 10.1007/s00214-018-2373-2.
- E. P. Hessou, M. Ponce-Vargas, J.-B. Mensah, F. Tielens, J. C. Santos, and M. Badawi. Dibenzyl Disulfide Adsorption on Cationic Exchanged Faujasites: A DFT Study. *Nanomaterials*, 9:715, 2019. DOI: 10.3390/nano9050715.
- F. M. Higgins, G. W. Watson, and S. C. Parker. Effect of Lattice Relaxation on Cation Exchange in Zeolite A Using Computer Simulation. *J. Phys. Chem. B*, 101:9964–9972, 1997. DOI: 10.1021/jp971752r.
- J.-R. Hill, A. R. Minihan, E. Wimmer, and C. J. Adams. Framework dynamics including computer simulations of the water adsorption isotherm of zeolite Na-MAP. *Phys. Chem. Chem. Phys.*, 2:4255–4264, 2000. DOI: 10.1039/b003771k.
- A. Hoffman, M. Deluca, and D. Hibbitts. Restructuring of MFI Framework Zeolite Models and Their Associated Artifacts in Density Functional Theory Calculations. *J. Phys. Chem. C*, 123:6572–6585, 2019. DOI: 10.1021/acs.jpcc.8b12230.
- P. Hohenberg and W. Kohn. Inhomogeneous Electron Gas. *Phys. Rev.*, 136:B864–B871, 1964. DOI: 10.1103/PhysRev.136.B864.
- J. M. Hu, J. P. Zhai, F. M. Wu, and Z. K. Tang. Molecular dynamics study of the structures and dynamics of the iodine molecules confined in AlPO<sub>4</sub>-11 crystals. *J. Phys. Chem. B*, 114:16481–16486, 2010. DOI: 10.1021/jp1076615.
- Z. Huang, S. Seo, J. Shin, B. Wang, R. G. Bell, S. B. Hong, and X. Zou. 3D-3D topotactic transformation in aluminophosphate molecular sieves and its implication in new zeolite structure generation. *Nature Commun.*, 11:3762, 2020. DOI: 10.1038/s41467-020-17586-7.
- Z. Huang, T. Willhammar, and X. Zou. Three-dimensional electron diffraction for porous crystalline materials: structural determination and beyond. *Chem. Sci.*, 12:1206–1219, 2021. DOI: 10.1039/d0sc05731b.
- W. Humphrey, A. Dalke, and K. Schulten. VMD - Visual Molecular Dynamics. *J. Molec. Graph.*, 14:33–38, 1996. DOI: 10.1016/0263-7855(96)00018-5.
- H. K. Hunt, C. M. Lew, M. Sun, Y. Yan, and M. E. Davis. Pure-silica LTA, CHA, STT, ITW, and -SVR thin films and powders for low-k applications. *Microporous Mesoporous Mater.*, 130:49–55, 2010. DOI: 10.1016/j.micromeso.2009.10.011.
- J. Ireta, J. Neugebauer, and M. Scheffler. On the Accuracy of DFT for Describing Hydrogen Bonds: Dependence on the Bond Directionality. *J. Phys. Chem: A*, 108:5692–5698, 2004. DOI: 10.1021/jp0377073.
- R. A. Jackson and C. R. A. Catlow. Computer Simulation Studies of Zeolite Structure. *Mol. Simul.*, 1:207–224, 1988. DOI: 10.1016/S0167-2991(08)60525-X.
- J. Jänchen and H. Stach. Shaping adsorption properties of nano-porous molecular sieves for solar thermal energy storage and heat pump applications. *Solar Energy*, 104:16–18, 2014. DOI: 10.1016/j.solener.2013.07.018.
- J. Jänchen, D. Ackermann, E. Weiler, H. Stach, and W. Brösicke. Calorimetric investigation on zeolites, AlPO<sub>4</sub>s and CaCl<sub>2</sub> impregnated attapulgitite for thermochemical storage of heat. *Thermochimica Acta*, 434:37–41, 2005. DOI: 10.1016/j.tca.2005.01.009.
- Y. Jeanvoine, J. G. Ángyán, G. Kresse, and J. Hafner. Brønsted Acid Sites in HSAPO-34 and Chabazite: An Ab Initio Structural Study. *J. Phys. Chem. B*, 102:5573–5580, 1998a. DOI: 10.1021/jp980341n.

- Y. Jeanvoine, J. G. Ángyán, G. Kresse, and J. Hafner. On the Nature of Water Interacting with Brønsted Acidic Sites. Ab Initio Molecular Dynamics Study of Hydrated HSAPO-34. *J. Phys. Chem. B*, 102:7307–7310, 1998b. DOI: 10.1021/jp981667z.
- J. Jiang, J. L. Jorda, M. J. Diaz-Cabanas, J. Yu, and A. Corma. The Synthesis of an Extra-Large-Pore Zeolite with Double Three-Ring Building Units and a Low Framework Density. *Angew. Chem. Int. Ed.*, 49:4986–4988, 2010. DOI: 10.1002/anie.201001506.
- R. D. E. Johnson. NIST Computational Chemistry Comparison and Benchmark Database, Release 22 (May 2022), Standard Reference Database 101, 2022. URL: <http://cccbdb.nist.gov/>.
- A. J. Jones and E. Iglesia. The Strength of Brønsted Acid Sites in Microporous Aluminosilicates. *ACS Catal.*, 5: 5741–5755, 2015. DOI: 10.1021/acscatal.5b01133.
- J. L. Jordá, L. B. McCusker, C. Baerlocher, C. M. Morais, J. Rocha, C. Fernandez, C. Borges, J. P. Lourenço, M. F. Ribeiro, and Z. Gabelica. Structure analysis of the novel microporous aluminophosphate IST-1 using synchrotron powder diffraction data and HETCOR MAS NMR. *Microporous Mesoporous Mater.*, 65:43–57, 2003. DOI: 10.1016/S1387-1811(03)00499-2.
- P. Jurečka, J. Černý, P. Hobza, and D. R. Salahub. Density functional theory augmented with an empirical dispersion term. Interaction energies and geometries of 80 noncovalent complexes compared with ab initio quantum mechanics calculations. *J. Comput. Chem.*, 28:555–569, 2007. DOI: 10.1002/jcc.20570.
- G. N. Kalantzopoulos, F. Lundvall, K. Thorshaug, A. Lind, P. Vajeeston, I. Dovgaliuk, B. Arstad, D. S. Wragg, and H. Fjellvåg. Factors Determining Microporous Material Stability in Water: The Curious Case of SAPO-37. *Chem. Mater.*, 32:1495–1505, 2020. DOI: 10.1021/acs.chemmater.9b04510.
- P. Kamakoti and T. A. Barckholtz. Role of Germanium in the Formation of Double Four Rings in Zeolites. *J. Phys. Chem. C*, 111:3575–3583, 2007. DOI: 10.1021/jp065092e.
- N. Katada, K. Nouno, J. K. Lee, J. Shin, S. B. Hong, and M. Niwa. Acidic Properties of Cage-Based, Small-Pore Zeolites with Different Framework Topologies and Their Silicoaluminophosphate Analogues. *J. Phys. Chem. C*, 115:22505–22513, 2011. DOI: 10.1021/jp207894n.
- E. Keller, W. Meier, and R. M. Kirchner. Synthesis, structures of  $\text{AlPO}_4\text{-C}$  and  $\text{AlPO}_4\text{-D}$ , and their topotactic transformation. *Solid State Ionics*, 43:93–102, 1990. DOI: 10.1016/0167-2738(90)90475-7.
- R. Khouzami, G. Coudurier, F. Lefebvre, J. C. Vedrine, and B. F. Mentzen. X-ray diffraction and solid-state n.m.r. studies of AEL molecular sieves: Effect of hydration. *Zeolites*, 10:183–188, 1990. DOI: 10.1016/0144-2449(90)90043-Q.
- J. Kim, L.-C. Lin, R. L. Martin, J. A. Swisher, M. Haranczyk, and B. Smit. Large-scale computational screening of zeolites for ethane/ethene separation. *Langmuir*, 28:11914–11919, 2012. DOI: 10.1021/la302230z.
- J. Kim, M. Abouelnasr, L.-C. Lin, and B. Smit. Large-scale screening of zeolite structures for  $\text{CO}_2$  membrane separations. *J. Am. Chem. Soc.*, 135:7545–7552, 2013. DOI: 10.1021/ja400267g.
- J. Klimeš and D. P. Tew. Efficient and accurate description of adsorption in zeolites. *J. Chem. Phys.*, 151:234108, 2019. DOI: 10.1063/1.5123425.
- J. Klimeš, M. Kaltak, E. Maggio, and G. Kresse. Singles correlation energy contributions in solids. *J. Chem. Phys.*, 143:102816, 2015. DOI: 10.1063/1.4929346.
- J. Klimeš, D. Bowler, and A. Michaelides. Chemical accuracy for the van der Waals density functional. *J. Phys.: Cond. Matt.*, 22:022201, 2010. DOI: 10.1088/0953-8984/22/2/022201.
- R. Kniep and D. Mootz. Metavariscite – a redetermination of its crystal structure. *Acta Cryst. B*, 29:2292–2294, 1973. DOI: 10.1107/S0567740873006503.
- R. Kniep, D. Mootz, and A. Vegas. Variscite. *Acta Cryst. B*, 33:263–265, 1977. DOI: 10.1107/S056774087700329X.

- P.-P. Knops-Gerrits, H. Toufar, X.-Y. Li, P. Grobet, R. A. Schoonheydt, P. A. Jacobs, and W. A. Goddard. The Structure of Water in Crystalline Aluminophosphates: Isolated Water and Intermolecular Clusters Probed by Raman Spectroscopy, NMR and Structural Modeling. *J. Phys. Chem. A*, 104:2410–2422, 2000. DOI: 10.1021/jp990817i.
- B. C. Knott, C. T. Nimlos, D. J. Robichaud, M. R. Nimlos, S. Kim, and R. Gounder. Consideration of the Aluminum Distribution in Zeolites in Theoretical and Experimental Catalysis Research. *ACS Catal.*, 8:770–784, 2018. DOI: 10.1021/acscatal.7b03676.
- T. Kohler, M. Hinze, K. Müller, and W. Schwieger. Temperature independent description of water adsorption on zeotypes showing a type V adsorption isotherm. *Energy*, 135:227–236, 2017. DOI: 10.1016/j.energy.2017.06.115.
- W. Kohn and L. Sham. Self-Consistent Equations Including Exchange and Correlation Effects. *Phys. Rev.*, 140:A1133–A1138, 1965. DOI: 10.1103/PhysRev.140.A1133.
- W. Kohn, Y. Meir, and D. E. Makarov. van der Waals Energies in Density Functional Theory. *Phys. Rev. Lett.*, 80:4153–4156, 1998. DOI: 10.1103/PhysRevLett.80.4153.
- H. Koller, R. F. Lobo, S. L. Burkett, and M. E. Davis. SiO<sup>-</sup> · · · HOSi Hydrogen Bonds in As-Synthesized High-Silica Zeolites. *J. Phys. Chem.*, 99:12588–12596, 1995. DOI: 10.1021/j100033a036.
- H. Koller, A. Wölker, H. Eckert, C. Panz, and P. Behrens. Five-Coordinate Silicon in Zeolites: Probing SiO<sub>4/2</sub>F<sup>-</sup> Sites in Nonasil and ZSM-5 with <sup>29</sup>Si Solid-state NMR Spectroscopy. *Angew. Chem. Int. Ed.*, 36:2823–2825, 1997. DOI: 10.1002/anie.199728231.
- H. Koller, A. Wölker, L. A. Villaescusa, M. J. Diaz-Cabañas, S. Valencia, and M. A. Cambor. Five-coordinate silicon in high-silica zeolites. *J. Am. Chem. Soc.*, 121:3368–3376, 1999. DOI: 10.1021/ja9840549.
- J. Kornatowski, G. Zadrozna, J. Wloch, and M. Rozwadowski. Compositional Heterogeneity of CrAPO-5 with Neutral Framework: Effect on Sorption Properties in Comparison to Other MeAPO-5 with Charged Frameworks and Analytical Evaluation of Adsorption Potentials. *Langmuir*, 15:5863–5869, 1999. DOI: 10.1021/la981419u.
- B. Koubaisy, G. Joly, I. Batonneau-Gener, and P. Magnoux. Adsorptive Removal of Aromatic Compounds Present in Wastewater by Using Dealuminated Faujasite Zeolite. *Ind. Eng. Chem. Res.*, 50:5705–5713, 2011. DOI: 10.1021/ie100420q.
- A. Krajnc, J. Varlec, M. Mazaj, A. Ristić, N. Z. Logar, and G. Mali. Superior Performance of Microporous Aluminophosphate with LTA Topology in Solar-Energy Storage and Heat Reallocation. *Adv. Energy Mater.*, 7:1601815, 2017. DOI: 10.1002/aenm.201601815.
- G. J. Kramer, A. J. M. De Man, and R. A. Van Santen. Zeolites versus aluminosilicate clusters: the validity of a local description. *J. Am. Chem. Soc.*, 113:6435–6441, 1991. DOI: 10.1021/ja00017a012.
- A. Kremleva, T. Vogt, and N. Rösch. Monovalent Cation-Exchanged Natrolites and Their Behavior under Pressure. A Computational Study. *J. Phys. Chem. C*, 117:19020–19030, 2013. DOI: 10.1021/jp406037c.
- A. Kremleva, T. Vogt, and N. Rösch. Potassium-Exchanged Natrolite Under Pressure. Computational Study vs Experiment. *J. Phys. Chem. C*, 118:22030–22039, 2014. DOI: 10.1021/jp505973r.
- G. Kresse and J. Furthmüller. Efficient iterative schemes for ab initio total-energy calculations using a plane-wave basis set. *Phys. Rev. B*, 54:11169–11186, 1996a. DOI: 10.1103/PhysRevB.54.11169.
- G. Kresse and J. Furthmüller. Efficiency of ab-initio total energy calculations for metals and semiconductors using a plane-wave basis set. *Comput. Mater. Sci.*, 6:15–50, 1996b. DOI: 10.1016/0927-0256(96)00008-0.
- G. Kresse and D. Joubert. From ultrasoft pseudopotentials to the projector augmented-wave method. *Phys. Rev. B*, 59:1758–1775, 1999. DOI: 10.1103/PhysRevB.59.1758.

- R. Krishna. Diffusion in porous crystalline materials. *Chem. Soc. Rev.*, 41:3099–3118, 2012. DOI: 10.1039/c2cs15284c.
- R. Krishna and J. M. van Baten. In silico screening of zeolite membranes for CO<sub>2</sub> capture. *J. Membr. Sci.*, 360: 323–333, 2010. DOI: 10.1016/j.memsci.2010.05.032.
- T. D. Kühne, M. Iannuzzi, M. Del Ben, V. V. Rybkin, P. Seewald, F. Stein, T. Laino, R. Z. Khaliullin, O. Schütt, F. Schiffmann, D. Golze, J. Wilhelm, S. Chulkov, M. H. Bani-Hashemian, V. Weber, U. Borštnik, M. Taillefumier, A. S. Jakobovits, A. Lazzaro, H. Pabst, T. Müller, R. Schade, M. Guidon, S. Andermatt, N. Holmberg, G. K. Schenter, A. Hehn, A. Bussy, F. Belleflamme, G. Tabacchi, A. Glöß, M. Lass, I. Bethune, C. J. Mundy, C. Plessl, M. Watkins, J. VandeVondele, M. Krack, and J. Hutter. CP2K: An electronic structure and molecular dynamics software package - Quickstep: Efficient and accurate electronic structure calculations. *J. Chem. Phys.*, 152: 194103, 2020. DOI: 10.1063/5.0007045.
- S. Kulprathipanja, editor. *Zeolites in Industrial Separation and Catalysis*. Wiley-VCH Verlag GmbH & Co. KGaA, Weinheim, Germany, 2010. DOI: 10.1002/9783527629565.
- K. Kunii, K. Narahara, and S. Yamanaka. Template-free synthesis and adsorption properties of microporous crystal AlPO<sub>4</sub>-H3. *Microporous Mesoporous Mater.*, 50:181–185, 2001. DOI: 10.1016/S1387-1811(01)00450-4.
- Å. Kvik and K. Ståhl. A neutron diffraction study of the bonding of zeolitic water in scolecite at 20 K. *Z. Kristallogr.*, 171:141–154, 1985. DOI: 10.1524/zkri.1985.171.14.141.
- Å. Kvik, G. Artioli, and J. V. Smith. Neutron diffraction study of the zeolite yugawaralite at 13 K. *Z. Kristallogr.*, 174:265–281, 1986. DOI: 10.1524/zkri.1986.174.1-4.265.
- F. Labat, A. H. Fuchs, and C. Adamo. Toward an Accurate Modeling of the Water–Zeolite Interaction: Calibrating the DFT Approach. *J. Phys. Chem. Lett.*, 1:763–768, 2010. DOI: 10.1021/jz100011p.
- F. Lagno and G. P. Demopoulos. Synthesis of Hydrated Aluminum Phosphate AlPO<sub>4</sub> · 1.5H<sub>2</sub>O (AlPO<sub>4</sub>-H3 by Controlled Reactive Crystallization in Sulfate Media. *Ind. Eng. Chem. Res.*, 44:8033–8038, 2005. DOI: 10.1021/ie0505559.
- A. V. Larin, D. N. Trubnikov, and D. P. Vercauteren. Influence of hydrogen bonding on the properties of water molecules adsorbed in zeolite frameworks. *Int. J. Quantum Chem.*, 92:71–84, 2003. DOI: 10.1002/qua.10496.
- A. V. Larin, D. N. Trubnikov, and D. P. Vercauteren. Improvement of X-ray diffraction geometries of water physisorbed in zeolites on the basis of periodic Hartree-Fock calculations. *Int. J. Quantum Chem.*, 102:971–979, 2005. DOI: 10.1002/qua.20463.
- L. Leardini, S. Quartieri, A. Martucci, G. Vezzalini, and V. Dmitriev. Compressibility of microporous materials with CHA topology: 2. ALPO-34. *Z. Kristallogr. - Cryst. Mater.*, 227:514–521, 2012. DOI: 10.1524/zkri.2012.1477.
- C. Lee, W. Yang, and R. G. Parr. Development of the Colle-Salvetti correlation-energy formula into a functional of the electron density. *Phys. Rev. B*, 37:785–789, 1988. DOI: 10.1103/PhysRevB.37.785.
- J. K. Lee, J. Shin, N. H. Ahn, A. Turrina, M. B. Park, Y. Byun, S. J. Cho, P. A. Wright, and S. B. Hong. A Family of Molecular Sieves Containing Framework-Bound Organic Structure-Directing Agents. *Angew. Chem. Int. Ed.*, 54: 11097–11101, 2015. DOI: 10.1002/anie.201504416.
- J. K. Lee, J. H. Lee, N. H. Ahn, K. H. Cho, and S. B. Hong. Solid solution of a zeolite and a framework-bound OSDA-containing molecular sieve. *Chem. Sci.*, 7:5805–5814, 2016. DOI: 10.1039/C6SC02092E.
- K. Lee, E. D. Murray, L. Kong, B. I. Lundqvist, and D. C. Langreth. Higher-accuracy van der Waals density functional. *Phys. Rev. B*, 82:081101, 2010. DOI: 10.1103/PhysRevB.82.081101.
- K. Lejaeghere, G. Bihlmayer, T. Bjorkman, P. Blaha, S. Blugel, V. Blum, D. Caliste, I. E. Castelli, S. J. Clark, A. Dal Corso, S. de Gironcoli, T. Deutsch, J. K. Dewhurst, I. Di Marco, C. Draxl, M. Du ak, O. Eriksson, J. A. Flores-Livas, K. F. Garrity, L. Genovese, P. Giannozzi, M. Giantomassi, S. Goedecker, X. Gonze, O. Granas, E. K. U. Gross, A. Gulans, F. Gygi, D. R. Hamann, P. J. Hasnip, N. A. W. Holzwarth, D. Iu an, D. B. Jochym,

- F. Jollet, D. Jones, G. Kresse, K. Koepernik, E. Kucukbenli, Y. O. Kvashnin, I. L. M. Locht, S. Lubeck, M. Marsman, N. Marzari, U. Nitzsche, L. Nordstrom, T. Ozaki, L. Paulatto, C. J. Pickard, W. Poelmans, M. I. J. Probert, K. Refson, M. Richter, G.-M. Rignanese, S. Saha, M. Scheffler, M. Schlipf, K. Schwarz, S. Sharma, F. Tavazza, P. Thunstrom, A. Tkatchenko, M. Torrent, D. Vanderbilt, M. J. van Setten, V. Van Speybroeck, J. M. Wills, J. R. Yates, G.-X. Zhang, and S. Cottenier. Reproducibility in density functional theory calculations of solids. *Science*, 351:aad3000, 2016. DOI: 10.1126/science.aad3000.
- D. W. Lewis, D. J. Willock, C. R. A. Catlow, J. M. Thomas, and G. J. Hutchings. De novo design of structure-directing agents for the synthesis of microporous solids. *Nature*, 382:604–606, 1996. DOI: 10.1038/382604a0.
- D. W. Lewis, G. Sankar, J. K. Wyles, J. M. Thomas, C. R. A. Catlow, and D. J. Willock. Synthesis of a Small-Pore Microporous Material Using a Computationally Designed Template. *Angew. Chem. Int. Ed.*, 36:2675–2677, 1997. DOI: 10.1002/anie.199726751.
- D. W. Lewis, A. R. Ruiz-Salvador, N. Almora-Barrios, A. Gómez, and M. Mistry. Modelling of hydrated Ca-rich zeolites. *Mol. Simul.*, 28:649–661, 2002. DOI: 10.1080/08927020210871.
- G. Li and E. A. Pidko. The Nature and Catalytic Function of Cation Sites in Zeolites: a Computational Perspective. *ChemCatChem*, 11:134–156, 2019. DOI: 10.1002/cctc.201801493.
- H. Li and O. M. Yaghi. Transformation of Germanium Dioxide to Microporous Germanate 4-Connected Nets. *J. Am. Chem. Soc.*, 120:10569–10570, 1998. DOI: 10.1021/ja982384n.
- H. Li, C. Paolucci, and W. F. Schneider. Zeolite Adsorption Free Energies from ab Initio Potentials of Mean Force. *J. Chem. Theory Comput.*, 14:929–938, 2018. DOI: 10.1021/acs.jctc.7b00716.
- Q. Li, A. Navrotsky, F. Rey, and A. Corma. Thermochemistry of  $(\text{Ge}_x\text{Si}_{1-x})\text{O}_2$  zeolites. *Microporous Mesoporous Mater.*, 59:177–183, 2003. DOI: 10.1016/S1387-1811(03)00309-3.
- Q. Li, A. Navrotsky, F. Rey, and A. Corma. Enthalpies of formation of Ge-zeolites: ITQ-21 and ITQ-22. *Microporous Mesoporous Mater.*, 74:87–92, 2004. DOI: 10.1016/j.micromeso.2004.06.010.
- Y. Li, X. Li, J. Liu, F. Duan, and J. Yu. In silico prediction and screening of modular crystal structures via a high-throughput genomic approach. *Nature Commun.*, 6:8328, 2015. DOI: 10.1038/ncomms9328.
- Y. Li, H. Li, F. C. Pickard, B. Narayanan, F. G. Sen, M. K. Y. Chan, S. K. R. S. Sankaranarayanan, B. R. Brooks, and B. Roux. Machine Learning Force Field Parameters from Ab Initio Data. *J. Chem. Theory Comput.*, 13:4492–4503, 2017. DOI: 10.1021/acs.jctc.7b00521.
- J. Lima-de Faria, E. Hellner, F. Liebau, E. Makovicky, and E. Parthé. Nomenclature of inorganic structure types. Report of the International Union of Crystallography Commission on Crystallographic Nomenclature Subcommittee on the Nomenclature of Inorganic Structure Types. *Acta Cryst. A*, 46:1–11, 1990. DOI: 10.1107/S0108767389008834.
- L.-C. Lin, A. H. Berger, R. L. Martin, J. Kim, J. A. Swisher, K. Jariwala, C. H. Rycroft, A. S. Bhowan, M. W. Deem, M. Haranczyk, and B. Smit. In silico screening of carbon-capture materials. *Nature Mater.*, 11:633–641, 2012. DOI: 10.1038/nmat3336.
- B. Liu, Y. Zheng, N. Hu, T. Gui, Y. Li, F. Zhang, R. Zhou, X. Chen, and H. Kita. Synthesis of low-silica CHA zeolite chabazite in fluoride media without organic structural directing agents and zeolites. *Microporous Mesoporous Mater.*, 196:270–276, 2014. DOI: 10.1016/j.micromeso.2014.05.019.
- X. Liu, U. Ravon, and A. Tuel. Evidence for  $\text{F}^-/\text{SiO}^-$  Anion Exchange in the Framework of As-Synthesized All-Silica Zeolites. *Angew. Chem. Int. Ed.*, 50:5900–5903, 2011a. DOI: 10.1002/anie.201101237.
- X. Liu, U. Ravon, and A. Tuel. Fluoride removal from double four-membered ring (D4R) units in As-synthesized Ge-containing zeolites. *Chem. Mater.*, 23:5052–5057, 2011b. DOI: 10.1021/cm2025735.

- Y. Liu and R. L. Withers. Rigid unit modes (RUMs) of distortion, local crystal chemistry and the inherent displacive flexibility of microporous  $\text{AlPO}_4$ -11. *J. Solid State Chem.*, 172:431–437, 2003. DOI: 10.1016/S0022-4596(03)00024-0.
- Y. Liu, R. L. Withers, and L. Norén. An electron diffraction, XRD and lattice dynamical investigation of the average structure and rigid unit mode (RUM) modes of distortion of microporous  $\text{AlPO}_4$ -5. *Solid State Sci.*, 5: 427–434, 2003. DOI: 10.1016/S1293-2558(03)00049-9.
- W. Loewenstein. The distribution of aluminum in the tetrahedra of silicates and aluminates. *Am. Miner.*, 39:92–96, 1954.
- T. Loiseau and G. Férey. Crystalline oxyfluorinated open-framework compounds: Silicates, metal phosphates, metal fluorides and metal-organic frameworks (MOF). *J. Fluor. Chem.*, 128:413–422, 2007. DOI: 10.1016/j.jfluchem.2006.09.009.
- P. Lu, L. Gómez-Hortigüela, and M. A. Cambor. Synthesis of Pure Silica MWW Zeolite in Fluoride Medium by Using an Imidazolium-Based Long Dication. *Chem. Eur. J.*, 25:1561–1572, 2019. DOI: 10.1002/chem.201804973.
- S. M. P. Lucena, R. Q. Snurr, and C. L. Cavalcante. Studies on adsorption equilibrium of xylenes in AEL framework using biased GCMC and energy minimization. *Microporous Mesoporous Mater.*, 111:89–96, 2008. DOI: 10.1016/j.micromeso.2007.07.021.
- A. Luna-Triguero, P. Gómez-Álvarez, and S. Calero. Adsorptive process design for the separation of hexane isomers using zeolites. *Phys. Chem. Chem. Phys.*, 19:5037–5042, 2017. DOI: 10.1039/C6CP08025A.
- S. Mal, A. Ristić, A. Golobič, and N. Zabukovec Logar. Tailoring Water Adsorption Capacity of APO-Tric. *Crystals*, 11:773, 2021. DOI: 10.3390/cryst11070773.
- P. P. Man, M. Briend, M. J. Peltre, A. Lamy, P. Beaunier, and D. Barthomeuf. A topological model for the silicon incorporation in SAPO-37 molecular sieves: Correlations with acidity and catalysis. *Zeolites*, 11:563–572, 1991. DOI: 10.1016/S0144-2449(05)80006-5.
- L. Marchese, J. Chen, P. A. Wright, and J. M. Thomas. Formation of hydronium at the Brønsted site in SAPO-34 catalysts. *J. Phys. Chem.*, 97:8109–8112, 1993. DOI: 10.1021/j100133a001.
- L. Marchese, A. Frache, E. Gianotti, G. Martra, M. Causà, and S. Coluccia. ALPO-34 and SAPO-34 synthesized by using morpholine as templating agent. FTIR and FT-Raman studies of the host–guest and guest–guest interactions within the zeolitic framework. *Microporous Mesoporous Mater.*, 30:145–153, 1999. DOI: 10.1016/S1387-1811(99)00023-2.
- N. Mardirossian and M. Head-Gordon. Thirty years of density functional theory in computational chemistry: An overview and extensive assessment of 200 density functionals. *Mol. Phys.*, 115:2315–2372, 2017. DOI: 10.1080/00268976.2017.1333644.
- G. A. V. Martins, G. Berlier, S. Coluccia, H. O. Pastore, G. B. Superti, G. Gatti, and L. Marchese. Revisiting the nature of the acidity in chabazite-related silicoaluminophosphates: Combined FTIR and  $^{29}\text{Si}$  MAS NMR study. *J. Phys. Chem. C*, 111:330–339, 2007. DOI: 10.1021/jp063921q.
- A. F. Masters and T. Maschmeyer. Zeolites - From curiosity to cornerstone. *Microporous Mesoporous Mater.*, 142: 423–438, 2011. DOI: 10.1016/j.micromeso.2010.12.026.
- Y. Mathieu, J. L. Paillaud, P. Caullet, and N. Bats. Synthesis and characterization of IM-10: A new microporous silicogermanate with a novel topology. *Microporous Mesoporous Mater.*, 75:13–22, 2004. DOI: 10.1016/j.micromeso.2004.06.023.
- S. L. Mayo, B. D. Olafson, and W. A. Goddard. DREIDING: a generic force field for molecular simulations. *J. Phys. Chem.*, 94:8897–8909, 1990. DOI: 10.1021/j100389a010.
- L. McCusker, C. Baerlocher, E. Jahn, and M. Bülow. The triple helix inside the large-pore aluminophosphate molecular sieve VPI-5. *Zeolites*, 11:308–313, 1991. DOI: 10.1016/0144-2449(91)80292-8.



- A. Meden, R. W. Grosse-Kunstleve, C. Baerlocher, and L. B. McCusker. Rietveld refinement of the as synthesized and partially calcined forms of the molecular sieve GaPO<sub>4</sub>-ZON. *Z. Kristallogr. - Cryst. Mater.*, 212:801–807, 1997. DOI: 10.1524/zkri.1997.212.11.801.
- R. H. Meinhold and N. J. Tapp. An NMR study of the reaction of water with AlPO<sub>4</sub>-5. *J. Chem. Soc. Chem. Commun.*, pages 219–220, 1990. DOI: 10.1039/C39900000219.
- F. Meunier. Adsorption heat powered heat pumps. *Appl. Therm. Eng.*, 61:830–836, 2013. DOI: 10.1016/j.applthermaleng.2013.04.050.
- A. Mięka, M. Król, and A. Kozłowski. Periodic model of an LTA framework. *J. Mol. Model.*, 21:275, 2015. DOI: 10.1007/s00894-015-2820-0.
- T. Mineva, E. Dib, A. Gaje, H. Petitjean, J. L. Bantignies, and B. Alonso. Zeolite Structure Direction: Identification, Strength and Involvement of Weak CH<sub>2</sub> ··· O Hydrogen Bonds. *ChemPhysChem*, 21:149–153, 2020. DOI: 10.1002/cphc.201900953.
- I. B. Minova, N. S. Barrow, A. C. Sauerwein, A. B. Naden, D. B. Cordes, A. M. Slawin, S. J. Schuyten, and P. A. Wright. Silicon redistribution, acid site loss and the formation of a core-shell texture upon steaming SAPO-34 and their impact on catalytic performance in the Methanol-to-Olefins (MTO) reaction. *J. Catal.*, 395:425–444, 2021. DOI: 10.1016/j.jcat.2021.01.012.
- S. Mintova, M. Jaber, and V. Valtchev. Nanosized microporous crystals: emerging applications. *Chem. Soc. Rev.*, 44:7207–7233, 2015. DOI: 10.1039/c5cs00210a.
- K. Momma and F. Izumi. VESTA 3 for three-dimensional visualization of crystal, volumetric and morphology data. *J. Appl. Cryst.*, 44:1272–1276, 2011. DOI: 10.1107/S0021889811038970.
- F. A. Mumpton. La roca magica: uses of natural zeolites in agriculture and industry. *Proc. Natl. Acad. Sci. U.S.A.*, 96:3463–3470, 1999. DOI: 10.1073/pnas.96.7.3463.
- K. Muraoka, W. Chaikittisilp, and T. Okubo. Energy Analysis of Aluminosilicate Zeolites with Comprehensive Ranges of Framework Topologies, Chemical Compositions, and Aluminum Distributions. *J. Am. Chem. Soc.*, 138:6184–6193, 2016. DOI: 10.1021/jacs.6b01341.
- L. Narasimhan, P. Boulet, B. Kuchta, C. Vagner, O. Schäf, and R. Denoyel. Adsorption of paracresol in silicalite-1 and pure silica faujasite. A comparison study using molecular simulation. *Appl. Surf. Sci.*, 256:5470–5474, 2010. DOI: 10.1016/j.apsusc.2009.12.142.
- A. Navrotsky, O. Trofymuk, and A. A. Levchenko. Thermochemistry of Microporous and Mesoporous Materials. *Chem. Rev.*, 109:3885–3902, 2009. DOI: 10.1021/cr800495t.
- E.-P. Ng and S. Mintova. Nanoporous materials with enhanced hydrophilicity and high water sorption capacity. *Microporous Mesoporous Mater.*, 114:1–26, 2008. DOI: 10.1016/j.micromeso.2007.12.022.
- E. Nusterer, P. Blöchl, and K. Schwarz. Interaction of water and methanol with a zeolite at high coverages. *Chem. Phys. Lett.*, 253:448–455, 1996. DOI: 10.1016/0009-2614(96)00273-4.
- S. O. Odoh, M. W. Deem, and L. Gagliardi. Preferential Location of Germanium in the UTL and IPC-2a Zeolites. *J. Phys. Chem. C*, 118:26939–26946, 2014. DOI: 10.1021/jp510495w.
- C. Otero Arean, M. R. Delgado, P. Nachtigall, H. V. Thang, M. Rubeš, R. Bulánek, and P. Chlubná-Eliášová. Measuring the Brønsted acid strength of zeolites—does it correlate with the O-H frequency shift probed by a weak base? *Phys. Chem. Chem. Phys.*, 16:10129–10141, 2014. DOI: 10.1039/c3cp54738h.
- J.-L. Paillaud, B. Marler, and H. Kessler. Synthesis and characterisation of the novel GIS-type AlPO<sub>4</sub>: [NH<sub>2</sub>Me<sub>2</sub>][Al<sub>2</sub>P<sub>2</sub>O<sub>8</sub>F]. *Chem. Commun.*, pages 1293–1294, 1996. DOI: 10.1039/cc9960001293.
- J.-l. Paillaud, B. Harbuzaru, J. Patarin, and N. Bats. Extra-large-pore zeolites with two-dimensional channels formed by 14 and 12 rings. *Science*, 304:990–992, 2004. DOI: 10.1126/science.1098242.

- J.-I. Paillaud, B. Harbuzaru, and J. Patarin. Synthesis and characterisation of as-synthesised Mu-26, a zeolitic material with the STF framework topology. *Microporous Mesoporous Mater.*, 105:89–100, 2007. DOI: 10.1016/j.micromeso.2007.03.046.
- M. C. Payne, T. A. Arias, and J. D. Joannopoulos. Iterative minimization techniques for ab initio total-energy calculations: molecular dynamics and conjugate gradients. *Rev. Mod. Phys.*, 64:1045–1097, 1992. DOI: 10.1103/RevModPhys.64.1045.
- A. Pedone, G. Malavasi, M. C. Menziani, U. Segre, F. Musso, M. Corno, B. Civalleri, and P. Ugliengo. FFSiOH: A new force field for silica polymorphs and their hydroxylated surfaces based on periodic B3LYP calculations. *Chem. Mater.*, 20:2522–2531, 2008. DOI: 10.1021/cm703437y.
- M. P. J. Peeters, J. W. de Haan, L. J. M. van de Ven, and J. H. C. van Hooff. Hydration of AlPO<sub>4</sub>-11 studied with x-ray powder diffraction and aluminum-27 and phosphorus-31 NMR. *J. Phys. Chem.*, 97:5363–5369, 1993. DOI: 10.1021/j100122a030.
- J. Perdew, A. Ruzsinszky, G. I. Csonka, O. A. Vydrov, G. E. Scuseria, L. A. Constantin, X. Zhou, and K. Burke. Restoring the Density-Gradient Expansion for Exchange in Solids and Surfaces. *Phys. Rev. Lett.*, 100:136406, 2008. DOI: 10.1103/PhysRevLett.100.136406.
- J. P. Perdew and A. Ruzsinszky. Fourteen easy lessons in density functional theory. *Int. J. Quantum Chem.*, 110:2801–2807, 2010. DOI: 10.1002/qua.22829.
- J. P. Perdew, K. Burke, and M. Ernzerhof. Generalized Gradient Approximation Made Simple. *Phys. Rev. Lett.*, 77:3865–3868, 1996. DOI: 10.1103/PhysRevLett.77.3865.
- C. Perego and A. Bosetti. Biomass to fuels: The role of zeolite and mesoporous materials. *Microporous Mesoporous Mater.*, 144:28–39, 2011. DOI: 10.1016/j.micromeso.2010.11.034.
- P. S. Petkov, H. A. Aleksandrov, V. Valtchev, and G. N. Vayssilov. Framework Stability of Heteroatom-Substituted Forms of Extra-Large-Pore Ge-Silicate Molecular Sieves: The Case of ITQ-44. *Chem. Mater.*, 24:2509–2518, 2012. DOI: 10.1021/cm300861e.
- G. Piccini, M. Alessio, J. Sauer, Y. Zhi, Y. Liu, R. Kolvenbach, A. Jentys, and J. A. Lercher. Accurate Adsorption Thermodynamics of Small Alkanes in Zeolites. Ab initio Theory and Experiment for H-Chabazite. *J. Phys. Chem. C*, 119:6128–6137, 2015. DOI: 10.1021/acs.jpcc.5b01739.
- P. M. Piccione, C. Laberty, S. Yang, M. A. Camblor, A. Navrotsky, and M. E. Davis. Thermochemistry of Pure-Silica Zeolites. *J. Phys. Chem. B*, 104:10001–10011, 2000. DOI: 10.1021/jp002148a.
- R. S. Pillai and R. V. Jasra. Computational study for water sorption in AlPO<sub>4</sub>-5 and AlPO<sub>4</sub>-11 molecular sieves. *Langmuir*, 26:1755–1764, 2010. DOI: 10.1021/la902629g.
- G. D. Pirngruber, P. Raybaud, Y. Belmabkhout, J. Cejka, and A. Zukul. The role of the extra-framework cations in the adsorption of CO<sub>2</sub> on faujasite Y. *Phys. Chem. Chem. Phys.*, 12:13534–13546, 2010. DOI: 10.1039/b927476f.
- J. J. Pluth and J. V. Smith. Accurate redetermination of crystal structure of dehydrated zeolite A. Absence of near zero coordination of sodium. Refinement of silicon,aluminum-ordered superstructure. *J. Am. Chem. Soc.*, 102:4704–4708, 1980. ISSN 0002-7863. DOI: 10.1021/ja00534a024.
- J. J. Pluth and J. V. Smith. A hydrated aluminophosphate with both 4 · 8<sup>2</sup> and 6<sup>3</sup> sheets in the 4-connected framework. *Nature*, 318:165–166, 1985. DOI: 10.1038/318165a0.
- J. J. Pluth and J. V. Smith. Hydrated aluminophosphate (AlPO<sub>4</sub>·1.5H<sub>2</sub>O) with PO<sub>4</sub>, AlO<sub>4</sub> and AlO<sub>4</sub>(H<sub>2</sub>O)<sub>2</sub> groups and encapsulated water. *Acta Cryst. C*, 42:1118–1120, 1986. DOI: 10.1107/S0108270186093198.
- J. J. Pluth, J. V. Smith, and J. M. Bennett. Microporous aluminophosphate number 17 with encapsulated piperidine, topological similarity to erionite. *Acta Cryst. C*, 42:283–286, 1986. DOI: 10.1107/S0108270186096476.

- M. D. Poojary and A. Clearfield. Crystal structure data of 14-ring aluminophosphate  $\text{AlPO}_4$ -8 from powder data. *Mater. Chem. Phys.*, 35:301–304, 1993. DOI: 10.1016/0254-0584(93)90146-D.
- R. Pophale, F. Daeyaert, and M. W. Deem. Computational prediction of chemically synthesizable organic structure directing agents for zeolites. *J. Mater. Chem. A*, 1:6750–6760, 2013. DOI: 10.1039/c3ta10626h.
- G. Poulet, P. Sautet, and A. Tuel. Structure of Hydrated Microporous Aluminophosphates: Static and Molecular Dynamics Approaches of  $\text{AlPO}_4$ -34 from First Principles Calculations. *J. Phys. Chem. B*, 106:8599–8608, 2002. DOI: 10.1021/jp020533p.
- G. Poulet, A. Tuel, and P. Sautet. A combined experimental and theoretical evaluation of the structure of hydrated microporous aluminophosphate  $\text{AlPO}_4$ -18. *J. Phys. Chem. B*, 109:22939–22946, 2005. DOI: 10.1021/jp050670x.
- G. Prandini, A. Marrazzo, I. E. Castelli, N. Mounet, and N. Marzari. Precision and efficiency in solid-state pseudopotential calculations. *npj Comput. Mater.*, 4:72, 2018. DOI: 10.1038/s41524-018-0127-2.
- M. Praprotnik, S. Hocevar, M. Hodosecek, M. Penca, and D. Janezic. New all-atom force field for molecular dynamics simulation of an  $\text{AlPO}_4$ -34 molecular sieve. *J. Comput. Chem.*, 29:122–129, 2008. DOI: 10.1002/jcc.20774.
- S. Prasad, I. Balakrishnan, and R. Vetrivel. Modeling and MASNMR spectroscopic studies on molecular sieves. 2. The nature of water molecules in hydrated  $\text{AlPO}_4$ -11 host lattice. *J. Phys. Chem.*, 96:3096–3100, 1992. DOI: 10.1021/j100186a059.
- A. Pulido, A. Corma, and G. Sastre. Computational study of location and role of fluoride in zeolite structures. *J. Phys. Chem. B*, 110:23951–23961, 2006a. DOI: 10.1021/jp064278a.
- A. Pulido, G. Sastre, and A. Corma. Computational study of  $^{19}\text{F}$  NMR spectra of double four ring-containing Si/Ge-zeolites. *ChemPhysChem*, 7:1092–1099, 2006b. DOI: 10.1002/cphc.200500634.
- A. Pulido, M. Moliner, and A. Corma. Rigid/Flexible Organic Structure Directing Agents for Directing the Synthesis of Multipore Zeolites: A Computational Approach. *J. Phys. Chem. C*, 119:7711–7720, 2015. DOI: 10.1021/jp512515y.
- J. Rabo and M. Schoonover. Early discoveries in zeolite chemistry and catalysis at Union Carbide, and follow-up in industrial catalysis. *Appl. Catal. A*, 222:261–275, 2001. DOI: 10.1016/S0926-860X(01)00840-7.
- V. Ramaswamy, L. McCusker, and C. Baerlocher. Rietveld refinement of the pure aluminophosphate  $\text{AlPO}_4$ -40. *Microporous Mesoporous Mater.*, 31:1–8, 1999. DOI: 10.1016/S1387-1811(99)00052-9.
- N. Rangnekar, N. Mittal, B. Elyassi, J. Caro, and M. Tsapatsis. Zeolite membranes – a review and comparison with MOFs. *Chem. Soc. Rev.*, 44:7128–7154, 2015. DOI: 10.1039/C5CS00292C.
- M. Råsander and M. A. Moram. On the accuracy of commonly used density functional approximations in determining the elastic constants of insulators and semiconductors. *J. Chem. Phys.*, 143:144104, 2015. DOI: 10.1063/1.4932334.
- F. R. Rehak, G. Piccini, M. Alessio, and J. Sauer. Including dispersion in density functional theory for adsorption on flat oxide surfaces, in metal-organic frameworks and in acidic zeolites. *Phys. Chem. Chem. Phys.*, 22:7577–7585, 2020. DOI: 10.1039/d0cp00394h.
- A. M. Reilly and A. Tkatchenko. Understanding the role of vibrations, exact exchange, and many-body van der Waals interactions in the cohesive properties of molecular crystals. *J. Chem. Phys.*, 139:024705, 2013. DOI: 10.1063/1.4812819.
- K. Remya and C. H. Suresh. Which density functional is close to CCSD accuracy to describe geometry and interaction energy of small non-covalent dimers? A benchmark study using Gaussian09. *J. Comput. Chem.*, 34:1341–1353, 2013. DOI: 10.1002/jcc.23263.

- J. W. Richardson, J. J. Pluth, and J. V. Smith. Rietveld profile analysis of calcined  $\text{AlPO}_4$ -11 using pulsed neutron powder diffraction. *Acta Cryst. B*, 44:367–373, 1988. DOI: 10.1107/S0108768188003076.
- R. T. Rigo, S. R. Balestra, S. Hamad, R. Bueno-Perez, A. R. Ruiz-Salvador, S. Calero, and M. A. Cambor. The Si-Ge substitutional series in the chiral STW zeolite structure type. *J. Mater. Chem. A*, 6:15110–15122, 2018. DOI: 10.1039/c8ta03879a.
- A. Ristić, N. Zabukovec Logar, S. K. Henninger, and V. Kaučič. The Performance of Small-Pore Microporous Aluminophosphates in Low-Temperature Solar Energy Storage: The Structure-Property Relationship. *Adv. Funct. Mater.*, 22:1952–1957, 2012. DOI: 10.1002/adfm.201102734.
- A. Ristić, F. Fischer, A. Hauer, and N. Zabukovec Logar. Improved performance of binder-free zeolite Y for low-temperature sorption heat storage. *J. Mater. Chem. A*, 6:11521–11530, 2018. DOI: 10.1039/C8TA00827B.
- A. Rojas and M. A. Cambor. A Pure Silica Chiral Polymorph with Helical Pores. *Angew. Chem. Int. Ed.*, 51: 3854–3856, 2012. DOI: 10.1002/anie.201108753.
- A. Rojas, E. Martínez-Morales, C. M. Zicovich-Wilson, and M. A. Cambor. Zeolite Synthesis in Fluoride Media: Structure Direction toward ITW by Small Methylimidazolium Cations. *J. Am. Chem. Soc.*, 134:2255–2263, 2012. DOI: 10.1021/ja209832y.
- E. I. Román-Román and C. M. Zicovich-Wilson. The role of long-range van der Waals forces in the relative stability of  $\text{SiO}_2$ -zeolites. *Chem. Phys. Lett.*, 619:109–114, 2015. DOI: 10.1016/j.cplett.2014.11.044.
- N. Roostaei and F. Tezel. Removal of phenol from aqueous solutions by adsorption. *J. Environ. Manag.*, 70:157–164, 2004. DOI: 10.1016/j.jenvman.2003.11.004.
- A. Rossner, S. A. Snyder, and D. R. Knappe. Removal of emerging contaminants of concern by alternative adsorbents. *Water Res.*, 43:3787–3796, 2009. DOI: 10.1016/j.watres.2009.06.009.
- A. Samanta, A. Zhao, G. K. H. Shimizu, P. Sarkar, and R. Gupta. Post-Combustion  $\text{CO}_2$  Capture Using Solid Sorbents: A Review. *Ind. Eng. Chem. Res.*, 51:1438–1463, 2012. DOI: 10.1021/ie200686q.
- M. J. Sanders, M. Leslie, and C. R. A. Catlow. Interatomic potentials for  $\text{SiO}_2$ . *J. Chem. Soc. Chem. Commun.*, pages 1271–1273, 1984. DOI: 10.1039/c39840001271.
- G. Sastre and A. Corma. Predicting Structural Feasibility of Silica and Germania Zeolites. *J. Phys. Chem. C*, 114: 1667–1673, 2010. DOI: 10.1021/jp909348s.
- G. Sastre and J. D. Gale. Derivation of an Interatomic Potential for Germanium- and Silicon-Containing Zeolites and Its Application to the Study of the Structures of Octadecasil, ASU-7, and ASU-9 Materials. *Chem. Mater.*, 15: 1788–1796, 2003. DOI: 10.1021/cm021262y.
- G. Sastre and J. D. Gale. Derivation of an interatomic potential for fluoride-containing microporous silicates and germanates. *Chem. Mater.*, 17:730–740, 2005. DOI: 10.1021/cm048406o.
- G. Sastre, D. W. Lewis, and C. R. A. Catlow. Structure and stability of silica species in SAPO molecular sieves. *J. Phys. Chem.*, 100:6722–6730, 1996. DOI: 10.1021/jp953362f.
- G. Sastre, D. W. Lewis, and C. R. A. Catlow. Modeling of Silicon Substitution in SAPO-5 and SAPO-34 Molecular Sieves. *J. Phys. Chem. B*, 101:5249–5262, 1997. DOI: 10.1021/jp963736k.
- G. Sastre, V. Fornes, and A. Corma. On the preferential location of Al and proton siting in zeolites: A computational and infrared study. *J. Phys. Chem. B*, 106:701–708, 2002. DOI: 10.1021/jp013189p.
- G. Sastre, A. Pulido, and A. Corma. An attempt to predict and rationalize relative stabilities and preferential germanium location in Si/Ge zeolites. *Microporous Mesoporous Mater.*, 82:159–163, 2005a. DOI: 10.1016/j.micromeso.2005.01.021.
- G. Sastre, A. Pulido, and A. Corma. Pentacoordinated germanium in AST zeolite synthesised in fluoride media. A  $^{19}\text{F}$  NMR validated computational study. *Chem. Commun.*, pages 2357–2359, 2005b. DOI: 10.1039/b419131e.

- J. E. Schmidt, M. W. Deem, and M. E. Davis. Synthesis of a Specified, Silica Molecular Sieve by Using Computationally Predicted Organic Structure-Directing Agents. *Angew. Chem. Int. Ed.*, 53:8372–8374, 2014. DOI: 10.1002/anie.201404076.
- J. E. Schmidt, M. W. Deem, C. Lew, and T. M. Davis. Computationally-Guided Synthesis of the 8-Ring Zeolite AEI. *Top. Catal.*, 58:410–415, 2015. DOI: 10.1007/s11244-015-0381-1.
- W. Schmidt, U. Wilczok, C. Weidenthaler, O. Medenbach, R. Goddard, G. Buth, and A. Cepak. Preparation and Morphology of Pyramidal MFI Single-Crystal Segments. *J. Phys. Chem. B*, 111:13538–13543, 2007. DOI: 10.1021/jp075934p.
- C. Schott-Darie, J. Patarin, P. Y. Le Goff, H. Kessler, and E. Benazzi. Synthesis, characterization and Rietveld refinement of the tetragonal variant of  $\text{AlPO}_4$ -16 prepared in fluoride medium. *Microporous Mater.*, 3:123–132, 1994. DOI: 10.1016/0927-6513(94)00014-X.
- L. Schreyeck, J. Stumbe, P. Caullet, J.-C. Mougenel, and B. Marler. The diaza-polyoxa-macrocycle ‘Kryptofix222’ as a new template for the synthesis of LTA-type  $\text{AlPO}_4$ . *Microporous Mesoporous Mater.*, 22:87–106, 1998. DOI: 10.1016/S1387-1811(98)00082-1.
- K.-P. Schröder, J. Sauer, M. Leslie, C. Richard, A. Catlow, and J. M. Thomas. Bridging hydroxyl groups in zeolitic catalysts: a computer simulation of their structure, vibrational properties and acidity in protonated faujasites (H-Y zeolites). *Chem. Phys. Lett.*, 188:320–325, 1992. DOI: 10.1016/0009-2614(92)90030-Q.
- D. Selassie, D. Davis, J. Dahlin, E. Feise, G. Haman, D. S. Sholl, and D. Kohen. Atomistic Simulations of  $\text{CO}_2$  and  $\text{N}_2$  Diffusion in Silica Zeolites: The Impact of Pore Size and Shape. *J. Phys. Chem. C*, 112:16521–16531, 2008. DOI: 10.1021/jp803586m.
- T. P. Senftle, S. Hong, M. M. Islam, S. B. Kylasa, Y. Zheng, Y. K. Shin, C. Junkermeier, R. Engel-Herbert, M. J. Janik, H. M. Aktulga, T. Verstraelen, A. Grama, and A. C. T. van Duin. The ReaxFF reactive force-field: development, applications and future directions. *npj Comput. Mater.*, 2:15011, 2016. DOI: 10.1038/npjcompumats.2015.11.
- R. Shah, J. D. Gale, and M. C. Payne. Methanol Adsorption In Zeolites - A First-Principles Study. *J. Phys. Chem.*, 100:11688–11697, 1996. DOI: 10.1021/jp960365z.
- M. Shamzhy, M. Opanasenko, Y. Tian, K. Konyshova, O. Shvets, R. E. Morris, and J. Čejka. Germanosilicate Precursors of ADORable Zeolites Obtained by Disassembly of ITH, ITR, and IWR Zeolites. *Chem. Mater.*, 26: 5789–5798, 2014. DOI: 10.1021/cm502953s.
- J. Shang, G. Li, R. Singh, P. Xiao, D. Danaci, J. Z. Liu, and P. A. Webley. Adsorption of  $\text{CO}_2$ ,  $\text{N}_2$ , and  $\text{CH}_4$  in Cs-exchanged chabazite: a combination of van der Waals density functional theory calculations and experiment study. *J. Chem. Phys.*, 140:084705, 2014. DOI: 10.1063/1.4866455.
- R. D. Shannon. Revised effective ionic radii and systematic studies of interatomic distances in halides and chalcogenides. *Acta Cryst. A*, 32:751–767, 1976. DOI: 10.1107/S0567739476001551.
- D. F. Shantz, J. Schmedt auf der Günne, H. Koller, and R. F. Lobo. Multiple-quantum  $^1\text{H}$  MAS NMR studies of defect sites in as-made all-silica ZSM-12 zeolite. *J. Am. Chem. Soc.*, 122:6659–6663, 2000. DOI: 10.1021/ja000374s.
- C. Shi, J. Wang, L. Li, and Y. Li. High-throughput Screening of Aluminophosphate Zeolites for Adsorption Heat Pump Applications. *Chem. Res. Chin. Univ.*, 38:161–166, 2022. DOI: 10.1007/s40242-021-1335-8.
- S. Shimooka, K. Oshima, H. Hidaka, T. Takewaki, H. Kakiuchi, A. Kodama, M. Kubota, and H. Matsuda. The evaluation of direct cooling and heating desiccant device coated with FAM. *J. Chem. Eng. Japan*, 40:1330–1334, 2007. DOI: 10.1252/jcej.07WE193.
- D. S. Sholl and J. A. Steckel. *Density functional theory - A practical introduction*. John Wiley & Sons, Inc, Hoboken, NJ, USA, 2009. DOI: 10.1002/9780470447710.
- L. Sierra, C. Deroche, H. Gies, and J. Guth. Synthesis of new microporous  $\text{AlPO}_4$  and substituted derivatives with the LTA structure. *Microporous Mater.*, 3:29–38, 1994. DOI: 10.1016/0927-6513(93)E0069-S.

- A. Sierraalta, R. Añez, D. S. Coll, and P. Alejos. New theoretical insight on the acid sites distribution, their local structures and acid strength of the SAPO-11 molecular sieve. *Int. J. Quantum Chem.*, 118:e25541, 2018. DOI: 10.1002/qua.25541.
- A. Sierraalta, R. Añez, D. S. Coll, and P. Alejos. Conversion of methanol to dimethyl ether over silicoaluminophosphates: Isolated acid sites and the influence of silicon islands. A DFT-ONIOM study. *Microporous Mesoporous Mater.*, 292:109732, 2020. DOI: 10.1016/j.micromeso.2019.109732.
- M. C. Silaghi, C. Chizallet, J. Sauer, and P. Raybaud. Dealumination mechanisms of zeolites and extra-framework aluminum confinement. *J. Catal.*, 339:242–255, 2016. DOI: 10.1016/j.jcat.2016.04.021.
- A. Simmen, J. Patarin, and C. Baerlocher. Rietveld Refinement of F-containing GaPO<sub>4</sub>-LTA. In *Proceedings from the Ninth International Zeolite Conference*, pages 433–440. Elsevier, 1993.
- S. Sircar and A. L. Myers. Gas Separation by Zeolites. In S. M. Auerbach, K. A. Carrado, and P. K. Dutta, editors, *Handbook of Zeolite Science and Technology*. CRC Press, 2003. DOI: 10.1201/9780203911167.
- B. Smit and T. L. M. Maesen. Molecular simulations of zeolites: adsorption, diffusion, and shape selectivity. *Chem. Rev.*, 108:4125–4184, 2008. DOI: 10.1021/cr8002642.
- J. V. Smith. Tetrahedral frameworks of zeolites, clathrates and related materials. In W. H. Baur and R. X. Fischer, editors, *Landolt-Börnstein - Group IV Physical Chemistry · Volume 14A: Microporous and other Framework Materials with Zeolite-Type Structures*. Springer-Verlag Berlin Heidelberg, 2000. DOI: 10.1007/b55613.
- L. Smith, A. K. Cheetham, L. Marchese, J. M. Thomas, P. A. Wright, J. Chen, and E. Gianotti. A quantitative description of the active sites in the dehydrated acid catalyst HSAPO-34 for the conversion of methanol to olefins. *Catal. Lett.*, 41:13–16, 1996a. DOI: 10.1007/BF00811705.
- L. Smith, A. K. Cheetham, R. E. Morris, L. Marchese, J. M. Thomas, P. A. Wright, and J. Chen. On the Nature of Water Bound to a Solid Acid Catalyst. *Science*, 271:799–802, 1996b. DOI: 10.1126/science.271.5250.799.
- S. Sneddon, D. M. Dawson, C. J. Pickard, and S. E. Ashbrook. Calculating NMR Parameters in Aluminophosphates: Evaluation of Dispersion Correction Schemes. *Phys. Chem. Chem. Phys.*, 16:2660–2673, 2014. DOI: 10.1039/c3cp54123a.
- M. Spanakis, N. Bouropoulos, D. Theodoropoulos, L. Sygellou, S. Ewart, A. M. Moschovi, A. Siokou, I. Niopas, K. Kachrimanis, V. Nikolakis, P. A. Cox, I. S. Vizirianakis, and D. G. Fatouros. Controlled release of 5-fluorouracil from microporous zeolites. *Nanomed.: Nanotechnol. Biol. Med.*, 10:197–205, 2014. DOI: 10.1016/j.nano.2013.06.016.
- K. Ståhl, Å. Kvik, and S. Ghose. One-dimensional water chain in the zeolite bikitaite: Neutron diffraction study at 13 and 295 K. *Zeolites*, 9:303–311, 1989. DOI: 10.1016/0144-2449(89)90076-6.
- K. Stanciakova, B. Ensing, F. Göttl, R. E. Buló, and B. M. Weckhuysen. Cooperative Role of Water Molecules during the Initial Stage of Water-Induced Zeolite Dealumination. *ACS Catal.*, 9:5119–5135, 2019. DOI: 10.1021/acscatal.9b00307.
- J. Sun, C. Bonneau, A. Cantín, A. Corma, M. J. Díaz-Cabañas, M. Moliner, D. Zhang, M. Li, and X. Zou. The ITQ-37 mesoporous chiral zeolite. *Nature*, 458:1154–1157, 2009. DOI: 10.1038/nature07957.
- J. Sun, A. Ruzsinszky, and J. P. Perdew. Strongly Constrained and Appropriately Normed Semilocal Density Functional. *Phys. Rev. Lett.*, 115:036402, 2015. DOI: 10.1103/PhysRevLett.115.036402.
- K. Suzuki, T. Nishio, N. Katada, G. Sastre, and M. Niwa. Ammonia IRMS-TPD measurements on Brønsted acidity of proton-formed SAPO-34. *Phys. Chem. Chem. Phys.*, 13:3311–3318, 2011. DOI: 10.1039/c0cp00961j.
- M. Tagliabue, D. Farrusseng, S. Valencia, S. Aguado, U. Ravon, C. Rizzo, A. Corma, and C. Mirodatos. Natural gas treating by selective adsorption: Material science and chemical engineering interplay. *Chem. Eng. J.*, 155: 553–566, 2009. DOI: 10.1016/j.cej.2009.09.010.

- O. Talu and A. L. Myers. Reference potentials for adsorption of helium, argon, methane, and krypton in high-silica zeolites. *Colloids Surf. A*, 187-188:83–93, 2001. DOI: 10.1016/S0927-7757(01)00628-8.
- J. Tan, Z. Liu, X. Bao, X. Liu, X. Han, C. He, and R. Zhai. Crystallization and Si incorporation mechanisms of SAPO-34. *Microporous Mesoporous Mater.*, 53:97–108, 2002. DOI: 10.1016/S1387-1811(02)00329-3.
- L. Tang. *Novel Framework Materials: Organically Templated Silicogermanates and Hybrid Fluorotitanates*. PhD thesis, PhD thesis, University of Stockholm, 2005.
- S. A. Tawfik, T. Gould, C. Stampfl, and M. J. Ford. Evaluation of van der Waals density functionals for layered materials. *Phys. Rev. Mater.*, 2:034005, 2018. DOI: 10.1103/PhysRevMaterials.2.034005.
- W. H. Taylor. I. The structure of analcite ( $\text{NaAlSi}_2\text{O}_6 \cdot \text{H}_2\text{O}$ ). *Z. Kristallogr.*, 74:1–19, 1930. DOI: 10.1524/zkri.1930.74.1.1.
- V. Termath, F. Haase, J. Sauer, J. Hutter, and M. Parrinello. Understanding the nature of water bound to solid acid surfaces. Ab initio simulation on HSAPO-34. *J. Am. Chem. Soc.*, 120:8512–8516, 1998. DOI: 10.1021/ja981549p.
- P. Tian, Y. Wei, M. Ye, and Z. Liu. Methanol to olefins (MTO): From fundamentals to commercialization. *ACS Catal.*, 5:1922–1938, 2015. DOI: 10.1021/acscatal.5b00007.
- A. Tkatchenko and M. Scheffler. Accurate Molecular Van Der Waals Interactions from Ground-State Electron Density and Free-Atom Reference Data. *Phys. Rev. Lett.*, 102:073005, 2009. DOI: 10.1103/PhysRevLett.102.073005.
- J. Toda, A. Corma, R. H. Abudawoud, M. S. Elanany, I. M. Al-Zahrani, and G. Sastre. Influence of force fields on the selective diffusion of para-xylene over ortho-xylene in 10-ring zeolites. *Mol. Simul.*, 41:1438–1448, 2015. DOI: 10.1080/08927022.2015.1047370.
- F. J. Torres, P. Ugliengo, B. Civalleri, A. Terentyev, and C. Pisani. A review of the computational studies of proton- and metal-exchanged chabazites as media for molecular hydrogen storage performed with the CRYSTAL code. *Int. J. Hydrogen Ener.*, 33:746–754, 2008. DOI: 10.1016/j.ijhydene.2007.09.039.
- R. P. Townsend and E. N. Coker. Chapter 11 Ion exchange in zeolites. *Stud. Surf. Sci. Catal.*, 137:467–524, 2001. DOI: 10.1016/S0167-2991(01)80253-6.
- M. Trachta, M. Rubeš, and O. Bludský. Toward accurate ab initio modeling of siliceous zeolite structures. *J. Chem. Phys.*, 156:094708, 2022. DOI: 10.1063/5.0083191.
- F. Tran and P. Blaha. Importance of the Kinetic Energy Density for Band Gap Calculations in Solids with Density Functional Theory. *J. Phys. Chem. A*, 121:3318–3325, 2017. DOI: 10.1021/acs.jpca.7b02882.
- F. Tran, J. Stelzl, and P. Blaha. Rungs 1 to 4 of DFT Jacob’s ladder: Extensive test on the lattice constant, bulk modulus, and cohesive energy of solids. *J. Chem. Phys.*, 144:204120, 2016. DOI: 10.1063/1.4948636.
- F. Tran, L. Kalantari, B. Traoré, X. Rocquefelte, and P. Blaha. Nonlocal van der Waals functionals for solids: Choosing an appropriate one. *Phys. Rev. Mater.*, 3:32–35, 2019a. DOI: 10.1103/PhysRevMaterials.3.063602.
- Y. T. Tran, J. Lee, P. Kumar, K.-H. Kim, and S. S. Lee. Natural zeolite and its application in concrete composite production. *Compos. B. Eng.*, 165:354–364, 2019b. DOI: 10.1016/j.compositesb.2018.12.084.
- F. Trudu, G. Tabacchi, and E. Fois. Computer modeling of apparently straight bond angles: The intriguing case of all-silica ferrierite. *Am. Miner.*, 104:1546–1555, 2019. DOI: 10.2138/am-2019-6951.
- A. Tuel, S. Caldarelli, A. Meden, L. B. McCusker, C. Baerlocher, A. Ristic, N. Rajic, G. Mali, and V. Kaucic. NMR Characterization and Rietveld Refinement of the Structure of Rehydrated  $\text{AlPO}_4\text{-34}$ . *J. Phys. Chem. B*, 104:5697–5705, 2000. DOI: 10.1021/jp000455a.
- A. Tuel, C. Lorentz, V. Gramlich, and C. Baerlocher.  $\text{AlPO}_4\text{-ERI}$ , an aluminophosphate with the ERI framework topology: Characterization and structure of the as-made and calcined rehydrated forms. *C. R. Chim.*, 8:531–540, 2005. DOI: 10.1016/j.crci.2004.11.012.

- D. Tunega, T. Bučko, and A. Zaoui. Assessment of ten DFT methods in predicting structures of sheet silicates: Importance of dispersion corrections. *J. Chem. Phys.*, 137:114105, 2012. DOI: 10.1063/1.4752196.
- A. Turrina, R. Garcia, A. E. Watts, H. F. Greer, J. Bradley, W. Zhou, P. A. Cox, M. D. Shannon, A. Mayoral, J. L. Casci, and P. A. Wright. STA-20: An ABC-6 Zeotype Structure Prepared by Co-Templating and Solved via a Hypothetical Structure Database and STEM-ADF Imaging. *Chem. Mater.*, 29:2180–2190, 2017. DOI: 10.1021/acs.chemmater.6b04892.
- E. L. Uzunova and H. Mikosch. Cation site preference in zeolite clinoptilolite: A density functional study. *Microporous Mesoporous Mater.*, 177:113–119, 2013. DOI: 10.1016/j.micromeso.2013.05.003.
- G. van de Goor, C. C. Freyhardt, and P. Behrens. The Cobalticinium Cation  $[\text{Co}^{\text{III}}(\eta^5\text{-C}_5\text{H}_5)_2]^+$ : A metal-organic complex as a novel template for the synthesis of clathrasils. *Z. Anorg. Allg. Chem.*, 621:311–322, 1995. DOI: 10.1002/zaac.19956210218.
- H. van Heyden, G. Munz, L. Schnabel, F. Schmidt, S. Mintova, and T. Bein. Kinetics of water adsorption in microporous aluminophosphate layers for regenerative heat exchangers. *Appl. Therm. Eng.*, 29:1514–1522, 2009. DOI: 10.1016/j.applthermaleng.2008.07.001.
- V. Van Speybroeck, K. Hemelsoet, L. Joos, M. Waroquier, R. G. Bell, and C. R. A. Catlow. Advances in theory and their application within the field of zeolite chemistry. *Chem. Soc. Rev.*, 44:7044–7111, 2015. DOI: 10.1039/C5CS00029G.
- J. Varlec, A. Krajnc, M. Mazaj, A. Ristić, K. Vanatalu, A. Oss, A. Samoson, V. Kaučič, and G. Mali. Dehydration of  $\text{AlPO}_4\text{-34}$  studied by variable-temperature NMR, XRD and first-principles calculations. *New J. Chem.*, 40: 4178–4186, 2016. DOI: 10.1039/C5NJ02838H.
- M. V. Vener, X. Rozanska, and J. Sauer. Protonation of water clusters in the cavities of acidic zeolites:  $(\text{H}_2\text{O})_n \cdot \text{H}$ -chabazite,  $n = 1\text{-}4$ . *Phys. Chem. Chem. Phys.*, 11:1702–1712, 2009. DOI: 10.1039/b817905k.
- W. Vermeiren and J.-P. Gilson. Impact of Zeolites on the Petroleum and Petrochemical Industry. *Top. Catal.*, 52: 1131–1161, 2009. DOI: 10.1007/s11244-009-9271-8.
- T. Verstraelen, B. M. Szyja, D. Lesthaeghe, R. Declerck, V. Van Speybroeck, M. Waroquier, A. P. J. Jansen, A. Aerts, L. R. A. Follens, J. A. Martens, C. E. A. Kirschhock, and R. A. van Santen. Multi-level Modeling of Silica–Template Interactions During Initial Stages of Zeolite Synthesis. *Top. Catal.*, 52:1261–1271, 2009. DOI: 10.1007/s11244-009-9275-4.
- L. Vidal, J. L. Paillaud, and Z. Gabelica. A novel monoclinic  $\text{AlPO}_4$ -sodalite formed in the presence of dimethylformamide as template and solvent. *Microporous Mesoporous Mater.*, 24:189–197, 1998. DOI: 10.1016/S1387-1811(98)00164-4.
- J. A. Vidal-Moya, T. Blasco, F. Rey, A. Corma, and M. Puche. Distribution of Fluorine and Germanium in a New Zeolite Structure ITQ-13 Studied by  $^{19}\text{F}$  Nuclear Magnetic Resonance. *Chem. Mater.*, 15:3961–3963, 2003. DOI: 10.1021/cm034515b.
- L. A. Villaescusa, P. A. Barrett, and M. A. Cambor. Calcination of octadecasil: Fluoride removal and symmetry of the pure  $\text{SiO}_2$  host. *Chem. Mater.*, 10:3966–3973, 1998. DOI: 10.1021/cm9804113.
- L. A. Villaescusa, P. A. Barrett, and M. A. Cambor. ITQ-7: A New Pure Silica Polymorph with a Three-Dimensional System of Large Pore Channels. *Angew. Chem. Int. Ed.*, 38:1997–2000, 1999. DOI: 10.1002/(SICI)1521-3773(19990712)38:13/14<1997::AID-ANIE1997>3.0.CO;2-U.
- L. A. Villaescusa, P. Lightfoot, and R. E. Morris. Synthesis and structure of fluoride-containing  $\text{GeO}_2$  analogues of zeolite double four-ring building units. *Chem. Commun.*, pages 2220–2221, 2002. DOI: 10.1039/b207374a.
- L. A. Villaescusa, I. Bull, P. S. Wheatley, P. Lightfoot, and R. E. Morris. The location of fluoride and organic guests in ‘as-made’ pure silica zeolites FER and CHA. *J. Mater. Chem.*, 13:1978–1982, 2003. DOI: 10.1039/B300728F.



- E. T. Vogt and B. M. Weckhuysen. Fluid catalytic cracking: recent developments on the grand old lady of zeolite catalysis. *Chem. Soc. Rev.*, 44:7342–7370, 2015. DOI: 10.1039/c5cs00376h.
- R. Vomscheid, M. Briend, M. J. Peltre, P. P. Man, and D. Barthomeuf. The Role of the Template in Directing the Si Distribution in SAPO Zeolites. *J. Phys. Chem.*, 98:9614–9618, 1994. DOI: 10.1021/j100089a041.
- O. von Lilienfeld, I. Tavernelli, U. Rothlisberger, and D. Sebastiani. Optimization of Effective Atom Centered Potentials for London Dispersion Forces in Density Functional Theory. *Phys. Rev. Lett.*, 93:153004, 2004. DOI: 10.1103/PhysRevLett.93.153004.
- B. Vujic and A. P. Lyubartsev. Transferable force-field for modeling of CO<sub>2</sub>, N<sub>2</sub>, Ar and O<sub>2</sub> in all silica and Na<sup>+</sup> exchanged zeolite. *Model. Simul. Mater. Sci. Eng.*, 24:045002, 2016. DOI: 10.1088/0965-0393/24/4/045002.
- T. Wang, S. Luo, G. A. Tompsett, M. T. Timko, W. Fan, and S. M. Auerbach. Critical Role of Tricyclic Bridges including Neighboring Rings for Understanding Raman Spectra of Zeolites. *J. Am. Chem. Soc.*, 141:20318–20324, 2019. DOI: 10.1021/jacs.9b10346.
- Y. Wang, J. Song, and H. Gies. The substitution of germanium for silicon in AST-type zeolite. *Solid State Sci.*, 5: 1421–1433, 2003. DOI: 10.1016/j.solidstatesciences.2003.09.003.
- A. E. Watts, M. M. Lozinska, A. M. Slawin, A. Mayoral, D. M. Dawson, S. E. Ashbrook, B. E. Bode, A. I. Dugulan, M. D. Shannon, P. A. Cox, A. Turrina, and P. A. Wright. Site-Specific Iron Substitution in STA-28, a Large Pore Aluminophosphate Zeotype Prepared by Using 1,10-Phenanthrolines as Framework-Bound Templates. *Angew. Chem. Int. Ed.*, 59:15186–15190, 2020. DOI: 10.1002/anie.202005558.
- O. Weigel and E. Steinhoff. IX. Die Aufnahme organischer Flüssigkeitsdämpfe durch Chabasit. *Z. Kristallogr.*, 61: 125–154, 1924. DOI: 10.1524/zkri.1924.61.1.125.
- S. A. Wells and A. Sartbaeva. GASP: software for geometric simulations of flexibility in polyhedral and molecular framework structures. *Mol. Simul.*, 41:1409–1421, 2015. DOI: 10.1080/08927022.2015.1032277.
- C. E. White, J. L. Provis, T. Proffen, D. P. Riley, and J. S. Van Deventer. Combining density functional theory (DFT) and pair distribution function (PDF) analysis to solve the structure of metastable materials: The case of metakaolin. *Phys. Chem. Chem. Phys.*, 12:3239–3245, 2010. DOI: 10.1039/b922993k.
- S. R. Whittleton, A. Vicente, C. Fernandez, S. F. Rastegar, A. V. Fishchuk, and S. Sklenak. Effect of Ge/Si substitutions on the local geometry of Si framework sites in zeolites: A combined high resolution <sup>29</sup>Si MAS NMR and DFT/MM study on zeolite Beta polymorph C (BEC). *Microporous Mesoporous Mater.*, 267:124–133, 2018. DOI: 10.1016/j.micromeso.2018.03.021.
- S. T. Wilson, B. M. Lok, C. A. Messina, T. R. Cannan, and E. M. Flanigen. Aluminophosphate molecular sieves: a new class of microporous crystalline inorganic solids. *J. Am. Chem. Soc.*, 104:1146–1147, 1982. DOI: 10.1021/ja00368a062.
- R. L. Withers and Y. Liu. A coupled electron diffraction and rigid unit mode (RUM) study of the crystal chemistry of some zeotypic AlPO<sub>4</sub> compounds. *J. Solid State Chem.*, 178:2647–2657, 2005. DOI: 10.1016/j.jssc.2005.06.003.
- D. S. Wragg, R. Morris, A. W. Burton, S. I. Zones, K. Ong, and G. Lee. The Synthesis and Structure of SSZ-73: an All-Silica Zeolite with an Unusual Framework Topology. *Chem. Mater.*, 19:3924–3932, 2007. DOI: 10.1021/cm0705284.
- D. S. Wragg, R. E. Morris, and A. W. Burton. Pure Silica Zeolite-type Frameworks: A Structural Analysis. *Chem. Mater.*, 20:1561–1570, 2008. DOI: 10.1021/cm071824j.
- D. S. Wragg, R. E. Johnsen, P. Norby, and H. Fjellvåg. The adsorption of methanol and water on SAPO-34: in situ and ex situ X-ray diffraction studies. *Microporous Mesoporous Mater.*, 134:210–215, 2010. DOI: 10.1016/j.micromeso.2010.06.002.
- P. A. Wright. *Microporous Framework Solids*. RSC Materials Monographs. Royal Society of Chemistry, Cambridge, UK, 2007. DOI: 10.1039/9781847557971.

- H. Yang, R. I. Walton, S. Biedasek, S. Antonijevic, S. Wimperis, A. J. Ramirez-Cuesta, J. Li, and A. I. Kolesnikov. Experimental Observations of Water-Framework Interactions in a Hydrated Microporous Aluminum Phosphate. *J. Phys. Chem. B*, 109:4464–4469, 2005. DOI: 10.1021/jp044924a.
- R. T. Yang. *Adsorbents: Fundamentals and Applications*. John Wiley & Sons, Inc, Hoboken, NJ, USA, 1st edition, 2003.
- X. Yang. Synthesis and crystal structure of tetramethylammonium fluoride octadecasil. *Mater. Res. Bull.*, 41:54–66, 2006. DOI: 10.1016/j.materresbull.2005.07.040.
- X. Yang, M. A. Camblor, Y. Lee, H. Liu, and D. H. Olson. Synthesis and crystal structure of as-synthesized and calcined pure silica zeolite ITQ-12. *J. Am. Chem. Soc.*, 126:10403–10409, 2004. DOI: 10.1021/ja0481474.
- B. D. Yuhas, J. P. S. Mowat, M. A. Miller, and W. Sinkler. AlPO-78: A 24-Layer ABC-6 Aluminophosphate Synthesized Using a Simple Structure-Directing Agent. *Chem. Mater.*, 30:582–586, 2018. DOI: 10.1021/acs.chemmater.7b04891.
- B. D. Yuhas, K. Wilson, M. A. Miller, W. Sinkler, H. Yu, and J. P. S. Mowat. AlPO-91: A 16-Layer ABC-6 Aluminophosphate with Five Distinct Cage Types. *ACS Mater. Lett.*, 3:1752–1756, 2021. DOI: 10.1021/acsmaterialslett.1c00524.
- ZeoTech GmbH. ZeoTech Company website, 2022. URL: <https://www.zeo-tech.de/>.
- D. Zhai, L. Zhao, J. Gao, and C. Xu. Effect of temperature on the diffusion mechanism of xylene isomers in a FAU zeolite: a molecular dynamics study. *Phys. Chem. Chem. Phys.*, 14:7296–7303, 2012. DOI: 10.1039/c2cp40584a.
- B. Zibrowius and U. Lohse. Multinuclear MAS NMR study of the microporous aluminophosphate AlPO<sub>4</sub>-17 and the related silicoaluminophosphate SAPO-17. *Solid State Nucl. Magn. Reson.*, 1:137–148, 1992. DOI: 10.1016/0926-2040(92)90014-Z.
- B. Zibrowius, E. Löffler, and M. Hunger. Multinuclear MAS n.m.r. and i.r. spectroscopic study of silicon incorporation into SAPO-5, SAPO-31, and SAPO-34 molecular sieves. *Zeolites*, 12:167–174, 1992. DOI: 10.1016/0144-2449(92)90079-5.
- C. M. Zicovich-Wilson, M. L. San-Román, M. A. Camblor, F. Pascale, and J. S. Durand-Niconoff. Structure, vibrational analysis, and insights into host-guest interactions in as-synthesized pure silica ITQ-12 zeolite by periodic B3LYP calculations. *J. Am. Chem. Soc.*, 129:11512–11523, 2007. DOI: 10.1021/ja0730361.
- C. M. Zicovich-Wilson, F. Gándara, A. Monge, and M. A. Camblor. In situ transformation of TON silica zeolite into the less dense ITW: Structure-direction overcoming framework instability in the synthesis of SiO<sub>2</sub> zeolites. *J. Am. Chem. Soc.*, 132:3461–3471, 2010a. DOI: 10.1021/ja9094318.
- C. M. Zicovich-Wilson, M. L. San Román, and A. Ramírez-Solís. Mechanism of F<sup>-</sup> Elimination from Zeolitic D4R Units: A Periodic B3LYP Study on the Octadecasil Zeolite. *J. Phys. Chem. C*, 114:2989–2995, 2010b. DOI: 10.1021/jp9088244.
- N. E. Zimmermann, M. Haranczyk, M. Sharma, B. Liu, B. Smit, and F. J. Keil. Adsorption and diffusion in zeolites: the pitfall of isotopic crystal structures. *Mol. Simul.*, 37:986–989, 2011. DOI: 10.1080/08927022.2011.562502.
- M. Zokaie, U. Olsbye, K. P. Lillerud, and O. Swang. Stabilization of Silicon Islands in Silicoaluminophosphates by Proton Redistribution. *J. Phys. Chem. C*, 116:7255–7259, 2012a. DOI: 10.1021/jp210537v.
- M. Zokaie, U. Olsbye, K. P. Lillerud, and O. Swang. A computational study on heteroatom distribution in zeotype materials. *Microporous Mesoporous Mater.*, 158:175–179, 2012b. DOI: 10.1016/j.micromeso.2012.03.005.
- S. I. Zones, S.-j. Hwang, S. Elomari, I. Ogino, M. E. Davis, and A. W. Burton. The fluoride-based route to all-silica molecular sieves; a strategy for synthesis of new materials based upon close-packing of guest–host products. *C. R. Chim.*, 8:267–282, 2005. DOI: 10.1016/j.crci.2004.12.009.

- S. I. Zones, A. W. Burton, G. S. Lee, and M. M. Olmstead. A study of piperidinium structure-directing agents in the synthesis of silica molecular sieves under fluoride-based conditions. *J. Am. Chem. Soc.*, 129:9066–9079, 2007. DOI: 10.1021/ja0709122.
- M. A. Zwijnenburg and R. G. Bell. Absence of Limitations on the Framework Density and Pore Size of High-Silica Zeolites. *Chem. Mater.*, 20:3008–3014, 2008. DOI: 10.1021/cm702175q.
- M. A. Zwijnenburg, F. Corá, and R. G. Bell. On the performance of DFT and interatomic potentials in predicting the energetics of (three-membered ring-containing) siliceous materials. *J. Phys. Chem. B*, 111:6156–6160, 2007. DOI: 10.1021/jp071060v.

## APPENDIX: ORIGINAL ARTICLES AND COPYRIGHT INFORMATION

The appendix gives information on all articles compiled in this thesis. Copyright information is given below, adhering to the guidelines of the respective publishers. It should be noted title case capitalisation was used for all article titles throughout the thesis. For the actual published articles, different publishers imposed different capitalisation guidelines. The list below includes the titles as used by the publishers. *For copyright reasons, the articles have not been included in the public version of the thesis, but they are available under the URLs provided below.*

- **Article A1:** *Structure and bonding of water molecules in zeolite hosts: Benchmarking plane-wave DFT against crystal structure data*, reprinted with permission from: M. Fischer, *Z. Kristallogr.* **2015**, 230, 325–336. *Zeitschrift für Kristallographie – Crystalline Materials* is published by Walter de Gruyter GmbH, Berlin, Germany.  
URL: <https://doi.org/10.1515/zkri-2014-1809>
- **Article A2:** *Benchmarking DFT-GGA calculations for the structure optimisation of neutral-framework zeotypes*, reprinted from: M. Fischer, F. O. Evers, F. Formalik, A. Olejniczak, *Theor. Chem. Acc.* **2016**, 135, 257, with the permission of Springer Publishing.  
URL: <https://doi.org/10.1007/s00214-016-2014-6>
- **Article A3:** *Accurate structures and energetics of neutral-framework zeotypes from dispersion-corrected DFT calculations*, reprinted from: M. Fischer, R. J. Angel, *J. Chem. Phys.* **2017**, 146, 174111, with the permission of AIP Publishing.  
URL: <http://doi.org/10.1063/1.4981528>
- **Article A4:** *Benchmarking the performance of approximate van der Waals methods for the structural and energetic properties of SiO<sub>2</sub> and AlPO<sub>4</sub> frameworks*, reprinted from: M. Fischer, W. J. Kim, M. Badawi, S. Lebègue, *J. Chem. Phys.* **2019**, 150, 094102, with the permission of AIP Publishing.  
URL: <https://doi.org/10.1063/1.5085394>
- **Article A5:** *Template effects on the pressure-dependent behavior of chabazite-type fluoroaluminophosphates: a computational approach*, reprinted from: M. Fischer, *Phys. Chem. Minerals* **2019**, 46, 385–401, with the permission of Springer Publishing.  
URL: <https://doi.org/10.1007/s00269-018-1010-x>
- **Article B1:** *Local Environment and Dynamic Behavior of Fluoride Anions in Silicogermanate Zeolites: A Computational Study of the AST Framework*, reprinted with permission from: M. Fischer, *J. Phys. Chem. C* **2019**, 123, 1852–1865.  
Copyright 2019 American Chemical Society.  
URL: <https://doi.org/10.1021/acs.jpcc.8b10770>
- **Article B2:** *Local Distortions in a Prototypical Zeolite Framework Containing Double Four-Ring Cages: The Role of Framework Composition and Organic Guests*, reprinted from: M. Fischer, L. Freymann, *ChemPhysChem* **2021**, 22, 40–54.  
Copyrighted under Creative Commons Attribution license (CC-BY 4.0), publisher: Wiley-VCH GmbH (2021).  
URL: <https://doi.org/10.1002/cphc.202000863>

- **Article B3:** *Influence of Organic Structure-Directing Agents on Fluoride Dynamics in As-Synthesized Silicalite-1*, reprinted with permission from: M. Fischer, *J. Phys. Chem. C* **2020**, *124*, 5690–5701. Copyright 2020 American Chemical Society.  
URL: <https://doi.org/10.1021/acs.jpcc.9b11608>
- **Article B4:** *Fluoride Anions in All-Silica Zeolites: Studying Preferred Fluoride Sites and Dynamic Disorder with Density Functional Theory Calculations*, reprinted with permission from: M. Fischer, *J. Phys. Chem. C* **2021**, *125*, 8825–8839. Copyright 2021 American Chemical Society.  
URL: <https://doi.org/10.1021/acs.jpcc.1c01440>
- **Article B5:** *Elucidating the Germanium Distribution in ITQ-13 Zeolites by Density Functional Theory*, reprinted from: M. Fischer, C. Bornes, L. Mafra, J. Rocha, *Chem. Eur. J.* **2022**, *28*, e202104298. Copyrighted under Creative Commons Attribution-NonCommercial license (CC-BY-NC 4.0), publisher: Wiley-VCH GmbH (2022).  
URL: <https://doi.org/10.1002/chem.202104298>
- **Article C1:** *Water adsorption in SAPO-34: Elucidating the role of local heterogeneities and defects using dispersion-corrected DFT calculations*, reproduced from: M. Fischer, *Phys. Chem. Chem. Phys.* **2015**, *17*, 25260–25271, with permission from the PCCP Owner Societies.  
URL: <http://doi.org/10.1039/c5cp04189a>
- **Article C2:** *Interaction of water with (silico)aluminophosphate zeotypes: a comparative investigation using dispersion-corrected DFT*, reproduced from: M. Fischer, *Phys. Chem. Chem. Phys.* **2016**, *18*, 15738–15750, with permission from the PCCP Owner Societies.  
URL: <http://doi.org/10.1039/c6cp02289h>
- **Article C3:** *First-Principles Study of AlPO<sub>4</sub>-H<sub>3</sub>, a Hydrated Aluminophosphate Zeotype Containing Two Different Types of Adsorbed Water Molecules*, reprinted from: M. Fischer, *Molecules*, **2019**, *24*, 922. Copyrighted under Creative Commons Attribution license (CC-BY 4.0), publisher: MDPI (2019).  
URL: <https://doi.org/10.3390/molecules24050922>
- **Article C4:** *Proton Acidity and Proton Mobility in ECR-40, a Silicoaluminophosphate that Violates Löwenstein's Rule*, reprinted from: M. Fischer, *Chem. Eur. J.* **2019**, *25*, 13579–13590. Copyrighted under Creative Commons Attribution-NonCommercial-NoDerivatives license (CC-BY-NC-ND 4.0), publisher: Wiley-VCH GmbH (2019).  
URL: <https://doi.org/10.1002/chem.201902945>
- **Article C5:** *Revisiting the Structure of Calcined and Hydrated AlPO-11 with DFT-Based Molecular Dynamics Simulations*, reprinted from: M. Fischer, *ChemPhysChem* **2021**, *22*, 2063–2077. Copyrighted under Creative Commons Attribution-NonCommercial license (CC-BY-NC 4.0), publisher: Wiley-VCH GmbH (2021).  
URL: <https://doi.org/10.1002/cphc.202100486>